



HAL
open science

Reduced basis methods for urban air quality modeling

Janelle K. Hammond

► **To cite this version:**

Janelle K. Hammond. Reduced basis methods for urban air quality modeling. Modeling and Simulation. Université Paris-Est, 2017. English. NNT : 2017PESC1230 . tel-01759410

HAL Id: tel-01759410

<https://theses.hal.science/tel-01759410>

Submitted on 5 Apr 2018

HAL is a multi-disciplinary open access archive for the deposit and dissemination of scientific research documents, whether they are published or not. The documents may come from teaching and research institutions in France or abroad, or from public or private research centers.

L'archive ouverte pluridisciplinaire **HAL**, est destinée au dépôt et à la diffusion de documents scientifiques de niveau recherche, publiés ou non, émanant des établissements d'enseignement et de recherche français ou étrangers, des laboratoires publics ou privés.



THÈSE DE DOCTORAT

DISCIPLINE: MATHÉMATIQUES APPLIQUÉES

Ecole Doctorale Mathématiques, et Sciences et Technologies de l'Information et de la Communication (MSTIC)

Méthodes des bases réduites pour la qualité de l'air en milieu urbain

Janelle K. HAMMOND

Préparée à l'Institut français des sciences et technologies des transports, de l'aménagement, et des réseaux (IFSTTAR)

Soutenue le 13 novembre, 2017

Jury

<i>Président</i>	Martin GREPL	RWTH Aachen
<i>Rapporteurs</i>	Ludovic CHAMOIN	ENS Paris-Saclay
	Anthony NOUY	Ecole Centrale de Nantes
<i>Examineurs</i>	Faker BEN BELGACEM	Université de Technologie Compiègne
	Christophe PRUD'HOMME	Université Strasbourg 1
<i>Directeur de thèse</i>	Frédéric BOURQUIN	Université Paris Est, IFSTTAR
<i>Co-directeur de thèse</i>	Yvon MADAY	Sorbonne Universités, UPMC Paris VI
<i>Encadrant de thèse</i>	Rachida CHAKIR	Université Paris Est, IFSTTAR

Abstract

Key Words: Reduced Basis Method, Model Order Reduction, Data Assimilation, Air Quality Modeling

The principal objective of this thesis is the development of low-cost numerical tools for spatial mapping of pollutant concentrations from field observations and advanced deterministic models. With increased pollutant emissions and exposure due to mass urbanization and development worldwide, air quality measurement campaigns and epidemiology studies of the association between air pollution and adverse health effects have become increasingly common. However, as air pollution concentrations are highly variable spatially and temporally, the sensitivity and accuracy of these epidemiology studies is often deteriorated by exposure misclassification due to poor estimates of individual exposures. Data assimilation methods incorporate available measurement data and mathematical model to provide improved approximations of the concentration. These methods, when based on an advanced deterministic air quality models (AQMs), could provide spatially-rich small-scale approximations and can enable better estimates of effects and exposures. However, these methods can be computationally expensive. They require repeated solution of the model, which could itself be costly.

In this work we investigate a combined reduced basis (RB) data assimilation method for use with advanced AQMs on urban scales. We want to diminish the cost of resolution, using RB arguments, and incorporate measurement data to improve the quality of the solution. We extend the Parameterized-Background Data-Weak (PBDW) method to physically-based AQMs. This method can rapidly estimate "online" pollutant concentrations at urban scale, using available AQMs in a non-intrusive and computationally efficient manner, reducing computation times by factors up to hundreds. We apply this method in case studies representing urban residential pollution of $PM_{2.5}$, and we study the stability of the method depending on the placement of air quality sensors. Results from the PBDW are compared to the Generalized Empirical Interpolation Method (GEIM) and a standard inverse problem, the adjoint method, in order to measure efficiency of the method. This comparison shows possible improvement in precision and great improvement in computation cost with respect to classical methods. We find that the PBDW method shows promise for the real-time reconstruction of a pollution field in large-scale problems, providing state estimation with approximation error generally under 10% when applied to an imperfect model.

Résumé

Mots Clés: Méthodes des Bases Réduites, Réduction de Modèle, Assimilation de Données, Modélisation de la Qualité de l’Air

L’objectif principal de cette thèse est le développement d’outils numériques peu coûteux pour la cartographie de concentrations de polluants à partir de mesures et de modèles déterministes avancés. L’urbanisation de la population et le développement mondial de ces dernières années a entraîné une hausse des émissions de polluants. Avec une population de plus en plus exposée à la pollution, les campagnes de mesure de qualité de l’air et les études sur les effets de la pollution sur la santé n’ont cessé d’augmenter. Cependant, la sensibilité et la précision de ces études est souvent altérée par des estimations grossières des taux d’expositions individuelles. Ceci à cause d’un manque d’information sur la concentration des polluants qui est très variable dans l’espace et dans le temps. Les méthodes d’assimilation de données intègrent des données de mesures et des modèles mathématiques afin de mieux approcher le champ de concentration. Quand ces méthodes sont fondées sur un modèle de qualité de l’air déterministe avancé, elles sont capables de fournir des approximations détaillées. Ces informations précises permettraient d’avoir de meilleures estimations des taux d’exposition. Néanmoins, ces méthodes sont souvent très coûteuses. En effet, elles nécessitent de multiples résolutions du modèle, souvent coûteuses.

Dans cette thèse nous nous intéressons à l’étude et la mise en oeuvre de méthodes reposant sur la méthode des bases réduites et l’assimilation des données pour des modèles déterministes de qualité de l’air à l’échelle urbaine. Nous souhaitons diminuer le coût de résolution en utilisant des bases réduites et incorporer des données de mesure afin d’améliorer la qualité de la solution. On étend la méthode *Parameterized-Background Data-Weak* (PBDW) à des modèles de qualité de l’air. Cette méthode est capable d’estimer *online* des concentrations de polluants rapidement, à l’échelle du quartier. Cette méthode, qui est non intrusive, permet de diviser le coût de résolution par cent, sans détériorer la qualité des solutions. Nous avons implanté cette méthode et étudié sa stabilité en fonction de la position des capteurs. Cette étude a été faite pour différents scénarios de pollution d’une zone résidentielle. Ces résultats ont été comparés à ceux donnés par la méthode d’interpolation empirique généralisée (GEIM) et ceux d’une méthode inverse de type problème adjoint. Cette comparaison montre la possibilité d’augmenter la précision de la solution et de réduire significativement les temps de calcul par rapport aux méthodes classiques. Lorsque la méthode PBDW est utilisée avec un modèle imparfait, elle donne des cartographies de concentration avec une erreur d’approximation de moins de 10%. Les résultats de la PBDW se montrent prometteurs pour la reconstruction en temps réel de champs de pollution à grande échelle.

Acknowledgments

Tout d'abord j'aimerais exprimer ma reconnaissance envers mes directeurs et mon encadrante. Je voudrais remercier mon directeur de thèse Frédéric BOURQUIN pour ses conseils scientifiques ainsi que ses critiques constructives sur mes communications scientifiques. Un grand merci pour la confiance qu'il m'a accordée en acceptant de diriger mon travail de thèse, et pour son optimisme et son ouverture vers les projets de collaboration. Je souhaiterais aussi remercier mon co-directeur de thèse Yvon MADAY, professeur très influent et pédagogue durant mes études de master, pour sa direction méthodologique et scientifique. Son soutien et sa patience m'ont été précieux tout au long de ce travail. J'ai particulièrement apprécié son optimisme et sa disponibilité régulière pour répondre à mes questions et me donner des conseils.

Je remercie mon encadrante Rachida CHAKIR, avec qui j'ai travaillé en étroite collaboration durant mon stage de master et ensuite durant ma thèse, pour la confiance qu'elle m'a accordée en me prenant sous son encadrement. Rachida m'a guidée en matière scientifique, professionnelle, pédagogique, et administrative, elle m'a encouragée à participer à des conférences et des colloques scientifiques, elle m'a aidée dans mes projets professionnels d'enseignements et de collaboration internationale. Sa porte fut toujours ouverte pour toute question méthodologique ou technique et sa patience sans limite. Son soutien m'a été énormément précieux durant ces trois années difficiles, et je n'aurai jamais pu souhaiter travailler avec une meilleur encadrante de thèse et collaboratrice.

Je souhaiterais remercier mes rapporteurs Ludovic CHAMOIN et Anthony NOUY pour le temps qu'ils ont accordé à la lecture de cette thèse. Leurs remarques et critiques m'ont aidé à améliorer mon manuscrit ainsi que ma présentation orale des travaux. Je remercie également Faker BEN BELGACEM, Martin GREPL, et Christophe PRUD'HOMME d'avoir accepté de participer à mon jury de thèse.

Je voudrais aussi remercier les collègues du laboratoire LISIS pour leur soutien et amitié. Plus particulièrement je remercie aussi Erick MERLIOT pour son aide avec la génération de géométries indispensables à mes simulations numériques. Je remercie Emmanuel BOURGEOIS pour sa collaboration sur une application de génie des tunnels durant mon stage de master. Je remercie Julien WAeyTENS pour ses conseils lors des diverses discussions avec Rachida, particulièrement sur la mise en oeuvre de la méthode adjointe. Je remercie Patrice CHATELLIER pour son soutien dans les nombreuses réunions de suivi, dans les communications, et pour ses conseils professionnels. Un grand merci aussi à Sylvie KOUDOOUHO pour son aide précieux en toute matière administrative au laboratoire.

I would like to thank Prof. A.T. PATERA for helpful discussions and advice on multiple occasions. I would also like to express sincere gratitude to Betsey NOTH and Prof. K. HAMMOND, for their willingness to collaborate in their projects in Fresno, as well as for the incredible opportunity to spend some time as a Visiting Student Researcher at the University of California Berkeley.

I thank my family and friends for supporting me throughout, mes amis et ma famille en France, mes amis co-doctorants du LISIS and those across the Atlantic. My parents and siblings for emotional support, and my Aunt Kathie for long discussions at all hours about my studies, research, and professional goals, providing endless support and pertinent advice. Enfin j'aimerais remercier mon conjoint Guillaume pour son soutien quotidien, son enthousiasme à l'égard de mes travaux, et pour sa compagnie et son affection en périodes difficiles.

Contents

Abstract	ii
Acknowledgments	iv
Contents	v
Introduction	1
Thesis Overview	9
I Background : air quality modeling, model order reduction and data assimilation methods	17
1 A review of current air quality models	19
1.1 Introduction	20
1.1.1 Air Pollution	20
1.1.2 Pollutants to monitor	21
1.1.3 Pollution sources and emissions	21
1.2 Air Pollution modeling	25
1.2.1 History and development	26
1.2.2 Model categories	27
1.2.3 Limitations and Uncertainties	43
1.2.4 Modeling chains	47
1.3 Improvements in Air Quality Modeling	50
1.3.1 Modeling advances	50
1.3.2 Techniques to improve results	53
2 A review of model reduction and data assimilation techniques	57
2.1 Model Order Reduction	58
2.1.1 Surrogate model methods	58
2.1.2 Projection-based methods	59
2.1.3 A decomposition method: Proper Generalized Decomposition	67
2.2 Data Assimilation	70
2.2.1 Linear Estimation Theory	71
2.2.2 Sequential Methods	71
2.2.3 Inverse Methods	73
2.2.4 Variational methods	75
2.3 Model Order Reduction and Data Assimilation in the Air Quality Modeling context	77

2.3.1	Data Assimilation for AQM	77
2.3.2	Model Order Reduction for AQM	80
II Reduced Order Data Assimilation Methods and Application in Air Quality Modeling		83
3	Reduced Order Data Assimilation: PBDW and GEIM	85
3.1	PBDW	86
3.1.1	Introduction	86
3.1.2	PBDW Formulation	87
3.1.3	PBDW error and stability considerations	92
3.2	GEIM	93
4	Adaptations for Complex Large-Scale Applications and Pollution Modeling	99
4.1	PBDW: technical details and analysis	100
4.1.1	PBDW in Practice	100
4.1.2	GEIM in the PBDW framework	108
4.1.3	Motivation for PBDW in air quality studies	108
4.2	Pollutant Transport Modeling	112
4.2.1	Wind field modeling for air quality studies	112
4.2.2	Transport modeling for air quality studies	114
4.2.3	Advection-Diffusion-Reaction	122
III Numerical Results: RB and PBDW		123
5	Application and Analysis in Exterior Air Quality Modeling: a 2D Case Study	125
5.1	Introduction to the Numerical Case Study	126
5.1.1	Velocity Field	126
5.1.2	Parameters	126
5.1.3	2D Case Study	128
5.2	Implementation of the PBDW method	130
5.2.1	Background RB space	130
5.2.2	Sensor locations and Update Space	132
5.3	State Estimation Results : PBDW	134
5.4	PBDW Norm modifications	148
5.4.1	Adapted sensor placement	153
5.5	Comparison to other methods: GEIM	158
5.5.1	Norm modifications	160
5.6	Comparison to other methods: the adjoint problem	161
5.6.1	Adjoint Transport Problem: problem definition	162
5.6.2	Definition of the parameters	163
5.6.3	State estimation results	165
5.7	Computational times	172

6	Application in Exterior Air Quality Modeling: a 3D Case Study	175
6.1	Initial study	177
6.1.1	Sensor locations and update space	179
6.1.2	PBDW state estimation	182
6.1.3	PBDW Norm Modifications	193
6.2	Adapted dimensionless case study	195
6.2.1	A Simpler Background Space	197
6.2.2	Sensor locations and Update space	199
6.2.3	PBDW state estimation	200
7	A Real-World Application: Air Quality Modeling for Fresno	205
7.1	Introduction	206
7.2	Fresno Case Study: a central neighborhood	208
7.2.1	Geometry and Mesh	209
7.2.2	A CFD wind field	211
7.2.3	Pollutant concentration fields	212
7.2.4	PBDW state estimation	215
7.3	Conclusion and Perspectives	221
IV A	Study in Tunnel Engineering	223
8	A non-intrusive reduced basis method for elastoplasticity problems in geotechnics	225
8.1	Introduction	225
8.2	The elastoplastic problem	228
8.2.1	From material behavior laws to the governing equations	228
8.3	Methodology	233
8.3.1	POD analysis	235
8.3.2	A non-intrusive reduced basis method : two-grid FE/RB method with a rectification approach	238
8.4	Numerical experiments	241
8.4.1	Single tunnel study case	241
8.4.2	Twin tunnel study case	245
8.5	Conclusions	247
Conclusion		249
V	Appendices and References	255
A	Introduction - English	257
B	Glossary	265
List of Figures		267
List of Tables		278

C	Technical Implementation Notes	281
C.1	Code_Saturne for Fluid Dynamics	281
C.2	MOR Algorithms	281
	Bibliography	285

Introduction

An English version of the introduction can be found in Appendix A.

L'objectif principal de cette thèse est le développement d'outils numériques pour la cartographie en temps réel de concentrations de polluants à partir de mesures et de modèles déterministes avancés.

Motivation et Contexte

D'après [101], au moins 40000 morts par an ont été attribués à la pollution extérieure en Autriche, en Suisse, et en France. Par ailleurs, une étude sur 22 groupes dans 13 pays d'Europe [18] a révélé que l'exposition à long terme aux particules fines $PM_{2.5}$ est associée à la mortalité par cause naturelle, et que cette association reste statistiquement significative pour des concentrations en-dessous des seuils annuels moyens en Europe ($25 \frac{\mu g}{m^3}$). D'autre part, d'après l'OMS (Organisation Mondiale de la Santé), un neuvième de la mortalité mondiale en 2012 pouvait être liée à la pollution de l'air, dont 3 millions uniquement dus à la pollution de l'air extérieur [144]. Des effets sur la santé tels que les infections respiratoires aiguës, la bronchopneumopathie chronique obstructive, les AVC (Accident Vasculaire Cérébral), les pathologies cardiaques et les cancers du poumon, avaient été analysés afin d'estimer la morbidité globale que représentent les maladies liées à la pollution de l'air. Néanmoins de nombreuses autres maladies associées à la pollution de l'air n'ont pas été incluses dans cette analyse en raison d'un manque de preuves suffisamment robustes. Point important à noter, ces études se concentrent sur la pollution aux particules fines, mais de multiples études, comme [147], ont démontré que d'autres espèces de polluants jouent un rôle important dans de nombreuses pathologies. C'est pourquoi, des estimations fiables d'expositions et une compréhension des impacts de la pollution de l'air sont indispensables pour mieux étayer les études sur la morbidité globale, en santé publique, pour le développement de réglementations, et le développement urbain.

Afin de mieux comprendre les conséquences sur la santé de l'exposition à la pollution de l'air il faut, pour chacune des espèces de polluant, étudier les relations exposition-réponse¹. Ces études comptent en général un très grand nombre de sujets (par exemple la cohorte de presque 43.000 naissances examinées dans [147] afin d'étudier le rapport entre l'exposition aux hydrocarbures aromatiques polycycliques et le risque de naissance prénatale) et nécessitent des données individuelles sur le taux d'exposition à la substance mise en cause avant et durant la période de l'étude [42]. Cependant la taille de l'échantillon empêche de réaliser des mesures individuelles pour chaque participant. Bien que la tech-

¹Les relations exposition-réponse sont les relations observées entre l'exposition à la pollution en tant que cause et les résultats particuliers en tant qu'effet.

nologie des capteurs de pollution de l'air ait beaucoup évolué ces dernières années, rendant ces capteurs plus économiques, plus petits, et plus mobiles, la complexité et la portée des effets de la pollution de l'air nécessitent plus d'outils pour améliorer la compréhension et le contrôle de la qualité de l'air. Par exemple, des informations sur la distribution spatiale des polluants sont nécessaires pour plusieurs types d'études, dont celles relatives aux effets sur la santé. En effet, plusieurs espèces de polluants ont des concentrations très variables dans la ville, comme on peut le voir dans le tableau 0.1 qui montre la variabilité spatiale de la concentration de cinq espèces de polluants dans le centre de Fresno, Californie.

Polluants	Points d'observations	Valeur Médiane	1 ^{er} quartile	3 ^{eme} quartile	Rapport P90/P10 (90 ^{eme} et 10 ^{eme} centiles) ¹
Particules HAP ²	171	0.45	0.25	0.67	9.1
Carbone élémentaire	114	0.77	0.42	1.10	6.4
Endotoxine	182	1.20	0.89	1.67	3.7
Particules PM_{10}	278	0.42	0.35	0.51	2.2
Particules $PM_{2.5}$	283	0.96	0.83	1.14	1.9

TABLE 0.1 – Variation spatiale de la concentration de polluants extérieurs sur un site d'observations dans le centre de Fresno (CA), durant la haute saison de chaque polluant [137].

De plus, pour certaines pathologies, l'analyse des effets se fait sur des expositions de courtes durées. C'est le cas, par exemple des anomalies congénitales dues à des expositions d'une à deux semaines. Ceci implique plus de variabilité spatiale et temporelle dans les évaluations. Dans une ville, les mesures de pollution en continue sur une longue période sont généralement faites sur un ou deux sites fixés. De plus, un unique profil d'exposition est attribué à toutes les personnes de l'étude épidémiologique. Des modèles de qualité de l'air (AQM, pour air quality model) peuvent fournir des approximations de concentration d'un ou plusieurs polluants à des échelles spatiales et temporelles variées. Ces informations sont nécessaires pour l'évaluation des taux d'exposition à partir des mesures lorsqu'on ne peut pas mettre un capteur à proximité de chaque zone d'intérêt. En plus de l'évaluation des taux d'exposition, la détection et l'identification des sources d'émission sont aussi des thèmes courants dans les études de qualité de l'air, les études préliminaires avant la mise en place de réglementation, ou de procédures d'urgence. Par ailleurs, comprendre le devenir de la pollution de l'air est nécessaire pour la prévision, la régulation (modification de la composition des carburants, restrictions de circulation pour certains véhicules) et le développement urbain. Les modèles permettent notamment de prévoir les effets de futurs accidents ou de pics de pollution sur la qualité de l'air. Ces prévisions peuvent être prises en compte par exemple dans la mise en place de nouvelles réglementations, mais aussi dans les études d'urbanisme pour les projets de nouvelles constructions. En effet, ces prévisions pourraient être utilisées afin de construire de nouveaux hôpitaux et écoles, là où il y aurait le moins de pollution. Sans modèle de qualité de l'air, aucune de ces études n'aurait la flexibilité nécessaire, voire ne serait faisable avant la prise de décision et la mise en place de nouveaux changements. Les prévisions à des échelles spatiales variées proposées par la simulation numérique, en complément de données de mesures clairsemées, peuvent fournir

¹Les centiles $P\alpha$ correspondent aux valeurs telles que $\alpha\%$ des mesures leur soient inférieures.

²Hydrocarbures Aromatiques Polycycliques

des informations avec un niveau de détail largement amélioré. Elles peuvent être utilisées dans les études sur l'exposition à la pollution à l'échelle de l'individu, et son effet sur la santé, la compréhension des émissions et de la dispersion de polluants, le développement de projets urbains intelligents, et la gestion des crises.

De l'enjeu de société à l'étude scientifique

Il existe de nombreuses méthodes de modélisation de la qualité de l'air de niveaux de sophistication variable (une excellente revue est donnée par [202]) : approches empiriques, modèles statistiques et méthodes déterministes. Parmi les modèles déterministes le niveau de sophistication des approches varie également, allant des simples modèles analytiques de panache gaussiens [180], en passant par des modèles Lagrangiens [89], jusqu'aux modèles Eulériens basés sur la CFD (Computational Fluid Dynamics) tel que le modèle simple utilisé dans cette thèse. Il est connu que la pollution de l'air est très variable à l'échelle urbaine. C'est pourquoi l'utilisation de modèles capables de fournir des approximations détaillées à l'échelle locale, et qui prennent en compte la physique est importante. Les modèles déterministes avancés, lorsqu'ils sont correctement calibrés et mis en œuvre avec des données précises sur l'environnement et sur les émissions de polluants, peuvent fournir des informations détaillées dans le temps et dans l'espace sur les concentrations de polluants, ainsi que sur les phénomènes physiques altérant la qualité de l'air. Cependant, la modélisation de la qualité de l'air est limitée par la nature complexe du problème (effets physiques non linéaires, géométries urbaines complexes), mais aussi par les incertitudes non négligeables sur les données d'entrée telles que les conditions météorologiques, conditions limites, et données d'émissions. Etant donnée la complexité des applications "in-situ", nous ne pouvons pas supposer que même les modèles déterministes les plus avancés et les mieux calibrés (ou bien des modèles non déterministes) puissent représenter de façon exacte tous les phénomènes physiques en jeu.

L'amélioration de la qualité des données disponibles (sur la météorologie, les émissions et les concentrations de fond, etc.), du traitement mathématique des phénomènes physiques (par exemple les schémas de turbulence pour la modélisation du vent) et des mécanismes chimiques ont permis d'augmenter considérablement la précision des modèles. Les modèles de qualité de l'air opérationnels peuvent aussi être améliorés en les couplant à des données de mesures de concentration. Pour cela, il existe des méthodes statistiques, tels que la correction de biais et la prévision probabiliste, la modélisation par ensemble (où plusieurs modèles ou données d'entrée sont utilisés et combinés aux solutions dans le but de réduire l'erreur globale de modélisation), mais aussi des méthodes d'assimilation de données. Celles-ci reposent sur l'intégration des connaissances de la physique décrites par un modèle mathématique déterministe et des observations expérimentales. Les méthodes sont variées et cherchent à corriger un ou plusieurs paramètres du modèle ou l'état du système. Les méthodes séquentielles (e.g. le filtre de Kalman [127]) se servent des données dès qu'elles sont disponibles pour trouver la meilleure approximation de l'état du système physique. Les méthodes inverses cherchent la valeur optimale d'un ou de plusieurs paramètres du modèle afin de minimiser l'écart aux mesures. Les méthodes variationnelles se basent sur la minimisation d'une fonction de coût qui quantifie l'écart entre l'approximation du modèle et les observations, dans le but de trouver l'état optimal du système. Ceci permet ainsi aux données de corriger l'erreur du modèle.

De nombreuses études ont été menées sur les processus qui influencent la qualité de l'air

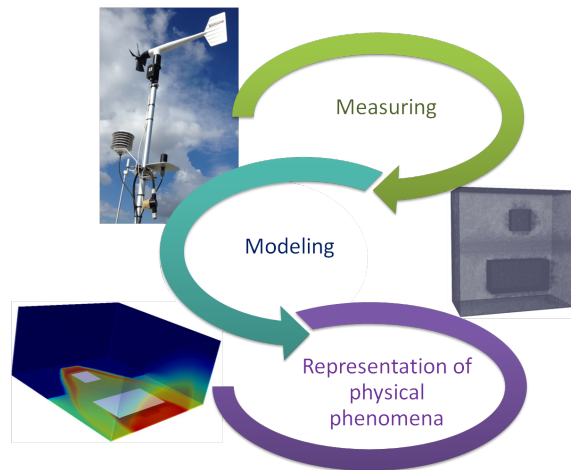


FIGURE 0.1 – Illustration de la procédure de modélisation de phénomènes physiques avec des données de mesure.

et sur les modèles d'exposition à la pollution. Elles vont de la modélisation du trafic, des émissions, du transport des polluants. L'implantation idéale de toutes ces connaissances nécessite une chaîne de modélisation, utilisant des sorties du "niveau" précédent comme données d'entrée pour le suivant. Les données sorties d'un modèle doivent souvent être converties avant d'être utilisées comme données d'entrée du modèle suivant. De plus ce chaînage de modèle implique le lancement de nombreux calculs coûteux à différentes étapes de la chaîne. Il existe des compagnies en France et dans le monde qui sont spécialisées dans la mise en œuvre de telles chaînes de modélisation. Pour répondre aux besoins des clients elles utilisent des techniques modernes. Elles contribuent ainsi, considérablement au développement de bibliothèques de logiciels de modélisation pour la qualité de l'air qui pourront être utilisées dans de futures études. Bien que cela représente un progrès significatif dans la modélisation de phénomènes physiques complexes et en partie inconnus, ces outils, de façon générale, sont confrontés au problème de l'explosion des temps de calcul, lorsqu'ils sont utilisés sur des domaines larges et complexes. C'est pourquoi, l'utilisation de la réduction de modèle est particulièrement pertinente dans ces applications. En effet, elles nécessitent toujours plus de précision, sur des échelles de plus en plus petites, afin d'être utilisées pour l'analyse des causes, du devenir et des effets de la pollution de l'air.

La réduction de modèle fait référence aux méthodes de réduction du coût de calcul d'une simulation par la simplification du problème ou bien par la réduction de la dimension du problème en utilisant des connaissances a priori sur le système. Parmi ces méthodes de réduction on trouve des méthodes de substitution des modèles ou des meta-modèles, pour lesquelles un modèle plus simple prend la place du modèle coûteux (que l'on nommera \mathcal{P}). Les méthodes de projection font également partie des méthodes de réduction. Elles utilisent un espace réduit sur lequel sont projetés les opérateurs du modèle. Cette dernière famille de méthodes, comprenant les méthodes des bases réduites, cherche à exploiter le caractère paramétrique du problème, et plus particulièrement la dimension de la variété de toutes les solutions possibles lorsque les paramètres varient. Parmi les méthodes de projection on trouve également les méthodes de décomposition telles que la décomposition orthogonale aux valeurs propres (POD) [22] et la décomposition propre généralisée (PGD) [41], mais aussi les méthodes telles que la méthode d'interpolation empirique (EIM) [16] qui utilise

la connaissance de la solution aux points d'interpolation dans le domaine.

L'objectif de cette thèse est de combiner la réduction de modèle et l'assimilation des données pour des applications dans la qualité de l'air. Le reste de cette introduction est organisé autour d'une série de questions à poser sur un projet de recherche, dénommée *Heilmeyer's Catechism*¹.

(1) Quel est le défi ? Les méthodes d'assimilation de données déterministes reposent sur le calcul de solutions de modèles. Ces modèles, parfois sophistiqués, dérivent d'équations aux dérivées partielles (EDP) qui dépendent d'un ou plusieurs paramètres. Notre objectif est de proposer des méthodes numériques qui rendraient ces modèles plus abordables, du point de vue des ressources et des temps de calcul nécessaires. Le fait de pouvoir effectuer les simulations rapidement sur des machines peu onéreuses, sans détériorer la qualité des résultats, serait très intéressant. Les modèles avancés de qualité de l'air pourraient ainsi être plus facilement utilisés pour des études in-situ, la réglementation et l'amélioration de la qualité de l'air.

(2) Quelle est la solution actuelle ? Il existe aujourd'hui de multiples méthodes numériques peu coûteuses qui permettent d'élaborer des cartographies de la qualité de l'air à partir de mesures. Les méthodes de Krigeage [203] qui sont des méthodes d'interpolation stochastiques, permettent de prendre en compte la structure spatiale du phénomène étudié. Cependant, elles nécessitent des données appropriées et suffisamment nombreuses pour décrire correctement les phénomènes physiques en jeu. Parmi les méthodes déterministes, les méthodes inverses peuvent être implantées de façon plus efficace en employant des méthodes des bases réduites pour réduire le coût de résolution. Cependant, la mise en œuvre peut se révéler compliquée, par exemple pour des problèmes non linéaires ou lorsque les données à traiter sont nombreuses. Par ailleurs, cette méthode traite uniquement l'erreur due à la variation paramétrique, non celle due à une éventuelle erreur de modèle.

(3) Que proposons-nous pour améliorer les solutions de demain ? Dans cette thèse nous proposons des outils numériques non (ou peu) intrusifs qui permettent d'effectuer rapidement des simulations pour l'élaboration de cartes détaillées de concentration d'un polluant dans un quartier. Ces outils utilisent des mesures de concentration et des solutions de modèles déterministes avancés (des EDPs qui dépendent de plusieurs paramètres). Pour cela nous avons utilisé des techniques qui reposent sur la méthode des bases réduites et l'assimilation de données : la méthode d'interpolation empirique généralisée (GEIM) [114, 115], ainsi que la plus récente méthode de PBDW (Parametrized Background Data Weak) [117, 118]. Nous avons étudié et mis en place ces méthodes pour les modèles de qualité de l'air où les méthodes de réduction usuelles sont souvent difficiles à utiliser à cause de la complexité du phénomène à modéliser. Les méthodes PBDW et GEIM sont non intrusives, directes (contrairement aux méthodes de type adjoint par exemple) et permettent de fournir des approximations de l'état du système physique en

¹G. Heilmeyer, "Some Reflections on Innovation and Invention," Founders Award Lecture, National Academy of Engineering, Washington, D.C., as published in *The Bridge*, National Academy of Engineering, Winter 1992.

temps réel, mais aussi de corriger l'erreur due à un modèle imparfait. Par ailleurs, la méthode PBDW est bien adaptée à l'idée d'objets connectés qui fournirait des données de mesures. Cela pourrait être fait sans avoir à modifier le modèle afin de prendre en compte un grand nombre de point de mesures, contrairement aux méthodes inverses.

(4) Qu'est-ce qui est nouveau dans notre approche ?

- Méthodes d'assimilation de données déterministes qui sont capables de corriger les erreurs de modèle.

Les modèles de qualité de l'air déterministes s'appuient sur les données géométriques, d'émission et météorologiques disponibles pour le site étudié. Ces informations constituent les données d'entrée du modèle. Cependant, l'utilisation de ce type de modèle est limitée par les incertitudes non négligeables sur certains phénomènes physiques qui sont partiellement ou pas connus. Un exemple serait la cinétique de réaction du polluant qui aurait mal été (ou pas) prise en compte dans le modèle. En effet, étant donnée la complexité des applications "in-situ", nous ne pouvons pas supposer que les modèles actuels, même les plus avancés puissent représenter de façon exacte tous les phénomènes physiques en jeu. L'incorporation de données de mesures pour corriger (a posteriori ou à volée) les modèles est une voie d'avenir pour améliorer la qualité des cartes de concentration fournies par les modèles déterministes.

- Méthodes d'ordre réduit et non intrusives pour la simulation en temps réel à partir de modèles physiques avancés.

Le caractère non intrusif de la PBDW et de la GEIM, ne demande aucune modification du code associé au modèle choisi, et permet une mise en œuvre avec tous les logiciels de calcul pour peu qu'ils soient suffisamment *ouverts* et adaptés aux études paramétriques. Ce caractère non intrusif permet également le prototypage rapide de ces méthodes numériques pour un problème donné. Ceci afin de les évaluer avant d'engager le développement nécessaire à les rendre plus robuste en vue d'une utilisation opérationnelle.

- Méthodes qui nécessitent peu de point de mesure des conditions météorologiques.

La PBDW et la GEIM ne sont pas des méthodes inverses, elles ne cherchent ni à identifier, ni à calibrer des paramètres du modèle. La formulation de ces méthodes permet de calculer les concentrations de polluants lorsque les paramètres du modèle varient, sans avoir besoin d'identifier (a priori ou à la volée) les nouvelles valeurs des paramètres. Ainsi, même si l'écoulement de l'air est considéré comme un paramètre variable du modèle, celui-ci n'a pas à être recalculé, contrairement au cas des méthodes de type adjoint. En effet, pour ces méthodes, il faut reconstruire l'écoulement soit uniquement à partir des données sur les conditions météorologiques (et donc disposer d'une grande base de données), soit à partir de méthodes d'assimilation de données pour les équations de Navier-Stokes et pour le modèle de turbulence. La mise à jour du champ de vitesse peut alors se révéler très coûteuse et/ou complexe à mettre en œuvre. De plus, les méthodes des bases réduites ne permettent pas toujours de calculer une approximation peu coûteuse du champ de vitesse lorsqu'il est turbulent. Cependant, l'intégration en temps permet de lisser les effets dus à la turbulence et d'améliorer la qualité de l'approximation base réduite. Dans notre cas, considérer le champ vitesse comme un paramètre et construire une base réduite uniquement pour la concentration, a le même effet de lissage sur l'écoulement turbulent.

(5) Comment évaluerons-nous nos résultats ? Nous commencerons par étudier les résultats à partir de données synthétiques sans erreur de modèle afin d'évaluer la capacité de la méthode PBDW à bien reconstruire des cartes de concentration, en corrigeant l'écart à la mesure dû uniquement à la variation paramétrique. Ensuite nous considérerons des mesures correspondantes à un modèle décalé, dénommé \mathcal{P}^{trial} dans le but d'estimer la capacité de la méthodes à corriger aussi l'erreur de modèle. Les résultats de la PBDW seront comparés à ceux donné par la GEIM. Nous comparerons également ces résultats à ceux donnés par une méthode classique d'inversion telle que la méthode de type adjoint [134, 193]. Cette comparaison est importante étant donnée l'utilisation courante de la méthode adjointe.

Plan de la thèse

Cette thèse est divisée en quatre parties.

Partie 1

Cette partie est dédiée à l'état de l'art pour les modèles de qualité de l'air, les méthodes de réduction de modèle et les méthodes d'assimilation de donnée. Dans le premier chapitre, on introduira le concept de qualité de l'air. Puis on présentera les espèces de polluant qui agissent sur la qualité de l'air, ainsi que les sources d'émission. Pour finir, on donnera une revue détaillée des modèles de qualité de l'air. Le chapitre 2 est consacré à une revue des méthodes de réduction de modèle et d'assimilation de donnée, suivie d'une discussion sur l'application de ces méthodes à la modélisation de la qualité de l'air.

Partie 2

La deuxième partie est dédiée à la présentation des méthodes PBDW et GEIM, du modèle de qualité de l'air choisi pour le calcul des concentrations. Dans le chapitre 3, on trouvera une présentation générale des méthodes PBDW et GEIM. Le chapitre 4 est consacré à l'adaptation de ces méthodes pour des applications à grande échelle. Le modèle de qualité de l'air choisi pour valider ces méthodes est également présenté dans ce chapitre.

Partie 3

La troisième partie contient l'étude numérique de la PBDW pour la modélisation de la qualité de l'air et les résultats numériques *in-situ* sur un quartier de Fresno en Californie. Le chapitre 5 est consacré à la mise en place et à l'étude numérique de la PBDW sur un problème bi-dimensionnel. Ce cas d'étude représente un site de $75\text{ m} \times 120\text{ m}$ qui comprend une maison, un bâtiment et une aire de jeu à proximité d'une route. Dans ce chapitre on trouvera une étude sur la stabilité et la convergence de la méthode en fonction du positionnement des capteurs de concentration et du choix de la norme utilisée dans la formulation PBDW. La méthode PBDW sera ensuite comparée à la méthode d'interpolation GEIM et à une méthode de type d'adjoint. Pour chacune des trois méthodes, nous étudierons leur capacité à reconstruire correctement une carte de concentration à partir de mesures en prenant en compte i) l'erreur due à la variabilité paramétrique, ii) l'erreur de modèle. Dans le chapitre 6, nous étendrons notre étude numérique à un problème tri-dimensionnel. Comme dans le cas 2D, nous étudierons la stabilité et la convergence de la

méthode PBDW en fonction du positionnement des capteurs, et de la norme choisie dans la formulation PBDW. Dans la seconde partie de ce chapitre nous nous intéresserons à la convergence de la formulation PBDW lorsque le modèle a été a-dimensionné. Le chapitre 7 portera sur la mise en place de la méthode PBDW pour une application *in-situ* sur un site de $800\text{ m} \times 800\text{ m}$ à Fresno en Californie.

Partie 4 :

Dans la dernière partie, le but est de mettre en avant la flexibilité et le potentiel d'une méthode alternative des bases réduites non intrusive (NIRB). Nous quitterons alors le thème principal de cette thèse : la modélisation de la qualité de l'air. On s'intéressera à la modélisation urbaine en géotechnique, et plus précisément au calcul des tassements lors de la construction d'un tunnel en milieu urbain. Contrairement à la PBDW et à la GEIM, la méthode NIRB n'a pas besoin de données de mesure sur l'état du système.

Overview of Methods and Contributions

In this section we present an overview of the methods studied in this thesis, as well as the results we obtained. Our principal contribution lies in the development of low-cost numerical methods for spatial mapping of pollutant concentration fields from advanced deterministic models and field observations.

We will treat stationary problems of the generic form

$$\mathcal{P} : \Omega \times \mathcal{D} \rightarrow \mathbb{R} \quad (1)$$

where \mathcal{P} represents a problem (we'll consider it a parameterized PDE), $\Omega \subset \mathbb{R}^d$ is a bounded domain, $d = 2$ or 3 , $\mathcal{D} \in \mathbb{R}^{N_p}$ the parameter domain, and N_p is the number of parameters. We will consider the solutions $u \in \mathcal{X}$ for some suitable Banach solution space \mathcal{X} . We assume the problem \mathcal{P} can be written in the form

$$\begin{aligned} \mathcal{L}(\mathbf{p})(u(\mathbf{p})) &= F(\mathbf{p}) \quad \text{in } \Omega \\ &+ \text{Conditions on } \partial\Omega \end{aligned} \quad (2)$$

We also assume we have a second source of information in the form of field observations. Given a(n unknown) parameter configuration $\mathbf{p} \in \mathcal{D}$ of the physical system represented by \mathcal{P} , and M experimental observations, we assume our data y_m^{obs} , $1 \leq m \leq M$, are of the form

$$y_m^{obs} = \ell_m(u^{true}(\mathbf{p})). \quad (3)$$

where $u^{true}(\mathbf{p})$ represents the true physical state of the system and $\ell_m \in \mathcal{X}'$ are linear functionals representing the sensors. The scheme used to solve the data assimilation problem defined by (2) and (3) varies greatly for different methods. The challenge lies in formulating a scheme to interpret and employ data from measurements in some optimal way to contribute to the knowledge of the state in the numerical model.

Reduced Order Data Assimilation: PBDW and the GEIM

We explore methods to find the best possible approximation of the physical system being studied while expending minimal resources, which translates in practice to using the best model possible and available data without requiring excessive computational investment to solve the problem, focusing here on methods combining reduction and data assimilation in a non-intrusive procedure. Here we introduce two such non-intrusive reduced order

methods of data assimilation for parameterized PDEs : the PBDW and the GEIM. These methods belong to the family of Reduced Basis (RB) methods. Standard reduced basis methods are projection-based model reduction methods relying on the relatively small dimension of the solution manifold \mathcal{M} associated to the problem \mathcal{P} for parameter configurations $\mathbf{p} \in \mathcal{D}$ (we note that not all problems have a low-dimensional solution manifold). If the manifold of solutions is of relatively small dimension, it can be approximated by a finite set of well-chosen solutions of \mathcal{P} , $(u(\mathbf{p}_1), \dots, u(\mathbf{p}_N))$, generating an N -dimensional space, called the RB space. This space is then used as approximation space in the discrete method of solving \mathcal{P} , for example replacing the large number of simple basis functions generating a finite element space with N solutions $u(\mathbf{p}_i)$ $1 \leq i \leq N$, to \mathcal{P} , each providing information on the solution manifold \mathcal{M} . The idea of reduced basis methods is to compute an inexpensive and accurate approximation, $u^N(\mathbf{p})$, of the solution $u(\mathbf{p})$ to problem \mathcal{P} for any $\mathbf{p} \in \mathcal{D}$ by seeking a linear combination of the particular solutions:

$$u^N(\mathbf{p}) = \sum_{i=1}^N \alpha_i(\mathbf{p}) u(\mathbf{p}_i). \quad (4)$$

Efficient implementation of traditional RBMs requires construction of all parameter-independent quantities during a prior *offline* stage, which requires modifying the calculation code, an intrusive procedure. The methods explored in this work take advantage of the reduction capacity of RBMs, but utilize the RB space in a non-intrusive manner.

The PBDW method considers our mathematical model to be the "best-knowledge" model \mathcal{P}^{bk} (i.e. the best adapted model available for the problem \mathcal{P}), and the set of admissible parameters \mathcal{D}^{bk} . The PDE model \mathcal{P}^{bk} is used to build an N -dimensional RB *background* space, \mathcal{Z}_N , representing solutions to the known problem, designed to handle parametric uncertainty. Information on physical location and form of the M sensors providing the data is used to build an M -dimensional *update* space, \mathcal{U}_M , representing the information gathered by the sensors. The PBDW solution, noted $u_{M,N}(\mathbf{p})$ is built from the two approximation spaces, \mathcal{Z}_N and \mathcal{U}_M . We thus aim to approximate the true physical state $u^{true}(\mathbf{p})$ by

$$u_{M,N}(\mathbf{p}) = u_N^{bk}(\mathbf{p}) + \eta_M \quad (5)$$

where $\eta_M \in \mathcal{U}_M$ is an *update* correction term associated to the experimental observations, and $u_N^{bk}(\mathbf{p}) \in \mathcal{Z}_N$ is a reduced basis approximation of the solution to the model \mathcal{P}^{bk} . The PBDW problem, as with many data assimilation methods, is posed as a minimization problem, in which we minimize the *update* contribution, keeping our approximation close to the solution manifold \mathcal{M}^{bk} associated to \mathcal{P}^{bk} for \mathcal{D}^{bk} , and imposing experimental observation values at the sensor points.

$$\left\| \begin{array}{l} \text{Find } (u_{N,M}, z_N, \eta_M) \text{ such that} \\ (u_{N,M}, z_N, \eta_M) = \underset{\substack{\tilde{u}_{N,M} \in \mathcal{X} \\ \tilde{z}_N \in \mathcal{Z}_N \\ \tilde{\eta}_M \in \mathcal{U}_M}}{\text{arginf}} \left\{ \begin{array}{l} \|\tilde{\eta}_M\|_{\mathcal{X}}^2 \\ \langle \tilde{u}_{N,M} - \tilde{z}_N, v \rangle_{\mathcal{X}} = \langle \tilde{\eta}_M, v \rangle_{\mathcal{X}}, \forall v \in \mathcal{X} \\ \langle \tilde{u}_{N,M}, \phi \rangle_{\mathcal{X}} = \langle u^{true}, \phi \rangle_{\mathcal{X}}, \forall \phi \in \mathcal{U}^M \end{array} \right\}. \end{array} \right. \quad (6)$$

We rely on the Euler-Lagrange equations, derived from the minimization problem (6), to find a linear system of size $(M + N) \times (M + N)$ for non-iterative solution of the problem. The procedure is decomposed into *offline* and *online* stages, where the approximation

space and linear system construction is done offline, allowing a very efficient online stage.

A closely related non-intrusive reduced order data assimilation method, the GEIM, also relies on a set of M linear forms representing sensors, as in equation (3) and a model \mathcal{P}^{bk} . From these linear forms and a set of *generating* functions (well-chosen solutions to the model, $u^{bk}(\mathbf{p}_i)$, $1 \leq i \leq M$), interpolating basis functions are derived, $(\tilde{q}_1, \dots, \tilde{q}_M)$. We then define the interpolation operator, for any $u \in \mathcal{X}$,

$$\mathcal{I}_M(u) = \sum_{j=1}^M \alpha_j \tilde{q}_j \quad \text{such that} \quad \ell_i(\mathcal{I}_M(u)) = \ell_i(u) \quad \forall 1 \leq i \leq M \quad (7)$$

and approximate the solution u^{true} by its GEIM interpolation with $\ell_i(u^{true}) = y_i^{obs}$

Applications in air quality

We want to apply these methods to a PDE problem representing a deterministic AQM modeling pollutant concentration based on a CFD wind field and a simplified Chemical Transport Model (CTM). The wind field carrying the pollution is solution of an incompressible Navier-Stokes equation with $k - \epsilon$ turbulent closure. We focus in this work on a stationary transport equation, simplifying for unknown physics, and defining our model \mathcal{P}^{bk} as

$$\underbrace{\rho \vec{v} \cdot \nabla c}_{\text{transport}} - \underbrace{\text{div}((\epsilon_{mol} + \epsilon_{turb}) \nabla c)}_{\epsilon_{tot}} = \underbrace{\rho F_{src}}_{\text{source}}, \quad (8)$$

along with appropriate boundary conditions for an exterior calculation domain with open-air boundaries. The velocity field \vec{v} and turbulent diffusion field ϵ_{turb} can be seen as parameters of the pollutant transport equation in a decoupling of the velocity and transport phenomena.

For ease of implementation in FreeFem++ [79], we chose to solve the transport equation (8) by finite elements with a Streamline Upwind Petrov-Galerkin (SUPG) stabilization scheme [28, 90]. Given the large scale of air quality modeling problems, and the numerical problems caused by differing orders of terms in the PDE, we also want to consider a dimensionless approach. A dimensionless approach generalizes the problem; it can give insight into which parameters may be of lesser importance and may be approximated or ignored, and can help scale the problem if the values of certain terms vary significantly from others.

In advection-diffusion problems the important physical quantities are the velocity, diffusion, and concentration. We thus a-dimensionalize with respect to these variables, and the spatial variable by a characteristic length, and consider a dimensionless problem \mathcal{P}_{adim} over a dilation Ω_0 of the domain Ω by the characteristic length.

In order to evaluate the capacity of our methods to treat imperfect models, specifically models which may not account for all physical processes, we used a shifted model \mathcal{P}^{trial} , an advection-diffusion-reaction model, to compute synthetic data representing a "true" solution used in our case studies.

$$\rho \vec{v} \cdot \nabla c - \text{div}((\epsilon_{mol} + \epsilon_{turb}) \nabla c) + \rho Rc = \rho F_{src}, \quad (9)$$

where ρRc represents a linear reaction term for coefficient R approximation total change from production and loss during reaction processes.

Case studies in exterior air quality

We first set a case study for a relatively simple (with respect to the complexity of a real-world case at urban scale with precise geometry and varying conditions) domain representing a small residential neighborhood polluted by traffic on a street and by combustion sources (not shown here) in residential yards. We define source parameter intensities based on reports made available to the public by the U.S. EPA and on municipality websites [45,85,188], and consider wind velocities \mathbf{p}_v within the *calm* and *light air* categories of the Beaufort scale (from $0.1 \frac{m}{s}$ to $1.3 \frac{m}{s}$). We study a particulate pollutant, $PM_{2.5}$, in this first study, which on the short term can be considered to have negligible reaction.

We start with a two-dimensional version of the domain of dimensions $75m \times 120m$, with a traffic pollution source \mathbf{p}_s , seen in Figure 0.2 along with an example of a solution $u^{bk}(\mathbf{p})$ to \mathcal{P}^{bk} , seen in figure 0.3 .

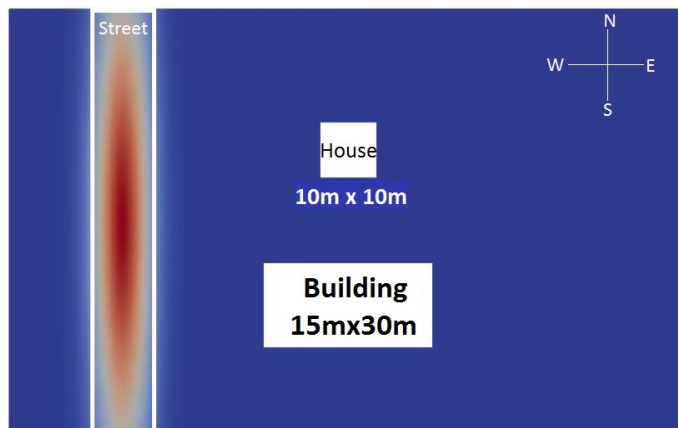


Figure 0.2 – 2D test domain with traffic pollution source.

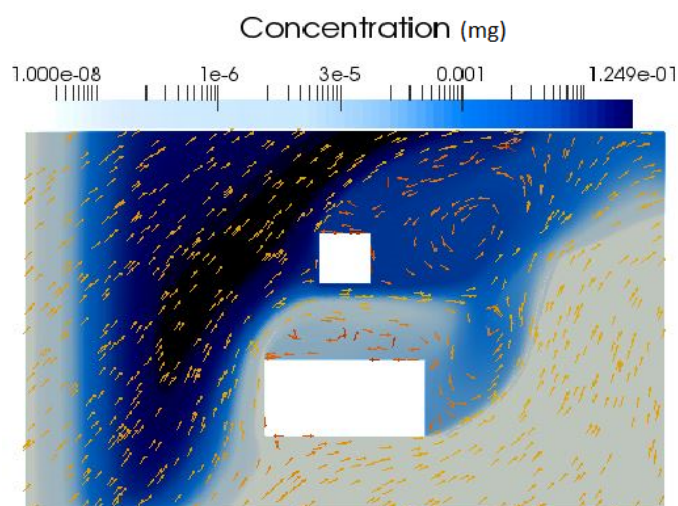


Figure 0.3 – Concentration solution (logarithmic scale) over velocity field with $\mathbf{p}_v = 0.1 \frac{m}{s}$ and $\mathbf{p}_s = 1 \times 10^{-3} \frac{mg}{m^3}$, and inflow velocity direction $\vec{d} = (1, 1)^T$.

We begin by computing a set of *training* solutions to the model \mathcal{P}^{bk} over the parameter set \mathcal{D}^{bk} and selecting the generators of a reduced basis. We compute two different Update spaces, from sensors placed randomly and sensors selected by a GEIM-based Greedy algorithm. In figure 0.4 we see this comparison.

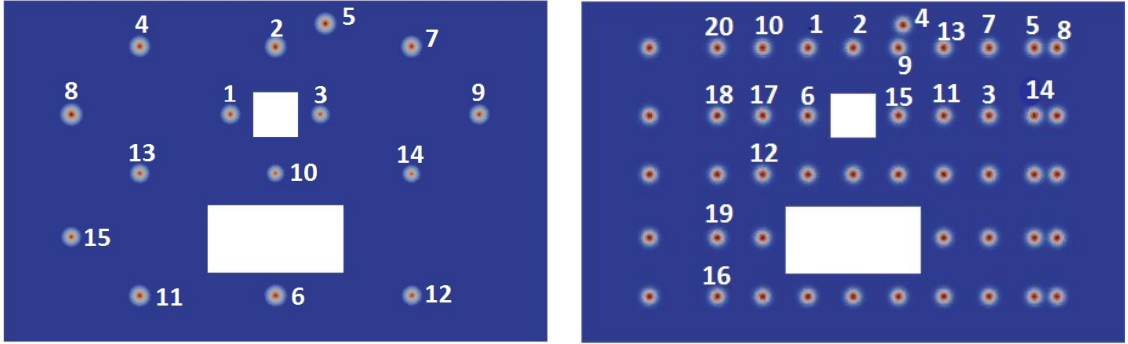


Figure 0.4 – Sensor locations chosen randomly (left) ; Sensor locations chosen by a Greedy algorithm (right).

We next provide PBDW state estimation results, comparing to a set of *trial* solutions of a shifted model \mathcal{P}^{trial} for advection-diffusion-reaction, with three sets of 6 trial solutions to test the method. We take parameters $\mathbf{p} \in \mathcal{D}^{bk}$ (but different from the solutions generating \mathcal{Z}_N), and each set corresponds to a different model shift, with $R \in (0, 0.001, 0.0001)$. In figure 0.5 we show relative mean PBDW approximation errors for $R = 0.001$ plotted over the calculation domain, and in figure 0.6 we see relative mean PBDW approximation errors in the H^1 -norm for each trial set, as a function of N for $M = 8, 13, 15$.

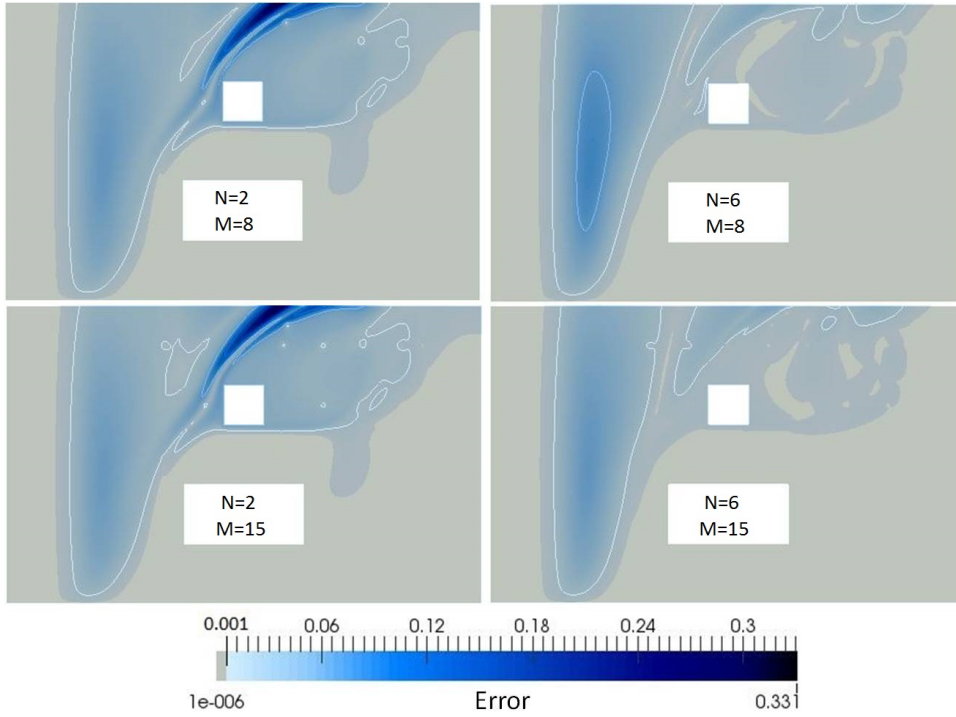


Figure 0.5 – Relative mean PBDW approximation error maps for $N = 2$ (left), $N = 6$ (right), and for $M = 8$ (top) and $M = 15$ (bottom). $\mathbf{p} \in \mathcal{D}^{trial}$, model error with $R = 0.001$. Sensors chosen by a Greedy procedure.

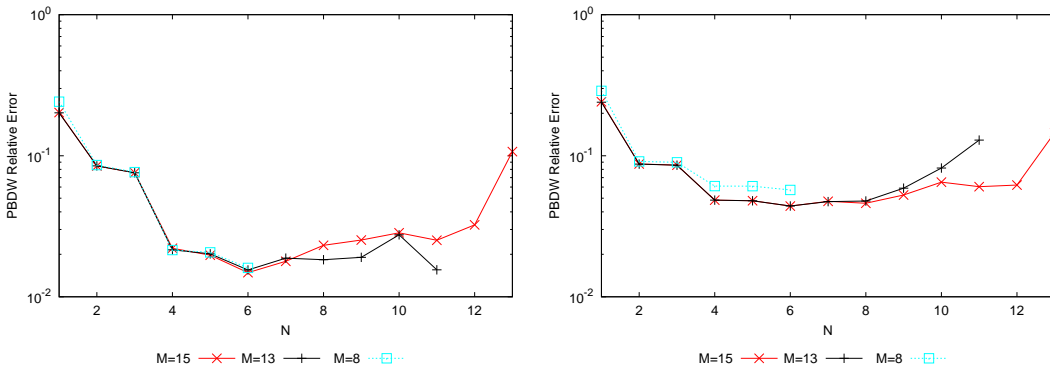


Figure 0.6 – Relative mean PBDW approximation error as a function of N for various M values, $\mathbf{p} \in \mathcal{D}^{trial}$. No model error (left), and model error with $R = 0.001$ (right). Sensors chosen by a Greedy procedure.

A Real-World Application

We extend our study to a real-world application over Fresno, California, city affected by particularly high pollutant concentrations. This application is in view of epidemiology exposure assessments employed by a research team at UC Berkeley (UCB). The long-term goal is to improve the methods for estimating individual exposures and expand the ability of current UCB epidemiological studies to evaluate the association of these exposures to

various health conditions. We aim to extend reduced order data assimilation methods for deterministic PDE-based models to a real-world inspired case study in the hopes of showing the feasibility of these methods in real applications. Below we can see a geometric representation of a neighborhood in Fresno, used as calculation domain in our study.

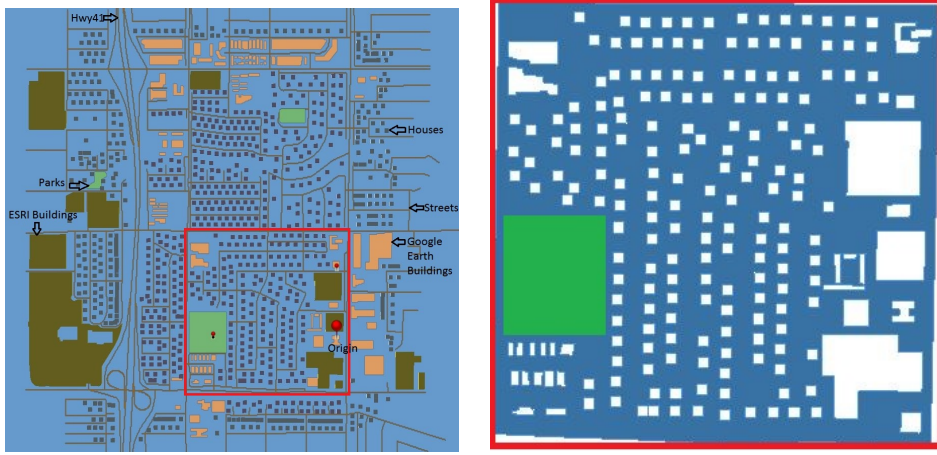


Figure 0.7 – Left: Neighborhood in Fresno over which a wind field was computed using *Code_Saturne*. Right: Fluid domain used to study pollutant concentrations.

In figure 0.8 we see a wind field with $\vec{v}_{in} = 1.3 * z^{0.4}$ in **SE** direction (308 deg) corresponding to real meteorological conditions on April 1, 2001, and an associated dimensionless trial solution to \mathcal{P}^{trial} with $R = 0.001$, where pollution sources are taken to be two streets.

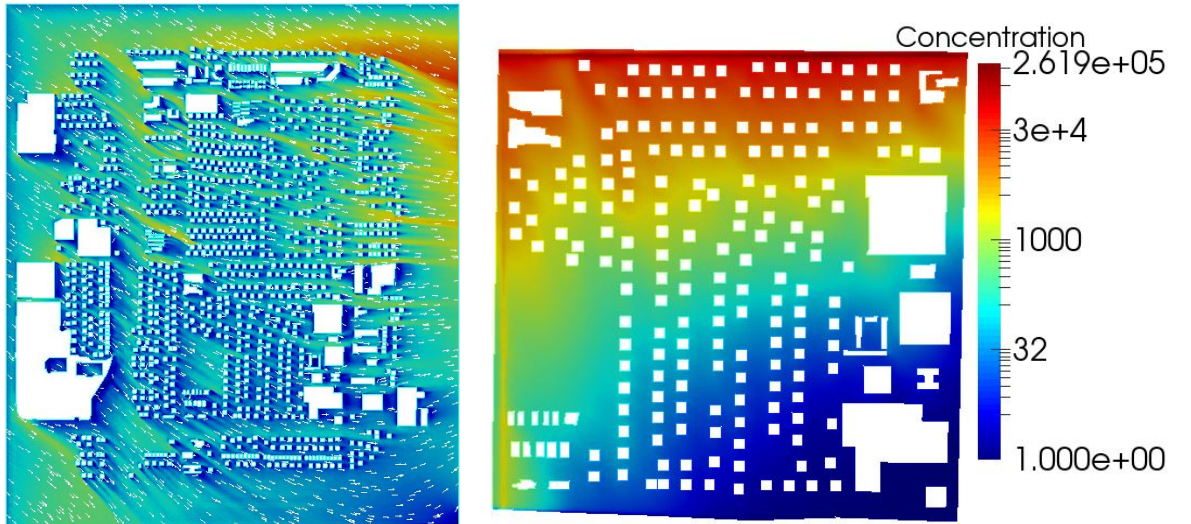


Figure 0.8 – Wind field corresponding to conditions over Fresno on April 1, 2001 (left). Dimensionless concentration solution to \mathcal{P}^{bk} with two pollution sources (right).

In figure 0.9 we show relative mean PBDW approximation errors for $R = 0.001$ plotted over the calculation domain over a set of 8 trial solutions to \mathcal{P}^{trial} . We can see for this simple first test on our real-world case study, with non-negligible model error by an added

reaction term, we can reconstruct the concentration field with under 1% error nearly everywhere, a promising result for future application of these methods.

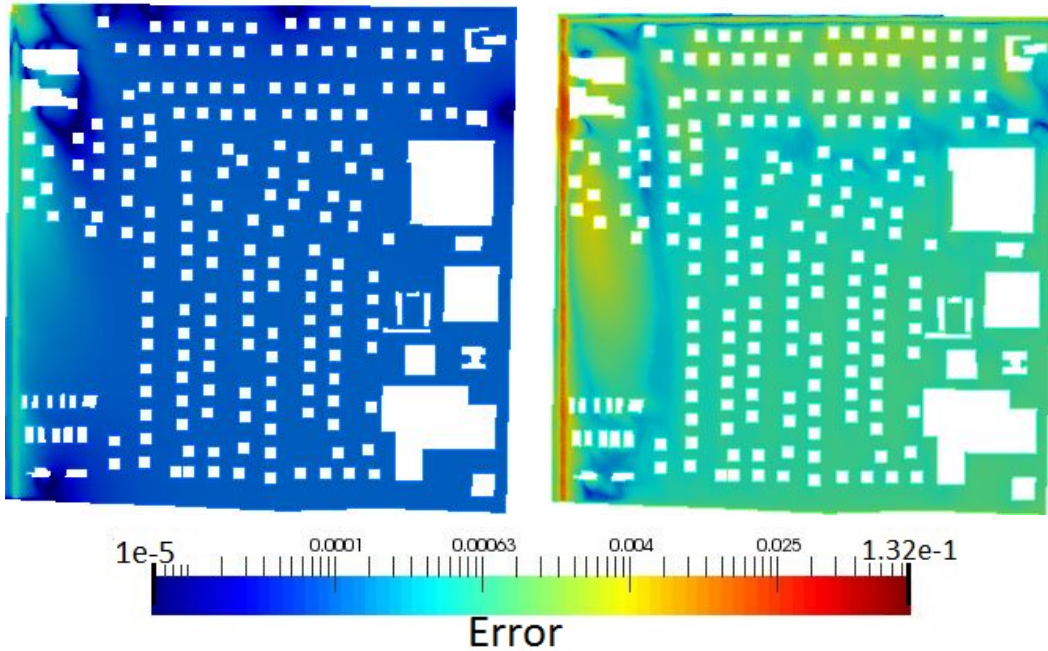


Figure 0.9 – Relative mean PBDW approximation error over a set of 8 trial solutions to \mathcal{P}^{trial} with no model error (left) and with $R = 0.0001$ (right). Here $M = 8$ and $N = 3$.

Non-intrusive RBMs in urban modeling

In a break from the air quality modeling theme of the thesis, we focus on a different reduced basis method and application in urban modeling: the two-grid non-intrusive reduced basis (NIRB) method applied to a problem in tunnel engineering. We would like to show by this example the flexibility of non-intrusive reduced basis methods and their interest in broader applications of urban modeling. As mentioned above, classical RBMs are intrusive methods of reduction for use in implicit studies (where we do not have access to measurements with exact values of the state, as opposed to the PBDW treatment of explicit measures). If we have an application using a black-box code, we can consider the NIRB as an alternative RBM. In this study we investigate the use of reduced basis (RB) methods to diminish the cost of numerical simulation of elastoplasticity problems arising from urban geotechnics modeling, and involving parameter-dependent partial differential equations (PDEs). The chosen application belongs to the field of tunnel engineering. We study the impact of the construction of a shallow tunnel on existing structures (buildings, foundations, etc.) by first examining the impact on the ground surface. In our study the geotechnical analysis requires very specific features such as highly non-linear constitutive laws, making the necessary modification of the FE calculation code for a standard RB method impossible. Our non-intrusive approach involves the computation of less expensive (but less accurate) FE approximation during the online stage and improvement of those solutions using a RB-based rectification method, by which we attain equivalent precision with respect to a standard FEM approximation over a sufficiently fine calculation mesh.

Part I

**Background : air quality
modeling, model order reduction
and data assimilation methods**

Chapitre 1

A review of current air quality models

Résumé :

Dans ce chapitre, nous introduisons le contexte de la modélisation pour la qualité de l'air. Le terme *qualité de l'air* fait référence à l'état chimique de l'atmosphère. Un polluant est une substance nocive pour les être vivants, la végétation, ou les bâtiments. Il existe deux catégories de sources de polluants : stationnaires et mobiles. Une source mobile particulièrement importante est la pollution de trafic routier. Afin de bien modéliser la qualité de l'air, il est souvent nécessaire d'abord, en fonction du modèle choisi, d'estimer les émissions de polluants, par exemple par un modèle d'émissions de trafic. Une fois qu'on a des informations sur le système physique, on peut considérer un modèle pour estimer la qualité de l'air.

Il existe de nombreuses méthodes de modélisation de la qualité de l'air de niveaux de sophistication variable : approches empiriques, modèles statistiques et méthodes déterministes. Parmi les modèles déterministes le niveau de sophistication des approches varie également, allant des simples modèles analytiques de panache gaussiens [180], en passant par des modèles Lagrangiens [89], jusqu'aux modèles Eulériens basés sur la CFD (Computational Fluid Dynamics) tel que le modèle simple utilisé dans cette thèse.

Tandis que ces méthodes ont été beaucoup améliorées au cours des dernières années, elles restent limitées. Par exemple, le traitement détaillé du trafic et la chimie atmosphérique est encore primitif. Des incertitudes dans les données météorologiques et sur les émissions, par exemple, se propagent dans les résultats du modèle sur la concentration. Les modèles opérationnels peuvent aussi être améliorés avec des techniques utilisant des données de mesures et des modèles statistiques, tels que la correction de biais et la prévision probabiliste, la modélisation par ensemble (où plusieurs modèles ou données d'entrée sont appliqués et les solutions sont combinées dans le but de réduire l'erreur globale de modélisation), et l'assimilation des données.

1.1 Introduction

In this chapter we will lay out a brief state of the science on modeling of air quality with the intent of developing and discussing tools to build sustainable cities. First we will define the concept of air pollution, discuss important contributing pollutant species, and discuss modeling. In the second part of this chapter, we will discuss pollution sources and emissions, including the modeling of emissions. In the third section we will discuss air quality models (AQMs) in greater detail, from categorizing existing models to limitations and uncertainties, and finally modeling chains composed of various models for each step of the air quality modeling process. Our last section will discuss improvements in air quality modeling, advances in technology, and improvement techniques such as data assimilation methods and ensemble forecasting.

1.1.1 Air Pollution

The atmosphere is a stratified fluid composed mainly of gasses such as nitrogen, oxygen, and argon, as well as traces of other elements. The term *air quality* refers to the chemical state of the atmosphere; air is deemed polluted if it contains composites able to cause damage to living beings, vegetation, or constructions. While the principal composites of the atmosphere are rather stable, minor composites can vary greatly [52]. Once a pollutant is released into the atmosphere, it undergoes the phenomena of transport (advection), diffusion, and reaction, often alongside the evolution of other composites. The combined effects of transport and diffusion are referred to as dispersion. Each pollutant evolves with a temporal and spatial scale; the lifetime of the pollutant will affect the spatial scale from micro to global scales.

When discussing a pollutant's spatial scale, near-field phenomena refers to the interaction of the plume of pollutant with the air flow field and obstacles in the domain, and involves a small spatial scale. Far-field phenomena, when horizontal motion prevails over vertical, involves a larger spatial scale, and the influence of small-scale obstacles (such as buildings) on the dispersion field becomes relatively small. [186]

Air pollutants include gaseous and particulate species which can lead to various adverse health effects, both non-carcinogenic and carcinogenic. Many studies have been performed on the effects of pollution exposure on human health, showing that health concerns can be caused by short-term exposure as well as long-term exposure. Children, the elderly, and those with pre-existing conditions are at even greater risk for pollution-related adverse health effects. Pollutants and their derivatives can also have negative effects on the environment and manufacture. [202]

1.1.2 Pollutants to monitor

It has been estimated that air pollution kills 3 million people each year worldwide. Particulate matter (PM) in particular has been directly linked to excess deaths in many countries.

The World Health Organization (WHO) and many countries or states have determined guidelines or regulations for common air pollutants. The United States Environmental Protection Agency (U.S. EPA) has regulations concerning sulfur dioxide (SO_2), nitrogen dioxide (NO_2), carbon monoxide (CO), ozone (O_3), lead (Pb), and particulate matter ($PM_{2.5}$ and PM_{10}). [66] The European Union has regulations for these six pollutants as well as for benzene (C_6H_6). The PNSE report in France (<http://www.cesel.org/IMG/pdf/PNSE2.pdf>) estimates societal costs of health effects from air pollution to be 50 billion euros over 30 years in the EU. These regulatory efforts stem from a desire to protect populations from the many adverse health effects caused by air pollution.

Fine particles smaller than ten micrometers can enter the respiratory system without being retained in the nose; the smaller they are, the further they can penetrate. CO_2 has higher concentrations in confined spaces. In some cities, particularly large cities in Asia, levels of CO_2 can be so elevated in the metro that passengers will feel the effects. CO is the number one gas responsible for intoxication in closed spaces. It is often emitted by poorly aerated heating devices. In naturally ventilated spaces, however, it shouldn't pose a serious health risk. Table 1.1 (below) briefly summarizes emissions and associated health concerns of these six major pollutants. [66, 202]

Our focus in this work will be the modeling of air pollution ; we will begin by discussing in more detail pollution sources, and emissions models which can be used to improve pollutant emissions knowledge (section 1.1.3). This information is necessary in the subsequent fate and transport modeling of the pollutants, which will be discussed in section 1.2.

1.1.3 Pollution sources and emissions

On an urban to regional scale, emissions of the pollutants discussed in section 1.1.2 are mostly from urban areas, road transport, and industrial plants. [52] In particular, traffic is a major source of pollution in cities. [70] While table 1.1 globally summarized the sources of these pollutants, we will discuss pollution sources and emissions in detail in this section, from an air-quality-modeling point of view.

1.1.3.1 Sources

Sources of pollution can be divided into two categories: stationary and mobile. The U.S. EPA defines mobile sources as including cars, trucks, airplanes, and lawn

Pollutant	Health Effects	Sources
<i>CO</i>	Depending on concentrations; behavior alteration, respiratory/cardiac problems, irreversible respiratory diseases (in the case of excessive concentrations).	63% road traffic, 17% waste treatment, industrial processes and transportation systems.
<i>NO₂</i> and <i>NO</i>	Effects on humans are not completely clear; high exposure levels have been linked to significant respiratory/nervous problems.	49% road transportation, 32% industrial combustion: manufacturing/energy production, 14% other transportation systems.
<i>SO₂</i>	Irritation to eyes and respiratory system, high exposure linked to acute bronchial constriction and alteration of the nervous system. <i>SO₂</i> can create a fine composite which penetrates deep in the lungs.	61% natural emissions (e.g. volcanos), 31% industrial combustion for manufacturing/energy production, 2% road transportation.
<i>O₃</i>	Can cause many health problems including: chest pain, coughing/throat irritation, respiratory difficulty. Exposure can worsen bronchitis, emphysema, and asthma, and can reduce lung function and inflame the linings of the lungs, possible scarring lung tissue. Children and the elderly are at particular risk.	Ground level ozone is created by reactions between nitrogen oxides and volatile organic compounds (VOC) (e.g. vehicle exhaust and benzene) in sunlight.
<i>Pb</i>	Can adversely affect the nervous system, kidney function, immune system, reproductive and developmental systems and the cardiovascular system (e.g. high blood pressure and heart disease). Exposure also affects the oxygen carrying capacity of the blood.	Fuels in road traffic and industrial processes, fuel combustion of aircraft. Can lead to lead-contaminated water and soil.
<i>PM</i>	<i>PM₁₀</i> has limited consequences on living beings (mucous membranes and nostril hairs can prevent penetration into lungs). <i>PM_{2.5}</i> can penetrate deep into lungs and reach the blood, leading to respiratory and cardiovascular diseases, increased cancer risk, and more.	<i>PM₁₀</i> generated principally by natural erosion and volcano eruption. <i>PM_{2.5}</i> mostly due to combustion, and by <i>NO_x</i> after combustion.

Table 1.1 – Pollutants to monitor, health concerns, and sources.

mowers, among others. Stationary sources can be subdivided into point sources, area sources, and biogenic sources. Point sources are single emissions sources with an identified location such as factories and electric power plants. Area sources consist of small emissions sources which are widely distributed, but may have substantial cumulative emissions. Examples include multiple gas stacks of a single industrial plant, evaporation of volatile liquid spills, open burning and forest fires, and even consumer products such as lighter fluid and hair spray. Trains on specific tracks are an example of a line source, which is also considered an area source. Biogenic sources are natural sources, such as soils, vegetation, volcanic emissions, lightning, and sea salt.

1.1.3.2 Emission models

The type of emissions input information necessary will depend on the type and scale of the model. For global models, anthropogenic emissions used are generally based on well-known global emissions inventories (e.g. Global Emissions Inventory Activity, Emission Database for Global Atmospheric Research). Regional models often use anthropogenic emissions data from the GEMS-TNO or MEGAPOLI-TNO emissions databases along with regional or local inventories. These emissions inventories are often poorly accurate. They can be based, for an example on the regional scale, on a classification of anthropogenic emissions by economic sector. The time discretization is often relatively coarse, more so than desired for input to many AQMs. The emissions can be processed into temporally-resolved gridded emissions using

emissions models (such as SMOKE or HERMES, see [202]). Modeling over smaller regions requires more accurate emissions data from inventories with local information.

Some models use projected or forecasted emissions information. Anthropogenic emissions can be calculated using statistic projection from historical with information on spatial and temporal variability (e.g. due to known source location), or using an "online" approach which depends on meteorology. As for Biogenic emissions, most models use the Biogenic Emissions Inventory System offline. A drawback to the use of historical emissions patterns for anthropogenic emissions is that variations in these emissions due to current conditions (such as current weather) is not accounted for. Emissions information could be improved by including more recent or even real-time emissions from mobile or biogenic sources, such as wildfires.

Instationary models requiring initial conditions to begin the process can use default settings based on climatology or measurements, simulations, model outputs from other (often larger scale) models, and observations (e.g. from satellite or surface data). Boundary conditions, information on the edges of the model domain, are often based on climatology or other model outputs. [202, 203]

Emissions due to road traffic:

Road traffic is considered to be a major contributor to city pollution, and the associated emissions have been the focus of much study. In 2008, 25% of CO emissions in France were from road traffic [107]. In [70] road traffic and emissions modeling are thoroughly reviewed, and the reader is encouraged to refer to the article for more detailed discussion.

Emissions from traffic can be classed into four categories: exhaust, evaporative, vehicle-wear, and road wear and dust. Models can use different input data, generally from traffic models (which will not be discussed here).

Models based on fuel quantities (e.g. IPCC [86]) use fuel consumption and vehicle categories as input data, but only produce large-scale emissions inventories. Models based on average traffic volume and vehicle category (e.g. NAEI and IVE [43, 51]) use a single emission factor for each vehicle category, which are means of measurements over varying driving cycles. The model user must provide vehicle volume and annual mileage per category. They can generate emissions inventories on the national or regional scale. These types of models cannot account for traffic variation.

Models based on average traffic speed (e.g. COPERT and MOBILE [65, 141]) estimate average emission factors for vehicle classes for varying driving patterns as a function of average speed, and can generate emissions data for exhaust and evapora-

tive emissions, and even vehicle and road wear. Models using detailed descriptions of traffic situations (e.g. HBEFA [78]) use explicit emissions factors for preset traffic situations and road configurations, and can be adapted to small scales as well. Vehicle kilometer traveled (VKT) data for each traffic situation is the required input, and the models estimate corresponding exhaust and evaporative emissions data for a large variety of pollutants. These two modeling techniques account for traffic condition via average values and for major emissions processes for small (road) to urban scales.

The precision of emissions estimations can be improved by using more detailed traffic-related input variables. These models (e.g. [125]) generate emissions from traffic variables such as average speed, density, etc. These models, however, may not be useful in determining the impact of traffic congestion. Models using more detailed speed information from kinematic parameters or instantaneous models can generate average or even explicit emissions estimates. These model types use either databases (limiting conditions and pollutions covered) or explicit information from measurements or microscopic traffic models.

Excellent reviews concerning the modeling of road traffic emissions, studying multiple models (e.g. COPERT, MOVES, MOBILE, and HBEFA) and the coupling of traffic and emissions models are available [106, 107]. Numerous projects studying traffic emissions have been conducted in recent years in France and internationally (e.g. TrafiPollu studying the modeling chain from traffic emissions models [105] to air quality models), and the platform ECOSTAND [30] provides input on best practices for traffic from pollution modeling.

Emissions due to stationary sources:

Emissions due to stationary sources can include area sources and point sources, from industrial sources such as factories or refineries, as well as combustion sources such as wood fires or cooking devices. Gas stations can also be considered stationary sources of pollution.

Limitations and uncertainties:

Accurate chemical input information (emissions data, initial conditions and boundary conditions) is necessary to reliable modeling, and inaccuracies lead to forecasting error. The use of input data from larger scale models, spatially or temporally, can lead to interpolation errors when fitting the data to a smaller scale. Satellite data used for initial or boundary conditions can be inaccurate due to retrieval algorithms, cloud contamination, etc. The level of modeling accuracy can also depend on the pollutant under consideration. Likewise, improving the accuracy of chemical species emissions information will directly improve modeling accuracy.

Uncertainty in road traffic emissions modeling, as for anthropogenic emissions in general, depends on uncertainties in model parameters (emissions factors) and input data. Particularly, uncertainty in traffic data, vehicle categories, emissions factors and level of detail, ambient conditions and temporal variations, vehicle parameters (e.g. milage), and fuel composition play important roles.

When considering an appropriate emissions model for AQM purposes, the need for spatial/temporal distribution of emissions should be taken into account. While macroscopic traffic models are accurate enough to estimate pollutant emissions, they are not suitable for air quality simulations for this reason. In addition, the accuracy of emissions models depends on the pollutant. The emissions of certain regulated pollutants such as CO , NO_x , VOC , PM mass, and CO_2 are relatively well known, while emissions estimates of NO_2 , NH_3 , PAH , PM as a function of size, and heavy metals are rather poor. [70] gives more detail on the limitations and uncertainties of emission models.

The importance of accurate emissions information to the efforts of air quality modeling is clear, and emissions models continue to be a subject of research.

1.2 Air Pollution modeling

Air pollution is highly heterogeneous and variable, which is greatly contributed to by turbulent air flows. Models have long been used as tools to explain various scientific phenomena and to make estimations when exact information is not available. Obtaining a comprehensive set of measurements on a system of interest is impractical or impossible. Short or long-term predictions may not coincide with measurement availability, and can be done with models, as can parametric studies, sensitivity analysis, and a priori assessment of development decisions. Air quality modeling is thus indispensable to understanding the effects of air pollution in both urban and rural areas, and to the development of sustainable urban areas. [84] Many countries use real-time air quality forecasting for pollutants of particular concern (e.g. O_3 , NO_2 , and PM). They can be used to provide early warnings to the populations to take measures to reduce pollution and limit exposure. [202]

Air quality modeling integrates science and technology from many domains: meteorology, atmospheric chemistry and air quality, fluid and transport mechanics, as well as mathematics and physics in general, environmental statistics, and computer science and engineering, to give a surely incomplete list.

All models are simplifications of reality; human and natural systems are more complex and heterogeneous than a model can capture. Complex relationships are reduced and some are unknown (or considered unimportant and eliminated), which leads to uncertainties in the results. More specifically, the inherent simplifications involved in modeling of scientific phenomena lead to two types of uncertainties: un-

certainty in the values of key parameters of the models, due to lack of knowledge and natural variability, and uncertainty in the structure of the model itself. Simplification means that spatial and temporal attributes of processes cannot be fully resolved; there is no single correct scale for the dynamics of a natural system. Additionally, cascading effects such as pollutants reacting among themselves can in the long-term create increasing error.

Over the past few decades there have been major increases in the variety and complexity of computational models available. Their sophistication and capabilities have been expanded thanks to advances in computing technology, data availability, developer creativity, and improved understanding of the phenomena studied. While models cannot be considered "truth-generating machines", they play an important role in the analysis of systems and available information.

Many regulatory agencies worldwide employ models for retrospective, current, or prospective evaluations. Air quality models (AQMs) are often used in regulatory activities, such as those of the U.S. EPA. The information provided by models can be used to support decision making, as obtaining a comprehensive set of measurements to support a decision is often impractical or even impossible. Model results must be used to augment and assess measured data. They can be the basis for decisions on environmental cleanup and regulation. [84]

In this section we will discuss the development of air quality models and current methods available. We will describe various categories of models, as well as the limitations and uncertainties involved in air quality modeling. We will consider modeling chain, used to integrate knowledge of multiple processes affecting air quality. We will also briefly discuss the connection with exposure modeling.

1.2.1 History and development

The first pollution models were forecasts of air stagnation or pollution potential based on forecast conditions conducive to poor air quality; these forecasts were from meteorological models, and did not account for emissions, transport, or chemistry of pollutants. In the 1970's various tools for pollution modeling in urban areas were developed, and were mostly based on empirical approaches and statistical models, which were fitted to historical air quality and meteorological data. In the 1990's more sophisticated techniques were developed to overcome the limitations of simpler approaches and to treat non-linearity of systems. Three-dimensional numerical air quality models with scales ranging from urban to global were developed from the 1970's, and with advances in computational technology the focus was shifted from postprocessing of meteorology and statistical methods to the use of 3D AQMs for meteorology, emissions, transport, chemistry, and removal processes.

Deterministic AQMs, such as chemical transport models (CTMs) have traditionally been used to retrospectively simulate poor air quality scenarios for regulation

and planning; computational constraints and lack of real-time chemical measurements limited real-time and predictive applications. A significant advance in technology was the development of real-time databases such as the AIRNow network (www.airnow.gov), providing air quality information from many centers to the public.

Many countries have been developing real-time air quality monitoring methods. More sophisticated techniques have been developed based on initial AQM techniques; ensemble modeling (discussed in 1.3.2.2) as well as chemical data assimilation have been significant advances. CTMs and CFD models have been developed in order to better model pollutant concentration in complex domains.

Below we will outline general model categories existing today. For an excellent overview of existing operational models, the reader is encouraged to refer to [202]

1.2.2 Model categories

Of the many different varieties of AQMs developed in recent decades, each was developed for a specific purpose, with inherent strengths and limitations. Here we will discuss some common types of models. We note that we will mostly treat physical phenomena in these models, as chemical reaction is particularly complex and is most often greatly simplified, even in deterministic models. Complex chemical treatments are considered in more detail in, for example, [89].

Models vary greatly in terms of scale and precision of the input and output information. Global approaches don't study fluid flow, but focus on scalar values (e.g. concentration of particles in interior or exterior air, exchange factors between interior and exterior air, emissions factors of a source, etc.). For the example of interior air quality, some models assess conservation of mass in each zone of a building, then in the entire building. These global methods are less precise, and undoubtedly not adapted to domains with high air velocity (and therefore greater turbulent complexity and mixing effects). However, they can be computationally inexpensive with low calculation times and no meshing of the domain required. More sophisticated deterministic models can provide more precision; for example, CFD modeling allows to model fluid flow and predict particle displacement.

Below is a diagram representing the categories of models which will be discussed here.

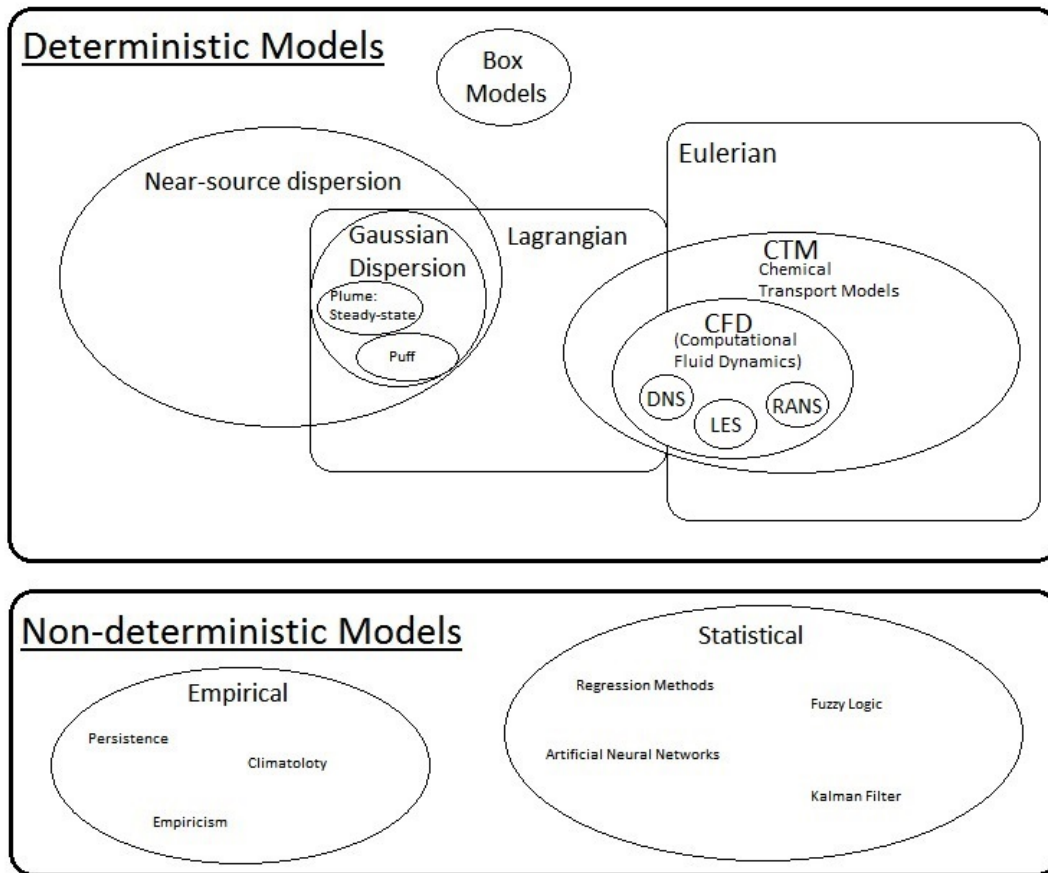


Figure 1.1 – Diagram representing various types of models used for air pollution studies.

Models can be classed into two broad categories: deterministic and non-deterministic. In this section we will first discuss common non-deterministic methods, from simpler empirical models to more sophisticated statistical models. We will then consider deterministic models, mainly Gaussian dispersion and Lagrangian and Eulerian approaches for AQMs, specifically in the dispersion and reaction framework. We will then develop the discussion on models based on computational fluid dynamics (CFD) in a third paragraph as these methods are of particular interest to this work.

1.2.2.1 Non-deterministic models

A non-deterministic system includes some stochastic elements, and a set of fixed input variables does not guarantee the same output for multiple model runs.

(i) Empirical approaches

We will begin by discussing relatively simple air quality modeling approaches: empirical methods.

The persistence method operates under the assumption that one day's observed pollution levels can serve as the next day's forecasted level. This is a very rapid method which can function relatively well under stationary conditions and consistently high or low pollution levels. However it fails to handle abrupt changes in weather, emissions, or air quality, and accuracy in the long term is rather low. It is primarily used as a reference or base method for other approaches.

The climatology method hypothesizes that air quality is highly dependent on weather. It is computationally rapid, using historical air pollution data (at least 2-5 years) to guide and bound forecasting. It cannot, however, handle abrupt changes due to emissions or non-historical weather patterns. While it is simple to use, it provides low accuracy in results, and like the persistence method, does not provide sufficient results to be used without combining with other methods.

Empirical approaches operate under the assumption that thresholds of parameters which influence pollution, such as meteorological variables, can indicate future high pollution levels; if the parameters are forecasted to reach a threshold, then high pollutant concentrations will be forecasted. Required inputs include observed and forecasted meteorological and air quality data. It is moderately accurate, although not for exact punctual concentrations. Empiricism cannot handle pollutants which are weakly dependent on weather conditions, such as carbon monoxide. It relies on the strong correlation between the pollutant considered and meteorological variables, such as ozone and temperature. These correlations, however, may not always hold—high temperatures are not necessarily sufficient for ozone formation—and can depend on the pollutant under consideration—PM species respond differently to temperature changes. Empiricism is primarily used to determine whether a more sophisticated approach is necessary. [202]

(ii) Statistical approaches

Statistical approaches hinge on the statistical relations between weather and air quality variables. Various functions, such as regression, are used to predict pollutant concentrations depending on external conditions.

Common methods include: classification and regression trees (CART), regression methods, artificial neural networks, fuzzy logic method, and Kalman filter methods. In order to predict pollutant concentrations from input parameters of air quality and meteorological variables, classification and regression trees use a decision tree, while regression methods employ regression equations. Artificial neural networks (ANNs) and fuzzy logic (FL) are based on artificial intelligence techniques. For example, fuzzy logic uses continuous variables from 0 to 1 representing a trueness spectrum. Both these methods are computationally rapid with moderate to high accuracy, but cannot accurately predict extreme concentrations and are limited by observation requirements. Some of these methods can handle non-linearities (CART, ANNs, FL,

and non-linear regression), which are more accurate than linear regression methods.

Statistical methods are generally best-suited to studying complex site-specific relationships between concentrations and predictors, and in this case can often have higher accuracy than deterministic models. However, they require much historical measured data under varying atmospheric conditions, and are hence confined to the area and conditions corresponding to the available measurement data; they cannot be generalized to regions with different chemical and meteorological conditions. In addition, statistical methods cannot handle significantly unusual emissions or meteorological conditions, nor can they take into consideration distant weather-dependent sources. Accuracy depends on the meteorological predictors used, which often neglect or simplify some meteorological processes which can be significant players in the development and dispersion of pollutants. It should also be noted that statistical models do not improve understanding of the physical and chemical processes governing the evolution and transport of air pollutants. Direct links between emissions and pollution concentrations and relationships between different pollutants cannot be described by statistical methods.

The reader is encouraged to refer to [202] for examples of models applying these statistical approaches, which have been applied in air quality modeling since the late 1970's.

1.2.2.2 Deterministic models

A deterministic model of a physical system is a model involving no randomness; the same output will always be produced from a given configuration of the model. Deterministic models for air quality discussed here are physically-based approaches, from basic to more advanced. These air quality models aim to calculate pollutant concentration spatially and temporally using mathematical equations which describe the processes of atmospheric transport and chemical and physical transformation. [70] Varying approaches exist on model inputs and outputs, structure, and spatial and temporal resolution.

The more advanced deterministic models can enable better understanding of physical and chemical processes, such as links between emissions and pollution concentrations and interactions between pollutants, which is essential to the understanding of the physical-chemical system, the improvement of air quality modeling capabilities, and to the development of integrated emission control strategies. [202]

In this paragraph we will first consider near-source dispersion models, then focus on Lagrangian approaches for modeling the trajectory in dispersion-reaction cases, and finally introduce an Eulerian approach for fluid and transport dynamics PDE models.

(i) Box models

Box models are very simple models in which large domains are considered as boxes (not gridded by small cells) and concentrations are considered homogeneous within the box. Pollutants are emitted, undergo chemical and physical processes, and are advected in and out of the box. While the computational cost is low, these models are not used operationally, but can be useful in the study of specific processes under simple configurations and controlled conditions or to study deposition fluxes. [70]

An Eulerian (see paragraph **(iv)**) box model for gas-phase pollutants would be based on an averaged dispersion equation of the form

$$\frac{\partial \langle c_i \rangle}{\partial t} + \text{div}(\langle V(x, t) \rangle \langle c_i \rangle) = \text{div} \left(\langle \rho \rangle \epsilon \nabla \left(\frac{\langle c_i \rangle}{\langle \rho \rangle} \right) \right) + \chi_i(\langle c_i \rangle \langle T(x, t) \rangle, t) + \langle S_i(x, t) \rangle - \langle \Lambda_i \rangle \langle c_i \rangle \quad (1.1)$$

where $\langle \cdot \rangle$ represents an average, c_i is the concentration of species i , $V(x, t)$ the air flow field and $T(x, t)$ the temperature, ρ is the air density, ϵ the diffusion coefficient, $S_i(x, t)$ the source term for species i describing emissions, χ_i the chemical source term of the species (i.e. reaction term), and Λ_i is a coefficient for wet scavenging (see 1.2.2.3), a function of meteorological fields and physical variables.

Boxes can be connected using flux terms at the interfaces, for example with one box representing the mixing layer (the part of the atmospheric boundary layer where pollutants mix during daytime, see paragraph on Atmospheric influence in 1.2.2.3) and another representing the residual layer above.

A Lagrangian (see paragraph **(iii)**) box model could for example treat equations for chemical kinetics (including deposition/scavenging and emissions), solving along the characteristic curves of the flow. [180]

(ii) Near-source dispersion models

Near-source dispersion models use parameterization to represent the transport and dispersion of pollutants from the source(s) selected. If the domain includes no obstacles to atmospheric transport and atmospheric conditions are stationary, the dispersion process can be modeled by a Gaussian distribution of time-averaged pollutant concentrations. Gaussian models are based on the assumption that atmospheric dispersion follows a Gaussian distribution of concentration both vertically and horizontally. Operational models based on Gaussian dispersion are widely used as "fast response models", principally to study near-field dispersion from a point source. [186] While often used in atmospheric dispersion, they are rarely used for interior dispersion; however they could be considered for air quality modeling in, for example, a train station, with trains treated as line sources.

Gaussian plume models can be used in steady-state atmospheric conditions (e.g. constant wind speed and direction) with continuous pollutant source. If we consider the following dispersion equation for the mixing ratio (defined as the ratio

of the mole number of the pollutant to the mole number of the air)

$$\frac{\partial C}{\partial t} + \vec{u} \cdot \nabla C = K_x \frac{\partial^2 C}{\partial x^2} + K_y \frac{\partial^2 C}{\partial y^2} + K_z \frac{\partial^2 C}{\partial z^2} \quad (1.2)$$

with velocity \vec{u} and K_x representing turbulent diffusion in the x -direction (respectively y and z), we can derive a solution $C(x, y, z, t)$ given by a Gaussian function. More specifically for the Gaussian plume model, if we consider a source at $x = y = 0$ and height $z = h$, wind velocity $\vec{u} = u_x$ and ground BC of total reflection (translating to a homogeneous Dirichlet BC), we have

$$C(x, y, z) = \frac{S}{2\pi u \sigma_y \sigma_x} \exp\left(-\frac{y^2}{2\sigma_y^2}\right) \left[\exp\left(-\frac{(z-h)^2}{2\sigma_z^2}\right) + \exp\left(-\frac{(z+h)^2}{2\sigma_z^2}\right) \right] \quad (1.3)$$

where the variances σ^2 are dependent on distance to the source and meteorological fields. [180]

These models, however, are not designed for atmospheric dispersion in cases of low wind speed. They can treat deposition processes and simple chemical reaction systems, however this is rather challenging and can be approached by several methods. Plume models can estimate concentrations up to 50km from a source, usually averaging times over one hour or less to accommodate the assumptions of constant meteorological conditions.

Gaussian puff models can handle variable atmospheric conditions and emissions, and more complex chemical reactions. Atmospheric dispersion is represented by releasing puffs from the source at specified time intervals. Each puff evolves by a Gaussian model independently of others, and the total concentration is the sum of all the puffs. If we consider N puffs at interval Δt , then $\forall t \geq N\Delta t$

$$C(x, y, z, t) = \frac{1}{(2\pi)^{3/2}} \sum_{i=1}^N \frac{S_i \Delta t}{\sigma_x \sigma_y \sigma_z} \exp\left[-\frac{(x-x_i(t))^2}{2\sigma_x^2} - \frac{(y-y_i(t))^2}{2\sigma_y^2}\right] \times \left[\exp\left(-\frac{(z-z_i(t)-h)^2}{2\sigma_z^2}\right) + \exp\left(-\frac{(z-z_i(t)+h)^2}{2\sigma_z^2}\right) \right] \quad (1.4)$$

where $S_i \Delta t$ is the emissions at time $t_i = i\Delta t$, and the evolution of the x -coordinate (respectively y or z) of puff i is given, as a function of the x -direction (resp. y or z) wind velocity $u(x, t)$, by [180]

$$x_i(t) = x_i(t - \Delta t) + u(x_i(t - \Delta t), t - \Delta t) \Delta t.$$

The process of following each puff involves greater computation requirements than plume models. These models are relatively easy to use and are popular for passive tracers and short-range dispersion. Puff models have been used for long-range pollutant dispersion impacts when meteorological fields are computed using an appropriate model (see [200]). However, they are limited to a small number of

specific sources, as puffs must be released from each source. The computational burden thus increases with each additional source. The extension to reaction is challenging as well, and the parameterization of the time-dependent variances σ^2 can prove more complicated than in the plume model.

Often modified Gaussian dispersion models are developed for different purposes. For example, hybrid models using both plume and puff techniques can better handle low wind speeds. Other modified models can handle many dispersion processes including atmospheric stratification, chemical reaction, deposition, and concentration fluctuation. Nevertheless these techniques remain limited by the effects of obstacles on the plume. [70, 186]

In the case of domains including obstacles to pollutant dispersion (e.g. buildings, noise barriers, or vegetation), other parameterizations must be used to model near-source impact. The case of dispersion around buildings can be treated by modifying dispersion coefficients to create a wake effect, but is limited to simple cases and does not treat recirculation effects from multiple buildings. When the domain represents a street canyon, parameterizations based on the assumptions that there is a well-mixed zone in the street canyon. For road pollution modeling, a method was proposed in [177, 178] which simulates each street using a simple box model, and calculates the advective flux balance at the intersections. Three major transport mechanisms in the urban canopy are considered by this method: advective mass transfer along the street due to mean wind along the street axis, turbulent mass transfer across the interface between streets and the overlying atmospheric boundary layer, and advective transport at street intersections. At the single-street scale, the method employs a Gaussian plume model for atmospheric transport and dispersion above roof level. [70]

(iii) Lagrangian models

Lagrangian models study fluid and particles separately, relying on Newton and Stokes laws. They provide realistic approximations and require little information on the particles, but are computationally expensive. A Lagrangian model follows the trajectory of an air mass along the mean wind flow. Gaussian dispersion models are included in this category (but were set apart due to their particular importance), along with numerical particle models and grid-based Lagrangian models (examples are provided in [70]).

Here we will discuss lagrangian particle trajectory models in more detail.

Particle-trajectory models are based on the tracking of so-called numerical particles using a stochastic interpretation of a passive dispersion equation. As the air mass moves along its trajectory, particles are advected with the flow and dispersed via turbulent diffusion. These models work well under stationary conditions over flat terrain as well as variable conditions over complex terrain. Grid-based trajectory models involve a 1D column or 2D wall of cells which is ad-

ected by the mean wind. Turbulent dispersion spreads pollutants among the cells as the air mass moves downwind along its trajectory from the pollutant source (e.g. [174]).

If we consider a 3D velocity field $V = (u_x, u_y, u_z)$ and turbulent diffusion coefficients K_x, K_y, K_z , then the trajectory of a numerical particle $(x(t), y(t), z(t))$ with

$$x(t_{n+1}) = x(t_n) + (u_x + \frac{\partial K_x}{\partial x})\Delta t + \sqrt{2K_x}\Delta W_x \quad (1.5)$$

For the x-direction trajectory (similar for y and z). W_* is a normal stochastic process of zero mean representing white noise. The concentration can then be calculated by summing all particles in a given grid cell. If an infinite number of particles are tracked this process has a continuous limit such that

$$\frac{\partial c}{\partial t} + \text{div}(Vc) = \text{div}(\epsilon_{turb}\nabla c), \quad (1.6)$$

which is precisely the advection-diffusion equation which will be discussed more in paragraph **(iv)** (conservation equations) and subsection 1.2.2.3 [180], and can be interpreted as passing from a statistical mechanics point of view to continuum mechanics as the Knudson number¹ decreases with increased number of modeled particles.

The computational expense of this method is due to the need for a high number of particles ($\mathcal{O}(10^4)$) to ensure convergence of the concentration result. The extension to model reaction is non-trivial, as interactions between particles must be tracked, however it is possible, and these models can handle non-linear chemistry owing to the grid. However, complex meteorological conditions such as wind shear, land-sea breezes, and mountain-valley winds, cause poor representation of pollutant dispersion. These models are commonly used to model overall dispersion patterns and temporal development of mean concentrations. An example of an operational Lagrangian model for air quality used in California can be found in [88, 89, 102].

(iv) Eulerian models

Eulerian models are based on the hypothesis that the particles form a continuum, a volume of, at the local scale, homogeneous properties (such as air pollutant concentration as a scalar value, or meteorological variables), and study the flow of those variables through a 3D gridded mesh of such volumes (cells). Eulerian models employ chemical transport models (CTMs) which rely on conservation equations, such as equation (1.6), solved over the discretization (grid), for each cell.

CTMs are deterministic models which can explicitly represent all major physical, meteorological, and chemical processes involved in the formulation, transport, and

¹The Knudsen number helps determine whether statistical mechanics or the continuum mechanics formulation of fluid dynamics should be used. If the Knudsen number $Kn = \frac{\lambda}{L}$, where λ is the mean free path (the average distance traveled by a moving particle between successive collisions) and L is a characteristic length of the problem, $Kn \geq 1$, then the mean free path of a molecule is comparable to a length scale of the problem, and the continuum assumption of fluid mechanics is no longer a good approximation.

accumulation of air pollutants. They can take meteorological variables as inputs (gridded meteorological fields previously calculated by meteorological models) as well as Initial Conditions (ICs) for the non-stationary case and boundary conditions (BCs) for treatment on domain boundaries. Conservation equations are solved for the mass of species of pollutants and for chemical reactions between pollutants. This type of model has been developed over multiple decades and is used in many countries. See [70, 202] for examples of operational CTMs. We will consider CTMs as Eulerian models, but will discuss their relation to Lagrangian trajectory models and equation (1.6) in the next paragraph.

The fixed grid used by Eulerian models facilitates the treatment of a larger number of sources and complex chemistry and atmospheric transport phenomena. They can be used at a variety of scales, from urban to global. [70] Compared with above-mentioned statistical methods, Eulerian CTM models have multiple strengths. They can approximate and forecast temporally and spatially resolved concentrations, even under atypical conditions. In addition, there is the advantage of the physically-based approach improving understanding of the processes. Long-range transport, interplay with meteorology, emissions, and chemistry, and air quality changes depending on meteorology and emissions can all be better addressed. Accuracy is moderate to high when the model is well-chosen (processes are correctly represented) and calibrated (accuracy of ICs, BCs, emissions, etc.). And of course, these models do not require large quantities of data as most statistical models do. However, the development and implementation of these models can be difficult and costly; knowledge of sources and emissions is required, and chemical and transport processes will be simplified and approximated. The accuracy of CTMs strongly depends on the accuracy of the meteorological input data (as is the case of Lagrangian trajectory models), and inaccuracies in any input can be propagated. It is also important to mention the computational cost of CTMs. These limitations will be discussed further in section 1.2.3.

As compared to Lagrangian models, which track particles by time-stepping and are therefore not iterative in the computation of concentrations, eulerian models usually need an iterative method of resolution in the steady state to achieve a convergent concentration field. In the transient case, the eulerian methods still often need an iterative method at each time step, depending on the time discretization scheme, while the Lagrangian models using flow field input still tracks the concentration by time stepping, saving concentrations at each time. This means that in some time-dependent cases, Lagrangian models may gain an advantage over eulerian methods with respect to computational time, depending on the number of particles tracked and computational architecture.

Specific examples and details are provided in [202]. Chemical transport modeling using fluid dynamics will be discussed in depth in the next paragraph.

Some models combine Eulerian and Lagrangian concepts: plume-in-grid models simulate selected sources with Lagrangian models (e.g. a Gaussian puff model)

embedded within a 3D Eulerian model which simulates the fate and transport of all other emissions. These models have the advantage of a large domain and multiple sources inherited from the Eulerian methods, and the fine resolution near a particular source inherited from the Gaussian model.

1.2.2.3 PDEs for air quality: CFD & CTM models

Key components of CTMs lie in the physical parameterizations (inputs and coefficients for physical quantities) associated to the modeled processes. We will give a brief overview of the major phenomena involved. [180]

Emissions can often simply be based on an emissions inventory. As mentioned in 1.1.3.2, however, the time discretization is often much coarser than that needed for a CTM, and detailed emissions for a specific pollutant may not be available (for instance, VOCs are treated as a single category). More sophisticated approaches couple emissions modeling for more accurate input into the AQM (see 1.2.4.2).

Diffusion is an important component, and varies greatly depending on atmospheric stability, temperature, and flow fields. It is made up of molecular diffusion and turbulent (eddy) diffusion, although molecular diffusion is often considered negligible with respect to turbulent diffusion. This will be discussed more in 4.2.2 and in paragraph (ii).

The chemical mechanisms of reaction must be parameterized, which depends on the pollutant modeled and other species present, and even on the altitude or solar exposure. This can prove complicated as there is no universal chemical mechanism. A gas-phase chemical mechanism parameterization may describe 100+ species with hundreds of reactions. In the case of passive tracers, this term can serve to model the atmospheric of the species (in practice the lifetime).

Wet scavenging is a poorly understood process accounting for the effects of clouds and precipitation on gas-phase and particulate species, which governs the atmospheric residence time of the pollutant. The parameterizing in AQMs is difficult given the lack of understanding of the phenomena.

Dry deposition depends on the pollutant species, meteorological conditions, and on land use category (LUC). It can be described by a deposition velocity, however uncertainty in seasonal variation of LUC means questionable accuracy.

Last among the physical processes we'll discuss here is the air flow field, perhaps the most important. A common technique is to map the outputs of meteorological models to the grid used for the CTM, however the required projection and interpolation will add to the modeling error.

(i) CFD and CTMs An alternative to meteorological inputs for CTMs from another model would be to rely on Computational Fluid Dynamics (CFD). In the past two decades, Computational Fluid Dynamics (CFD) simulation has been widely used for pollutant dispersion in urban areas. CFD modeling for pollution, closely linked to the broader category of CTMs, involves the modeling by partial differential equations (PDEs) of fluid flow based on the Navier-Stokes equations, and of pollutant

transport to approximate the dispersion of pollutants. Examples of this method are given in [70]. These models consist in a transport equation (advection and diffusion, and possibly reaction) for the concentration of the chosen pollutant, which is highly dependent on the velocity field provided by the resolution of the Navier-Stokes equations.

This method is well-suited to studying the relationship between atmospheric chemistry and meteorology, as well as to air quality forecasting. While CFD models are quite time-consuming and the dispersion processes involved can be difficult to implement, they can give detailed spatially-rich information on the flow and concentration of pollutants. The coupling of air flow and chemical transport models can enhance our understanding of the interplay (and of what interplay is possible) between meteorology, emissions, and chemistry; model evaluations have shown that these coupled models can provide results which are consistent with or improve upon those from statistical methods.

Applications of CFD to near-field pollutant dispersion modeling around buildings have been rapidly increasing in recent years, and the range of competencies has expanded to include chemical reaction, fine particle dispersion, etc. CFD modeling has great potential, however to be used correctly, careful attention must be paid to the theory and implementation of the models. [186]

(ii) CFDs and Turbulence In order to treat turbulent flow, one needs a turbulence closure equation of the governing PDEs of the CFD models for fluid flow. Various techniques exist, each of which handles turbulence differently, some being more accurate than others. However, the relevance of turbulence model choice in model accuracy for CFD simulations is only significant when other sources of error, such as numerical and convergence errors, or input and boundary errors, have been controlled. [70, 186]

Common techniques include Direct Numerical Simulation (DNS), Large-Eddy Simulation (LES), and Reynolds-Averaged Navier-Stokes (RANS).

DNS solves the Navier-Stokes equations without approximation on a very fine (and well-adapted) grid to catch small eddies in the flow. However, this is very time-consuming, (although can be useful in studying the minute complexities of turbulent flow), and does not perform well for high Reynolds numbers as varying scales of turbulent motions require a very fine mesh; DNS is not feasible for environmental simulations.

LES separates turbulent motion into large and small eddies. Small eddies are modeled independently from the flow geometry with parametrization. Large eddies are simulated explicitly for time-dependent flow. This method is more practical than DNS, though still relatively time-consuming. It is applied mostly in meteorological simulations and simple configurations for air quality modeling (such as street canyons or single stack plumes). LES is not a common approach in operational air pollution

applications at this time.

RANS solves the time-averaged Navier-Stokes equations with approximation to simplify turbulent flow. This is the fastest method and has proven useful in air quality modeling (e.g. in [130] and [62]). This is limited to local applications currently, such as a single source in complex terrain where flow is complex. Chemical transformations have been incorporated in recent applications.

For an example of the mathematical equations involved, in [130] Boussinesq's turbulent diffusivity model (which accounts for atmospheric stratification, refer to article for details) is used, which closes the conservation of mass and momentum equations in the CFD model using the RANS $k - \epsilon$ technique.

(iii) Concentration Modeling A simple CFD-CTM model considered in [52] for a pollutant which on urban or regional scales does not significantly react with other composites follows the Eulerian approach to modeling diffusion and transport via the advection-diffusion equation.

$$\left\{ \begin{array}{l} \frac{\partial C}{\partial t} - \nabla \cdot (\epsilon_{tot} \nabla C - \vec{v}C) = f \quad \text{in } \Omega \times (0; T_f) \\ + BC_s \text{ AND } IC_s \end{array} \right. \quad (1.7)$$

where $\epsilon_{tot} = \epsilon_m + \epsilon_t$ is the diffusion (molecular and turbulent/eddy) of the pollutant in the air, \vec{v} is the advection (velocity) field, and f represents the pollutant source. These parameters usually depend on space and time. If the velocity field of the fluid is suitably described (e.g. by the Navier-Stokes equations with a turbulence model), then the turbulent diffusion ϵ_t will dominate the molecular diffusion ϵ_m . We neglect the deposition term here, an assumption which holds, for example, for smaller particles. In [206] it was considered that for particles of size $0.3 - 1 \mu m$ ($PM_{0.03} - PM_{0.1}$), the deposition velocity was $v_d \simeq 10^{-5} - 10^{-6} \frac{m}{s}$ in ventilated indoor chambers. A particle loss coefficient was calculated as $\beta = v_d \frac{A}{V}$ depending on the area (A) of the room and volume (V) if the interior surfaces, which was of two magnitude orders lower than the air exchange rate considered in the problem, and was therefore neglected.

This model, with suitable BCs and IC, could be applied to pollutants such as CO , NO_x , SO_2 , and PM_x on an urban scale, if we choose to consider the reaction term negligible for the purpose of transport modeling (this assumption would not be valid in general, and could only be considered reasonable on a case-by-case basis). This model could be extended by considering parameterizations for the neglected processes, and will be revisited in part III.

The computational cost of this problem being impractical often leads to replacing ν with a tensor \mathbf{K} for turbulent diffusivity in each direction, giving:

$$\left\{ \begin{array}{l} \frac{\partial C}{\partial t} - \nabla \cdot (\mathbf{K} \nabla C - \vec{v}C) = f \quad \text{in } \Omega \times (0; T_f) \\ + BC_s \text{ AND } IC_s \end{array} \right. \quad (1.8)$$

where the components of \mathbf{K} depend on the properties of the problem (e.g. the Reynolds number) and are generally unknown. AQMs employing CFD methods often differ in the choice of the components of \mathbf{K} . Models for pollutant concentration based on the transport equation can also be tweaked to solve for mean concentration or concentration variance, and used, for example, to predict an annual mean and standard deviation of a pollutant concentration. [130]

Atmospheric influence

Pollutant dispersion in urban environments is characterized by atmospheric boundary flow and flow around buildings; accurately simulating boundary flow is necessary. The atmospheric boundary layer (ABL) is the part of the atmosphere sensitive to varying conditions at the surface of the Earth in the short term (in terms of hours). Turbulent properties corresponding to actual weather conditions are needed at the inflow boundaries; this is simpler in RANS than in LES. Studies on the reproduction of the influence of atmospheric stability on near-field dispersion using CFD modeling, such as [14, 39, 126, 172, 198, 205], confirm that atmospheric stability conditions significantly affect plume spread and concentration levels. [186]

Even in the case of neutrally- to stably-stratified atmospheric conditions outside the urban setting, stability effects inside the urban canopy should not be neglected. Solar energy increases air temperature in the lower levels of the urban canopy during the day, generating turbulent heat fluxes, and at sunset the transfer of stored heat within the canopy means warmer air than upwind at the same height. Stability inside the canopy increases during the night in the absence of solar radiation. [130] In the case of a neutral ABL, within the surface boundary layer (tens of meters at the surface) wind velocity can be considered mostly horizontal with a vertical profile of modulus $\sim \ln(z + z_0)$ (for $z_0 \geq 1$). Atmospheric stability is a complicated phenomena, discussed in more detail in [179], which is not taken into account in every AQM.

Coupling Flow and CTMs

The coupling of meteorological models and CTMs can be done "offline" or "online", which we refer to as decoupled and coupled, respectively. Decoupled models, where the meteorological or CFD field is calculated and given as input to the CTM, can not provide meteorology-chemistry feedbacks (e.g. aerosol feedbacks to radiation and photolysis, see [202]); these feedbacks can be important to future air quality predictions. Biases could also be introduced into the system; for example [59, 145] reported poor performance due to neglecting aerosol feedbacks to radiation and cloud formation processes. Additionally, if the CTM requires atmospheric input at a smaller time scale than the output of the offline meteorological model, information is lost.

Coupled methods, where meteorology or CFD fields and concentration fields are solved jointly, are increasingly used when feedbacks are deemed important, such as

in locations with high frequencies of clouds and high concentrations of larger particles, and when the local winds can change quickly; coupled meteorology-CTMs can be essential for accurate model simulations. These models can provide more realistic treatments of the atmosphere, particularly in locations with fast-changing meteorological variables, however the cost of computing both flow and concentration fields simultaneously is higher.

In the case of particulate species, the volume fraction (fraction of pollutant to air volume) is generally low, and the effect of the pollutant on air flow can be neglected [206], a practice which is often extended to gas-phase pollutants, permitting the decoupling of CFD and CTM computations.

(iv) Eulerian vs. Lagrangian in the CFD-CTM framework Here we will briefly discuss a comparison done by [206] of Lagrangian and Eulerian models for indoor particle dispersion with the intent of showing the relation between a Lagrangian particle trajectory model and a CTM.

Considering a time-dependent advection-diffusion eulerian method (equation 1.7) for the eulerian continuum, this was compared to a Lagrangian method solving for particle trajectory (as opposed to particle position equations given in (1.5)). [206]

$$\frac{d\vec{u}_p}{dt} = C(\vec{u} - \vec{u}_p) + \frac{\vec{g}(\rho_p - \rho)}{\rho_p} + F \quad (1.9)$$

where the left-hand-side of the equation describes inertial force per unit mass, \vec{u}_p is the particle velocity, \vec{u} the air velocity, the right-hand-side represents a drag term with constant C , Gravity, and buoyancy. ρ (respectively ρ_p) represent the density of the air (particles), and F additional forces per unit mass.

The same CFD flow field can be used in both methods. A comparison between the two methods can be performed once the Lagrangian particle model results are summed over the grid cells to calculate a concentration, a process which is statistically stable and convergent to (1.6) if the number of particles is sufficiently high. Results of the specific applications in [206] will be discussed in paragraph (v). The Lagrangian model depending on a high number of particles, a balance is needed between instability in the concentration (fewer particles trajectories) and increased computation time (many trajectories). The eulerian resolution of conservation equations, while often done iteratively, is stable once converged.

(v) Applications in urban environments Here we discuss the CFD studies performed on various configurations, the most simple being an indoor or single-building configuration, which have helped to shed light on the nuances which are not captured by other modeling methods.

In [206] indoor particle dispersion was studied in a chamber and an airplane cabin for steady and transient cases, using decouple CFD flow and comparing Lagrangian trajectory and eulerian continuum methods. In the chamber an eulerian grid of

60,000 nodes was used, and 100,000 particle trajectories were studied. The Lagrangian method gave less diffusive effects in convection-dominated regions, giving sharp concentration gradient, while the Eulerian method provided a smooth continuum, but overall concentration distributions were similar. In a steady-state problem the Eulerian method calculated concentrations faster, while the Lagrangian method gives more information on individual particle trajectories. If concentration is not being calculated, the Lagrangian model could be applied with fewer trajectories, making it an attractive option for complicated problems. A transient problem with non-constant particle emission rate again showed less smoothness via Lagrangian model, however the Eulerian model surpassed the Lagrangian in computation time. More detail is given in [206]

In [23] simulations of the single-building configuration were performed using a steady RANS model and found lower lateral turbulent diffusion as compared to wind tunnel testing.

The street canyon configuration has been the subject of much study. [108] published a review of developments of CFD models for wind fields and pollutant transport in street canyons. Simulations in both 2D and 3D have highlighted the high variability induced by turbulent mixing and diffusion, a phenomena which is highly three-dimensional; 3D CFD models provide a more complex flow field than 2D.

To take the street canyon configuration to the next level a building array configuration can be studied. While studies have shown that the time-averaged plume profile far enough into the obstacle arrays can be modeled with a Gaussian distribution with appropriate diffusion parameters, CFD methods have been shown to be better for applications with complex geometry. However, more study is necessary for CFD ability with varying atmospheric conditions. CFD model performance with RANS has been evaluated in various studies: [29, 57, 99, 171, 195]. A validation study of CFD models has been performed using the Mock Urban Setting Test (MUST) observation data by [201], and [7, 55, 170] compared CFD model results to experimental data. [27] used DNS, and their results helped to further understanding of the processes affecting plume structure, such as lateral dispersion, secondary-source dispersion and plume skewing.

A more involved configuration is that of a building complex, on which many CFD studies using RANS and LES have been performed to provide reasonably accurate results: [11, 151, 152, 207]. However for this configuration it can be difficult to get reliable observations for validation: [181] performed detailed wind tunnel experiments on a building group in Montreal, and the resulting data has been used for CFD validation. [76] compared five CFD models in New York City, and projects in London (e.g. EPSRC, DAPPLE) have provided data used in CFD simulations.

CFD studies of air quality in 3D urban environments have found that the flow structure around buildings is highly three-dimensional, depending on the building configuration and wind direction. Near-field phenomena has been shown to have a fully 3D nature; pollutants can be transported opposite the wind due to eddies and mean flows caused by structures, caught in recirculation zones, an effect which is more prevalent in building groups.

In addition to the 3D flow caused by structures, flow around buildings is known to be highly unsteady due to oncoming unsteady flow, interaction with the wake flows caused by structures, and contributed to by ventilation systems (HVAC). This influences the complex behavior of pollutant dispersion due to advection and turbulent diffusion. We will note here that the full complexity of these flow features can be modeled by DNS with the appropriately refined grid, but will not be fully captured by a steady RANS approach, contrarily to unsteady RANS approaches. [186]

(vi) Comparisons of Turbulence Models (for CFD-CTM AQMs) The RANS model can be used with various turbulence models, where the turbulent viscosity is defined differently. The standard $k - \epsilon$ model is commonly used for its good convergence properties. This model poorly represents separated flow, however, and has been observed to overestimate turbulent kinetic energy near the upwind corner of a building. This results in poor concentration predictions if the source is located in recirculation regions on the roof or walls.

Modified $k - \epsilon$ models, such as RNG $k - \epsilon$ model, can provide an alternative. Only small differences were observed between modified and standard $k - \epsilon$ when applied to dispersion in the street canyon and building complexes; turbulence produced by surrounding buildings is dominant. Reynolds stress turbulence models have often given the worst results in comparative studies, but can occasionally capture near-wall phenomena. This method requires the optimization of many numerical parameters as there are many equations to be solved. It depends highly on the mesh used, and has more difficulty converging than $k - \epsilon$ models. However, this turbulence model can account for certain effects of complex turbulent flows. A turbulence model similar to $k - \epsilon$ is the $k - \omega$ model. While the $k - \omega$ model is more precise near walls, it is also more sensitive to the initialization, and may have difficulties converging if the turbulence initialization differs too much from the final solution. $k - \epsilon$ models are often the preferred choice for various urban flow fields for their robustness.

In $k - \epsilon$ models, scalar flux estimation is done using the standard gradient diffusion hypothesis with eddy diffusivity typically expressed by eddy viscosity and the turbulent Schmidt number sc_t . Using sc_t is a compromising method which corresponds to the simplicity of $k - \epsilon$ turbulence models. [184] found that the optimal value of sc_t can vary widely, depending on local flow properties. Studies have shown that the underestimation of turbulent diffusion of momentum by steady RANS models can be compensated by small values of sc_t . [38] found that turbulent mixing augmented by buildings can obscure the underestimation of turbulent diffusion by RANS models.

In developing AQMs, LES and RANS are the turbulence models most often considered. LES resolves large-scale unsteady motions and requires only small-scale modeling. Dynamic properties such as the flux of wind pressure on buildings, primarily due to large-scale motions, can be directly represented. Studies show that LES agrees with experimental data for mean value and turbulent energy approximations around a simple building. In [55, 74, 75, 168, 170, 185, 199] results are compared from RANS and LES models for dispersion around buildings. LES was found to

better estimate concentration distribution results, but the mean value differences were small.

A study over Montreal compared RANS $k - \epsilon$ to LES turbulence models, finding estimated surrounding concentrations were lower with LES. LES simulation results showed very diffusive concentrations, and were more accurate when compared to experimental data. Complicated turbulent mass diffusion around buildings is considered too complex for the standard gradient diffusion hypothesis employed by RANS models; these effects can only be captured by LES models. However, the CPU time required for LES simulations is about 10-25 longer than steady RANS models. Unsteady RANS models can reproduce large unsteady structures with lower spatial and temporal resolution than LES models. Very few studies have tested unsteady RANS, however results have been better in comparison to experimental data than steady RANS models. RANS is computationally attractive, and can reproduce concentration variance in idealized urban environments or lab conditions; however models for closure of the transport equations should be improved. [186]

1.2.3 Limitations and Uncertainties

1.2.3.1 Limitations Inherent to Air Quality Modeling

While AQMs have improved vastly in the past decades, there remain nontrivial limitations and uncertainties. The limitations of most models include (but are not limited to)

- the dispersion in urban areas being complicated by aerodynamic effects of the street and building geometry and traffic-induced turbulence; unresolved obstacles and multiscale nature of modeled phenomena.
- the impacts of traffic on air quality, which include a local component as well as an urban background component, which differs according to the pollutant species and its temporal and spatial scales
- the estimation of dry or wet atmospheric deposition fluxes strongly depends on particle size distribution for particulate pollutants' wet scavenging and dry deposition velocities still remain difficult to estimate as a function of particle size, atmospheric conditions, and surface configuration.
- the treatment of atmospheric chemistry, reactions among many different pollutants, secondary reactions and compounding effects.

The multiscale nature of the physical phenomena at play with models relying on approximated subgrid parametrization may limit AQM outputs. Unresolved obstacles can be a source of major uncertainty in physically-based models which reproduce the detailed movement of air and pollutants. Many advances have been made in this area: 3D models of obstacles can be used on relatively small scales. Canopy models can represent surface roughness effects on wind profiles, and aerodynamic effects of

unknown obstacles. These canopy models have extra terms added to the governing equations for drag and increased turbulence.

An example of unresolved obstacles is trees, which reduce wind velocity. Many studies have been performed on forested areas and trees in street canyons, referenced in [186].

The effects of moving vehicles on dispersion around street canyons, often neglected in operational models, was studied by [5, 12]. Large variability was observed between individual concentration time series with moving vehicles in a wind tunnel, and ensemble averaging was needed. [95] used a 3D Eulerian-Lagrangian approach, and [131] extended canopy methods to incorporate effects of vehicles based on a $k-\epsilon$ model adding terms in the transport equations. [189] performed CFD computations in a moving coordinate system. Advances have been made in the field of obstacle effects, but this remains a significant limitation in operational physically-based models. [186]

1.2.3.2 Uncertainties in AQMs

Model performance for AQMs on an urban scale has been observed in the following studies

- $\sim 35\%$ error and $\sim 15\%$ bias for hourly O_3 concentrations
- $\sim 20\%$ error and bias for annual NO_2
- $\sim 75 + \%$ error and $\sim 60\%$ bias for annual PM concentrations.

Near urban sources found less impressive model performance, where a factor of two for error is considered acceptable in the short term (e.g. hourly) for gas and particulate pollutants. [70]

Model inputs (such as emissions, meteorology, and BCs) are the first major source of uncertainty in AQMs. A review of the sensitivity and uncertainty analysis of model applications has been done by [163]. Some studies have found that uncertainty in all input data can be $\sim 50\%$, and even greater for emissions data.

A second significant source of error is the mathematical representation of physiochemical processes simulated by the model; chemical mechanisms include many simplifying assumptions and atmospheric turbulence is highly parametrized, for example.

A third error source is in numerical approximation, related to the applied numerical scheme, time step, and horizontal and vertical resolutions.

Difficulty remains in categorizing and analyzing the error and uncertainties in AQMs. ERCOFTAC [31] developed Best Practice guidelines to categorize the error and uncertainty in CFD simulations using:

- model uncertainty: reality vs. best knowledge exact solution

- discretization and numerical error
- iteration and convergence error
- round-off error
- uncertainty inherent to the particular application
- user and code error

The impact of these uncertainties on model output depends on the level of uncertainty and the sensitivity (e.g. [163]) of the output to the input or parameter of interest. We can assign confidence levels (H/M/L) to various inputs, representing the uncertainty associated to each of them.

- Meteorological variables for the urban background, in general representing $\pm 20\%$ of the model uncertainty:
 - Wind speed/direction (M)
 - Temperature (H)
 - Relative humidity (H)
 - Pressure (H)
- Meteorology within the urban canopy (street or neighborhood scale) :
 - Wind speed/direction (L)
 - Temperature (M)
 - Relative humidity (M)
- Boundary Conditions : depend on the source.
 - BCs from good model simulations with observational data or comprehensive monitoring network (M)
 - BCs from sparse monitoring networks, unevaluated model simulations or generic literature data (L)
 - Errors in land use data may propagate
- Emissions data :
 - Some regulated gaseous pollutants (e.g. NO_x , CO_x , and SO_2) (M)
 - PM , VOC , and non-regulated gaseous pollutants (L)
 - Anthropogenic emissions: $\pm 50\%$ uncertainty (L)
 - Biogenic emissions: only known within a factor of 2 (L)

As for model components, confidence depends on spatial and temporal scales involved (and the type of model considered, needless to say). At urban to regional scales :

- Transport processes (M)
- Chemical transformation (M)
- Atmospheric deposition over long periods (several months) (M)
- Atmospheric deposition over short periods (week or individual events) (L)
- Atmospheric deposition in the urban canopy with complex building/vegetation configurations (L-M)

On short time scales over a street-neighborhood spatial scale, chemical transformation is typically less important. Important transformations (e.g. for NO_x and O_3 are well known (H confidence), however conversion of emitted gases to PM is poorly understood (L-M confidence) [70].

More discussion of uncertainty and challenges, and recent improvements of input data for meteorology and emissions, and of model treatment of physics, can be found in section 1.3.1.

Uncertainty in CFD models

Model uncertainty includes the first two error sources mentioned above, which are particularly significant in the case of physically-based models. We will focus primarily on CFD and CTM models here.

CTMs require knowledge of sources and emissions (in contrast to simple statistical models which only use measurements), as well as of the processes governing the fate and transport of pollutants. Approximations and simplifications will always be involved, which can lead to inaccuracies. Lack of data and high computation costs may lead to simplified chemical and dynamical mechanisms. Development can be costly. [202] The challenge of CFD modeling for real meteorological conditions is the inherently non-stationary conditions and different inflow wind directions, speeds, and turbulent kinetic energy for each case. Similarly, accuracy of CTMs depends strongly on the accuracy of the meteorological model providing input data. The overestimation of mean concentrations has been found to be inherent to Eulerian models. [130]

The relevance of the chosen turbulence model is only significant in CFD simulations once other error sources (e.g. pollutant sources, particular numerical and convergence error) have been removed or controlled, however the treatment of flow as laminar would generally induce more significant error than varying the turbulence model. Accuracy is also affected by uncertainty in the precise geometry (e.g. unresolved obstacles) and uncertain data and models used in boundary conditions. Concentration fields and the relationship between dispersion and flow structure should be investigated, and model results should be compared with experimental data on both concentration and velocity fields. [186]

1.2.3.3 Model Evaluation

In order to understand the limitations and uncertainties of various available AQMs, we must have a means of evaluating different types of models. The evaluation of physically-based models on an urban scale is a difficult question; accuracy tests are complicated by the high variation in space and time of concentrations around buildings. Many methods and guidelines exist. In [173] protocol is outlined for microscale urban meteorology, which helps in model evaluation for the use of microscale meteorological models in flow and pollutant dispersion modeling.

Evaluation protocol has several elements:

- scientific evaluation process
- verification process
- provision of the appropriate quality datasets
- model validation process
- operational evaluation process reflecting the needs of the user

An important question to consider is which variables should be used for evaluation? Maximum concentration is a key metric for most air quality applications. However low values are also important: in population exposure assessment, for example, dilute plumes affect large areas. Time-averaged concentration, which is easier to obtain, is often used.

In the case of CFD models, boundary conditions and meteorology inputs should be evaluated. Ensembles of observations over varying exterior parameters (such as wind direction) should be obtained. Sufficient data is a constraint in short-range urban dispersion modeling due to high variability and confounding factors (e.g. traffic). Experimental data sets from wind tunnel sets are available online: CEDVAL [1], DAPPLE [3], and MUST [37]. [186]

For example, the MUST database is data from a near full-scale experiment conducted for the US Defense Threat Reduction Agency. Neutral gases (point sources) were released in an array of shipping containers in a Utah desert. Releases were performed at dusk and dawn, periods of relatively stable or neutral atmospheric stratification conditions. In [37] model performance is evaluated using MUST data on 20 simulations employing statistical measures: mean bias, geometrical variance, and fraction of prediction within a factor of 2 of observations, considering the influence of various parameters such as pollutant sources. [130]

1.2.4 Modeling chains

While air pollution modeling involves many uncertainties, much knowledge has been developed on important components; fully utilizing the information that is available

is not a trivial matter. A modeling chain could be implemented to this effect, consisting of, for example, traffic models to predict position and kinematic parameters of vehicles, emissions models to estimate the amounts of pollutants released by the vehicles, and air quality models for the dispersion and transformation of pollutants in the atmosphere. [70] Meteorological data also plays an important role in air quality modeling. Depending on the model, economic activity or impact modeling, anthropogenic and natural emissions modeling, transport modeling, exposure and human health effect modeling, and environmental and ecosystem impact modeling can be considered. [84]

Below is a diagram of the main building blocks involved in a modeling chain from traffic to air and water quality.

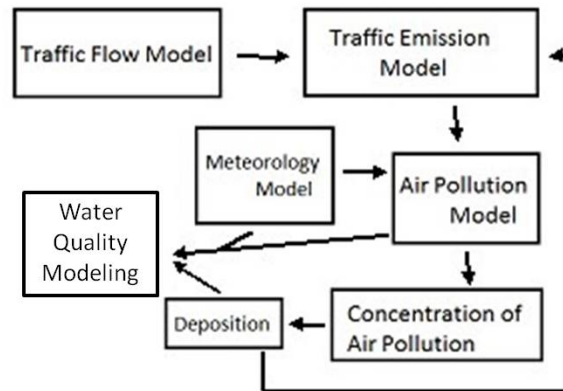


Figure 1.2 – Diagram representing the structure of a modeling chain from traffic to air and water quality models.

We will note that proper interfaces between output from one model and input to the next must be established. Examples of studies on modeling chains for air and water quality models are listed in [70].

1.2.4.1 Traffic to Emissions

Important factors in the estimation of vehicle emissions include vehicle operation (speed, acceleration, engine load, etc.), traffic flow conditions, and road and vehicle characteristics. These factors lead to the determination of parameters in traffic models. The traffic model can be chosen based on input parameters and compatibility of outputs with the input requirements of emissions models. To give a general overview, major coupling methods in practice can be divided into four types :

- Macroscopic: static or aggregated dynamic traffic models coupled with aggregated emissions models. Uses macroscopic emissions for large road networks ; high level of uncertainty.
- Mesoscopic (1): macroscopic traffic models coupled with microscopic emissions models. Uses more accurate emissions models with speed and acceleration as inputs ; calculation of acceleration data from the macroscopic traffic model is required ; less time-consuming than microscopic traffic models.
- Mesoscopic (2): microscopic traffic model coupled with macroscopic emissions models. Another method to increase accuracy while decreasing computation time ; advantageous for high numbers of pollutants ; less accurate with congestion.
- Microscopic: microscopic traffic models coupled with instantaneous emissions models. Computed for short time steps ; predicts individual vehicle emission rates as a function of time and driver behavior ; computes traffic emissions with great spatial and temporal detail.

The reader is encouraged to refer to [70] for more detail.

1.2.4.2 Emissions to AQMs

In order to couple emissions models and AQMs, atmospheric dispersion modeling is necessary to predict spatial and temporal variation of concentrations. Spatial and temporal emissions, meteorological data, and background concentrations of pollutants are necessary inputs. To account for dispersion from vehicle-induced turbulence, traffic model output is required. Atmospheric dispersion in urban areas is of course complicated by obstacles, as discussed in previous sections; we recall that CFD modeling gives detailed representations but is computationally costly. Gaussian models for atmospheric dispersion of traffic emissions near a road without considering vehicle-induced turbulence can provide good results. [70] Most emissions model results are not valid for short time scales, and output from macroscopic emissions models, often around one-hour time scale, are adapted for input to most AQMs. The output of instantaneous emissions models, up to temporal resolution of one second, can only be used by CFD models, but can be averaged over time for use by Gaussian models, which can be advantageous in terms of computation time. In practice, Gaussian and CFD models are most commonly used; roads are divided into segments and considered as line sources. Emissions models estimate emissions on each segment.

In a case study on atmospheric dispersion and deposition of pollution emitted from traffic on a freeway in eastern France, three steps were involved: emissions calculation, atmospheric concentration estimation, and finally calculation of atmospheric deposition fluxes. An average-speed emissions model CopCETE was used in the first step, a Gaussian plume model in the second, and a post-processing step

for deposition. More detail can be found in [70]. We will note that results showed rapid decrease in deposition with distance from the roadway.

1.2.4.3 Exposure modeling

Some air quality forecasting models also include forecasts for human exposure to certain pollutants, e.g. UAQIFS-Norway, -Finland and -Italy² for NO_2 and PM . This could be another step in modeling chains, useful in the assessment of health effects on humans. We will not discuss great detail here, but will mention a few established concepts. The index of instant exposition is the instantaneous concentration in the air around the subject. The index of point exposition refers to the maximum instant concentration of the pollutant in the air around the subject in a time range T , while the integrated average exposition index is the average concentration over T , and the additive effect index is a sum calculated from the concentration of all pollutants present and an acceptable threshold of each. Each of these indexes could be used in exposure modeling, depending on the desired output information. [196]

Exposure modeling of the occupants of a building, for an indoor example, can involve modeling the movement of the occupants in addition to the air quality factor. Exposition modeling can be done 'indirectly' using CFD modeling of the air around subjects, 'directly' using measurements of exposition, concentrations, and statistical regression models, or stochastically by giving a distribution of the exposition of the population. Again, the choice of technique would depend on the desired output information.

1.3 Improvements in Air Quality Modeling

As discussed in the previous section, many factors contribute to uncertainties and inaccuracies in AQMs. Many studies on various factors are mentioned in [203]. Improvements are being made not only in the form of scientific advances to improve air quality forecasts, but techniques are being developed to improve results from currently available AQMs. In this section we will focus on recent improvements, both modeling advances which improve uncertainties and inaccuracies, and techniques to improve AQMs based on available knowledge and data.

1.3.1 Modeling advances

Here we discuss advances in modeling ability from improved inputs to the mathematical treatment of physical phenomena.

1.3.1.1 Meteorological data

Concentrations of ambient air pollutants depend largely upon emissions of the pollutants and precursors and meteorological conditions. Typically it is local-scale circulation and diurnal meteorological variations such as solar intensity, temperature, and wind which determine concentration variations. Meteorological forecast error is

thus propagated into the AQMs using the meteorological input data; studies have even reported higher sensitivity to meteorological data than to emissions inputs and the chemical mechanism treatment by the AQM.

Conventional numerical meteorological models were not designed for pollution propagation, and thus effective use in AQMs requires improvements to these models. Conventional models do not treat small-scale physical processes, nor do they provide additional measurements (such as mixing height) which would be useful in pollution modeling.

Meteorological models also use larger-scale grids than the often smaller-scaled AQMs; simulations with grids under $1km$ are needed for urban AQM implementation. Often the parameterizations of physical processes modeled in meteorological models are developed for larger scales and thus need improvement to more accurately represent effects such as convection and turbulence. In operational larger-scale models, the parameterization of urban areas is important. This has been considered in multiple studies, where land-surface modeling incorporating urban structures and vegetative canopies have been developed and tested. These advances promise to improve representation of urban sub-flows such as wind fields and turbulence. [203]

1.3.1.2 Chemical inputs: emissions and background concentrations

Initial conditions and boundary conditions are generally derived via three methods: output data from a global (or larger-scale) CTM, assumed climatological profiles, and adaptation of satellite or surface data for chemical profiles. However, using output from a global CTM, which are temporally and spatially coarse, would require interpolation, introducing additional error into the AQM. Global-through-urban models (e.g. [94, 135]) can help to reduce errors. Satellite measurements can improve initial and boundary conditions, however there may be uncertainties in retrieval algorithms, cloud contamination, etc.

Of course, accurate characterization of emissions will directly improve modeling capabilities; most models use historically generated offline emissions. Real-time emissions could greatly improve accuracy, particularly for mobile sources, biogenic sources, power generation, surface coating, wildfires, dust events, sea salt, and re-emission from surfaces. Data assimilation (see 1.3.2.3) can be an important technique in reflecting actual online emissions levels. [203]

1.3.1.3 Treatments of physics in the model

The modeling of pollutant transport in AQMs is highly dependent on the many parameters involved and the processes governing the model. Improving these processes and parameters will thus have a significant and continuous effect on AQM accuracy. Particularly important aspects are the parametrization of the urban environment, the representation of gas-phase chemistry (essential for O_3 , NO_2 , and secondary PM), and aerosol dynamics and chemistry.

Parameterizations for urban environments

Much focus has been placed on improving parametrization of urban processes, given the rapid urbanization of world populations. Micro- and meso-scale urban features can influence urban processes such as atmospheric flow, turbulence effects, and urban micro-climate, which in turn modifies the transport, dispersion, and deposition of air pollutants. The improvement of meteorological fields over urban areas is a significant method of improving modeling of urban effects. Street-scale CFD models coupled with mesoscale AQMs are in development. Three methods exist for the parametrization of urban canopy: single-layer and bulk-type schemes, multi-layer schemes, and obstacle-resolved microscale models. While the first two methods are simple enough for operational AQMs, the third requires CFD-type explicit building scale models. The simplest method is to modify existing non-urban approaches.

Other features of urban air quality modeling

In order to treat different pollution deposition rates on surfaces, sub-grid scale emissions (e.g. from traffic), indoor-outdoor pollutant interaction effects, and exposure and health effects, more detailed models are needed than an urbanization of global meteorological models; CTMs are well-adapted to considering these specific features affecting urban air pollution.

While most AQMs show overall satisfactory ability to forecast O_3 and $PM_{2.5}$ on average over a domain for monthly or seasonal time periods, poor performance of simulations for hourly localized concentrations has been observed, particularly in capturing diurnal variations such as daytime peaks, spatial variations between areas with different source profiles, weekend vs. weekday variations, and magnitudes at locations with special terrain/emission/meteorological characteristics. Meteorological forecast and emissions inaccuracies surely contribute to these errors; the treatment of physical, dynamical, and chemical processes in these models may contribute significantly to the error as well. [203]

1.3.1.4 Chemical mechanisms

Limitations in the representation of chemical kinetic mechanisms in operational AQMs were recently identified. Uncertainties remain in the representation of organic chemistry in current gas-phase mechanisms. Additionally, gas-phase mechanisms are largely developed for summer conditions, and chemical reactions are often misrepresented (or not included at all). Some solutions exist, improvements developed based on identified deficiencies, and are discussed further in [203]

Inaccuracies in aerosol chemical and dynamical mechanisms lead to bias in aerosol concentration estimations. This is particularly relevant in the case of PM .

In the case of chemical modeling in urban environments, CTMs are needed to treat chemical transfer specificities such as the effect of street canyons on species lifetimes and photochemical reaction due to solar radiation.

1.3.2 Techniques to improve results

In this section we discuss techniques to improve upon results provided from available models.

1.3.2.1 Statistical Methods

Zhang et al discuss statistical methods and examples of studies in more detail in [202, 203].

Bias Correction Bias refers to a systematic error due to a small number of causes (e.g. model mechanisms or parameters), and is in principle correctable. The simplest method of bias correction would be mean subtraction, where the mean bias is subtracted from the estimated solution at each monitoring site. Other methods exist, such as multiplicative factors from bias calculations and empirical linear fitting between estimated and bias-corrected values.

In the case of CTMs, a linear regression model can be developed between a set of variables from the CTM and an observed variable, in order to correct AQ approximation bias for a given site.

However, the bias correction approach may not be effective in the case random errors; it doesn't give insight into model performance, and may prevent identification of problematic areas and model uncertainties. The more sophisticated approaches are also computationally expensive and complex, requiring expertise to implement.

Probabilistic forecast Another approach in the case of a CTM is a probabilistic forecast. Probabilistic forecasts can be advantageous, providing an estimate of likelihood of occurrence of an event. The simplest probabilistic methods use a dichotomous (yes-no) predictand, while multi-category probabilistic methods can handle several categories using a set of probability values, and methods with ensembles approximate the full distribution of probabilities (continuous variable) rather than categories. Ensembles can perform well with uncertainties, but require knowledge of model errors and uncertainties in model inputs, and multiple different models. This approach is computationally expensive and requires expertise, leading to a high operational cost. The MACC project (<http://gems.ecmwf.int/d/products/raq/>) involves ten AQMs over Europe, representing the operational state of the art in ensemble forecasting.

Data fusion combines data from multiple sources to give a single more accurate output. Such data sources can be observations, reanalysis, and model data, often using kriging or interpolation for observations. It can be used for AQMs with statistical methods, deterministic models, and observations. Post-simulation data fusion (e.g. a regression model with historical data) can be used to improve model deficiencies.

1.3.2.2 Ensemble Modeling

Ensemble modeling is a numerical method of producing a representative sample of possible air quality states. This can be done with multiple models or one model and varying inputs (parameters, configurations). The case of a single model with varying parameters is related to the concept of Reduced Basis methods, introduced in section 2.1.2. Significant improvement has been made with this technology in O_3 and $PM_{2.5}$ modeling. This is perhaps because ensemble forecasting could remove some unpredictable components of the physical or chemical processes modeled, as compared to a single deterministic model. Ensemble forecasts are usually weighted linear combinations of the ensemble members, meaning the accuracy and limitations of the resulting forecast may be sensitive to accuracy and limitations of the ensemble members, and to the weighting coefficients used. While some methods do not account for error with respect to observations, some more sophisticated methods combine ensemble forecasting and data assimilation.

As discussed in section 1.2.3, uncertainties in physical and numerical formulation, discretization, and input data are not negligible in air quality modeling. Given these limitations, choosing a single deterministic model with a single set of input data may not be the best solution for accurate air quality modeling. For example, a stochastic view allows the concentration to be seen as a random variable. Ensemble forecasting aims to account for all sources of uncertainty, using several forecasts by different numerical models relying on different physical formulations and input data sets.

Major techniques for ensemble forecasting include:

- Monte Carlo (MC) simulations
- Multimodel ensembles
- Sequential aggregation
- Coupled sequential aggregation and classical data assimilation

Monte Carlo simulations: Monte Carlo simulations are a form of ensemble forecasting where a single model is used with varying input data (chosen based on probability distributions chosen by the modeler) to generate an ensemble of solutions. The mean, standard deviation, and possibly the probability distribution of the output concentrations are determined for a large number of simulations. This mean converges to the expectation of the concentrations at a rate independent of the dimension (number of pollutant species or discretization), but slowly. These simulations are relatively simple to implement, however uncertainties in the chosen model are not treated and may be perpetuated in the ensemble result.

Multimodel ensembles: Multimodel ensembles employ different models (with or without different input data). These ensembles are often more complex, as they rely on CTMs with different physical and numerical formulations, and may be difficult

to implement in practice. However, the question of structural uncertainty (i.e. the uncertainty in the mathematical mechanism representing the physical phenomena and numerical resolution) is addressed, in contrast to Monte Carlo schemes. If the various models are built from the same platform allowing for changes in the model formulation, one can better control the design of the ensemble, as opposed to models from different modeling teams. Multimodels have been shown to better handle cases of high spatio-temporal variability, as input data perturbation failed to compensate for this variability. In [150] Monte Carlo and multimodel methods were combined.

Uncertainty Estimation: An important concern in ensemble forecasting is the representation of uncertainties; the main source of this information is prior knowledge on the model(s) used and observations. A method to score ensemble models is to compare each individual model to observations, and for each observation determine how many forecasted above or below the observation. If the rank is consistent for all observations (i.e. the same number of individual models over-shoot and under-shoot), then the ensemble is well-balanced. To estimate the reliability of the probability forecast determined from the ensemble model simulations, one determines consistency between observed concentration occurrence frequency and the probabilistic forecasts. Ensembles are also scored based on resolution (the ability to produce significantly different probabilistic forecasts for the same subsets of events) and sharpness (the ability to forecast extreme events). More input variation for MC simulations and more models for multi-model ensembles can improve the ensemble score. Optimization procedures are not currently feasible due to computational costs, but automated improvement methods would greatly improve ensemble forecasting ability. For example, in [72], a general large ensemble overestimating uncertainty was used, and a more appropriate subensemble was chosen based on the ensemble scores.

Sequential Aggregation: In order to produce a single improved forecast from the ensemble, one can use a median or mean solution, but this gives no guarantee of improvement. Sequential aggregation is a weighted linear combination, where the weights are computed from past simulations, repeated sequentially before each forecast. Methods to determine weights include least squares methods (e.g. [122], practically efficient, but no theoretical guarantee of performance), and regression methods (e.g. [148]). However, while the framework of these methods guarantees performance in the long-run, no observational error is considered, and no method to compute weighting for multivariate fields (multiple observed pollutant species) has been proposed, nor to account for spatial variation of the weights. The results for pollutant species without observational data may not be improved with these methods.

1.3.2.3 Data Assimilation

Data assimilation refers to a process by which measurements of a physical state in question are used in conjunction with a model of the system to provide an improved

approximation of reality. These methods require a set of observations of the state, a mathematical model, and a data assimilation scheme.

The overall goal of data assimilation methods is to combine observations and numerical simulations to provide accurate and realistic state estimations. While this seems simple enough, the challenge lies in formulating a method to interpret and employ data from often sparse or noisy measurements in some optimal way to contribute to the knowledge of the state in the numerical model. We must consider that there will be not only the anticipated error in numerical simulations from varying parameters, but also unanticipated error due to the shortcomings of the mathematical model itself and its imperfect representation of reality.

For example, a solution to determining weights for simulations of multiple species is coupling sequential aggregation with classical data assimilation, using concentration forecasts from data assimilation methods instead of simple observations in the sequential aggregation framework. The weights can be computed independently for each grid cell and chemical species, giving temporally constant but space/species dependent weights. However, this requires the implementation of an ensemble and data assimilation, which can be complex or impractical.

Data assimilation can be used to improve AQ modeling, and is a major focus of this work. It will thus be discussed in more detail in 2.2 and 2.3.

Chapter 2

A review of model reduction and data assimilation techniques

Résumé :

Dans ce chapitre nous présentons des méthodes actuelles de réduction de modèle et d'assimilation de données, suivi d'une discussion de l'application de ces techniques pour la qualité de l'air.

Soit $\Omega \subset \mathbb{R}^d$ est un domaine borné, on s'intéresse à des problèmes stationnaires \mathcal{P} de la forme

$$\mathcal{L}u = F \text{ dans } \Omega,$$

où l'opérateur \mathcal{L} est associé à une EDP qui dépend d'un jeu de paramètres \mathbf{p} . La réduction de modèle consiste à réduire le coût de calcul d'une solution, en utilisant des connaissances à priori sur le système, soit par la simplification du problème \mathcal{P} ou bien par la réduction de la dimension du problème lorsque les paramètres varient. Parmi les méthodes de réduction on trouve les modèles de substitution ou meta-modèles et les méthodes de projection. Celles-ci utilisent un espace de dimension réduite sur lequel sont projetés les opérateurs du modèle. Dans ce chapitre nous présentons plusieurs méthodes de réduction : des méthodes d'interpolation, de décomposition, des bases réduites, et d'inférence.

L'assimilation des données repose sur l'intégration des observations expérimentales et des connaissances sur la physique décrite par un modèle mathématique. Les méthodes sont variées, cherchant à corriger un ou plusieurs paramètres du modèle ou l'état du système. Dans ce chapitre on présente des méthodes d'assimilation de données séquentielles telles que le filtre de Kalman, la méthode inverse de type problème adjoint, et des méthodes variationnelles telles que le 4D-Var.

Finalement, nous donnons des exemples d'études couplant l'assimilation de données et réduction de modèle dans le contexte de la qualité de l'air.

2.1 Model Order Reduction

Numerical modeling has become indispensable in many scientific fields where mathematical equations can be used to describe physical phenomena, including but not limited to fields involved in urban modeling: air and water quality modeling, geotechnics modeling, network modeling, and acoustics modeling.

Computation times for large three-dimensional analysis commonly take tens of hours, making many-query contexts, such as sensitivity analysis and optimization, hardly feasible. Model reduction methods are of great interest to applications of parametrized problems involving many-query or real-time study.

Parameters of numerical models can generally be divided into three classes: control parameters (as will be clarified in 2.3.2.2), physical (as we will see in 4.2.2), and geometrical (we will see examples in 2.3) [156]. The AQM problem introduced in equation (1.7) is an intriguing candidate for MOR in the (quasi-)real-time and many-query context for each of the three classes of parameters.

In this section we will briefly review common surrogate model, projection-based methods, and a decomposition method of MOR.

We will consider a generic problem (1) as introduced in the Introduction .

$$\mathcal{P} : \Omega \times \mathcal{D} \rightarrow \mathbb{K}$$

where \mathcal{P} represents a problem (we'll consider it a parameterized PDE), $\Omega \subset \mathbb{R}^d$ is the physical domain of dimension $d = 2, 3$, \mathcal{D} the parameter domain, and \mathbb{K} a field (\mathbb{R} or \mathbb{C}). We will consider the solutions $u \in \mathcal{X}$ for some suitable Banach solution space \mathcal{X} . The problem \mathcal{P} can be written in the form (2)

$$\mathcal{L}(\mathbf{p})(u(\mathbf{p})) = F(\mathbf{p}) \tag{2.1}$$

$$+ \text{ Conditions on } \partial\Omega, \tag{2.2}$$

where $\partial\Omega$ represents the domain boundary.

We will consider that the associated variational problem is of the form: find $u(\mathbf{p}) \in \mathcal{X}$ such that for any $v \in \mathcal{X}_{test}$ appropriate test space, we have, for parameter $\mathbf{p} \in \mathcal{D}$,

$$a(u, v; \mathbf{p}) = b(v; \mathbf{p}) \tag{2.3}$$

We define here \mathcal{X}_h a discrete approximation space of dimension \mathcal{N}_h for use in classical approximation methods (e.g. finite elements).

2.1.1 Surrogate model methods

A common approach is to develop simplified models, such as surrogate models, to approximate the model without significant loss of accuracy. Data-fit surrogate models, or metamodels, can be built using interpolation and regression methods. The goal is to discretely describe an input-to-output map, which avoids the construction of reduced models or operators. Some methods, discussed in [149] construct reduced

spaces and build a surrogate model which maps inputs to the coefficients of representations of full states in the reduced space.

These methods are often applied to different applications than projection-based models, such as when the notion of state is not important, and regression or interpolation of outputs provide sufficiently accurate results. We will not go deeper into this topic here, but more information can be found for example in the following reviews of metamodeling techniques [17, 109].

2.1.2 Projection-based methods

Another approach to rapidly compute reliable approximations of solutions to complex problems with many parameters is by projection-based MOR methods, such as reduced basis (RB) methods [153]. Projection-based methods aim to reduce the complexity of the model using the, when applicable, relatively small "width" (in the sense of Kolmogorov (2.4)) of the manifold of all possible solutions for varying parameters, relying on the information given by a well-chosen set of particular solutions to the problem. A basis is constructed of a reduced space, which is a low-dimensional subspace of the solution space. The equations of the full model are projected onto the reduced space, which provide the operators of the reduced model [149].

A key factor of these methods is the small Kolmogorov n-width, implying that the solution manifold $\mathcal{M}_h = \{u_h(\mathbf{p}) \in \mathcal{X}_h \mid \mathbf{p} \in \mathcal{D}\}$ for discrete solutions $u_h(\mathbf{p})$ to \mathcal{P} , depending on parameters \mathbf{p} may be approximable by a finite set of well-chosen solutions. We define the Kolmogorov n-width [100] as follows:

Definition Let \mathcal{M} be a subset of a Banach space \mathcal{X} , and Y_n a generic n-dimensional subspace of \mathcal{X} . The angle between \mathcal{M} and Y_n is

$$E(\mathcal{M}; Y_n) = \sup_{x \in \mathcal{M}} \left(\inf_{y \in Y_n} \|x - y\|_{\mathcal{X}} \right) \quad (2.4)$$

The Kolmogorov n-width of \mathcal{M} in \mathcal{X} is

$$d_n(\mathcal{M}, \mathcal{X}) = \inf \{ E(\mathcal{M}; Y_n) ; Y_n \text{ is an n-dimensional subspace of } \mathcal{X} \}$$

The n-width measures to what extent the set \mathcal{M} can be approximated by an n-dimensional subspace of \mathcal{X} [46]. In order to determine if projection-based model reduction approaches can be applied to a problem \mathcal{P} , we evaluate the complexity of the manifold \mathcal{M}_h of all possible solutions induced by varying parameters. This analysis consists in a singular value decomposition method applied to the correlation matrix of solutions of \mathcal{P} computed for different values of the parameters. For example, this correlation matrix for a set of particular parameter values can be computed as we will detail in section 2.1.2.2. In [114] the reader can find more discussion of n-width in the framework of non-POD reduction methods.

Once the rapid decay rate of the singular values is confirmed, one can assume that a projection-based method is worth investigating. Classical projection-based

MOR methods include interpolation methods, Proper Orthogonal Decomposition (POD), Reduced Basis methods (RBM), and Krylov subspace methods. In the case of the latter three methods, a reduced basis is constructed and a reduced model is build with a (often intrusive) projection step. For example, in the case of a system of ordinary differential equations of the form

$$d_t u = \mathbf{A}u + \mathbf{F}u^2 \quad (2.5)$$

the reduced model is defined as

$$d_t \tilde{u} = \tilde{\mathbf{A}}\tilde{u} + \tilde{\mathbf{F}}\tilde{u}^2 \quad (2.6)$$

where operators $\tilde{\mathbf{A}}$ and $\tilde{\mathbf{F}}$ could be derived for example via a Galerkin projection onto a reduced basis space.

For further reading we mention the methods of Krylov subspaces [10], reduced order modeling in the Loewner framework [93], and Balanced Truncation [20], but we will not discuss these methods in detail here. Below we will describe in more detail Empirical Interpolation 2.1.2.1, POD 2.1.2.2, Certified RBMs 2.1.2.3, Proper Generalized Decomposition (PGD) 2.1.3, and Operator Inference 2.1.2.4.

2.1.2.1 Empirical Interpolation

The Empirical Interpolation Method (EIM) [16] can build a linear combination of fully determined solutions from values of the quantity at some interpolating points and from some solutions to \mathcal{P} for certain instances of the parameter \mathbf{p} . The method simultaneously defines the set of so-called generating functions in \mathcal{M} and the associated interpolation points. The generating functions are chosen from a sample of states in \mathcal{M} , and the interpolation points are chosen from a pre-defined sample of points $x \in \bar{\Omega}$ over the calculation domain.

The first chosen generating function ψ_1 is the "largest" by L^∞ -norm (we assume implicitly that the elements of \mathcal{M} also belong to $L^\infty(\Omega)$), and the associated interpolation point x_1 (chosen among the points at which we can easily evaluate the state) is the point which gives the most "information" on ψ_1 . A basis function is defined by $q_1 = \frac{\psi_1}{\psi_1(x_1)}$.

The interpolation problem is to find $\{\alpha_j^{m-1}(\psi)\}_{1 \leq j \leq m}$ such that

$$\forall 1 \leq i \leq m-1 \quad \mathcal{I}_{m-1}(\psi)(x_i) = \psi(x_i), \quad (2.7)$$

and the EIM operator is

$$\mathcal{I}_{m-1}[\psi] = \sum_{j=1}^{m-1} \alpha_j^{m-1}(\psi) q_j. \quad (2.8)$$

The generating functions at each iteration M are then defined recursively by maximizing the error of the $M-1$ interpolator over the solution space \mathcal{M} in the L^∞ -norm (over the functions). The associated interpolation point is taken to maximize the

pointwise interpolation error of the M^{th} interpolation over the domain $\bar{\Omega}$. On each generating function a sort of "orthonormalization" operation is performed by the interpolation operator to construct a basis function $q_M = \frac{\psi_M - \mathcal{I}_{M-1}(\psi_M)}{\psi_M(x_M) - \mathcal{I}_{M-1}(\psi_M(x_M))}$. The L^∞ norm of the EIM interpolation error bound depends on the best fit on the function space generated by the basis functions $X_M = \text{span}\{\psi_i\}_{1 \leq i \leq M} = \text{span}\{q_i\}_{1 \leq i \leq M}$ and the Lebesgue constant [114].

The EIM can be a useful tool in the implementation of Reduced Basis Methods (see 2.1.2.3) when the problem does not satisfy affine decomposition with respect to varying parameters (2.13). The EIM can treat nonaffine operators and approximate them on the linear combination form. This will be discussed in subsection 2.1.2.3.

There exists a generalized form of the EIM (the GEIM), used when available data are not pointwise values of the state, which will be discussed in detail in section 3.2, and applied in part III.

2.1.2.2 The Proper Order Decomposition (POD) method

The Proper Order Decomposition (POD) method, first introduced in [113] and also referred to as Karhunen-Loève, is widely used, applied to numerous research fields including computational fluid dynamics (CFD).

Given a set Ξ^{POD} of N_t solutions $u_h(\mathbf{p}; x) \in \mathcal{X}_h$ to the problem \mathcal{P} , for varying values of \mathbf{p} (a parameter in \mathcal{D} or the time component), we want to approximate any $u_h(\mathbf{p}; x) \in \Xi^{POD}$ by a linear combination of basis function $\Psi_k(x)$ such that

$$u_h(\mathbf{p}; x) \simeq \sum_{k=1}^K \alpha_k(\mathbf{p}) \Psi_k(x).$$

The POD method relies on the fact that the first few basis functions $\Psi_k(x)$ are computed in order to represent the most energetic parts of the system. These basis functions are called POD modes and are obtained via a spectral decomposition of a correlation matrix.

Let $M \in \mathbb{R}^{N_t \times N_t}$ be the correlation matrix of components

$$\mathbf{M}_{ij} = \langle u_h(\mathbf{p}_i; x), u_h(\mathbf{p}_j; x) \rangle_W, \quad 1 \leq i, j \leq N_t, \quad (2.9)$$

associated to the set Ξ^{POD} and an appropriate scalar product $\langle \cdot, \cdot \rangle_W$, and V_k the k^{th} eigenvector associated to λ_k the k^{th} largest non-zero eigenvalue of the matrix \mathbf{M} . The basis function $\Psi_k(x)$ is given by

$$\Psi_k(x) = \frac{1}{\sqrt{\lambda_k}} \sum_{\ell=1}^{N_t} V_k(\ell) u_h(\mathbf{p}_\ell; x), \quad (2.10)$$

where $V_k(\ell)$ is the ℓ^{th} component of the eigenvector V_k . By construction, the POD basis is orthonormal.

The size K of the POD approximation is chosen, such that K is small enough while $I(K)$, the Relative Information Content [4]

$$I(K) = \frac{\sum_{k=1}^K \lambda_k}{\sum_{k=1}^N \lambda_k}$$

is close to one. Let P_K be the projection operator on each POD mode $\Psi_k(x)_{1 \leq k \leq K}$, defined as, for any $v \in \mathcal{X}$,

$$P_K v = \sum_{k=1}^K \langle v, \Psi_k \rangle_W \Psi_k. \quad (2.11)$$

The optimal coefficients $\alpha_k(\mathbf{p})$ when measured in the norm associated to the scalar product $\langle \cdot, \cdot \rangle_W$, are

$$\alpha_k(\mathbf{p}) = \langle u_h(\mathbf{p}; x), \Psi_k(x) \rangle_W$$

which correspond the coefficients of the projection of $u_h(\mathbf{p}; x)$ on each POD mode $\Psi_k(x)$

Note that the POD procedure is mostly the same regardless if \mathbf{p} is in the time interval or in the parameter space.

The POD functions (2.10) constitute a basis of a reduced-order approximation of the solution manifold \mathcal{M}_h

$$\mathcal{X}_N^{POD} = \text{span}\{\Psi_k\}_{k=1}^N. \quad (2.12)$$

This reduced approximation space can be used in the construction of reduced models, for example by projection of the full model operators (2.3) onto \mathcal{X}_N^{POD} , by a Galerkin method as in the following section 2.1.2.3, or by a nonintrusive method [149] described in section 2.1.2.4.

2.1.2.3 Certified Reduced Basis

The Reduced Basis (RB) method relies on the fact that when the parameters vary, the set of solutions is often of small Kolmogorov dimension, implying that $\mathcal{M}_h = \{u_h(\mathbf{p}) \in \mathcal{X}_h \mid \mathbf{p} \in \mathcal{D}\}$, the manifold of all solutions can be approximated by a finite set of well-chosen FE solutions of the parametrized PDE. One can identify a set of parameters, $S_N = (\mathbf{p}_1, \mathbf{p}_2, \dots, \mathbf{p}_N) \in \mathcal{D}^N$, to generate this low-dimension space made up the particular solutions $(u_h(\mathbf{p}_1), \dots, u_h(\mathbf{p}_N))$ to \mathcal{P} . We perform a Galerkin method on this RB approximation space, essentially replacing the approximation space (e.g. by finite element) generated by \mathcal{N}_h simple basis functions with a RB space generated by $N \ll \mathcal{N}_h$ particular solutions to \mathcal{P} . The idea of reduced basis methods is to compute an inexpensive and accurate approximation, $u_h^N(\mathbf{p})$, of the solution to problem \mathcal{P} for any $\mathbf{p} \in \mathcal{D}$ by seeking a linear combination of the particular solutions:

$$u_h^N(\mathbf{p}) = \sum_{i=1}^N \alpha_i^h(\mathbf{p}) u_h(\mathbf{p}_i). \quad (2.13)$$

For a stable implementation of the reduced basis method, it is common practice to improve the basis of the RB space from the one composed of the $\{u_h(\mathbf{p}_i)\}_{1 \leq i \leq N}$, usually by a Gram-Schmidt method. In what follows, we denote by $\{\xi_1, \dots, \xi_N\}$ these \mathcal{X} -orthonormalized basis functions, and by X_h^N the approximation space which they span: the reduced basis space.

Let $\{\phi_h^i\}_{1 \leq i \leq N_h}$ be the basis functions of \mathcal{X}_h . The solution of the variational problem (2.3) in \mathcal{X}_h is equivalent to the solution $\mathbb{U}_h(\mathbf{p}) \in \mathbb{R}^{N_h}$ of the following linear system

$$\mathbb{A}_h(\mathbf{p}) \mathbb{U}_h(\mathbf{p}) = \mathbb{B}_h(\mathbf{p}) \quad (2.14)$$

where $[\mathbb{A}_h(\mathbf{p})]_{i,j} = a(\phi_h^i, \phi_h^j; \mathbf{p})$ with $\mathbb{A}_h(\mathbf{p}) \in \mathbb{R}^{N_h \times N_h}$ and $[\mathbb{B}_h(\mathbf{p})]_j = b(\phi_h^j; \mathbf{p})$ with $\mathbb{B}_h(\mathbf{p}) \in \mathbb{R}^{N_h}$.

The usual RB method is a Galerkin method on the space X_h^N , which is of much smaller dimension than the original approximation space \mathcal{X}_h ; the resolution of the problem in X_h^N is less expensive than in the true finite element space \mathcal{X}_h . Thereby, the solution of the variational problem (2.3) in X_h^N is equivalent to the solution $\mathbb{U}_N(\mathbf{p}) \in \mathbb{R}^N$ of the following linear system

$$\mathbb{A}_N(\mathbf{p}) \mathbb{U}_N(\mathbf{p}) = \mathbb{B}_N(\mathbf{p}), \quad (2.15)$$

where $[\mathbb{A}_N(\mathbf{p})]_{i,j} = a(\xi_i, \xi_j; \mathbf{p})$ with $\mathbb{A}_N(\mathbf{p}) \in \mathbb{R}^{N \times N}$ and $[\mathbb{B}_N(\mathbf{p})]_j = b(\xi_j; \mathbf{p})$ with $\mathbb{B}_N(\mathbf{p}) \in \mathbb{R}^N$.

We also define an output quantity

$$s(\mathbf{p}) = \ell^\circ(u^{bk}(\mathbf{p}); \mathbf{p}), \quad (2.16)$$

where $\ell^\circ(\cdot; \mathbf{p}) : \mathcal{X} \times \mathcal{D} \rightarrow \mathbb{R}$ is a linear and continuous functional (we note that ℓ_m in (3) can be considered a special case of the family of output functionals ℓ° here). The output quantity on the RB solution $u_h^N(\mathbf{p})$ is

$$s_N(\mathbf{p}) = \ell^\circ(u_h^N(\mathbf{p}); \mathbf{p}), \quad (2.17)$$

During the implementation of the reduced basis method, the computational work is separated into two stages: *offline* and *online*. This decomposition is a key ingredient of the method. The reduced basis functions, $\{\xi_1, \dots, \xi_N\}$, as well as all expensive parameter-independent terms are computed once during the *offline* stage and stored, whereas during the online stage – for each new value of the parameters – inexpensive parameter-dependent quantities are evaluated, together with the computation of the solution $\mathbb{U}_N(\mathbf{p})$. However, to perform the online stage efficiently, one must isolate the parametric contribution to the matrix $\mathbb{A}_N(\mathbf{p})$ and the vector $\mathbb{B}_N(\mathbf{p})$ of (2.15), allowing all parameter-independent matrices and vectors to be built only once and saved during the offline stage, allowing for a cheap online state of complexity $\mathcal{O}(N^3)$ depending on the RB size.

If the linear system (2.15) satisfies the affine assumption that

$$\mathbb{A}_N(\mathbf{p}) = \sum_{n=1}^{N_a} \theta_n^a(\mathbf{p}) \mathbb{A}_n \quad \text{and} \quad \mathbb{B}_N(\mathbf{p}) = \sum_{n=1}^{N_b} \theta_n^b(\mathbf{p}) \mathbb{B}_n, \quad (2.18)$$

where θ_n^a and θ_n^b are parameter dependent functions and \mathbb{A}_n and \mathbb{B}_n are parameter independent matrices and vectors, the decomposition of the computational work into a offline/online strategy is straightforward. However, in the case of non-affine parameter dependence of the problem (2.15) the EIM (subsection 2.1.2.1) can be used to approximate the non-affine operators in the form of (2.18) and allow us to maintain a *low cost* online stage (for example in [50], used for CRB implementation with non-linear industrial problems). The EIM provides a set of parameter $\tilde{S}_N = \{\tilde{\mathbf{p}}_1, \dots, \tilde{\mathbf{p}}_{\tilde{N}}\}$ such that, for example, the matrix $\mathbb{A}_N(\mathbf{p})$ can be approximated by

$$\mathbb{A}_N^{EIM}(\mathbf{p}) = \sum_{i=1}^{\tilde{N}} \beta_n(\mathbf{p}) \mathbb{A}_N(\tilde{\mathbf{p}}_n). \quad (2.19)$$

The parameter set \tilde{S}_N used to generate the EIM formula is chosen from the same discrete training set $\Xi_{train} \subset \mathcal{D}$ as in the construction of the reduced basis, however \tilde{S}_N can be chosen differently for example using greedy algorithms improved for the EIM [82].

While the construction of the EIM basis can be costly, it has been done simultaneously with the construction of the RB, as in [49], to reduce offline costs. Once the matrices $\mathbb{A}_N(\tilde{\mathbf{p}}_n)$ are assembled during the offline stage, during the online stage a small ($\tilde{N} \times \tilde{N}$) linear system is solved to compute the coefficient $\beta_n(\mathbf{p})$.

Error estimates [146], [192]

The numerical analysis of reduced basis methods relies on standard techniques, such as finite elements, and therefore inherits discretization error from the so-called truth approximations:

$$\epsilon_h(\mathbf{p}) = \|u(\mathbf{p}) - u_h(\mathbf{p})\|_{\mathcal{X}} \quad (2.20)$$

The subsequent use of the reduced basis to rapidly approximate new solutions will then add what we will call the RB error.

$$\epsilon_h^N(\mathbf{p}) = \|u_h(\mathbf{p}) - u_h^N(\mathbf{p})\|_{\mathcal{X}} \quad (2.21)$$

Then the total error committed is bounded by:

$$\epsilon_{tot}(\mathbf{p}) := \|u(\mathbf{p}) - u_h^N(\mathbf{p})\|_{\mathcal{X}} \leq \epsilon_h(\mathbf{p}) + \epsilon_h^N(\mathbf{p}) \quad (2.22)$$

The approximation error, FEM error here (we'll consider the finite element method for example), $\epsilon_h(\mathbf{p})$ depends on the discretization, and will decrease as the step size $h \rightarrow 0$. Likewise, an a priori error given in [53] shows that $\epsilon_h^N \rightarrow 0$ as $N \rightarrow \infty$, provided the usual assumptions on operator $a(\cdot, \cdot)$ of equation (2.3) are satisfied.

As the total error is the sum of these two pieces, increasing N can reduce the total error. However for a fixed RB size N , as $h \rightarrow 0$, the RB error could increase, as in the a priori estimate given in [53] for an SDFE-stabilized advection-reaction problem, which authors attributed to increasing "complexity" of the problem when discretized on a finer mesh.

If we want to bound the error of our CRB method, without knowing the true solution, we need an *a posteriori* error bound. This can be approached by a primal-dual strategy [175]. A dual problem associated to (2.3) and the problem output (2.16) is defined as follows.

Given a parameter $\mathbf{p} \in \mathcal{D}$, find the dual solution $\psi_h \in \mathcal{X}_h$ such that for any $v_h \in \mathcal{X}_h$,

$$a(v_h, \psi_h; \mathbf{p}) = -\ell^o(v_h; \mathbf{p}). \quad (2.23)$$

We then want to define a RB reduced problem associated to (2.23), as in (2.15), over a RB approximation space associated to the dual problem, X_h^{Ndu} constructed from particular dual solutions for parameters $(\mathbf{p}_1^{du}, \dots, \mathbf{p}_{Ndu}^{du})$. The RB dual solution will be $\psi_h^N(\mathbf{p})$.

Let us define the following error functions for the primal RB solution $u_h^N(\mathbf{p})$ and the dual RB solution $\psi_h^N(\mathbf{p})$.

$$e_N^{pr}(\mathbf{p}) = u_h(\mathbf{p}) - u_h^N(\mathbf{p}) \quad (2.24)$$

$$e_N^{du}(\mathbf{p}) = \psi_h(\mathbf{p}) - \psi_h^N(\mathbf{p}) \quad (2.25)$$

Let us also define the following residuals, for $v_h \in \mathcal{X}_h$

$$\mathcal{R}_N^{pr}(v_h; \mathbf{p}) = b(v_h; \mathbf{p}) - a(u_h^N(\mathbf{p}), v_h; \mathbf{p}) = a(e_N^{pr}(\mathbf{p}), v_h; \mathbf{p}) \quad (2.26)$$

$$\mathcal{R}_N^{du}(v_h; \mathbf{p}) = -\ell^o(v_h; \mathbf{p}) - a(v_h, \psi_h^N(\mathbf{p}); \mathbf{p}) = a(v_h, e_N^{du}(\mathbf{p}); \mathbf{p}) \quad (2.27)$$

$$(2.28)$$

Next we define the *deflated* output [53, 175].

$$\tilde{s}_N(\mathbf{p}) := s_N(\mathbf{p}) - \mathcal{R}_N^{pr}(\psi_h^N(\mathbf{p}); \mathbf{p}). \quad (2.29)$$

We are interested in the output error $s(\mathbf{p}) - \tilde{s}_N(\mathbf{p})$. In [175] it is shown that

$$s(\mathbf{p}) - \tilde{s}_N(\mathbf{p}) = -\mathcal{R}_N^{du}(e_N^{du}(\mathbf{p}); \mathbf{p}). \quad (2.30)$$

This ensures quadratic convergence, as can be shown with a simple application of the Cauchy-Schwarz inequality .

Proposition (Prop. 6.3 [175])

The output error satisfies

$$|s(\mathbf{p}) - \tilde{s}_N(\mathbf{p})| \leq \Delta_N^s(\mathbf{p}) \quad \forall \mathbf{p} \in \mathcal{D}$$

where

$$\Delta_N^s(\mathbf{p}) = \frac{1}{\tilde{\beta}(\mathbf{p})} \|\mathcal{R}_N^{pr}(\cdot; \mathbf{p})\|_* \|\mathcal{R}_N^{du}(\cdot; \mathbf{p})\|_*, \quad (2.31)$$

with dual norm $\|w(\cdot)\|_*$ for any functional $w \in \mathcal{X}'$ defined as

$$\|w\|_* = \sup_{v \in \mathcal{X}} \frac{w(v)}{\|v\|_{\mathcal{X}}}, \quad (2.32)$$

and $\tilde{\beta}(\mathbf{p})$ depends on the classical inf-sup parameter associated to the problem, and is defined in [175]. Proposition 6.1 in [175] gives a similarly formed error bound for $e_N^{pr}(\mathbf{p})$.

A discussion of a posteriori error for RB methods applied to the Navier-Stokes equations with physical and geometrical parameters, based on the inf-sup stability factor, can be found in [123], including an online-offline decomposition of these quantities. The proposed a posteriori error bound is a joint quantity for both velocity and pressure, and can account for problems with parameterized trilinear terms in the variational formulation, which may arise in the case of geometrical parameters, by considering the continuity factory in the error bound. The stability factor is approximated by a lower bound, extended to non-linear parameterizations, and an online-offline strategy is proposed for its evaluation.

In other applications of RBMs, an a posteriori error bound may not be available, or may not be sufficiently sharp, for example in the selection of basis functions by a Greedy algorithm. In these cases, some surrogate error estimators have been represented by the coarse bound:

$$\bar{e}_N^s(\mathbf{p}) = s_N(\mathbf{p}) - s_{N/2}(\mathbf{p}), \quad (2.33)$$

proposed in [191], and the more computationally expensive

$$\hat{e}_N^s = \|b(\cdot; \mathbf{p}) - a(u_N(\mathbf{p}), \cdot; \mathbf{p})\|_{\mathcal{X}}, \quad (2.34)$$

for any $v_h \in \mathcal{X}_h$.

2.1.2.4 Data-driven Operator Inference

Data-driven operator inference (DDOI) [149] is a non-intrusive method of projection-based model reduction which derives approximations of reduced operators from information on the full model, without knowing the full operators. This is in contrast to the above-presented CRB methods of section 2.1.2.3 which project fully-known operators onto reduced approximation spaces. Information on the full model can include, for example, information known from the implementation of a black-box software for the full model, such as initial conditions, boundary conditions, inputs, trajectories of the physical states, and outputs. In this summary of the method we consider the available information to be parameters and physical states. This method can be used for nonlinear PDEs with polynomial nonlinear terms of low order (computational costs of the operator inference grows exponentially with the polynomial order).

We consider here a problem, for example of the form (2.5)

$$d_t u = \mathbf{A}u(t, \mathbf{p}) + \mathbf{F}u^2(t, \mathbf{p}),$$

with full-model discrete operators $\mathbf{A}(\mathbf{p}) \in \mathbb{R}^{\mathcal{N} \times \mathcal{N}}$ and $\mathbf{F}(\mathbf{p}) \in \mathbb{R}^{\mathcal{N} \times \mathcal{N}}$ associated to a discretization of dimension \mathcal{N} . We could construct an associated projection-based reduced model, for example of the form (2.6),

$$d_t \tilde{u}(t, \mathbf{p}) = \tilde{\mathbf{A}}\tilde{u}(t, \mathbf{p}) + \tilde{\mathbf{F}}\tilde{u}^2(t, \mathbf{p}),$$

where reduced operators of dimension N , $\tilde{\mathbf{A}}(\mathbf{p})$ and $\tilde{\mathbf{F}}(\mathbf{p})$, are constructed from some usual projection-based method, such as Galerkin CRB. The goal of the DDOI method is to approximate the reduced operators $\tilde{\mathbf{A}}(\mathbf{p})$ and $\tilde{\mathbf{F}}(\mathbf{p})$ by inferred reduced operators $\hat{\mathbf{A}}(\mathbf{p})$ and $\hat{\mathbf{F}}(\mathbf{p})$, built with a non-intrusive procedure.

As is the case in POD based methods, DDOI first uses a training set of N_{train} particular solutions from the full model for parameters $(\mathbf{p}_1, \dots, \mathbf{p}_{N_{train}})$ to build a reduced N -dimensional space X_N representing the solution manifold. In [149] the reduced space is built by the first N POD basis functions.

The full model solutions $u(t, \mathbf{p}_i)$, $1 \leq i \leq N_{train}$, from the black-box full model are then projected onto X_N , noted $\hat{u}(t, \mathbf{p}_i) \in X_N$. The construction of the reduced operators $\hat{\mathbf{A}}(\mathbf{p}_i)$ and $\hat{\mathbf{F}}(\mathbf{p}_i)$ is based on a least squares problem to infer the operators from the available particular solutions to the model. Provided sufficient and accurate solutions are available, inferred operators will converge toward the reduced operators $\tilde{\mathbf{A}}(\mathbf{p})$ and $\tilde{\mathbf{F}}(\mathbf{p})$ constructed by intrusive means.

If the dynamic full-model states are discretized in K time steps t_j , $1 \leq j \leq K$, then for each training parameter \mathbf{p}_i we can infer the associated reduced operators by posing a minimization problem:

$$\min_{\hat{\mathbf{A}}(\mathbf{p}_i), \hat{\mathbf{F}}(\mathbf{p}_i) \in \mathbb{R}^{N \times N}} \sum_{j=1}^K \|d_t \hat{u}(t_j, \mathbf{p}_i) - \hat{\mathbf{A}}(\mathbf{p}_i) \hat{u}(t_j, \mathbf{p}_i) - \hat{\mathbf{F}}(\mathbf{p}_i) \hat{u}^2(t_j, \mathbf{p}_i)\|^2 \quad (2.35)$$

For an arbitrary parameter $\mathbf{p} \in \mathcal{D}$, the reduced operators can be derived from these N_{train} operators by elementwise spline interpolation [149].

The offline computational cost of this method is dependent of the number of time steps and the degrees of freedom of the offline model, and on eventual polynomial nonlinear terms in the full model. The online cost is comparable to that of the POD method. This has been applied in numerical experiments with nonlinear terms up to third order on a large-scale model. Convergence of the inferred reduced operators towards the intrusive classical reduced operators is discussed in [149].

2.1.3 A decomposition method: Proper Generalized Decomposition

The Proper Generalized Decomposition (PGD) method is based on a separation of variables to break down the solution into less costly pieces.

Here we will describe the dynamic case, as PGD methods are most commonly used to reduce solution cost of transient problems. Let us consider our general problem depending on spatial coordinates, time, and physical parameters $(\mathbf{x}, t, \mathbf{p}) \in \Omega \times [0 : T] \times \mathcal{D}^{bk}$.

$$\partial_t u(\mathbf{x}, t; \mathbf{p}) + \mathcal{L}(\mathbf{p})(u(\mathbf{x}, t; \mathbf{p})) = F(\mathbf{p}) \quad (2.36)$$

We consider that our physical state $u(\mathbf{x}, t; \mathbf{p})$ can be written $u(x_1, \dots, x_d)$, where $(x_1, \dots, x_d) \in \Omega_1 \times \dots \times \Omega_d$ denote coordinates related to physical space or time, or parameters of the model. The PGD is an approximation of the form

$$u(x_1, \dots, x_d) \simeq \sum_{i=1}^N F_i^1(x_1) \cdots F_i^d(x_d), \quad (2.37)$$

where the functions $F_i^j(x_j)$ are unknown a priori. The $F_i^j(x_j)$ will be defined by successive enrichment, where each functional product for $1 \leq i \leq N$ is determined in sequence. We note that the number N necessary for a sufficiently precise PGD approximation is not dependent on the problem dimension d , but on the regularity of the true solution u .

This PGD formulation can be computed by multiple methods, as described in [6]. In [140], for example, PGD is used on a transient advection-diffusion-reaction problem, with

$$u(\mathbf{x}, t) \simeq u_N(\mathbf{x}, t) = \sum_{i=1}^N X_i(\mathbf{x}) \cdot T_i(t), \quad (2.38)$$

constructed using two of these techniques, a minimum residual formulation, and a Galerkin PGD formulation. For our purposes, we chose to describe in more detail the Galerkin method used in [40, 176] for a parametrized transient PDE model \mathcal{P} for its simple and surprisingly robust iterative method and treatment of parameters.

We consider the following PGD formulation to treat the problem's parameter dependence:

$$u(\mathbf{x}, t, \mathbf{p}) \simeq u_N(\mathbf{x}, t, \mathbf{p}) = \sum_{i=1}^N X_i(\mathbf{x}) \cdot T_i(t) \cdot P_i(\mathbf{p}), \quad (2.39)$$

where the $(n+1)^{th}$ level approximation is given by

$$u_{n+1}(\mathbf{x}, t, \mathbf{p}) = u_n(\mathbf{x}, t, \mathbf{p}) + X_{n+1}(\mathbf{x}) \cdot T_{n+1}(t) \cdot P_{n+1}(\mathbf{p}). \quad (2.40)$$

Our weak formulation of (2.36) reads,

$$\int_{\Omega \times [0:T] \times \mathcal{D}} v (\partial_t u(\mathbf{x}, t, \mathbf{p}) + \mathcal{L}[u(\mathbf{x}, t, \mathbf{p})] - F) d\mathbf{x} dt d\mathbf{p} = 0, \quad (2.41)$$

for any test function $v(\mathbf{x}, t, \mathbf{p})$ in an appropriate function space \mathcal{V} over $\Omega \times [0 : T] \times \mathcal{D}$. Problem (2.41) is related to the standard weak form of problem (2.36), however in this PGD formulation we integrate over each domain $\Omega \times [0 : T] \times \mathcal{D}$, and we consider $v : \Omega \times [0 : T] \times \mathcal{D} \rightarrow \mathbb{R}$. This is because we can view the parameter \mathbf{p} as a new coordinate defined in \mathcal{D} . Instead of solving the problem for discrete values of \mathbf{p} , this approach generalizes the problem at the cost of an increase in the problem dimension.

Let us assume we have computed the first n terms of (2.39), i.e. $u_n(\mathbf{x}, t, \mathbf{p})$. In order to compute the $(n+1)^{th}$ functional product of (2.39), we want to use the formulation (2.40) and insert the approximation $u_{n+1}(\mathbf{x}, t, \mathbf{p})$ into the weak form (2.41). This leads to a non-linear problem:

$$\begin{aligned} \int_{\Omega \times [0:T] \times \mathcal{D}} & v \left(\partial_t u_n(\mathbf{x}, t, \mathbf{p}) + \mathcal{L}[u_n(\mathbf{x}, t, \mathbf{p})] - F \right. \\ & + X_{n+1}(\mathbf{x}) \cdot \partial_t T_{n+1}(t) \cdot P_{n+1}(\mathbf{p}) \\ & \left. + \mathcal{L}[X_{n+1}(\mathbf{x}) \cdot T_{n+1}(t) \cdot P_{n+1}(\mathbf{p})] \right) d\mathbf{x} dt d\mathbf{p} = 0 \end{aligned} \quad (2.42)$$

such that

$$\begin{aligned}
& \int_{\Omega \times [0:T] \times \mathcal{D}} v \left(X_{n+1}(\mathbf{x}) \cdot \partial_t T_{n+1}(t) \cdot P_{n+1}(\mathbf{p}) \right. \\
& \quad \left. + \mathcal{L}[X_{n+1}(\mathbf{x}) \cdot T_{n+1}(t) \cdot P_{n+1}(\mathbf{p})] \right) d\mathbf{x} dt d\mathbf{p} \\
& = - \int_{\Omega \times [0:T] \times \mathcal{D}} v \mathcal{R}_n d\mathbf{x} dt d\mathbf{p}, \tag{2.43}
\end{aligned}$$

where $\mathcal{R}_n = \partial_t u_n(\mathbf{x}, t, \mathbf{p}) + \mathcal{L}[u_n(\mathbf{x}, t, \mathbf{p})] - F$ is the residual of the PGD approximation at enrichment step n . This nonlinear problem can be solved by an iterative method such as Newton or a fixed point algorithm. In order to approximate $X_{N+1}(\mathbf{x})$, $T_{N+1}(t)$, and $P_{N+1}(\mathbf{p})$, one must choose an appropriate test function for the weak form (2.42). For example in [40], the test function is set to $v = X^*(\mathbf{x}) \cdot T_n(t) \cdot P_n(\mathbf{p}) + X_n(\mathbf{x}) \cdot T^*(t) \cdot P_n(\mathbf{p}) + X_n(\mathbf{x}) \cdot T_n(t) \cdot P^*(\mathbf{p})$, where $X^*(\mathbf{x})$, $T^*(t)$, and $P^*(\mathbf{p})$ are unknown test functions in each of the input domains Ω , $[0 : T]$, and \mathcal{D} , respectively. We want to solve individually for $X_{n+1}(\mathbf{x})$, $T_{n+1}(t)$, and $P_{n+1}(\mathbf{p})$; a fixed-point algorithm is chosen for simplicity. Thus, each iteration would be composed of three steps.

First, to solve for X_{n+1} we can fix $T^* = T_n$, and $P^* = P_n$ from the previous iteration n , and set $v = X^*(\mathbf{x}) \cdot T_n(t) \cdot P_n(\mathbf{p})$ in equation (2.43):

$$\begin{aligned}
& \int_{\Omega \times [0:T] \times \mathcal{D}} X^*(\mathbf{x}) \cdot T_n(t) \cdot P_n(\mathbf{p}) \left(X_{n+1}(\mathbf{x}) \cdot \partial_t T_n(t) \cdot P_n(\mathbf{p}) \right. \\
& \quad \left. + \mathcal{L}[X_{n+1}(\mathbf{x}) \cdot T_n(t) \cdot P_n(\mathbf{p})] \right) d\mathbf{x} dt d\mathbf{p} \\
& = - \int_{\Omega \times [0:T] \times \mathcal{D}} (X^*(\mathbf{x}) \cdot T_n(t) \cdot P_n(\mathbf{p})) \mathcal{R}_n d\mathbf{x} dt d\mathbf{p}. \tag{2.44}
\end{aligned}$$

Integrating over $[0 : T] \times \mathcal{D}$ reduces to the weak form of an elliptic steady-state boundary value problem over Ω , which we can solve for the unknown X_{n+1} by classical techniques.

Once we have computed X_{n+1} , we follow a similar procedure for a new test function $v = X_{n+1}(\mathbf{x}) \cdot T^*(t) \cdot P_n(\mathbf{p})$, and integrating over $\Omega \times \mathcal{D}$, the problem reduces to an ordinary differential equation, which can be solved by classical techniques for T_{n+1} .

In the case of the third component of the $(n+1)^{th}$ functional product, we consider test function $v = X_{n+1}(\mathbf{x}) \cdot T_{n+1}(t) \cdot P^*(\mathbf{p})$ and integrate over $\Omega \times [0 : T]$. This problem may no longer contain any differential operator, if no differential operator is applied to the parameter \mathbf{p} in problem (2.36), and the integral problem can be solved algebraically.

The complexity of the PGD procedure to build the approximation (2.39) is N times the iterative procedure involving at each iteration one elliptic steady-state approximation, one ordinary differential equation approximation, and one algebraic problem. The size of the PGD decomposition N is determined depending on the

complexity of the problem, but in many practical applications, an accurate approximation can be obtained with a small number of terms, $\mathcal{O}(10)$ or $\mathcal{O}(100)$ [40]. This means we have computational time of some tens of steady-state 3D problems, as compared to a classical approach where for each parameter value \mathbf{p} one must solve a 3D problem at each time step, which can imply several millions of 3D solutions. The computational time savings can be of multiple orders, particularly in the case of high-dimensional models (e.g. many parameters), and can be quite advantageous in other cases such as problems over degenerate domains where at least one characteristic dimension is multiple orders smaller than the others [41]. An in-depth discussion of PGD error estimates can be found in [103]. The reader is encouraged to refer to recent works involving PGD including [124, 155].

2.2 Data Assimilation

Data assimilation refers to combining models and measurements for optimal representation of the physical state. Methods include nudging, statistical, variational, and sequential methods, for example. Here we will briefly introduce linear statistical methods, and focus on more sophisticated physically-based methods of sequential and variational categories.

The general framework of the data assimilation problem is based on the parameterized PDE problem (2.1), with the additional constraints on the solution to match the observations as given by (3).

$$\begin{cases} \mathcal{L}(\mathbf{p})(u(\mathbf{p})) = F(\mathbf{p}) \\ \mathbf{Y}^{obs} = \mathbb{L}(u(\mathbf{p})) + \epsilon \end{cases} \quad (2.45)$$

where $\mathbf{Y}^{obs} \in \mathbb{R}^M$ represents the M experimental data, $\mathbb{L}(u(\mathbf{p}))$ represents the functionals $\ell_m(u(\mathbf{p}))$, $1 \leq m \leq M$ as in (3), and ϵ represents any eventual error in the measurements, assumed to a zero-mean Gaussian variable.

The goal of data assimilation methods is to improve the approximation of a physical state using the associated mathematical and available data on the system. While this seems simple enough, the challenge lies in formulating a scheme to interpret and employ data from (often sparse or noisy) measurements in some optimal way to contribute to the knowledge of the state in the numerical model. We must consider that there will be not only the anticipated error in numerical simulations from varying parameters, but also unanticipated error due to the shortcomings of the mathematical model itself and its imperfect representation of reality.

Many data assimilation methods involve the minimization of a cost function, such as least-squares type, designed to compute the mismatch between the model approximation and the observations. Inverse methods seek the optimal parameter value \mathbf{p}^{opt} or state source for the parameterized model, approximating the true state by the PDE solution $u(\mathbf{p}^{opt})$. On the other hand, many data assimilation methods use the measurements to correct the model approximation, rather than the parameter.

2.2.1 Linear Estimation Theory

Estimation theory, a branch of statistics, provides a basis for data assimilation techniques. Here we briefly discuss linear least squares estimation, as well as two probabilistic methods [160].

Linear least squares estimation is based on the minimization of a cost functional of the type

$$J(u) = \frac{1}{2} \|\mathbf{Y}^{obs} - \mathbb{L}(u(\mathbf{p}))\|^2 \quad (2.46)$$

This minimization is generally treated by a gradient method.

The least squares estimation can be generalized by considering a weighting of the norm described by the observation covariance matrix.

Another linear estimation technique is the Bayesian approach, in which the physical state u is treated as a random variable with probability distribution $P(u)$, which serves as the prior distribution (to be updated with the data) and is based on the physical model. The observations vector \mathbf{Y}^{obs} is also treated as a random variable. Given the data set \mathbf{Y}^{obs} , The Bayesian estimator \hat{u} is built by minimizing the cost functional

$$J_{Bay}(\hat{u}) = \mathbb{E}(\|\hat{u} - u\|^2 | \mathbf{Y}^{obs}), \quad (2.47)$$

which depends on the conditional probability $P(u | \mathbf{Y}^{obs})$ and is approximated by a gradient method.

A third linear estimation theory approach, the Best Linear Unbiased Estimator (BLUE), relies on knowledge of the error covariance matrices, without knowledge of the probability densities $P(u)$ and $P(u | \mathbf{Y}^{obs})$. This method also relies on the minimization of a cost function to find the updated *analysis* state u^a ,

$$J_{BLUE}(u^a) = \mathbb{E}(\|u^a - u^{true}\|^2), \quad (2.48)$$

depending on the error covariance matrices of the data and with respect to the true state u^{true} [160].

These estimation theory methods can be relatively simple to implement, but do not account for physical state dynamics. The probabilistic methods also require knowledge of either the probability distribution of the state u or of the error covariance matrices with respect to the true state, which may require large quantities of historical data.

We next move on to Sequential and variational methods, which rely on the mathematical model \mathcal{P} .

2.2.2 Sequential Methods

Sequential methods, based on the coupling of the results of the BLUE method and the dynamical model, rely on the assimilation of observations as they arrive to find the best estimate of the physical state between the observations and prior information [160]. Examples include Kalman Filter (KF) [96] and Optimal Interpolation.

Kalman filtering is a recursive computational solution for real-time tracking of a state vector with a noisy evolution equation and measurements.

Given a linear dynamical model and a set of observations \mathbf{Y}^{obs} , the KF seeks a so-called *analysis* state, $u^a(\cdot, \mathbf{p})$ which corrects the prior state, $u^{bk}(\cdot, \mathbf{p})$ solution to the dynamical model. If we consider a transient state, the true state at instant t_{k+1} is assumed to be representable as

$$u^{true}(t_{k+1}, \mathbf{p}) = \mathbf{A}_{k,k+1}u^{true}(t_k, \mathbf{p}) + e_k, \quad (2.49)$$

where e_k represents the model error and $\mathbf{A}_{k,k+1}$ represents the model operator from timestep k to instant $k + 1$. The KF hypothesizes that model error and observation noise ϵ are uncorrelated. The update of the prior state to find the analysis state at time step t_k is done using an operator \mathbf{K}_k called the Kalman gain filter matrix. \mathbf{K}_k is built from the observation operator \mathbf{Y}^{obs} , the covariance matrix of the expected value of bias in the model approximation, $\mathbb{E}(\|u^{bk} - u^{true}\|^2)$, and the covariance matrix associated to the observation noise. As each observational measurement arrives, the model approximation $u^{bk}(t_k, \mathbf{p})$ is corrected to give the analysis state at time step t_k

$$u^a(t_k, \mathbf{p}) = u^{bk}(t_k, \mathbf{p}) + \mathbf{K}_k(\mathbf{Y}^{obs} - \mathbb{L}(u^{bk}(t_k, \mathbf{p}))) \quad (2.50)$$

The prior analysis state can then be used to provide input to the next model approximation.

The Extended Kalman Filter (EKF) extends this procedure to handle non-linear dynamics and observation operators. In this case the covariance matrix of the model forecast is computed not from the expected bias in the model approximation, but from a tangent linear operator of the model and the adjoint dynamical model [160].

The KF and EKF can provide estimations of physical states and associated uncertainties while allowing for time dependence, however it does not perform well for highly non-linear systems [202], and the computation of the covariance and Kalman gain filter matrices requires computational and storage resources dependent on the size of the state space vector, making it less optimal for large systems.

The Ensemble Kalman Filter (EnKF) is an alternative to the EKF using Monte Carlo methods [160]. Given a prior analysis state $u^a(t_{k-1}, \mathbf{p})$ from a previous approximation at time step t_{k-1} , this is used as an initial condition input. A randomization of the dynamical model, obtained by perturbing the parameters or initial conditions around $u^a(t_{k-1}, \mathbf{p})$, is used to compute a set of state approximations $\{u^{bk}(t_k, \mathbf{p}_1), \dots, u^{bk}(t_k, \mathbf{p}_N)\}$.

The ensemble mean and covariance matrix are computed from this set of state approximations, and an empirical expression is used to build approximations of the gain matrix \mathbf{K}_k and covariance matrices required by the EKF. The Kalman gain matrix is approximated from an estimated ensemble covariance matrix and the observation operator \mathbb{L} , and is used to build the analysis state $u^a(t_k, \mathbf{p})$ from associated observations $\mathbf{Y}^{obs}(u^{true})$ and model approximations $u^{bk}(t_k, \mathbf{p}_i)$.

2.2.3 Inverse Methods

Inverse methods are developed considering the often inevitable error introduced in the parameters and inputs of the model. The goal is to identify the optimal parameter \mathbf{p}^{opt} to minimize the mismatch between model approximation and available data.

Inverse methods can be considered a specific case of variational data assimilation, but we separate the two cases to simplify the discussion here, and to insist on the different viewpoints of parameter optimization and state optimization.

2.2.3.1 Adjoint Method

An example of a typical method to treat the reconstruction of a physical state from a model and measurement data, the adjoint method poses a least squares problem on the error between model solution and data, often with Tikhonov regularization. The problem is solved via iterative resolution of the adjoint problem and direct problem [134, 193].

We consider that we have a parameterized PDE model \mathcal{P} over a calculation domain Ω and parameter domain \mathcal{D} , as in equation (1), with the strong form as in (2) with, as an example, non-homogeneous Dirichlet and homogeneous Neumann boundary conditions:

$$\mathcal{L}(\mathbf{p})(u(\mathbf{p})) = F(\mathbf{p}) \quad \text{in } \Omega \quad (2.51)$$

$$u = u_d \quad \text{on } \Gamma_D \quad (2.52)$$

$$\nabla u \cdot \vec{n} = u_n \quad \text{on } \Gamma_N \quad (2.53)$$

Assume a variational form as in (2.3): find $u \in \mathcal{X}$ such that for any $v \in \mathcal{X}_{test}$ appropriate test space, we have, for parameter $\mathbf{p} \in \mathcal{D}$,

$$a(u, v; \mathbf{p}) = b(v; \mathbf{p}) \quad (2.54)$$

This is the direct problem. Assume we are given M sensors represented by functionals $\sigma_k(w)$

$$\sigma_k(w) = \varphi_k w, \quad 1 \leq k \leq M$$

where φ_k are chosen such that the linear form $\int_{\Omega} \sigma_k(w)$ is continuous in L^2 for all $w \in \mathcal{X}$. We denote by $e_k(u(\mathbf{p}))$ the difference between the solution $u(\mathbf{p})$ of the direct model and the measurement u_{mes}^k given by the k^{th} sensor:

$$e_k(u(\mathbf{p})) = \int_{\Omega} \sigma_k(u(\mathbf{p})) d\Omega - u_{mes}^k. \quad (2.55)$$

The inverse problem consists in finding the optimal set of parameters \mathbf{p}^{opt} by minimizing the cost functional:

$$J(\mathbf{p}) = \frac{1}{2} \sum_{k=1}^M \|e_k(u(\mathbf{p}))\|^2 \quad (2.56)$$

where e_k is defined by equation (2.55). This problem is equivalent to the minimization of the functional

$$I(u) = \frac{1}{2} \sum_{k=1}^M \|e_k(u)\|^2, \quad (2.57)$$

under the constraint that u is a solution to the direct problem of form (2.54).

We then define the Lagrangian \mathcal{L} associated to the cost functional (2.56) and the direct problem (2.54):

$$\mathcal{L}(p, u, \phi, \psi) = I(u) - a(u, \phi; \mathbf{p}) - b(\phi; \mathbf{p}) \quad (2.58)$$

$$- \int_{\Gamma_D} (u - u_d)\psi, \quad (2.59)$$

where ϕ and ψ are the Lagrange multipliers associated to the constraints from the direct problem (2.51):

- $\phi \in \mathcal{X}$: multiplier associated to the constraint “ u is a solution of (2.54)”
- $\psi \in \mathbb{R}$: multiplier associated to, e.g., the constraint of a Dirichlet boundary condition on (2.51).

If we differentiate the Lagrangian (2.58) along a test function $w \in \mathcal{X}$ in the solution space, and with respect to the direct solution u , we can deduce a variational inverse equation from depending on parameters $u(\mathbf{p})$ and $e_k(u(\mathbf{p}))$ from

$$\left\langle \frac{\partial \mathcal{L}}{\partial u}(\mathbf{p}, u, \phi, \psi), w \right\rangle = \sum_{k=1}^M e_k(u) \int_{\Omega} \sigma_k(w) d\Omega - a(w, \phi; \mathbf{p}) - \int_{\Gamma_D} w\psi \quad (2.60)$$

Setting (2.60) equal to zero, we can derive the adjoint problem of the form

$$a^{adj}(\phi, w; \mathbf{p}) = b^{adj}(w; \mathbf{p}), \quad (2.61)$$

with

$$a^{adj}(\phi, w; \mathbf{p}) = a(w, \phi; \mathbf{p}) + \int_{\Gamma_D} w\psi$$

and

$$b^{adj}(w) = \sum_{k=1}^M e_k(u) \int_{\Omega} \sigma_k(w) d\Omega.$$

Suppose that $\mathbf{p} = (p_1, \dots, p_{N_p})$ where N_p is the number of parameters of our model. Then,

$$\frac{\partial J(\mathbf{p})}{\partial p_i} \lambda_i = \frac{\partial \mathcal{L}}{\partial p_i}(\mathbf{p}, c(\mathbf{p}), \phi(\mathbf{p})) \lambda_i \quad (2.62)$$

where $\lambda_i \in \mathbb{R}$ and $1 \leq i \leq N_p$.

For a stable implementation, it is necessary to add a regularization term depending of the parameter to the cost function $J(\mathbf{p})$. We denote by $T(\mathbf{p})$ the regularization term

$$T(\mathbf{p}) = \frac{\xi}{2} \|\mathbf{p} - \mathbf{p}^0\|^2,$$

where \mathbf{p}^0 is a parameter set close to the solution and ξ a positive constant. We thus introduce a new cost functional

$$J_T(\mathbf{p}) = J(\mathbf{p}) + T(\mathbf{p})$$

The derivative of the cost functional with respect to the parameters is now given as follows

$$\frac{\partial J_T(\mathbf{p})}{\partial p_i} \lambda_i = \frac{\partial J(\mathbf{p})}{\partial p_i} \lambda_i + \frac{\partial T(\mathbf{p})}{\partial p_i} \lambda_i$$

with

$$\frac{\partial T(\mathbf{p})}{\partial p_i} \lambda_i = \xi(p_i - p_i^0) \lambda_i, \quad \forall \lambda_i \in \mathbb{R}.$$

This method employs an iterative procedure in which at each step n , the direct solution $u(\mathbf{p}^n)$, the data gap $e_k(u(\mathbf{p}^n))$ for $1 \leq k \leq M$, the adjoint solution ϕ_n , and the derivatives with respect to each parameter $\frac{\partial J_T(\mathbf{p})}{\partial p_i}$ will be used to compute the next parameter set \mathbf{p}^{n+1} via a gradient-type method to minimize $J_T(\mathbf{p})$.

Given the costly nature of this method, techniques to reduce computational effort have been considered. In [36] the adjoint frame work is used for goal-oriented improvement of mechanical models over a quantity of interest by a partial model calibration in which the most influential parameters are updated first. RBMs have also been used in the adjoint inverse method, see [9,104,136]. For the implementation of CRBMs, a reduced basis is necessary for the solutions to the direct problem (2.54) to represent the solution space over the parameter set \mathcal{D} , for any varying state taken as a parameter (e.g. a wind or turbulence field), as well as a second reduced basis for the adjoint solutions (2.61) over the parameters $u(\mathbf{p})$ and $e_k(u(\mathbf{p}))$ associated to the direct solution and data. The steps of approximating the direct and adjoint solutions are thus replaced by two linear systems of small dimension, N^{dir} and N^{adj} respectively, solved for each new parameter value \mathbf{p}^n . The RB solutions $u^N(\mathbf{p})$ and ϕ^N can then be used in the gradient descent method by derivative of the Lagrangien.

2.2.4 Variational methods

Variational methods involve the minimization of a cost function, such as least-squares type, designed to compute the mismatch between the model approximation and the observations, based in techniques of optimal control theory, by imposing the dynamic model as a constraint. These methods work on a given assimilation time window, given a background trajectory $u^{bk}(t, \mathbf{p})$ from the model \mathcal{P} and observations \mathbf{Y}^{obs} .

2.2.4.1 Least-Squares based assimilation

Least-squares based variational data assimilation relies on a least-squares type cost function J dependent on the background and observation covariance matrices, the mismatch between the background initial condition (a guess) and the optimal initial condition, and the mismatch on the observational data over the time window. Unlike the linear version used in sequential methods (section 2.2.2), this cost function minimizes over an assimilation window $[t_0 : T]$, and unlike the cost function (2.56) commonly used in inverse methods (section 2.2.3), here we minimize over the initial condition u_0 , not the parameter \mathbf{p} .

The minimization problem is solved by a gradient-based algorithm, which can be done in several ways. For example, the gradient can be approximated by a finite differences scheme, using a sensitivity equation describing the differential of the cost function in a given direction, or using an adjoint formulation based on a concept similar to that in section 2.2.3.1, and described in more detail in [160].

2.2.4.2 4DVar and Variations

The 4D-Var method [58] operates on a time window, using the cost function to optimize results over the time period of the 3D atmosphere (hence 4D variables). However the minimization of the cost functions requires computing the adjoint of the tangent linear of the forecast model in addition to the observation operator, which can be a complex task. The advantages of the 4D-Var method include no loss of information in the time window and optimal treatment of non-linear operators.

The 4D-Var method also aims to minimize a cost function, generally with respect to the initial state u_0 or in the steady-state case (3D-Var), the state u , minimizing the difference between the model trajectory from the dynamical model \mathcal{P} and the observation data \mathbf{Y}^{obs} by controlling the initial state u_0 . The cost function can take the form

$$J(u_0, u^a, \mathbf{p}) = \frac{1}{2} \|u_0 - u_0^{bk}\|^2 + \frac{\tau}{2} \sum_{k=1}^K \|\mathbf{Y}^{obs} - \mathbb{L}(u_k^a)\|^2 \quad (2.63)$$

where u_0^{bk} represents the so-called background initial state, which can be from the best-knowledge model or a guess. (In the steady-state 3D case this would be u^{bk} the best-knowledge solution or a state from another model.) The trajectory solution u_k represents the model trajectory at instant t_k from the initial state u_0 . $\tau = \frac{T-t_0}{K}$ is the time step for K steps between time t_0 and T . The norm can be chosen in the dynamical state to be an L^2 or H^1 norm weighted by a covariance matrix of the dynamical trajectories $u(t, \mathbf{p})$ and initial states u_0 .

The minimization problem is under strong constraint by the dynamical model. The optimal initial state for the cost function J is found by an iterative optimization method. This can prove costly, considering the solution of the direct and adjoint problem at each iteration. Reduction methods have been successfully applied to

4D-Var, as in [97, 159] for example. This can be done with reduced basis methods, or using a reduced order model.

A weak constraint form of the 4D-Var method [187] can be used to treat an unknown initial condition and model error (e.g. a bias in the mathematical model or state estimation error due to parametric variation) [64, 97]. This approach relaxes the constraint that the solution satisfy exactly the model \mathcal{P} , and allows for deviation from the model depending on what is known about the model error (e.g. a simple deterministic form as in [97] or a stochastic form as in [64]). Model error can be treated by adding a *forcing* term in the minimization equation

$$J(u_0, u^a, e, \mathbf{p}) = \frac{1}{2} \|u_0 - u_0^{bk}\|^2 + \frac{\tau}{2} \sum_{k=1}^K \|e^k\|^2 + \frac{\tau}{2} \sum_{k=1}^K \|\mathbf{Y}_k^{obs} - \mathbb{L}(u_k^a)\|^2, \quad (2.64)$$

over K time steps for time-step length τ , where e^k represents the model error at the k^{th} time step. The state u^a is the equivalent of an analysis approximation to the model (variational problem (2.3)) with an added forcing term for model error represented by a bilinear form $c(e^k, v)$ in the constraint:

$$a(u^a, v; \mathbf{p}) + c(e^k, v) = b(v; \mathbf{p}) \quad (2.65)$$

We clarify that $u^a \in \mathcal{X}^K$, $u_0 \in L^2$, and $e \in (L^2)^K$. For example in (2.64), $c(e^k, v) = \langle e^k, v \rangle_{L^2(\Omega)}$.

The norms in equation (2.64) depend on the application, and can be dependent on a covariance matrix associated to the states and measurements [87].

In [97], a posteriori error bounds are proposed for both classical (strong) and weak 4D-Var RBM approximations, relying on the residual norms of the state u^a , the adjoint, the model error, and the control variable (the initial condition). The CRB formulation of problem (2.64), as seen in [97], involves an integrated RB space for both the state and the adjoint, and two separate spaces for the initial condition and for the model error. Computational times for the 4D-Var problem using a conjugate gradient iterative procedure were reduced by $\mathcal{O}(10)$ per resolution over a small test domain and 8-second time window, depending on the number of iterations necessary.

2.3 Model Order Reduction and Data Assimilation in the Air Quality Modeling context

In this section we wish to discuss MOR and data assimilation methods in the context of air quality modeling, and give examples of previous studies using these techniques for pertinent applications.

2.3.1 Data Assimilation for AQM

Data assimilation is a promising method of improving air quality modeling. It can be used to calibrate existing models to poorly known conditions and to correct state estimation error in imperfect models, both particularly pertinent to AQ studies.

The use of data assimilation and its impact on AQM results depends on the specific dynamics of the model, and data can be in varying forms such as in-situ, air borne, satellite, and/or observation data. In meteorological models, initial conditions tend to be very important. However, in CTMs, the initial conditions are less influential when compared to emissions and boundary conditions, particularly in the case of small-scale domains and long-lived pollutants. As discussed in chapter 1, error in model inputs (such as BCs and emissions) and model parameters (such as chemical reaction coefficients) will persist through an AQM simulation, generally unlike initial condition (IC) uncertainties [203]. Emissions uncertainty for common air pollutants can range from 20 – 60% [77].

Difficulties in parameter improvement Improving knowledge of model parameters has interest beyond the estimation of the air quality state at hand; for example emissions inventories and spatial representation can be improved. However the improvement of model parameters is no simple task; it can require specifying the uncertainty, difficult in and of itself, of parameters of very different natures. When applied to atmospheric chemistry, controlling for positivity of the resulting concentration and emission approximations is a particular issue. A common solution is to set negative concentrations or emissions to zero, however this should be treated with caution as it does not obey the physics of the mechanisms involved.

Another complication is that in practice, emissions fields often depend on many more variables than data observation points, and these observations of course cannot provide information over the entire domain. A possible solution is to define an adaptive grid for the emissions field, which is coarse in areas with no effect on observations, and refined near measurement stations. The goal is to optimize the assimilation of the available observations. Another possible solution is the optimization of monitoring networks (i.e. monitoring locations) for an optimal approximation. This is not always an option, and on the global scale the observation network is relatively dense, meaning the advantages of this method could be limited currently. [203]

Sequential methods For linear or linearizable models, direct linear sequential methods can be applied to fit BCs to observations, e.g. over Europe [162]. When few parameters are to be improved, stochastic filters may be more appropriate than 4D-Var; for example, in [15] a chemical conversion rate of sulfur oxides was estimated.

Statistical methods, such as the global data assimilation model in [111] and the land-use regression model [138], have been in use for many years. Data assimilation methods can be very useful for improving sophisticated CTMs, allowing for the use of real-time or quasi-real-time measurements. Several techniques have been developed to improve initial conditions and boundary conditions, emissions, and meteorology models for use in a CTM. (Multiple interesting studies are cited in [202]). A statistical interpolation method is used in [24] for O_3 measurements and

CHIMERE approximations. Two techniques are compared in [56] for regional PM_{10} in Europe: statistical interpolation based on residual kriging after a linear regression of the model, and ensemble Kalman filter.

Common issues with sequential methods for air quality modeling are inflation, localization, and model error. The sampling of error statistics only being an approximation can lead to underestimation of true error, which when compensated by inflation could lead to divergence of the assimilation method.

Model error, such as emissions and boundary conditions, is very significant, but not always identifiable directly. Unidentified error can be modeled through stochastic perturbation schemes, adding a stochastic error term to each member of the ensemble, where each perturbation is a linear combination of sources of errors. The finer these sources of model errors are diagnosed, the better the filter should perform.

Additionally, the sampling schemes can generate unphysical blobs of pollution in AQM results, which need to be removed. Localization schemes can be used to consider the error covariance matrix, or to use observation data only locally [203].

Variational and Inverse Methods Adjoint methods have been used in the case of air quality modeling in [54, 156], both employing RBMs. In [169] a sensitivity analysis of the adjoint problem is considered for data assimilation on an air quality model.

In [44] a modified inversion technique using Bayesian inference and Monte Carlo (see section 2.2.2) was used to identify source position and intensity in an urban setting.

4D-Var (see 2.2.4.2) has been demonstrated successful for NO_X by [157], and for precursors of O_3 , SO_2 , SO_4^{2-} , NH_3 , $VOCs$, etc. by [63]. The 4D-Var method has also been successfully implemented in meteorology [61]. However if the retrieval of emissions parameters is not considered, some sequential methods can perform better than 4D-Var, which may not account for model error (unless a weak constraint 4D-Var version is considered). 4D-Var lends itself to the optimization of parameters and initial conditions: a bonus if considering traditional data assimilation techniques for the optimization of parameters via inverse modeling [203].

Difficulties in the 4D-Var method for AQM include background inter-species error covariance at the initial time, emissions over the whole time window, computation of the adjoint, and nonlinearities in the chemistry.

We recall here the convection-diffusion problem considered in [97], where 4D-Var is applied with RBMs to reduce computational times. A weak 4D-Var formulation, described above in section 2.2.4, is used to account for an unknown initial condition as well as model error. The application considered is over a small 2×2 domain with low Peclet number and 5 measurement points for concentration value with Gaussian-variable noise, over an 8-second time window. We mention this small-scale application here for its potential in extension to larger-scale air quality modeling endeavors, however this current application does not quite fit in the AQM context.

2.3.2 Model Order Reduction for AQM

Data assimilation methods often require the resolution of the problem \mathcal{P} for many parameter values, which can prove costly, particularly in the case of complex models on large domains, common in air quality modeling. MOR can offer highly advantageous reduction of computational effort in this context.

In [112] for example, a sort of surrogate model is developed for reduced chemical models in tropospheric chemistry.

Projection-based MOR methods are notoriously difficult in cases dominated by transport, if the diffusion term is negligible with respect to the advection term. We note that unstable atmospheric conditions induce more diffusion, which renders the MOR problem less complex. RBMs can be more stably applied to advection-diffusion problems in the case of unstable atmosphere [156]

Below we mention some particularly pertinent examples of MOR applied to applications in AQM.

2.3.2.1 Stabilized Reduced Order Transport Modeling

In [146] the Streamline Upwind Petrov-Galerkin (SUPG) stabilization method (described in detail in section 4.2.2.2) was used for a parameterized advection-diffusion PDE model with high Peclet number and RBMs. The study considered two methods of implementing RBMs: *Offline-Online* SUPG, and *Offline-only* SUPG. In both techniques, SUPG stabilization was used in the computation of snapshot solutions $u^{bk}(\mathbf{p}_1), \dots, u^{bk}(\mathbf{p}_{N_t})$ in the offline stage. The difference was in the construction of the reduced-order models by Galerkin projection: in the Offline-Online technique, the SUPG full model was projected onto the reduced approximation space, whereas in the Offline-only technique only the usual advection-diffusion model was projected. In applications with both physical and geometrical parameters, the offline-only method was found to have instabilities, while the offline-online stabilization method performed well.

In [73] a dynamical SUPG stabilized advection-diffusion model was also considered, using POD-based MOR. While POD-based reduced models can be efficient and accurate, they can also be numerically unstable and have non-physical peaks, such as when applied to Navier-Stokes problems. If unstable snapshot solutions to the advection-diffusion model are used in the POD basis, oscillatory effects increase. However, if the snapshots are stabilized by the SUPG (i.e. there are no major perturbations), the POD can be stable. A centered-trajectory implementation in which the POD modes were computed from fluctuations of the snapshots $u^{bk}(\mathbf{p}_i) - \bar{u}$ for some aggregated solution \bar{u} containing Dirichlet boundary condition information, and the fluctuations can be treated with homogeneous Dirichlet boundaries. The reduced model is then built using the SUPG-stabilized full model to approximate the fluctuations by $u_{ROM}(t, x) \simeq u^{bk}(\mathbf{p}_i) - \bar{u}$, and the reduced approximation is $u_N = u_{ROM}(t, x) + \bar{u}$. The SUPG-stabilized reduced model was here too found to be more stable suppressing instabilities.

In [53] RBMs are studied for application to an advection-reaction model stabilized by the Streamline Diffusion Finite Element (SDFE) method. A primal-dual approach is considered, in which the primal problem is the SDFE-stabilized parameter-dependent advection-reaction problem with weak problem of the form (2.3), and the goal is to calculate an output quantity $s(\mathbf{p}) = \ell^o(u^{bk}(\mathbf{p}); \mathbf{p})$, where ℓ^o is defined by (2.16). The dual problem is then defined by (2.23).

Two reduced basis are computed, one for the primal problem (2.3) and one for the dual problem (2.23), during an offline stage, along with the operators for the reduced models. During the online stage, for each new parameter \mathbf{p} , the primal and dual reduced models are solved, the dual solution $\psi(\mathbf{p})$ is used to correct the RBM-approximated output $s_N(\mathbf{p})$ defined in (2.17), as defined by (2.29). This technique allows to improve accuracy of the output computation without increasing computational time with respect to the primal-only approach, which would require a higher-dimensional basis for the same accuracy. In [53] the same author studies these problems for applications in optimal control.

2.3.2.2 Optimal Control for AQM

In [156] RBMs are used in an optimal control problem in air quality modeling. The problem is to find optimal emissions rates from factory stacks to minimize pollution over a nearby area of interest, the control parameter being the emissions. A transport-dominated advection-diffusion problem is used, and solved for the optimal parameters by inverse method with a stabilized Lagrangien (as opposed to stabilizing the primal and adjoint problems) solved by gradient method using an adjoint problem, employing reduced basis approximation spaces for the direct and adjoint problems.

Part II

Reduced Order Data Assimilation Methods and Application in Air Quality Modeling

Chapter 3

Reduced Order Data Assimilation: PBDW and GEIM

Résumé :

Dans ce chapitre, nous introduisons deux méthodes d'assimilation de données pour les EDP paramétrées, la PBDW et la GEIM, qui sont non intrusives et d'ordre réduit. Soient un modèle \mathcal{P}^{bk} dépendant d'un jeu de paramètres \mathbf{p} et M données d'observations (y_m^{obs}) , $1 \leq m \leq M$.

La méthode PBDW est une méthode de minimisation de type moindres carrés qui s'appuie sur deux espaces d'approximation. Le premier est l'espace *background* de type "bases réduites", nommé \mathcal{Z}_N et de dimension N , représentant le modèle \mathcal{P}^{bk} . Le second est l'espace *update* nommé \mathcal{U}_M de dimension M , représentant l'information collectée par les M capteurs. Nous voulons approcher $u^{true}(\mathbf{p})$, l'état physique du système, par l'approximation PBDW

$$u_{M,N}(\mathbf{p}) = u_N^{bk}(\mathbf{p}) + \eta_M$$

où $\eta_M \in \mathcal{U}_M$ est un terme de correction *update* associé aux données d'observation, et $u_N^{bk}(\mathbf{p}) \in \mathcal{Z}_N$ est une approximation de RB de la solution à \mathcal{P}^{bk} . L'approximation PBDW est obtenue par la résolution d'un problème de minimisation sous contrainte. La fonctionnelle à minimiser est la contribution *update* $\eta_M \in \mathcal{U}_M$, et les contraintes sont $y_m^{obs} = \ell_m(u^{true}(\mathbf{p}))$, $1 \leq m \leq M$, où ℓ_m représente le $m^{\text{ième}}$ capteur. Le problème de minimisation peut s'écrire sous forme d'un système linéaire de taille $M + N \times M + N$. Dans ce chapitre on introduit la constante de stabilité $\beta_{M,N}$ et une estimation a priori de l'erreur d'approximation PBDW.

La GEIM est une méthode d'interpolation qui utilise des solutions du problème \mathcal{P}^{bk} et les M données. Soit $\mathcal{I}_M(u)$ l'opérateur d'interpolation défini tel que :

$$\mathcal{I}_M(u) = \sum_{j=1}^M \alpha_j \tilde{q}_j \quad \text{et} \quad \ell_m(\mathcal{I}_M(u)) = \ell_m(u) \quad \forall 1 \leq m \leq M,$$

où \tilde{q}_j sont les fonctions d'interpolation construites à partir de solutions de \mathcal{P}^{bk} .

In most modeling and data assimilation endeavors, the overall goal is to find the best possible approximation of the physical system being studied while expending minimal resources. In practice this can translate to using the best model possible and available data without requiring excessive computational investment required to solve the problem. These goals are clear in the above-discussed data assimilation methods (section 2.2), and the goal of reducing computational effort is central to the MOR methods discussed in section 2.1. In this chapter we will expose two non-intrusive reduced order methods of data assimilation for parameterized PDEs: the generalized EIM (GEIM), based on the empirical interpolation in section 2.1.2.1, first introduced in [114, 115], and the more recent Parameterized-Background Data-Weak (PBDW) method developed in the reduced basis framework, first introduced in [117, 118]. These methods, born of the need common to other data assimilation methods to find the best approximation of a true physical state given a mathematical model and some observation data, are non-intrusive and non-iterative, providing real-time state estimation. The methods aim to optimally employ model order reduction methods combined with data assimilation to best approximate a physical state, taking into consideration not only parametric variation, but also model error in an imperfect mathematical model.

3.1 PBDW

3.1.1 Introduction

Given a parameterized model \mathcal{P}^{bk} for a physical system, which we will refer to as the "best-knowledge" (bk) model, and a number of measurements of the quantity we wish to approximate, this PBDW formulation for variational data assimilation aims to achieve the most precise real-time approximation of the physical state.

Some advantages of this formulation are:

- Correction of unmodeled physics, or unanticipated and non-parametric uncertainty, through an *update* to the best-knowledge approximation constructed from M observations.
- Simple non-intrusive and non-iterative implementation.
- Online computational efficiency for real-time state estimation.
- A low-dimensional Reduced Basis space from the best-knowledge model, designed to handle anticipated parametric uncertainty.
- The approximation of the true physical state without identifying the model parameters.
- In the case of decoupled pollutant transport modeling, independence of the online stage from fluid calculations.

- The capability to handle data abundance without up-scaling the model complexity.

As in RBMs, the efficiency of the PBDW formulation depends on an online-offline breakdown of computations. The PDE model \mathcal{P}^{bk} is used to build a RB *background* space of low dimension representing solutions to the known problem, designed to handle parametric uncertainty. Information on physical location and form of the sensors used in measurements are used to build an *update* space of low dimension representing the information gathered by the sensors. The construction of these two approximation spaces require expensive computations, but is completed offline and only once for a given system, parameter range, and set of sensors. A linear system representing the PBDW formulation is also constructed offline, as will be described in section 3.1.2. The online stage requires only the input of PBDW data and resolution of the linear system, allowing for highly efficient state estimation. In the three-dimensional case study considered in this work, computation time by \mathbb{P}_1 finite elements took over 26 minutes for a single concentration field, while the PBDW approximation required under 40 seconds for a full reconstruction of the field.

The weak formulation of the PBDW method is based on least-squares approximation, as is the case of the adjoint inverse method and many variational data assimilation methods. A brief discussion of similarities with 3D-VAR (first introduced in [111] and expanded to MOR applications in [190], gappy proper orthogonal decomposition [69], empirical interpolation, and the use of a Riesz representation in correcting unmodeled physics [21], can be found in [119].

A recent PhD thesis [182] gives detailed analysis of PBDW error and stability, as well as discussion of treatment in the case of noisy data. The case of noisy data, which was first considered in the PBDW formulation in [117], is treated with a probabilistic distribution, for example independent normal distributions, with an added regularization term over the observations (similarly to the 3D-var formulation), dependent on the variance of the distribution, in the minimization statement. In this study we will not consider the case of noisy data, considering that a proposed extension for this case has been well documented by Taddei [182]. In addition, we could consider that pollution sensors are not just noisy: relative errors may be large, but are small on a log scale, which is more pertinent to air quality modeling. We consider relative errors plotted on log axes to provide insight into the methods from a mathematical point of view, as our approximation errors are small here.

3.1.2 PBDW Formulation

Let us denote $\mathbf{p} \in \mathcal{D}$, where \mathcal{D} is the set of all parameters of interest, the parameter configuration of the physical system, encoding information such as operation conditions (e.g. emissions or frequency), environmental factors (e.g. temperature), and physical components.

Let $\Omega \subset \mathbb{R}^d$ be a bounded domain. We will consider a solution space \mathcal{X} , a Hilbert space, such that $H_0^1(\Omega) \subset \mathcal{X} \subset H^1(\Omega)$, and associated inner product $\langle \cdot, \cdot \rangle_{\mathcal{X}}$. We will

denote \mathcal{X}' its dual space.

We assume we have some knowledge of the system encoded in the parameterized PDE model \mathcal{P}^{bk} , resulting in the best-knowledge state $u^{bk}(\mathbf{p}) \in \mathcal{X}$. The goal of this formulation is to estimate the true deterministic state $u^{true}(\mathbf{p}) \in \mathcal{X}$ (or desired output quantity $\ell^{out}(u^{true}(\mathbf{p})) \in \mathbb{R}$ for some linear functional $\ell^{out} \in \mathcal{X}'$) using the model \mathcal{P}^{bk} and M observations associated to the parameter configuration \mathbf{p} .

In order to combine the best knowledge of the system modeled by \mathcal{P}^{bk} and the experimental observations of the physical state, we will consider a PBDW solution of two parts: background and update. The goal of the following paragraphs is to formulate the PBDW method in which we will approximate the true physical state $u^{true}(\mathbf{p})$ by

$$u^{bk}(\mathbf{p}) + \eta \tag{3.1}$$

where $\eta \in \mathcal{X}$ is an *update* correction term associated to the experimental observations, which will be defined more precisely in section 3.1.2.2.

3.1.2.1 Reduced basis background

We will exploit the above-mentioned RBMs (section 2.1.2) for the construction of a low-dimensional approximation space representing the manifold of solutions to the parameterized PDE model \mathcal{P}^{bk} over the parameter space $\mathcal{D}^{bk} \subset \mathcal{D}$. This allows for significant reduction of computation costs in the incorporation of background information on the physical system.

As discussed in section 2.1.2, a relatively small Kolmogorov dimension (defined in section 2.1.2) is necessary to measure to what extent the solution manifold $\mathcal{M}^{bk} = \{u^{bk}(\mathbf{p}) \in \mathcal{X} \mid \mathbf{p} \in \mathcal{D}^{bk}\}$, where $u^{bk}(\mathbf{p})$ are solutions to the mathematical problem \mathcal{P}^{bk} , can be approximated by an n -dimensional subset of \mathcal{X} , formed by a set of well-chosen solutions to \mathcal{P}^{bk} , or to what extent $u^{bk}(\mathbf{p})$ can be approximated by

$$u_N^{bk}(\mathbf{p}) := \sum_{i=1}^N \beta_i(\mathbf{p}) u^{bk}(\mathbf{p}_i),$$

as in equation (2.13).

This RB approximation space will be henceforth referred to as the Background space \mathcal{Z}_N , representing solutions to the model \mathcal{P}^{bk} in the PBDW method. We will construct our Background spaces as a sequence of nested RB spaces

$$\mathcal{Z}_1 \subset \dots \subset \mathcal{Z}_N \subset \dots \subset \mathcal{X}.$$

We perform a Gram-Schmidt orthonormalization, and introduce new orthonormal basis functions $\{\zeta_i\}_{i=1}^N$ and denote our background RB space as

$$\mathcal{Z}_N := span\{\zeta_i\}_{i=1}^N \subset \mathcal{X} \tag{3.2}$$

To minimize the PBDW approximation error from discretization error, we need to construct a suitably precise RB space \mathcal{Z}_N such that, for a tolerance ϵ_Z ,

$$\inf_{w \in \mathcal{Z}_N} \|u^{true}(\mathbf{p}) - w\|_{\mathcal{X}} \leq \epsilon_Z \quad \forall \mathbf{p} \in \mathcal{D} \text{ and } N \geq N_{min}. \quad (3.3)$$

The construction of the Background RB space takes place *offline*, as it is computationally expensive, allowing for an efficient *online* phase. The parameters generating RB spaces can be chosen by multiple methods, and we chose to focus on Greedy algorithms (see algorithm 3 in appendix C).

This RB space representing the solution manifold to the model described by \mathcal{P}^{bk} can now be used in various RBMs, such as the certified RBM for example, allowing to rapidly represent the solution to the model \mathcal{P}^{bk} for a given parameter. In order to use CRBMs in the context of data assimilation, we need a mechanism to treat observational knowledge of the system, such as the implementation of CRBMs in the framework of an inverse problem. However we will note that in certified RBMs (CRBMs), the Galerkin method on the RB space requires the modification of the calculation code, an intrusive procedure which can be unfeasible or undesirable, and non-affine parameter-dependence in the PDE model may require online interpolation, rendering the process less computationally efficient. Here we wish to take advantage of the simple and non-intrusive character of the PBDW method as an alternative to this integration of MOR into a classical technique.

3.1.2.2 Data-informed update

Taking the background piece of the PBDW approximation from the RB space \mathcal{Z}_N of the model \mathcal{P}^{bk} , we will consider the experimental observations to contribute in the update piece. If we consider that we have M sensors, which we will mathematically represent as follows (for example) for $1 \leq m \leq M$ and appropriate constant c :

$$\varphi_m = \frac{1}{c} \exp\left(\frac{-(x - x_m)^2}{2r^2}\right) \text{ such that } \int_{\Omega} \varphi_m(x) d\Omega = 1, \quad (3.4)$$

where $x_m \in \mathbb{R}^d$ is the center of the m^{th} sensor of radius r . The underlying idea of such a representation is that a sensor, especially a gas sensor (as well as particulate sensors), is a complex system with spatial extension. Such a sensor does not sense pointwise, but rather performs some averaging around the sensor location. In practice, some advanced "lab-on-a-chip" devices also introduce a time-delay or even a time-averaging of the quantity to be observed. But we shall not discuss this issue any further and consider a simple operational "sensor model". From the mathematical point of view, (3.5) makes the observation continuous over all Sobolev spaces where the concentration is usually approximated.

To evaluate the information these sensors can gather from a physical state $v \in \mathcal{X}$, we define the following linear functionals $\ell_m \in \mathcal{X}'$

$$\ell_m(v) = \int_{\Omega} \varphi_m(x) v(x) d\Omega \quad 1 \leq m \leq M \quad (3.5)$$

Given a parameter configuration \mathbf{p} , we assume our M observations $y_m^{obs}(\mathbf{p})$, $1 \leq m \leq M$, are of the form

$$y_m^{obs}(\mathbf{p}) = \ell_m(u^{true}(\mathbf{p})). \quad (3.6)$$

We need to use these representations to construct a second approximation space $\mathcal{U}_M \subset \mathcal{X}$ in which we will find the update η from equation (3.1). If we consider that this approximation space will represent the information which the sensors can provide, we want the basis functions of \mathcal{U}_M , denoted q_m , $1 \leq m \leq M$, to represent the functionals ℓ_m . Let us thus define the Riesz operator $\mathcal{R}_{\mathcal{X}} : \mathcal{X}' \rightarrow \mathcal{X}$ such that

$$\langle v, \mathcal{R}_{\mathcal{X}} \ell \rangle_{\mathcal{X}} = \ell(v), \quad \forall v \in \mathcal{X}. \quad (3.7)$$

We then introduce the so-called update basis functions $q_m = \mathcal{R}_{\mathcal{X}} \ell_m \in \mathcal{X}$ such that

$$\langle v, q_m \rangle_{\mathcal{X}} = \ell_m(v), \quad \forall v \in \mathcal{X}, \quad (3.8)$$

and for any physical state u^{true} of the configuration

$$\langle u^{true}, q_m \rangle_{\mathcal{X}} = \ell_m(u^{true}). \quad (3.9)$$

Let us define the Update Space by $\mathcal{U}_{M_{max}} = \text{span}\{q_m\}_{m=1}^{M_{max}}$, where M_{max} is the maximum number of sensors available. The construction of this space takes place *offline*, as it can be relatively computationally expensive, although often less so than the construction of the background space.

3.1.2.3 PBDW problem statement

The PBDW aims at approximating the true physical state $u^{true}(\mathbf{p})$ for some configuration \mathbf{p} by

$$u_{N,M} = z_N + \eta_M. \quad (3.10)$$

where the first right-hand-side term z_N is in \mathcal{Z}^N and corresponds RB approximation of the best-knowledge solution $u^{bk}(\mathbf{p})$, and the second right hand side term η_M is in \mathcal{U}^M and is a correction term associated with the M observations. We pose the PBDW approximation as the solution to the following minimization problem. Find $(u_{N,M} \in \mathcal{X}, z_N \in \mathcal{Z}_N, \eta_M \in \mathcal{U}_M)$ such that

$$(u_{N,M}, z_N, \eta_M) = \underset{\substack{\tilde{u}_{N,M} \in \mathcal{X} \\ \tilde{z}_N \in \mathcal{Z}_N \\ \tilde{\eta}_M \in \mathcal{U}_M}}{\text{arginf}} \left\{ \|\tilde{\eta}_M\|_{\mathcal{X}}^2 \left| \begin{array}{l} \langle \tilde{u}_{N,M} - \tilde{z}_N, v \rangle_{\mathcal{X}} = \langle \tilde{\eta}_M, v \rangle_{\mathcal{X}}, \forall v \in \mathcal{X} \\ \langle \tilde{u}_{N,M}, \phi \rangle_{\mathcal{X}} = \langle u^{true}, \phi \rangle_{\mathcal{X}}, \forall \phi \in \mathcal{U}^M \end{array} \right. \right\}. \quad (3.11)$$

The minimization over the update term η_M translates to requiring the PBDW approximation to remain close to the manifold \mathcal{M}^{bk} represented by the RB approximation space \mathcal{Z}_N . This requirement ensures that the approximation maintains a physical sense with respect to the physics of the model \mathcal{P}^{bk} . The constraints on the minimization impose the two-part background-update PBDW solution, and the measured values at sensor locations. This minimization problem can be expressed

by a Lagrangian and the derivation of Euler-Lagrange equations, as shown in [119]. Simplifying the Euler-Lagrange equations, the PBDW estimation statement can be written, for a given physical configuration $\mathbf{p} \in \mathcal{D}$, as the following mixed problem [117, 119].

Find $(\eta_M(\mathbf{p}) \in \mathcal{U}_M, z_N(\mathbf{p}) \in \mathcal{Z}_N)$ such that:

$$\langle \eta_M, q \rangle_{\mathcal{X}} + \langle z_N, q \rangle_{\mathcal{X}} = \langle u^{true}(\mathbf{p}), q \rangle_{\mathcal{X}} \quad \forall q \in \mathcal{U}_M, \quad (3.12)$$

$$\langle \eta_M, p \rangle_{\mathcal{X}} = 0 \quad \forall p \in \mathcal{Z}_N. \quad (3.13)$$

We recall here that given the definition of the update basis functions $q_m \in \mathcal{X}$ in equation (3.8), the right-hand-side of this formulation is assumed to be $\langle u^{true}(\mathbf{p}), q_m \rangle_{\mathcal{X}} = y_m^{obs}(\mathbf{p})$, with $y_m^{obs}(\mathbf{p}) = \ell_m(u^{true}(\mathbf{p}))_{\mathcal{X}}$, $1 \leq m \leq M$.

The corresponding algebraic formulation to problem (3.12) is : find $(\vec{\eta}_M \in \mathbb{R}^M, \vec{z}_N \in \mathbb{R}^N)$ such that

$$\begin{pmatrix} \mathbf{A} & \mathbf{B} \\ \mathbf{B}^T & \mathbf{0} \end{pmatrix} \begin{pmatrix} \vec{\eta}_M \\ \vec{z}_N \end{pmatrix} = \begin{pmatrix} \vec{y}^{obs} \\ \mathbf{0} \end{pmatrix} \quad (3.14)$$

where

$$(\vec{y}^{obs})_m = y_m^{obs}, \quad \mathbf{A}_{m,m'} = \langle q_m, q_{m'} \rangle_{\mathcal{X}} \quad \text{and} \quad \mathbf{B}_{m,n} = \langle \zeta_n, q_m \rangle_{\mathcal{X}} \quad 1 \leq m, m' \leq M ; 1 \leq n \leq N$$

The PBDW approximation can then be rewritten as

$$u_{N,M} = \sum_{m=1}^M (\vec{\eta}_M)_m q_m + \sum_{n=1}^N (\vec{z}_N)_n \zeta_n.$$

The desired output functional can be evaluated without reconstructing the full solution:

$$\ell^{out}(u_{N,M}) = \sum_{m=1}^M (\vec{\eta}_M)_m \ell^{out}(q_m) + \sum_{n=1}^N (\vec{z}_N)_n \ell^{out}(\zeta_n).$$

This mixed problem is not directly a function of the original PDE, making the method non-intrusive. Once the background RB space has been constructed from particular solutions to the model \mathcal{P}^{bk} , the procedure can be independent of the \mathcal{P}^{bk} computational code provided the mesh information is available.

For a more stable numerical implementation, we can consider solving:

$$\mathbf{B}^T \mathbf{A}^{-1} \mathbf{B} \vec{z}_N = \mathbf{B}^T \mathbf{A}^{-1} \vec{y}^{obs} \quad (3.15)$$

$$\vec{\eta}_M = \mathbf{A}^{-1} (\vec{y}^{obs} - \mathbf{B} \vec{z}_N) \quad (3.16)$$

The construction of the background space \mathcal{Z}^N , update space \mathcal{U}^M , as well as the matrices A and B , takes place during the *offline* stage — as computation time of these procedures depends on the mesh with \mathcal{N}_h degrees of freedom — allowing for an efficient *online* phase. Thus, when observation data is collected, the linear system

can generally be solved online in $\mathcal{O}((N + M)^3)$ operations ($\mathcal{O}((N + M)^2)$ once the system is factorized).

RBM are particularly well-suited to problems in which the quantity of interest is not the full reconstruction of the solution, but the evaluation of a linear output functional over the solution, allowing for complete independence from the calculation mesh in the online stage. A quantity of interest could, for example, be the average value over a domain of interest. In this case, the output quantity over the basis functions of the two approximation spaces can be precalculated, allowing for evaluation of the output of the PBDW approximation in $\mathcal{O}(N + M)$ operations, without fully reconstructing the PBDW approximation from the basis functions $\{\zeta_n\}_{n=1}^N$ and $\{q_m\}_{m=1}^M$, a procedure in $\mathcal{O}(\mathcal{N}_h)$ operations. However depending on the visualization method, reconstruction of full solutions can be very efficient, making RBMs equally suitable for the general case.

3.1.3 PBDW error and stability considerations

The well-posedness of the problem depends on the construction of the Background and Update spaces. In fact we can define the inf-sup stability constant depending on the two approximation spaces.

$$\beta_{N,M} = \inf_{w \in \mathcal{Z}_N} \sup_{v \in \mathcal{U}_M} \frac{\langle w, v \rangle_{\mathcal{X}}}{\|w\|_{\mathcal{X}} \|v\|_{\mathcal{X}}}. \quad (3.17)$$

$\beta_{N,M}$ is a non-increasing function of N and a non-decreasing function of M , with $\beta_{N,M} = 0$ for $N > M$.

In [119] an *a priori* error estimation is derived for the formulation as a function of the stability constant and the best-fit of the approximation spaces.

$$\|u^{true} - u_{N,M}\|_{\mathcal{X}} \leq \left(1 + \frac{1}{\beta_{N,M}}\right) \inf_{q \in \mathcal{U}_M} \inf_{z \in \mathcal{Z}_N} \|u^{true} - z - q\|_{\mathcal{X}} \quad (3.18)$$

Given the strong dependence of the PBDW approximation error on the stability constant, we need to build the approximation spaces in a manner to maximize the stability of the formulation.

If we have the option of choosing the M best measurements, we want to:

- (a) Maximize the stability constant $\beta_{N,M}$ for each M with respect to the Background Space
- (b) Minimize the best-fit error in the secondary approximation provided by the update space:

$$\inf_{\eta \in \mathcal{U}_M \cap \mathcal{Z}_N^\perp} \|\Pi_{\mathcal{Z}_N^\perp} u^{true} - \eta\|,$$

where \mathcal{Z}_N^\perp is the orthogonal to \mathcal{Z}_N in \mathcal{X}

If we consider that the model \mathcal{P}^{bk} provides the majority of the information about the solution, the primary approximation will be taken from the background space

\mathcal{Z}_N , as imposed by equation (3.11). The update term η will be taken from outside the background space, as stated in equation (3.12). The best-fit error in the update space is thus given by the projection of the portion of the true state not approximated by the background space onto the update space orthogonal to the background space.

This can be attempted through optimal construction of the update space offline employing a Greedy-type selection of sensor functions (among a set of possible locations) to improve the space in the sense of **(a)** or **(b)**. The latter **(b)** can be done using for example a double greedy algorithm in order to minimize the GEIM error interpolation [114, 115], which selects background space basis functions and update space basis functions simultaneously, as described in section 4.1.2. The former **(a)** can be done for example using an algorithm to maximize $\beta_{N,M}$ under a certain tolerance, reverting otherwise to minimization of the best-fit error, as in [182].

Extended error analysis in [119] gives the following *a priori* estimate on output quantity of interest for $\ell^{out} \in \mathcal{X}'$

$$\begin{aligned} |\ell^{out}(u^{true}) - \ell^{out}(u_{N,M})| &= |\langle u^{true} - u_{N,M}, \psi - \Pi_{\mathcal{U}_M} \psi \rangle_{\mathcal{X}}| \\ &\leq \|u^{true} - u_{N,M}\|_{\mathcal{X}} \|\psi - \Pi_{\mathcal{U}_M} \psi\|_{\mathcal{X}} \end{aligned} \quad (3.19)$$

where $\psi = \mathcal{R}_{\mathcal{X}} \ell^{out} \in \mathcal{X}$, and $\Pi_{\mathcal{U}_M} \cdot$ is the orthogonal projection operator onto the update space \mathcal{U}_M .

The following *a posteriori* error estimates are also introduced in [118], for $M \leq M' \leq M_{max}$ the number of observations.

$$E_{N,M,M'} := \|u_{N,M'} - u_{N,M}\|_{\mathcal{X}} \quad (3.20)$$

$$O_{N,M,M'} := |\ell^{out}(u_{N,M'}) - \ell^{out}(u_{N,M})| \quad (3.21)$$

3.2 GEIM

The GEIM [114, 115] is a non-intrusive MOR and data assimilation method relying on the knowledge of some particular solutions in a function space \mathcal{X} to the parameterized model \mathcal{P}^{bk} , and some measurements over the physical state to be approximated, from which an empirical interpolation is constructed. From evaluations by general measures of the state given by linear forms (i.e. functions representing sensors) defined on a suitable functional space and the manifold of solutions to the parameterized problem, the GEIM allows to build an interpolation formula to approximate solutions to the model \mathcal{P}^{bk} for certain instances of the parameter \mathbf{p} .

The GEIM replaces the M pointwise evaluations used by the EIM in section 2.1.2.1 by general measures, linear forms defined on a superspace of the manifold \mathcal{M}^{bk} of solutions to the parameterized problem. If we don't have pointwise information on the function we wish to approximate, $u^{bk}(\mathbf{p}) \in \mathcal{M}^{bk}$, but we have a set Σ of linear forms $\sigma \in \Sigma$ which we can evaluate on the function $\sigma(u)$, where the linear forms

are continuous in some way, we want to use this data in a generalization of the EIM procedure described in section 2.1.2.1. The idea is the same as that of the PBDW linear functionals ℓ , in that real-world data over a physical state is generally not a punctual measurement, but some sort of average function.

GEIM Formulation

The GEIM procedure defines a set of generating functions in \mathcal{M}^{bk} , $(u^{bk}(\mathbf{p}_1), \dots, u^{bk}(\mathbf{p}_M))$ and a set Σ of associated linear forms $(\sigma_1, \dots, \sigma_M)$, from which interpolating basis functions are derived, $(\tilde{q}_1, \dots, \tilde{q}_M)$.

We then define the interpolation operator

$$\mathcal{I}_M(u) = \sum_{j=1}^M \alpha_j \tilde{q}_j \quad \text{such that} \quad \sigma_i(\mathcal{I}_M(u)) = \sigma_i(u) \quad \forall 1 \leq i \leq M \quad (3.22)$$

We will note that if Σ is a dictionary of Dirac masses, the GEIM is equivalent to the EIM.

Ideally we want to choose the linear forms $\sigma_i \in \Sigma$ and basis functions $\tilde{q}_i \in \mathcal{M}^{bk}$ in an optimal manner. In order to do this, we will consider a Greedy algorithm aiming at minimizing the interpolation error. The construction of the interpolation functions $\tilde{q} \in \mathcal{X}$ and selection of the linear forms $\sigma \in \Sigma$ is done recursively. Given a first generating function $u(\mathbf{p}_1) \in \mathcal{M}^{bk}$, chose as the "largest" of the generating functions in $\|\cdot\|_{\mathcal{X}}$, we can choose the associated linear form as that which gives the "most" information over u :

$$\sigma_1 := \underset{\sigma \in \Sigma}{\operatorname{argsup}} |\sigma(u(\mathbf{p}_1))| \quad (3.23)$$

The interpolating basis function is defined as

$$\tilde{q}_1 := \frac{u(\mathbf{p}_1)}{\sigma(u(\mathbf{p}_1))} \quad (3.24)$$

We then define

$$\begin{aligned} u(\mathbf{p}_2) &:= \underset{u \in \mathcal{M}^{bk}}{\operatorname{argsup}} \|u - \sigma(u)\tilde{q}_1\|_{\mathcal{X}} \\ \sigma_2 &:= \underset{\sigma \in \Sigma}{\operatorname{argsup}} |\sigma(u(\mathbf{p}_2) - \sigma_1(u(\mathbf{p}_2))\tilde{q}_1)| \\ \tilde{q}_2 &:= \frac{u(\mathbf{p}_2) - \sigma_1(u(\mathbf{p}_2))\tilde{q}_1}{\sigma_2(u(\mathbf{p}_2) - \sigma_1(u(\mathbf{p}_2))\tilde{q}_1)} \end{aligned} \quad (3.25)$$

and so on by induction. For $M > 2$, we solve the linear system for the state $u \in \mathcal{M}^{bk}$ to find the associated interpolation coefficients $(\tilde{\alpha}_j^{M-1}(u))_{1 \leq j \leq M-1}$

$$\sigma_i(u) = \sum_{j=1}^{M-1} \tilde{\alpha}_j^{M-1}(u) \sigma_i(\tilde{q}_j) \quad \forall 1 \leq i \leq M \quad (3.26)$$

and use the interpolation to define the M^{th} generating function $u(\mathbf{p}_M)$, linear form σ_M , and interpolating basis function \tilde{q}_M :

$$\begin{aligned}\mathcal{I}_{M-1}(u) &= \sum_{j=1}^{M-1} \tilde{\alpha}_j^{M-1}(u) \tilde{q}_j \\ u(\mathbf{p}_M) &:= \operatorname{argsup}_{u \in \mathcal{M}^{bk}} \|u - \mathcal{I}_{M-1}(u)\|_{\mathcal{X}} \\ \sigma_M &:= \operatorname{argsup}_{\sigma \in \Sigma} |\sigma(u(\mathbf{p}_M) - \mathcal{I}_{M-1}(u(\mathbf{p}_M)))| \\ \tilde{q}_M &:= \frac{u(\mathbf{p}_M) - \mathcal{I}_{M-1}(u(\mathbf{p}_M))}{\sigma_M(u(\mathbf{p}_M) - \mathcal{I}_{M-1}(u(\mathbf{p}_M)))}.\end{aligned}\tag{3.27}$$

The detailed GEIM algorithm can be found in appendix C (see algorithm 5).

We can define the interpolation matrix by

$$\mathbf{B}_{i,j}^M = \sigma_i(\tilde{q}_j) \quad 1 \leq i, j \leq M,$$

\mathbf{B}^M is lower triangular with unity diagonal (and non-singular), with other entries $\mathbf{B}_{i,j}^M \in [-1, 1]$.

The basis functions \tilde{q}_i are linearly independent, and we can define the M -dimensional subspace $\tilde{\mathcal{X}}_M := \operatorname{span}\{\tilde{q}_j\}_{j=1}^M = \operatorname{span}\{u(\mathbf{p}_j)\}_{j=1}^M \subset \mathcal{M}^{bk}$, proven in [154]. The method is well-posed in L^2 .

GEIM error and noise

Let us consider $\mathcal{X} = L^2(\Omega)$. Interpolation error through the GEIM is dependent again on the best fit by the basis functions \tilde{q}_i , and on the Lebesgue constant in the $L^2(\Omega)$ -norm, representing the $L^2(\Omega)$ -norm of \mathcal{I}_M :

$$\Lambda_M = \sup_{u \in \mathcal{M}^{bk}} \frac{\|\mathcal{I}_M(u)\|_{L^2(\Omega)}}{\|u\|_{L^2(\Omega)}},\tag{3.28}$$

where Λ_M is the inverse of the stability constant β_M .

Lemma: [114]-2.3 $\forall u \in \mathcal{M}^{bk}$, the interpolation operator satisfies:

$$\|u - \mathcal{I}_M(u)\|_{L^2(\Omega)} \leq (1 + \Lambda_M) \inf_{w_M \in \tilde{\mathcal{X}}_M} \|u - w_M\|_{L^2(\Omega)}$$

where a (very) pessimistic upper bound for Λ_M (found to be much smaller in practice) is:

$$\Lambda_M \leq 2^{M-1} \max_{1 \leq i \leq M} \|\tilde{q}_i\|_{L^2(\Omega)}$$

A high order of convergence was shown in practice for the Laplace problem in [114], and numerical results were compared to POD projection errors.

In [114] a method of filtering noisy data is discussed. It is assumed that the sensors measure, for example, an average value computed from a random variable $u_\epsilon \simeq \mathcal{N}(u, \epsilon^2)$ of normal distribution and variance ϵ , and that the physical state is

noisy, not the measurements. Then the GEIM interpolator is also a random variable following the same law. If many data points $M_{max} \gg M$ are available, then $P \leq M_{max}/M$ distinct series of sensor forms $\{\sigma_m^p\}_{m,p}$ could be selected and the GEIM performed P times. Averaging these P reconstructions of the physical state, we expect to improve the variance of the state estimate, and thus reduce the error induced by noise.

Specific applications studied with the GEIM, particularly its implication in data assimilation processes, has been discussed in 2.3.

This method provides tools that can optimally select from available sensors providing data, and even propose optimal placement of new sensors, which we will see more in chapter 4.1, on adaptations of the PBDW method for pollutant transport applications.

Numerical Implementation of the GEIM

We will note here some details of the numerical implementation of the GEIM and give the algorithm used in chapters 5 and 6. Firstly, the resolution of the interpolation problem in the recursive loop of algorithm 5 (see appendix C) can be done by solving a linear system:

$$\left(\Sigma\mathbf{Q}\right)\left(\alpha_k\right)=\left(\Sigma\mathbf{U}_k\right) \quad (3.29)$$

where $\Sigma\mathbf{Q}_{i,j} = \sigma_i(\tilde{q}_j)$ for \tilde{q}_j corresponding to the j^{th} interpolation function built during the GEIM algorithm on the training set of the bk model, and $\sigma_i \in \Sigma$ corresponding to the i^{th} linear form (e.g. the functionals ℓ_m from equation (3.5)). $(\alpha_k)_i$ is the i^{th} interpolation coefficient from equation (4.28) for the k^{th} training function $u^{bk}(\mathbf{p}_k) \in \mathcal{M}^{bk}$, and $(\Sigma\mathbf{U}_k)_i = \sigma_i(u^{bk}(\mathbf{p}_k))$.

As noted in section 2.1.2.1, the matrix $\Sigma\mathbf{Q}$ is lower triangular with unity diagonal. We can thus avoid the numerical inversion of the matrix and solve the system of M equations to find $\mathcal{I}_M[u^{bk}(\mathbf{p}_k)]$.

$$\begin{cases} \alpha_1(u^{bk}(\mathbf{p}_k)) = \sigma_1(u^{bk}(\mathbf{p}_k)) \\ \alpha_2(u^{bk}(\mathbf{p}_k)) = \sigma_2(u^{bk}(\mathbf{p}_k)) - \sigma_2(\tilde{q}_1)\alpha_1 \\ \dots \\ \alpha_m(u^{bk}(\mathbf{p}_k)) = \sigma_m(u^{bk}(\mathbf{p}_k)) - \sum_{i=1}^{M-1} \sigma_M(\tilde{q}_i)\alpha_i \end{cases} \quad (3.30)$$

This gives us the recursive formula for the m^{th} interpolating operator:

$$\mathcal{I}_M(u(\mathbf{p})) = \mathcal{I}_{M-1}(u(\mathbf{p})) + \frac{\sigma_M(u(\mathbf{p}) - \mathcal{I}_{M-1}(u(\mathbf{p})))}{\sigma_M(u(\mathbf{p}_M) - \mathcal{I}_{M-1}(u(\mathbf{p}_M)))} \left(u(\mathbf{p}_M) - \mathcal{I}_{M-1}(u(\mathbf{p}_M))\right) \quad (3.31)$$

This dependence of the m^{th} interpolating basis function \tilde{q}_m on the $m - 1^{th}$ interpolation \mathcal{I}_{m-1} is an iterative procedure which could cause the accumulation of

numerical errors. We chose to implement a stabilized numerical algorithm for this part of the GEIM, much like a numerically stabilized version of Gram-Schmidt orthonormalization. If we want to construct the interpolating operators \tilde{q}_m :

$$\tilde{q}_m = \frac{u^{bk}(\mathbf{p}_m) - \mathcal{I}_{m-1}[u^{bk}(\mathbf{p}_m)]}{\sigma_m(u^{bk}(\mathbf{p}_m) - \mathcal{I}_{m-1}[u^{bk}(\mathbf{p}_m)])}$$

but want to account for numerical error, we can use the following procedure.

Algorithm 1 : A more stable numerical algorithm for the computation of the m^{th} GEIM interpolation function.

- 1: **Input:** we consider we've already found $u^{bk}(\mathbf{p}_m)$ and σ_m .
- 2: Set $w = u^{bk}(\mathbf{p}_m) \in \mathcal{X}_h$.
- 3: **for** $j = 1$ to $m - 1$ **do**
- 4: Set:

$$\begin{aligned} r_{j,m} &= \alpha_j(w) \\ &= \sum_{i=0}^{m-1} (\Sigma \mathbf{Q}^{-1})_{j,i} \sigma_i(w) \end{aligned}$$

- 5: Compute $w = w - r_{j,m} \tilde{q}_j$
 - 6: **end for**
 - 7: Set $r_{m,m} = \sigma_m(w)$
 - 8: Compute $\tilde{q}_m = \frac{w}{r_{m,m}}$
-

We recall that the construction of the GEIM interpolation functions and sensor set is done during an offline stage. This stage can also be computed using a POD basis for which we select appropriate sensors by a Greedy algorithm. Once the matrix \mathbf{LQ} is constructed for a fixed M -value, we need only plug in the data in the right-hand-side of the linear system (3.29) (or the corresponding values in equation (3.30)), which corresponds to the first M values of the right-hand-side of the PBDW linear system (3.14), \mathbf{y}^{obs} . We can thus solve for the interpolation coefficients $\alpha(u^{bk}(\mathbf{p}_k))$ in $\mathcal{O}(M^3)$ operations.

Chapter 4

Adaptations for Complex Large-Scale Applications and Pollution Modeling

Résumé :

Ce chapitre est divisé en deux parties.

La première est une discussion sur l'adaptation des méthodes PBDW et GEIM pour des applications de qualité de l'air à l'échelle urbaine. Nous réfléchissons sur la stabilité du système en fonction du choix des fonctions de base q_m de l'espace *update* \mathcal{U}_M . Nous introduisons pour cela la norme \tilde{H}^1 , équivalente à la norme H^1 , qui sera utilisée afin d'élargir le support des fonctions de base de l'espace *update*. Nous considérons deux méthodes pour la construction de l'espace réduit *background* \mathcal{Z}_N : la POD (Proper Orthogonal Decomposition) et une méthode reposant sur un algorithme de type glouton (appelé aussi *greedy*). Le positionnement optimal (quand il est possible) des capteurs est également considéré dans ce chapitre. Celui-ci est obtenu par un algorithme de double *greedy* basé sur la GEIM. Cette partie se finit par une discussion sur les différences, les avantages et les inconvénients de la méthode PBDW par rapport aux méthodes inverses de type problème adjoint.

Dans la seconde partie, nous présentons en détail les modèles mathématiques utilisés dans nos applications inspirées par la modélisation de la qualité de l'air. Le modèle "best-knowledge", \mathcal{P}^{bk} est donné par l'EDP d'advection-diffusion suivante

$$\rho \vec{v} \cdot \nabla c - \operatorname{div}(\epsilon_{tot}(x) \nabla c) = \rho F_{src}.$$

Cette EDP et son équivalent adimensionnelle sont résolues par une méthode d'éléments finis avec stabilisation SUPG. Pour évaluer la capacité de notre méthode à traiter des modèles erronés (c'est à dire qui n'auraient pris pas en compte tous les phénomènes physiques), nous considérons un second modèle : \mathcal{P}^{trial} . Ce modèle qui repose sur une EDP d'advection-diffusion-réaction, sera utilisé pour calculer des données synthétiques.

We introduced in chapter 3 two non-intrusive reduced order data assimilation methods of particular interest. We want to adapt these methods to problems inspired by physically-based air quality models. These applications are complex due to the turbulent fluid flow underlying a pollutant concentration field, the transport phenomena, and more physical phenomena such as chemical reaction and deposition effects. Additionally, calculation domains for AQM problems are commonly very large, while studies employing the output predictions of these models (e.g. epidemiology studies) can benefit from very small scale precision. Over urban areas, which are often the most pertinent regions of study for air quality modeling, the geometries can be complex and induce complex fluid flows. We thus find ourselves applying difficult-to-solve equations over complex CFD wind fields and geometries in large dimension for small-scale results. We must consider adaptations to these methods for our complex large dimension problems to ensure stability of the problem and precision of the results.

4.1 PBDW: technical details and analysis

In this section we will discuss procedural details of the implementation of the PBDW method to the environmental modeling problems discussed in chapters 4.2, 5, and 6.

4.1.1 PBDW in Practice

Consider the following finite element approximation spaces:

- $\mathcal{X}_h \subset \mathcal{X} \subset H^1(\Omega)$ and $\dim(\mathcal{X}_h) = \mathcal{N}_h$.
- $\mathcal{Z}_N \subset \mathcal{X}_h$, $\mathcal{Z}_N = \text{span}\{\zeta_n\}_{n=1}^N$, where $\zeta_n \in \mathcal{X}^{\mathcal{N}}$ are RB basis functions associated to the model \mathcal{P}^{bk} , obtained for example via a greedy algorithm.
- $\mathcal{U}_M \subset \mathcal{X}_h$, $\mathcal{U}_M = \text{span}\{q_m\}_{m=1}^M$, where $q_m = \mathcal{R}_{\mathcal{X}}\ell_m \in \mathcal{X}_h$ and $\mathcal{R}_{\mathcal{X}}$ is the Riesz operator associated to \mathcal{X}_h .

The implementation of the PBDW approximation with the discrete space \mathcal{X}_h follows directly, and below we summarize the steps of the method.

1. Build the background space \mathcal{Z}^N with orthonormal basis $\{\zeta_n\}_{n=1}^N$.
2. Given sensor locations and size, define measurement functionals $\ell_m(v)$, $1 \leq m \leq M$ for M sensors.
3. Build update space \mathcal{U}_M with basis $\{q_m\}_{m=1}^M$ for M sensors
4. Build matrices $(\mathbf{A})_{i,j} = \langle q_j, q_i \rangle_{H^1}$ and $(\mathbf{B})_{i,j} = \langle \zeta_j, q_i \rangle_{H^1}$ from basis functions:

5. Build full PBDW matrix :

$$\mathbb{K}^{PBDW} = \begin{pmatrix} \mathbf{A} & \mathbf{B} \\ \mathbf{B}^T & \mathbf{0} \end{pmatrix}$$

Once we've constructed our linear system and solved for

$$\begin{pmatrix} \vec{\eta}_M \\ \vec{z}_N \end{pmatrix} = (\mathbb{K}^{PBDW})^{-1} * \begin{pmatrix} \vec{y}^{obs} \\ \vec{0} \end{pmatrix}$$

we can fully reconstruct the PBDW solution:

$$c_{N,M} = \sum_{i=1}^M (\eta_M^i q_i) + \sum_{i=1}^N (z_N^i \zeta_i) \in \mathcal{X}_h. \quad (4.1)$$

4.1.1.1 Evaluating the stability coefficient

We've seen that the *a priori* error bound given in equation (3.18) depends on the stability coefficient defined by equation (3.17). Here we will apply a Galerkin analysis as used in [81, 116] based on analysis first given in [121] to calculate $\beta_{N,M}$ for given approximation spaces \mathcal{Z}_N and \mathcal{U}_M . Let us first recall the following expression of our approximation spaces.

$$\begin{aligned} \mathcal{Z}_N &= \text{SPAN}\{\zeta_j \mid 1 \leq j \leq N\} \\ \mathcal{U}_M &= \text{SPAN}\{q_j \mid 1 \leq j \leq M\} \end{aligned} \quad (4.2)$$

Let us recall the matrices of scalar products of \mathcal{Z}_N and \mathcal{U}_M from equation (3.14):

$$\begin{aligned} \mathbf{A}_{i,j} &= \langle q_i, q_j \rangle_{H^1(\Omega)}, & \mathbf{A} &\in \mathbb{R}^{M \times M} \\ \mathbf{B}_{j,i} &= \langle \zeta_i, q_j \rangle_{H^1(\Omega)}, & \mathbf{B} &\in \mathbb{R}^{M \times N} \end{aligned} \quad (4.3)$$

$$(4.4)$$

We note, for any $v = \sum_{i=1}^M y_i q_i \in \mathcal{U}_M$ and $w = \sum_{i=1}^N x_i \zeta_i \in \mathcal{Z}_N$,

$$\langle v, w \rangle_{H^1} = (\vec{y})^T \mathbf{B} \vec{x} \in \mathbb{R}. \quad (4.5)$$

We then define

$$\mathbf{C}_{i,j} = \langle \zeta_i, \zeta_j \rangle_{H^1(\Omega)}, \quad \mathbf{C} \in \mathbb{R}^{N \times N} \quad (4.6)$$

We thus represent the inf-sup problem posed in equation (3.17) as the following matricial problem.

$$\beta_{N,M} = \inf_{x \in \mathbb{R}^N} \sup_{y \in \mathbb{R}^M} \frac{y^T \mathbf{B} x}{(x^T \mathbf{C} x)^{1/2} (y^T \mathbf{A} y)^{1/2}}. \quad (4.7)$$

The matrices \mathbf{A} and \mathbf{C} are symmetric positive-definite, as $y^T \mathbf{A} y = \|Y\|_{H^1}^2$ for $Y = \sum_{i=1}^M y_i q_i \in \mathcal{U}_M$, and similarly for \mathbf{C} . They can thus be written (theorem 4.1 [142]) as

$$\begin{aligned} \mathbf{A} &= \mathbf{U}^T \mathbf{U} \\ \mathbf{C} &= \mathbf{V}^T \mathbf{V} \end{aligned} \quad (4.8)$$

and we can thus rewrite equation (4.7) as follows:

$$\beta_{N,M} = \inf_{x \in \mathbb{R}^N} \sup_{y \in \mathbb{R}^M} \frac{\langle y, \mathbf{B}x \rangle}{|\mathbf{V}x| |\mathbf{U}y|}. \quad (4.9)$$

Let us consider the maximization problem. We have

$$\begin{aligned} \sup_{y \in \mathbb{R}^M} \frac{\langle y, \mathbf{B}x \rangle}{|\mathbf{U}y|} &= \sup_{w \in \mathbb{R}^M} \frac{\langle w, \mathbf{U}^{-T} \mathbf{B}x \rangle}{\|w\|} \\ &= \|\mathbf{U}^{-T} \mathbf{B}x\|, \end{aligned} \quad (4.10)$$

and can write

$$\begin{aligned} \beta_{N,M} &= \inf_{x \in \mathbb{R}^N} \sup_{y \in \mathbb{R}^M} \frac{\langle y, \mathbf{B}x \rangle}{|\mathbf{V}x| |\mathbf{U}y|} \\ &= \inf_{x \in \mathbb{R}^N} \frac{\|\mathbf{U}^{-T} \mathbf{B}x\|}{|\mathbf{V}x|} \\ &= \inf_{x \in \mathbb{R}^N} \frac{\|\mathbf{U}^{-T} \mathbf{B} \mathbf{V}^{-1} x\|}{\|x\|}, \end{aligned} \quad (4.11)$$

which is the square root of the Rayleigh quotient of $(\mathbf{U}^{-T} \mathbf{B} \mathbf{V}^{-1})^T \mathbf{U}^{-T} \mathbf{B} \mathbf{V}^{-1}$, whose infimum is given by $\sqrt{\lambda_{\min}((\mathbf{U}^{-T} \mathbf{B} \mathbf{V}^{-1})^T (\mathbf{U}^{-T} \mathbf{B} \mathbf{V}^{-1}))}$. This gives us:

$$\begin{aligned} (\mathbf{U}^{-T} \mathbf{B} \mathbf{V}^{-1})^T (\mathbf{U}^{-T} \mathbf{B} \mathbf{V}^{-1}) &= \mathbf{V}^{-T} \mathbf{B}^T \mathbf{U}^{-1} \mathbf{U}^{-T} \mathbf{B} \mathbf{V}^{-1} \\ &= \mathbf{V}^{-T} \mathbf{B}^T \mathbf{A}^{-1} \mathbf{B} \mathbf{V}^{-1} \\ (\mathbf{V}^{-T} \mathbf{B}^T \mathbf{A}^{-1} \mathbf{B} \mathbf{V}^{-1})_s &= \lambda_s \end{aligned} \quad (4.12)$$

We then want to solve the following eigenvalue problem

$$(\mathbf{B}^T \mathbf{A}^{-1} \mathbf{B})_s = \lambda C_s \quad (4.13)$$

in order to approximate the stability coefficient $\beta_{N,M}$ corresponding to the approximation spaces \mathcal{Z}_N and \mathcal{U}_M by $\sqrt{\lambda_{\min}}$ the smallest eigenvalue of (4.13).

4.1.1.2 Evaluating the PBDW approximations

In this section we will give the equations used to evaluate error in the PBDW approximations. We will consider both normed and FE function errors, relative with respect to the concentration measured in the H^1 or L^∞ norm.

We stress the importance of relative errors in this context. Not only is an absolute error all but meaningless without some order of magnitude, percentage errors being much more useful, but in the case of air pollutant concentrations the evaluation of interest may well be the order of the concentration on a logarithmic scale. Relative errors are the answer to both these questions.

When considering simulated model error (using a shifted model \mathcal{P}^{trial}), we want to determine how much (relative) error we are introducing and trying to correct. We can consider:

$$E_{mod}(c^{bk}(\mathbf{p})) = \frac{\|c^{bk}(\mathbf{p}) - c^{trial}(\mathbf{p})\|_{\mathcal{X}}}{\|c^{bk}(\mathbf{p})\|_{\mathcal{X}}} \quad (4.14)$$

In order to estimate the precision of the resolution of the PBDW system from an algebraic point of view, we can look at the residual of the system (3.14) in the relative ℓ^∞ euclidean norm:

$$\frac{\|\mathbb{K}^{PBDW} \mathbf{c}_{M,N} - \mathbf{Y}\|_{\ell^\infty}}{\|\mathbf{Y}\|_{\ell^\infty}} \quad (4.15)$$

with

$$\mathbb{K}^{PBDW} = \begin{pmatrix} \mathbf{A} & \mathbf{B} \\ \mathbf{B}^T & \mathbf{0} \end{pmatrix},$$

$$\mathbf{Y} = \begin{pmatrix} y^{obs} \\ \mathbf{0} \end{pmatrix}$$

and

$$\mathbf{c}_{M,N} = \begin{pmatrix} \vec{\eta}_M \\ \vec{z}_N \end{pmatrix}$$

or the relative weak residual at each data point $\langle c_{M,N}, q_i \rangle_{H^1} - y_i^{obs}$:

$$\frac{\|\vec{z}^T \mathbf{B} + \vec{\eta}^T \mathbf{A} - \vec{y}^{obs}\|_{\ell^\infty}}{\|\vec{y}^{obs}\|_{\ell^\infty}}, \quad (4.16)$$

where \mathbf{A} and \mathbf{B} are defined in equation (3.14).

We recall that in the RBM context, we are commonly interested in a Quantity of Interest (QoI), and the full reconstruction of the PBDW state estimate is unnecessary. In this case the errors are calculated over the QoI in absolute value.

For purposes of analyzing results and numerically calculating the error bound in equation (3.18), we will consider the following relative *best-fit* error onto what we'll refer to as the PBDW approximation space $\mathcal{Z}_N \oplus (\mathcal{U}_M \cap \mathcal{Z}_N^\perp)$:

$$\frac{\|c^{true} - \Pi_{\mathcal{Z}_N \oplus (\mathcal{U}_M \cap \mathcal{Z}_N^\perp)} c^{true}\|_{\mathcal{X}}}{\|c^{true}\|_{\mathcal{X}}} \quad (4.17)$$

We can thus consider the relative version of the bound in equation (3.18).

$$\frac{\|c^{true} - c_{N,M}\|_{\mathcal{X}}}{\|c^{true}\|_{\mathcal{X}}} \leq \left(1 + \frac{1}{\beta_{N,M}}\right) \frac{\|c^{true} - \Pi_{\mathcal{Z}_N \oplus (\mathcal{U}_M \cap \mathcal{Z}_N^\perp)} c^{true}\|_{\mathcal{X}}}{\|c^{true}\|_{\mathcal{X}}} \quad (4.18)$$

4.1.1.3 Reflections on Stability and Approximation Quality

In this section we will discuss choices that were made over the course of the applications to better adapt the PBDW method to the chosen case studies.

Update Space We've seen in section 3.1.3 that the PBDW approximation error bound (3.18) depends on the stability constant $\beta_{N,M}$, which depends by equation (3.17) on the approximation spaces. Here we wish to consider the effect of the choice of the Update space \mathcal{U}_M has on the stability of the problem and quality of the PBDW state estimation.

The Update space depends firstly on the placement of the data points. In some applications, the data points may be pre-fixed, in which case only the order in which these data are used may be chosen. In other applications the location of each data point may be optimized (under constraints dependent on the system and domain). As discussed in section 3.1.3, we wish to build the update space to both optimize the stability coefficient $\beta_{M,N}$ (3.17) and optimize the state estimation.

A logical method is to choose data points which bring the most information on the physical state to approximate. We considered in this work methods different from those employed in [118, 119, 182]: random selection, manual selection, and selection by a Greedy algorithm over the set of solutions to \mathcal{P}^{bk} and a set of possible data points (discussed in more detail in section 4.1.2).

In large-scale applications of the PBDW method considered in chapters 5 and 6, we found some instability in the method, perhaps not only linked to the sensor placement, but also to the form of the associated Update basis functions.

Given the application in pollution field reconstruction, the linear forms ℓ_m , $1 \leq m \leq M$, described in equation (3.5) induced by the mathematical representation of the sensors (3.4) should be appropriately chosen to represent air pollutant measurements. We chose to use the form presented in (3.4) following the example for similar representation of water quality sensors in [194]. This formulation is a choice which could be reconsidered, as the form of the sensor functions φ can play a role in the quality of the Update space. Initial tests using a characteristic function over the ball of radius r multiplied by the sensor function:

$$\varphi_m(x) = \frac{1}{c} \chi_{B(x_m, r)}(x) f(x; x_m, r) \text{ such that } \int_{\Omega} \varphi_m(x) d\Omega = 1 \quad (4.19)$$

where

$$f(x; x_c, r) = \exp\left(\frac{-(x - x_m)^2}{2r^2}\right) \quad (4.20)$$

and where $\chi_{B(x_c, r)}$ represents a characteristic function over the ball $B(x_c, r) \in \Omega$ of center x_c and radius r . This resulted in a loss of smoothness of the sensor functions, which translates to the update basis functions. We can see these less smooth update basis functions build a less stable PBDW system in the following figure 4.1. While the difference is minimal (a factor of 2), this could contribute to less precise PBDW approximations.

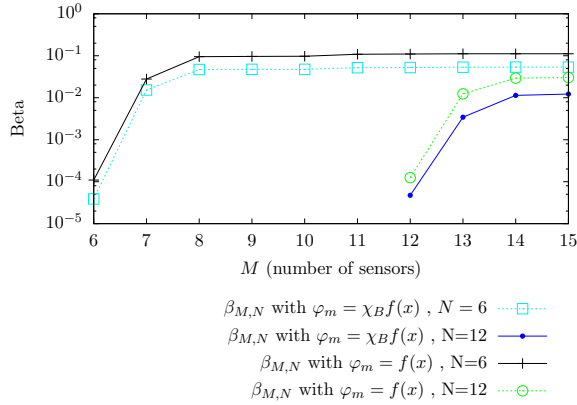


Figure 4.1 – $\beta_{M,N}$ stability coefficients (3.17) for the 2D case study presented in chapter 5. Comparing stability coefficients for the PBDW system with update basis functions defined by (3.8) where the functional φ is represented with a characteristic function as in (4.19), or without the characteristic function as in (3.4).

We note that, in real-world applications (e.g. in chapter 7), the actual diameter of common air quality sensors is generally quite small (in the range of a few centimeters). Given the scale of the calculation domains, this is quasi-pointwise. For numerical stability over a reasonably fine mesh, we set $r = 25\text{cm}$.

For a given background RB dimension N , we want to evaluate the contribution of the Update space to the approximation quality using equation (4.17). We will also note that relatively local data can lead to a poor secondary approximation by the Update space, as we will see in chapter 5. We can in this case use the L^∞ -norm in equation (4.17) in order to see the effect of local improvement on the state estimation.

Inner Product Given the relatively small size of the sensors providing our observational data with respect to the large domain of study, we chose to consider a more drastic method of improving the continuity of the Update basis functions. We thus consider modifications to the norm used in the definition of the update basis functions by Riesz representation in equation (3.8). We introduce the \tilde{H}^1 norm associated to the following scalar product for $u, v \in H^1$.

$$\langle u, v \rangle_{\tilde{H}^1(\Omega)} = \langle u, v \rangle_{L^2} + L_g^2 \langle \nabla u, \nabla v \rangle_{L^2}, \quad (4.21)$$

where $L_g > 1$ is some characteristic length of the domain. Noticing that

$$\frac{1}{L_g^2} \|\cdot\|_{H^1} \leq \|\cdot\|_{\tilde{H}^1(\Omega)} \leq L_g \|\cdot\|_{H^1},$$

the \tilde{H}^1 norm is clearly equivalent to the H^1 norm.

In figure 4.2 we can see the different basis functions q_m obtained by either using the H^1 or the \tilde{H}^1 norm (4.21). In the case of the \tilde{H}^1 norm, the support of each basis function is much larger, and the peak much lower, providing more smooth functions over the domain for a smoother and spatially wider basis for the correction term η_M .

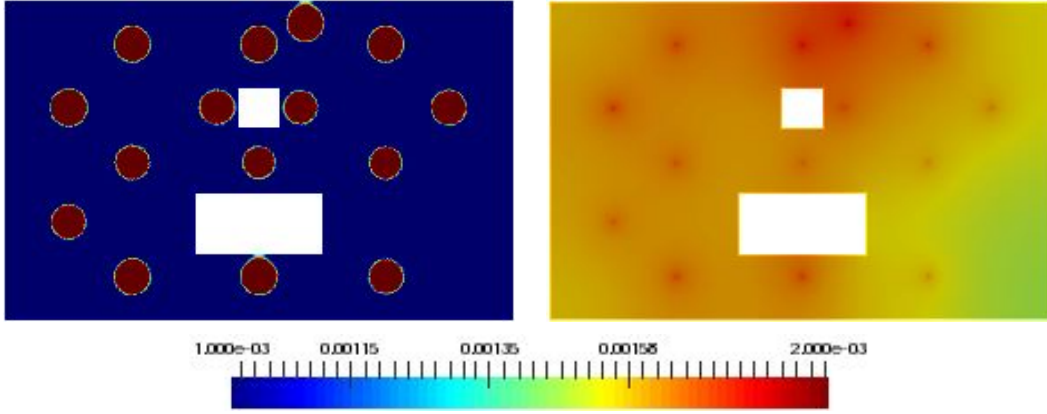


Figure 4.2 – q_m basis functions constructed with the H^1 norm (left) and constructed with the \tilde{H}^1 norm with $L_g = 75m$ (right), over the 2D case study introduced in chapter 5

For consistency with observational data in the constraints of the PBDW problem statement (3.11), the same norm must be used in the variational formulation (3.12) and linear system (3.14). Given the equivalence of the right-hand-side of equation (3.12) to our observational data by (3.9), which is only the case if the norm $\|\cdot\|_{\mathcal{X}}$ is the norm used in the Riesz definition (3.8) of the update basis functions For \tilde{q}_m representing the m^{th} basis function constructed by the Riesz representation in the \tilde{H}^1 norm, we have:

$$\underbrace{\langle \tilde{q}_m, c \rangle_{\tilde{H}^1}}_{\text{RHS of (3.12) with } \|\cdot\|_{\tilde{H}^1}} \stackrel{\text{Riesz}}{=} \overbrace{\int_{\Omega} c \varphi_m}^{\text{data}} = y_m^{\text{obs}} \quad (4.22)$$

$$\neq \underbrace{\langle \tilde{q}_m, c \rangle_{H^1}}_{\substack{\text{RHS of (3.12) \\ \text{with } \|\cdot\|_{H^1}}} \quad (4.23)$$

The following equivalent formulation of the norm was also tested, but provided no improvement in practice, giving intermediate results between the H^1 - and \tilde{H}^1 -norms.

$$\langle u, v \rangle_{\tilde{H}_L^1} = \langle u, v \rangle_{L^2} + L_g \langle \nabla u, \nabla v \rangle_{L^2},$$

which gives $\text{supp}(q_m)$ between the H^1 and \tilde{H}^1 formulations.

RB Background The reduced basis background space \mathcal{Z}_N (3.2) can be constructed by different methods. We chose to focus on Greedy algorithms (see algorithm 3 in appendix C), but another common technique as discussed in 2.1.2.3 is construction by POD. POD basis have the advantage that each basis function is constructed using pieces from the full set of training solutions. This means a POD basis of dimension N could potentially contain more information than its N -dimensional Greedy RB counterpart.

We can consider that, for a model \mathcal{P}^{bk} over a parameter space \mathcal{D}^{bk} , the POD method is optimal in the L^2 -norm, but the strong greedy algorithm is nearly optimal as well.

Let $\Pi_{\mathcal{Z}_N}$ be the \mathcal{X} orthogonal projection operator from \mathcal{X}_h onto the background space \mathcal{Z}_N such that for any $f \in \mathcal{X}_h$

$$\Pi_{\mathcal{Z}_N} f = \sum_{k=1}^N \langle f, \zeta_k \rangle_{H^1} \zeta_k, \quad (4.24)$$

where $(\zeta_k)_{1 \leq k \leq N}$ are \mathcal{X} -orthonormal basis functions of \mathcal{Z}_N , and the projection error

$$E_N(c) = c - \Pi_{\mathcal{Z}_N} c, \quad (4.25)$$

for any $c \in \mathcal{X}_h$. In the following work, we will denote by *mean* error the average of the projection errors $E_N(c(\mathbf{p}_i))$

$$\frac{1}{N_p} \sum_{i=1}^{N_p} \frac{\|E_N(c^{bk}(\mathbf{p}_i))\|_{\mathcal{X}}}{\|c^{bk}(\mathbf{p}_i)\|_{\mathcal{X}}}, \quad (4.26)$$

from a family of N_p parameters $\mathbf{p}_i \in \mathcal{D}^{bk}$.

The *maximal* error corresponds to

$$\max_{1 \leq i \leq N_p} \frac{\|E_N(c^{bk}(\mathbf{p}_i))\|_{\mathcal{X}}}{\|c^{bk}(\mathbf{p}_i)\|_{\mathcal{X}}} \quad (4.27)$$

In figure 4.3 we compare these mean and maximal projection errors onto a Greedy or POD RB of the training set for the case study presented in chapter 5.

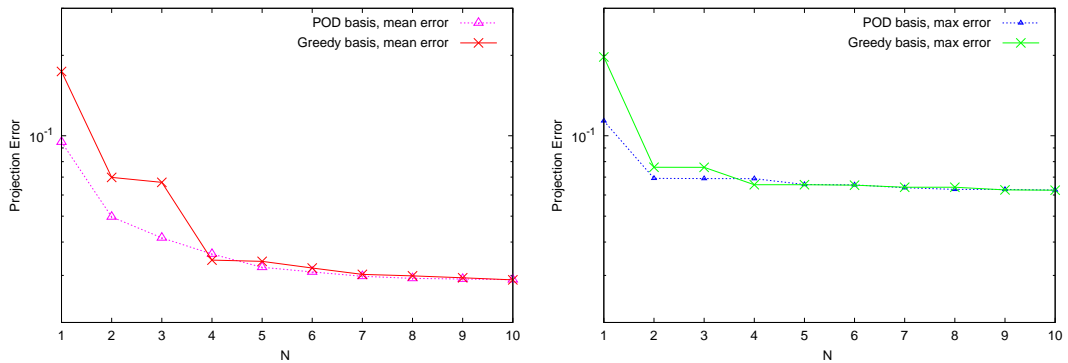


Figure 4.3 – Relative mean (4.26) (left) and maximal (4.27) (right) projection errors for the 2D case study presented in chapter 5. Comparing RB background spaces constructed using a POD method and a Greedy algorithm over an identical set of training solutions for parameters $\mathbf{p} \in \mathcal{D}^{bk}$.

We chose to focus on Greedy methods in what follows.

4.1.2 GEIM in the PBDW framework

In this section we will elaborate on the use of the GEIM method [114], introduced in section 3.2, in the PBDW framework.

We recall the interpolation operator corresponding to equation (3.22):

$$\mathcal{I}_M(u^{bk}) = \sum_{j=1}^M \beta_j \xi_j \text{ such that } \ell_i(\mathcal{I}_M(u^{bk})) = \ell_i(u^{bk}) \forall 1 \leq i \leq M \quad (4.28)$$

4.1.2.1 Improved selection of sensor locations

For more precise (and stable) implementation of the PBDW method, we want to choose the linear forms ℓ_i in an optimal manner. In the context of PBDW state estimation, we can consider the GEIM not only as a closely-related reduced order data assimilation method, but as a tool for the greedy selection, from an available set, of the sensors which will give the most information on the solution space, \mathcal{M}^{bk} . If we choose sensors by hand, we may end up with some which give little to no information, which is at best a waste of a sensor (and increased dimension of the reduced problem), and at worst could make the linear system ill-posed or poorly conditioned.

Using GEIM-based tools to choose linear forms ℓ_m over a set of generating functions in the manifold \mathcal{M}^{bk} associated to \mathcal{P}^{bk} allows to select which sensors will give the most information on the solution manifold from a set of possible locations or forms. This choice places faith in the precision of the model; as we will see in applications in chapters 5 and 6, the sensor placement may not be optimal for capturing the effects of unmodeled physics not accounted for in the mathematical problem. However this method does give us insight into the best way to capture information on the physics described by the model, which is (as will be shown in chapter 5 to be) a clear improvement from random placement.

In this framework, we consider that we have a set of functions φ_m representing the sensors corresponding to a set of linear functionals $\ell_m \in \mathcal{X}'$ from equation (3.5) where the centers $x_m \in \mathbb{R}^d$ and radius r_m may vary. Hence for consistency with the PBDW notation, we consider the set of linear forms $\ell_m \in \Sigma$, for $1 \leq m \leq M$. The set of generating functions will be the training set of solutions to the model \mathcal{P}^{bk} considered in section 3.1.2.1, which is a representative sample of \mathcal{M}^{bk} .

4.1.3 Motivation for PBDW in air quality studies

We aim, in the following chapters, to demonstrate that the modeling of physical phenomena such as pollutant transport by PBDW can be feasible thanks to the strategic treatment of parameters (e.g. the careful selection of the parameter space or eventual decomposition into local RB spaces in view of Kolmogorov dimensionality) and the non-intrusive data assimilation allowing to correct for unmodeled physics.

4.1.3.1 Advantages of the PBDW method

The PBDW method provides multiple advantages of particular interest in the air quality modeling context. A notable feature, the non-intrusive characteristic means the method can be applied to *any* suitable parameterized calculation code, allowing for application with the *true* best-knowledge model available.

In addition, the PBDW method employs variational data-assimilation techniques to correct unmodeled physics. Particularly in the field of air quality modeling, parameters such as meteorology, emissions, reaction, and more are not well known. The prospect of correcting, to some extent, our lack of knowledge in the final approximation of air quality is particularly attractive.

Another remarkable feature, and perhaps most importantly, if the physical states under varying conditions can be represented by a set of RB spaces (note that we do not expect all meteorological conditions to be represented by a single reduced basis of small dimension), not only does this allow for online efficiency, but the pollutant concentration can be estimated by the PBDW method *without first reconstructing the meteorological field* separately. With respect to other comparable methods such as the adjoint method, this characteristic could prove very advantageous.

We also do not aim to identify the parameters involved in the equations; while this can be a goal of some studies, parameter-identification is often non-trivial and could complicate approximation procedures when this information is not necessary. Our goal being to reconstruct the physical state (or a physical output quantity on it), not needing to identify the parameter is a considerable advantage.

4.1.3.2 Comparing the PBDW to Inverse methods in AQ modeling

In this paragraph we discuss the similarities and differences between the PBDW method and inverse methods via adjoint problem. As discussed in sections 2.2 and 2.3 of chapter 2, inverse methods by the adjoint problem are typical in treating the reconstruction of a physical state from a (relatively) precise mathematical model and measurement data.

Both methods are based on a least-squares type minimization problem with constraints. As the PBDW formulation, like certain other variational data assimilation methods, aims to rectify the model approximation using measurements, and the minimization statement is thus linearly constrained by the form of the approximation in $\mathcal{Z}_N \oplus \mathcal{U}_M$ and imposed values at the data points. The adjoint method, on the other hand, aims to find the optimal parameter of the model, which minimizes the gap between the approximation the the measurements. A regularizing term based on a control parameter or state (e.g. the Tikhonov regularization) is often needed to ensure well-posedness. The PDE model, providing the physical sense of the solution, plays a role in the constraints of the minimization problem, whereas in the PBDW formulation the PDE only intervenes in the background RB space. In certain cases the PDE can lead to nonlinear constraints in the adjoint minimization problem,

while the PBDW minimization constraints are always linear. The physical sense is guaranteed by minimizing the contribution of the update outside the RB space, keeping the PBDW approximation close to the manifold \mathcal{M}^{bk} , and by requiring the Update space to be a subspace of the global function space (e.g. H^1) in which the state estimates lie.

From the minimization problem, each method relies on the Lagrangian, standard step in the resolution of a constrained minimization problem. The adjoint method presented in section 2.2 [193] then relies on the adjoint to the PDE to optimize the parameter by descent method, hence the iterative procedure, contrary to the non-iterative linear system resulting from the PBDW formulation.

One of the drawbacks of the general adjoint approach is that it is intrusive from a computational point of view, requiring the development of an adjoint calculation code. While PBDW method is relatively non-intrusive, the adjoint method requires a more intrusive offline phase for the construction of a linear system associated to the discrete approximation of the adjoint problem. In some cases this could mean relatively small modification of the calculation code, while in others more significant modifications could be required. An additional constraint stemming from usual RBM implementation to reduced computational cost of the adjoint method, online interpolation procedure dependent on the parameter in cases of non-affine parameter dependence. For these reasons, less intrusive options can be valuable.

Inverse methods use available measurement data to optimize the parameter, while some variational data assimilation methods, the PBDW method included, use the data to correct the inevitably flawed model.

If we consider the case of, for example, varying wind fields taken as a parameter in the transport of pollutants, as in section 5.1, the PBDW method relies on RB representation of variation induced by varying wind fields and avoids the costly reconstruction of CFD states. On the other hand, the implementation of the adjoint method would in this case still require the reconstruction of the wind field at each iteration of the adjoint algorithm. The velocity field is necessary during the approximation of the optimal parameter (i.e. for each approximation of adjoint solution), which can be done using RB spaces, making the online phase relatively efficient, but requiring a more costly offline phase as compared to the PBDW method with a single solution space to reduce. This could possibly be advantageous also from the materials perspective; costly velocity and pressure sensors are not necessary in the PBDW method if the background space is appropriately chosen, while they are mandatory in the adjoint method to reconstruct velocity fields.

An advantage of the adjoint method, with respect to the PBDW method, is that it works well with a smaller number of sensors: one per parameter to be optimized generally suffices. The PBDW method requires $M > N$, where the RB dimension N depends on the dimension of the solution manifold \mathcal{M}^{bk} . This can be relatively elevated in cases with complex physical models, of which we see a simple example in section 6. In cases of saturation measurement campaigns, where many data points are available, this may not be a negative; the treatment of many sensors in the

adjoint method results in a more complicated numerical procedure and possibly more iterations before convergence, meaning higher computation times.

In cases of many query applications where computation time is of importance, the MOR character of the PBDW method may provide significant gain with respect to the iterative adjoint method, provided the expensive offline setup stage of the PBDW method gives adequate return on the investment during repeated online evaluations.

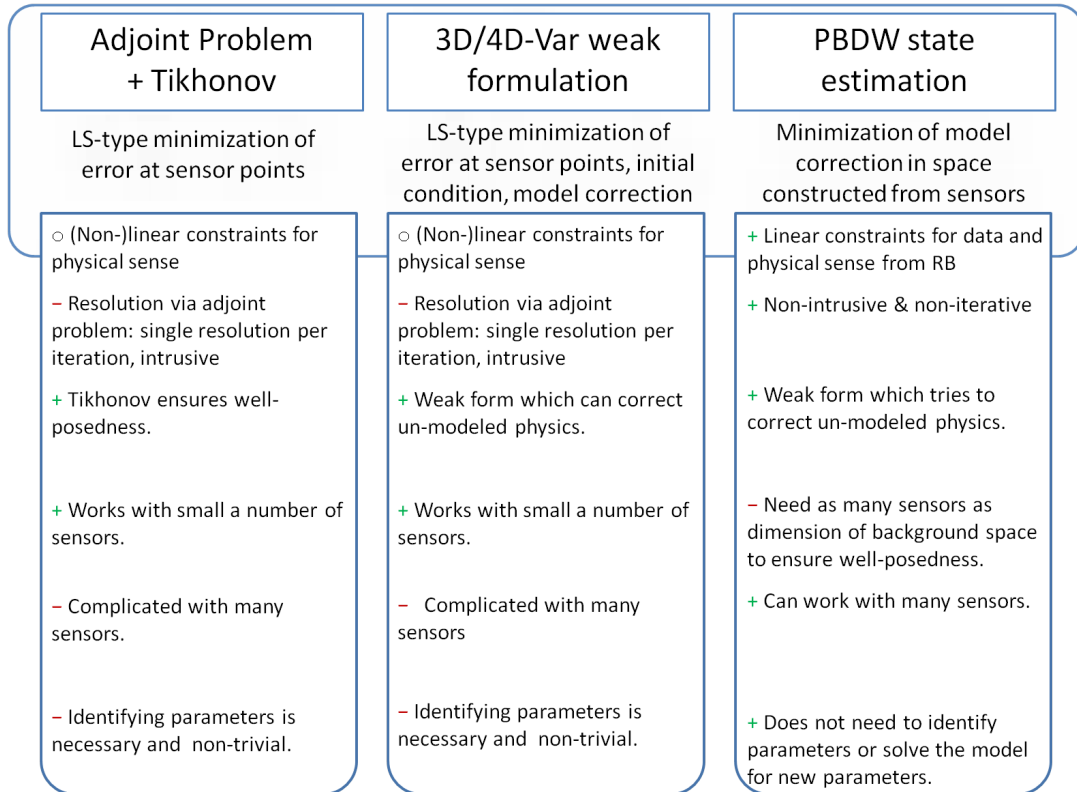


Figure 4.4 – Chart summarizing differences between the PBDW and classical inverse method by adjoint problem, as well as the weak constraint 4D-Var.

In figure 4.4 we summarize this comparison in a chart, and we add a brief comparison to the weak formulation of the 4D-Var method presented in section 2.2.4.2. We see similarities between both the adjoint and PBDW methods when compared to the weak constraint 4D-Var.

4.2 Pollutant Transport Modeling

As discussed in 1.2.2, we will consider CFD and CTM modeling of particle concentration for the application of RB and PBDW methods. The specific mathematical models considered for validation of the introduced methods are described below.

4.2.1 Wind field modeling for air quality studies

For increased accuracy of the chemical transport model, we chose to use wind fields simulated by CFD modeling. This can be coupled with transport equations, or decoupled from the transport phenomenon in practice and precalculated if the same wind field will serve for multiple transport simulations. Relatively low concentrations involved in air quality modeling do not have an impact on the velocity field.

In our studies, we chose to decouple the computation of the wind fields. We used *Code_Saturne*, a general purpose CFD software [8], for the CFD simulations. We first compute the relevant wind fields, then use the velocity and turbulent viscosity fields in the transport model.

The incompressible Navier-Stokes equations will be considered for the simulation of fluid flow:

Conservation of mass:

$$\frac{\partial \rho}{\partial t} + \text{div}(\rho \mathbf{v}) = 0 \quad (4.29)$$

Conservation of the quantity of movement:

$$\rho \left(\overbrace{\frac{\partial \mathbf{v}}{\partial t} + (\mathbf{v} \cdot \nabla) \mathbf{v}}^{\text{acceleration forces}} \right) + \underbrace{\nabla p - \nabla \cdot (\mu (\nabla \mathbf{v}^T + \nabla \mathbf{v}))}_{\text{interior forces}} = \mathbf{F}_e \quad (4.30)$$

where the interior forces include pressure forces and viscosity force, and \mathbf{F}_e represents exterior forces. $p(x, t)$ is the pressure, $\mathbf{v}(x, t)$ the velocity field, $\rho(x, t)$ the density, and μ the viscosity.

When incompressible flow is considered, $\rho(x, t)$ is constant in space and time and equation (4.29) becomes:

$$\frac{\partial \rho}{\partial t} + \text{div} \rho \mathbf{v} = \rho \text{div} \mathbf{v} = 0 \quad \Rightarrow \quad \text{div} \mathbf{v} = 0. \quad (4.31)$$

The stationary incompressible Navier-Stokes equations with the kinematic viscosity $\nu = \frac{\mu}{\rho}$ are written:

$$\begin{cases} -\nabla \cdot (\mu (\nabla \mathbf{v}^T + \nabla \mathbf{v}) + \mathbf{v} \cdot \nabla \mathbf{v} + \frac{1}{\rho} \nabla p) = 0 \\ \text{div}(\mathbf{v}) = 0. \end{cases} \quad (4.32)$$

The incompressible Navier-Stokes equations (4.31), in addition to suitable boundary conditions, will be the system of equations used for our fluid flow calculations. Turbulence will be modeled using RANS $k - \epsilon$ closure (see Turbulence in 1.2.2 for discussion) in *Code_Saturne*. We define a generic representation of the variables k and ϵ in the case of two-dimensional mean flow as follows [132]

$$\begin{cases} \frac{\partial k}{\partial t} + \mathbf{v} \cdot \nabla k - \frac{c_\nu}{2} \frac{k^2}{\epsilon} |\nabla \mathbf{v} + \nabla \mathbf{v}^T|^2 - \nabla \cdot (c_\nu \frac{k^2}{\epsilon} \nabla k) + \epsilon = 0 \\ \frac{\partial \epsilon}{\partial t} + \mathbf{v} \cdot \nabla \epsilon - \frac{c_1}{2} k |\nabla \mathbf{v} + \nabla \mathbf{v}^T|^2 - \nabla \cdot (c_\epsilon \frac{k^2}{\epsilon} \nabla \epsilon) + c_2 \frac{\epsilon^2}{k} = 0 \end{cases} \quad (4.33)$$

along with suitable boundary conditions (see [60, 132]), and with $c_\nu = 0.09$, $c_1 = 0.126$, $c_2 = 1.92$, $c_\epsilon = 0.07$. $k - \epsilon$ turbulence modeling in three dimensions can be done with an added production term created by gravity effects, as described in [60]. The turbulent viscosity variable is then described by

$$\nu_t = \rho c_\nu \frac{k^2}{\epsilon} \quad (4.34)$$

Below we will discuss some details specific to wind field modeling for air quality studies.

First we need a geometry which is large enough to provide a "buffer zone" around any obstacles. A standard rule is for the exterior obstacle of size L , one must leave $15L$ extra distance between the obstacle and the outlet boundary, and $5L$ between the obstacle and any other domain boundary. This is to avoid numerical implementation of boundary conditions such as a Neumann free outlet causing non-physical features in the wind field. We will note that it is computationally interesting to simulate decoupled transport on a reduced domain without the "buffer zone" needed for CFD simulations.

General consensus is that a vertical logarithmic (or exponential) velocity profile is appropriate on the inlet boundary (Dirichlet condition), of the form

$$\vec{U}_{in} = (0, u_y, 0) = (v_0 \ln(\frac{z + z_0}{z_0})x^*, v_0 \ln(\frac{z + z_0}{z_0})y^*, 0) \quad (4.35)$$

in direction $(x^*, y^*)^T$, where the constants v_0 and z_0 depend on the environment.

An exponential profile can be appropriate, of the form

$$v_0 z^\alpha \quad (4.36)$$

In practice $\alpha = 0.4$ provides a similar profile to equation (4.35).

In figure 4.6 we can see a representation of the 3D wind field calculated in *Code_Saturne*.

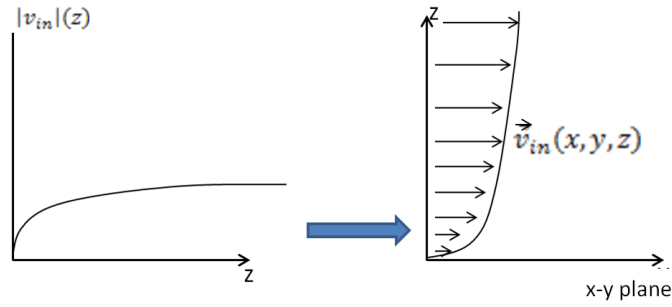


Figure 4.5 – Representation of wind field inflow profile: graph of $|v_{in}|(z)$ (left), 2D-view physical representation of the inflow boundary condition over a 3D domain (right).

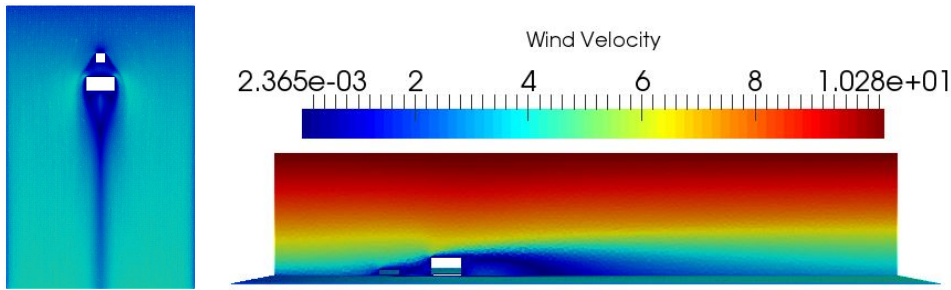


Figure 4.6 – Left: Section at $z = 1m$ of velocity field. Right: vertical section of velocity field showing vertical logarithmic flow profile.

Following standard practice, all open-air boundaries except explicitly outflow boundaries are set to this Dirichlet condition as "inlets" with $\|\vec{u}\|_2 = cz^\alpha$ and direction $(x^*, y^*)^T$.

For more information on the implementation of wind field simulation using *Code_Saturne*, refer to Appendix C.

4.2.2 Transport modeling for air quality studies

Here we consider the general details of transport modeling for pollutant concentration in the context of air quality modeling, and expose the specifics of implementation in exterior modeling.

As discussed in section 1.2.2, the advection-diffusion equation can represent pollutant transport in air or water. We consider first a model with terms for time-dependent transport, settling (a term dependent on particle size), diffusion (both molecular and turbulent), non-linear reaction, a pollutant source, and vegetation

deposition [19].

$$\begin{aligned}
 & \overbrace{\rho \frac{\partial c}{\partial t} + \underbrace{\nabla(\rho c \vec{v})}_{\text{convection}}}^{\text{transport}} - \overbrace{(\rho c v_s)_z}^{\text{settling}} = \nabla \cdot \left[\overbrace{(\epsilon_{mol} + \epsilon_{turb}) \nabla c}_{\text{diffusion}} \right] - \overbrace{[P(c) - D(c)]c}_{\text{reaction}} + \overbrace{\rho F_{src}}^{\text{source}} + \overbrace{s_w}_{\text{deposition}} \\
 & \hspace{20em} (4.37)
 \end{aligned}$$

v_s is the settling velocity of the particulate pollutant dependent on the diameter, given by the Stokes equation as described in [19], and parameters of velocity \vec{v} , turbulence $\epsilon_{tot} = \epsilon_{mol} + \epsilon_{turb}$, and pollutant source F_{src} .

Treatment of the source term F_{src} will be discussed in section 4.2.2.1.

The molecular diffusion $\epsilon_{mol} = \epsilon_{air}$ depends on the temperature; around $T = 22^\circ C$, $\epsilon_{air} \sim 1.72 \times 10^{-5} \frac{m^2}{s}$. Similarly for $\rho = \text{air density}$: $\rho(T) \sim 1.225 \frac{kg}{m^3}$

The total diffusion term $\epsilon_{tot} = \epsilon_{mol} + \epsilon_{turb}$ where ϵ_{turb} depends on ν_t , the turbulent viscosity and can be calculated using the Prandtl number:

$$\sigma_t \simeq \frac{\nu_t}{\epsilon_{turb}}, \quad (4.38)$$

which is often considered to have experimental values of $0.7 \leq \sigma_t \leq 1$. With a k- ϵ turbulence model in the fluid simulations, turbulent viscosity $\nu_t = 0.09 \rho \frac{k^2}{\epsilon}$, and with a k- ω turbulence model, $\nu_t = \rho \frac{k}{\omega}$ [13].

In our notation, we have $\epsilon_{turb} = \frac{\nu_t}{\sigma_t} := \frac{\nu_t}{0.7}$, where ν_t is a variable solved for in the velocity field simulations using *Code_Saturne*.

Let us note in table 4.1 the units associated to each term for a coherent transport model.

Transport model units		
Viscosity	dynamic μ ; dynamic turbulent μ_t	$Pa - s \sim \frac{kg}{m-s}$
	kinematic turbulent (eddy viscosity) ν_t	$\frac{\mu_t m^2}{\rho s}$
Density	ρ	$\frac{kg}{m^3}$
Diffusion	molecular ϵ	$\frac{m^2}{s}$
	turbulent (eddy) ϵ_{turb}	$\frac{\nu_t}{sc_t} = \frac{\mu_t m^2}{\rho sc_t s}$
Schmidt number	$sc = \frac{\text{viscous diff. rate}}{\text{molec. diff. rate}}$	dimensionless
	turbulent $sc_t = \frac{\nu_t}{\epsilon_{turb}}$	dimensionless
Concentration	c	$\frac{kg}{m^3}$
	Emissions rate $s(c) = s$	$\frac{kg}{m^3-s}$

Table 4.1 – Table summarizing units in equation (4.37).

We will also introduce a simplified model by neglecting the time-dependent, settling, reaction, and deposition terms, and using the velocity field \vec{v} from decoupled velocity-field simulations. Thus, considering a stationary equation, and recalling that the velocity field is such that $div(\vec{v}) = 0$, we have:

$$\left\{ \begin{array}{l} \overbrace{\rho \vec{v} \cdot \nabla c}^{\text{transport}} - \overbrace{div((\epsilon_{mol} + \epsilon_{turb}) \nabla c)}^{\text{diffusion}} = \overbrace{\rho F_{src}}^{\text{source}} \\ + \text{Boundary Conditions} \end{array} \right. \quad (4.39)$$

4.2.2.1 Boundary Conditions and Pollution Sources

Commonly used Neumann boundary conditions for transport are:

$$\epsilon_{turb} \nabla c \cdot \vec{n} = -\beta_a(c) \quad (4.40)$$

where β_a is a coefficient of absorption intensity.

More specifically, for the open-air boundaries of our exterior domain we will consider:

$$\left\{ \begin{array}{l} c = c_0 \quad \text{on } \Gamma_D = \{x \in \partial\Omega | \vec{v}(x) \cdot \vec{n} < 0\} \\ -\epsilon_{turb}(x) \frac{\partial c}{\partial z} = -\epsilon_{turb}(x) \nabla c \cdot \vec{n} = 0 \quad \text{on } \Gamma_N = \partial\Omega \setminus \Gamma_D \end{array} \right. \quad (4.41)$$

where ϵ_{turb} is the turbulent diffusion [52,180]. Γ_D is the (strict) inflow boundary, and Γ_N represents non-inflow boundaries.

The homogeneous Neumann condition on the non-inflow boundaries represents null diffusive flux, and can be interpreted as c being (locally) constant on the boundary; $c_{outside}|_{\partial\Omega} = c_{inside}|_{\partial\Omega}$. The Dirichlet condition on the (strict) inflow boundary can be interpreted as an entering pollutant concentration of c_0 . If we add background concentration as a uniform value, this boundary condition set to homogeneous Dirichlet could be appropriate, however a background concentration of c_0 could otherwise be treated as a constant or appropriately profiled inflow conditions and posed as a non-homogeneous Dirichlet condition.

To treat a pollutant source interior to the domain we have two options. We could consider the source in the right-hand-side of the equation as F_{src} using a characteristic function over a domain Ω_{src} (see 6 implementation and (4.43)) [52]:

$$F_{src} = \begin{cases} c_{src} & \Omega_{src} \\ 0 & \Omega \setminus \Omega_{src} \end{cases} \quad (4.42)$$

or we could consider the source as a non-homogeneous Neumann boundary condition in the case of ground-level sources.

In the case of a source representing a street, the domain Ω_{src} can be defined for example using a parabolic function of maximum height $1.5m$ in the $x-y-z$ domain to define the source region Ω_{st} by:

$$z \leq \frac{1.5}{r^2}(y - y_1)(y - y_2) \quad (4.43)$$

where the street is parallel to the x-axis, y_1 and y_2 are its boundaries, and $r = \left(\frac{1}{2}(y_2 - y_1)\right)$. This would be an alternative to non-homogeneous Neumann boundaries, representing that traffic pollution does not come directly from the street surface.

Otherwise, we could consider the source as a boundary condition with a non-homogeneous Neumann condition:

$$-\epsilon_{turb} \frac{\partial c}{\partial z} = F_N(x, t) - v_{dep}(x, t)c \quad (4.44)$$

where F_N is the surface source emission rate and v_{dep} is the dry deposition velocity of the pollutant considered, which depends on ground type [180].

In the variational form this translates to:

$$\begin{aligned} -\epsilon_{turb} \int_{\Omega} \Delta c d \, d\Omega &= \epsilon_{turb} \int_{\Omega} \nabla c \cdot \nabla d \, d\Omega - \int_{\partial\Omega} \epsilon_{turb} \frac{\partial c}{\partial n} d \, d\Gamma \\ &= \epsilon_{turb} \int_{\Omega} \nabla c \cdot \nabla d \, d\Omega + \int_{\partial\Omega_{st}} F_N(x, t) d \, d\Gamma \\ &\quad - \underbrace{\int_{\partial\Omega \setminus \partial\Omega_{st}} \epsilon_{turb} \frac{\partial c}{\partial n} d \, d\Gamma}_{=0} \end{aligned}$$

4.2.2.2 Finite Element Formulation

The variational form corresponding to equation (4.39) will be

$$a(c, d) = l(d) \quad \forall d \in V \quad (4.45)$$

where $V = \{c \in H^1(\Omega) | c|_{\Gamma_D} = c_0\} \subset H^1(\Omega)$, is the Hilbert approximation space and

$$\begin{cases} a(c, d) := \int_{\Omega} \left((\epsilon_{mol} + \epsilon_{turb}) \nabla c \cdot \nabla d + \nabla(\rho c \cdot \vec{v}) d \, d\Omega \right. \\ \left. l(d) := \int_{\Omega} \rho F_{src} d \, d\Omega \left[+ \overbrace{\int_{\Gamma_N} F_N d \, d\Gamma}^{\text{if non-hom. Neu.}} \right] \right. \end{cases} \quad (4.46)$$

where $a(r_{c_0}, d)$ is a lifting, and F_N represents an eventual non-homogeneous Neumann boundary condition.

We want to approximate the solution by the Finite Element (FE) Method, chosen for ease of implementation in FreeFem++. We consider a conforming triangularization over the calculation domain \mathcal{T}_h , consisting of triangles T_k for $1 \leq k \leq \mathcal{N}_T$ the number of triangles. h represents the step size of the mesh, locally noted h_k . We will note \mathcal{N}_h the number of degrees of freedom associated to the mesh for the chosen FE type. We define a discrete approximation space V_h , for example for \mathbb{P}^ℓ finite

elements $V_h = \{c \in V \mid c|_{T_k} \in \mathbb{P}^\ell(T_k) \forall 1 \leq k \leq \mathcal{N}_T\}$, and consider the associated FE basis functions $\{\xi_i\}_{i=1}^{\mathcal{N}_h}$.

We thus pose the discrete form of problem (4.39) as follows: find $c_h \in V_h$ such that

$$a(c_h, d_h) = l(d_h) \quad \forall d_h \in V_h, \quad (4.47)$$

where

$$\begin{cases} a(c_h, d_h) = \int_{\Omega_h} \left(\epsilon_{tot} \nabla c_h \cdot \nabla d_h + \nabla(\rho c_h \cdot \vec{v}) d_h \right) d\Omega_h \\ l(d_h) = \int_{\Omega_h} \rho F_{src} d_h d\Omega_h \\ \epsilon_{turb} \frac{\partial c}{\partial z} = \epsilon_{turb} \nabla c_h \cdot \vec{n} = 0 \quad \text{on } \Gamma_N = \partial\Omega_h \setminus \Gamma_D \end{cases} \quad (4.48)$$

It is well documented that a standard Galerkin finite element method is not optimal for some first-order problems [67] in that numerical instabilities can occur, and more particularly in the case of advection-dominated transport problems a stabilization is necessary in the resolution by finite elements to avoid non-physical instabilities. An indicator of the influence of advection is the Peclet number, which can be expressed locally (over the triangulation) as

$$Pe_k = \frac{h_k \|\vec{v}\|_{\infty, K}}{2\epsilon_{tot}}, \quad (4.49)$$

or globally (over the entire calculation domain Ω) as

$$Pe_\Omega = \frac{L_\Omega \|\vec{v}\|_{\infty, \Omega}}{\|\epsilon_{tot}\|_{\infty, \Omega}}, \quad (4.50)$$

for L_Ω representing a characteristic length of the domain.

Let us consider the Streamline Upwind Petrov-Galerkin (SUPG) stabilization scheme [28, 90].

We can define:

$$\begin{cases} a^{SUPG}(c_h, d_h) := a(c_h, d_h) + \sum_k \tau_k (\mathcal{L}c_h, \vec{v} \cdot \nabla d_h)_k \\ l^{SUPG}(d_h) := l(d_h) + \sum_k \tau_k (\rho F_{src}, \vec{v} \cdot \nabla d_h)_k \end{cases} \quad (4.51)$$

where $\mathcal{L}c_h = \rho \vec{v} \cdot \nabla c_h - \text{div}(\epsilon_{tot} \nabla c_h)$ and τ_k is a stabilization parameter over each element T_k in the triangulation over the domain Ω . The finite element formulation (4.47) will be replaced by: find $c_h \in V_h$ such that

$$a^{SUPG}(c_h, d_h) = l^{SUPG}(d_h) \quad \forall d_h \in V_h. \quad (4.52)$$

A common choice of τ_k is [143]:

$$\tau_k = \begin{cases} \frac{\delta h_k}{\|\vec{v}\|_k} & \text{if } Pe_k > 1 \text{ (convection-dominated)} \\ \frac{\delta h_k^2}{\epsilon_{tot}} & \text{if } Pe_k \leq 1 \text{ (diffusion-dominated)} \end{cases} \quad (4.53)$$

with h_k the step size of the K^{th} element of the mesh and δ variable [26, 71], where Pe_k is the local Peclet number. Three possibilities for δ were considered:

- $\delta = 0.5$: this is similar to the choice in [26, 71],
- $\delta = 1$: this increases the stabilization,
- $\delta = \frac{1}{2}(\coth(Pe_k) - \frac{1}{Pe_k}) \in \mathcal{P}_0$: used in [33].

However we found in practice that the following stabilization coefficient [26] provided more stable results:

$$\tau_k = \frac{1}{\frac{4\epsilon_{tot}}{h_k^2} + \frac{2\|\vec{v}\|_{\infty,K}}{h} + |s_k|} \quad (4.54)$$

where s_k is the source intensity on the K^{th} element. In fact, we noticed great instability near interior source terms, so a stabilization coefficient depending on source terms performs better.

Expanding, we have

$$\begin{aligned} a^{SUPG}(c_h, d_h) &= \int_{\Omega} (\epsilon_{mol} + \epsilon_{turb}) \nabla c_h \cdot \nabla d_h + (\rho \vec{v} \cdot \nabla c_h) d_h \\ &\quad + \sum_k \tau_k \int_k \left[-\operatorname{div} \left((\epsilon_{mol} + \epsilon_{turb}) \nabla c_h \right) + (\rho \vec{v} \cdot \nabla c_h) \right] \left[\vec{v} \cdot \nabla d_h \right] \\ &= a(c_h, d_h) + \int_{\Omega} \tau_k [-\nabla \epsilon_{tot} \cdot \nabla c_h - \epsilon_{tot} \Delta c_h + \rho \vec{v} \cdot \nabla c_h] [\vec{v} \cdot \nabla d_h] \end{aligned} \quad (4.55)$$

and (in the case of homogeneous boundary conditions)

$$l^{SUPG}(d_h) = \int_{\Omega} \rho F_{src} d_h + \sum_k \tau_k \int_k (\rho F_{src}) (\vec{v} \cdot \nabla d_h) \quad (4.56)$$

We note here that in practice, if the background concentration c_0 in equation (4.41) is null (i.e. a homogeneous Dirichlet boundary condition on the strict inflow boundaries), the stabilization scheme will have more difficulty rectifying instabilities near any interior sources, as in equation (4.42), due to increased gradient terms in the transport problem. We will see examples of this in section 6.

4.2.2.3 Dimensionless Transport Simulations

Here we will give a dimensionless formulation of the transport problem (4.39).

The dimensionless formulation can help scale the problem: if the values of certain terms vary significantly from others, the problem may have a large condition number and be difficult to solve numerically. Scaling the problem can make many terms be of the same order, minimizing numerical errors when calculating the residual.

Advection-diffusion problems being notoriously difficult to solve numerically, and our domains of study being relatively large, make this application an excellent candidate for study in dimensionless form.

We considered a dimensionless formulation for equation (4.39) similar to the one applied in [161].

We will consider $v_{max} = \|\vec{v}\|_\infty$, c_g is a characteristic or background concentration, L_g is a characteristic length of the domain (e.g. the width of the calculation domain), and $\epsilon_{min} = \min_{T_k \in \Omega} \epsilon_{tot}$ to a-dimensionalize the stationary convection-diffusion equation:

$$\rho \vec{v} \cdot \nabla c - \text{div}((\epsilon_m + \epsilon_t) \nabla c) = \rho F_{src} \quad (4.57)$$

$$v_{max} \frac{\vec{v}}{v_{max}} \cdot \frac{d}{L_g d \frac{x}{L_g}} \frac{c}{c_g} c_g - \frac{1}{\rho} \frac{d}{L_g d \frac{x}{L_g}} \left(\epsilon_{min} \frac{\epsilon_t + \epsilon_m}{\epsilon_{min}} \frac{d}{L_g d \frac{x}{L_g}} \frac{c}{c_g} c_g \right) = c_g \frac{F_{src}}{c_g} \quad (4.58)$$

$$\frac{c_g v_{max}}{L_g} \tilde{v} \cdot \tilde{\nabla} \tilde{c} - \frac{1}{\rho} \frac{c_g \epsilon_{min}}{L_g^2} \tilde{\text{div}} \left(\tilde{\epsilon}_{tot} \tilde{\nabla} \tilde{c} \right) = c_g \tilde{F}_{src} \quad (4.59)$$

where $\tilde{v} = \frac{\vec{v}}{v_{max}}$, $\tilde{c} = \frac{c}{c_g}$, $\tilde{F}_{src} = \frac{F_{src}}{c_g}$, $\tilde{x} = \frac{x}{L_g}$ and $\tilde{\text{div}}$ or $\tilde{\nabla}$ represent $\frac{d}{L_g d \frac{x}{L_g}} = \frac{1}{L_g} \frac{d}{d\tilde{x}}$. We can then simplify to write:

$$\frac{L_g v_{max}}{\epsilon_{min}} \tilde{v} \cdot \tilde{\nabla} \tilde{c} - \frac{1}{\rho} \tilde{\text{div}} \left(\tilde{\epsilon}_{tot} \tilde{\nabla} \tilde{c} \right) = \frac{L_g^2}{\epsilon_{min}} \tilde{F}_{src} \quad (4.60)$$

We note that $\frac{L_g v_{max}}{\epsilon_{min}} = Pe_{max}$ represents a form of a global Peclet number. In dimensionless formulations, dimensionless quantities of the problem become more evident. In the case of transport problems, the global Peclet number, becomes a coefficient in the equation, giving insight into which mechanism is dominant, advection or diffusion.

We thus find the general dimensionless form:

$$\vec{V} \cdot \nabla c - \frac{1}{\rho} \nabla \cdot (E \nabla c) = S \quad (4.61)$$

with $\vec{V} = Pe_{max} \tilde{v}$, $E = \tilde{\epsilon}_{tot}$, and $S = \frac{L_g^2}{\epsilon_{min}} \tilde{F}_{src}$.

We then need to transform our calculation domain according to the adimensionalizing parameter L_g to build the dimensionless formulation domain Ω_0 . The simplest way to do this is a linear transformation:

$$(x, y, z)_{\Omega_0} = \left(\frac{x_\Omega}{L_g}, \frac{y_\Omega}{L_g}, \frac{z_\Omega}{L_g} \right) \quad (4.62)$$

We illustrate this in figure 4.7 on a two-dimensional domain (used in section 5.1). This transformation can be applied to a mesh built on the original domain Ω .

We then consider our basic approximation space to be $V(\Omega_0)$.

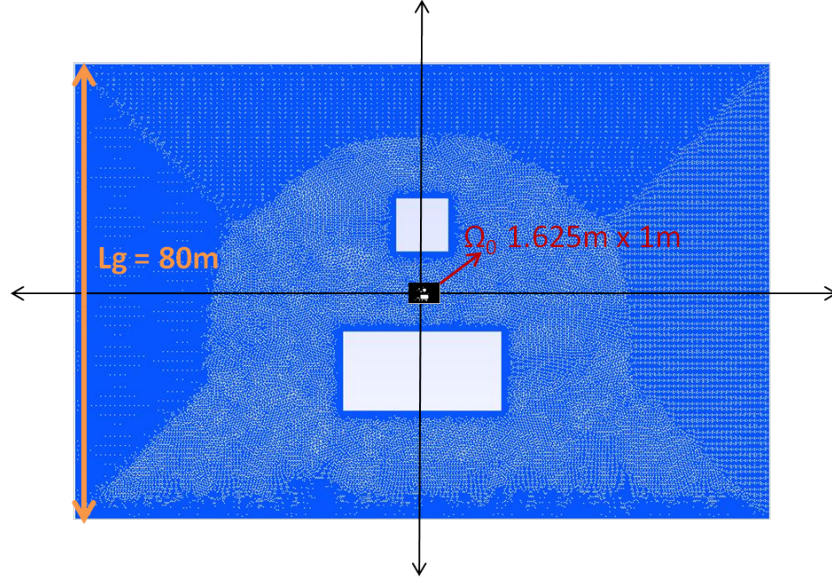


Figure 4.7 – Illustration of domain transformation for the dimensionless formulation on a two-dimensional example which has already been meshed.

The boundary conditions may also need to be in dimensionless form. In the case of a concentration imposed by non-homogeneous Dirichlet conditions (e.g. for exterior concentration in the case of interior air quality modeling, or background concentration in the case of exterior air quality modeling), we have:

$$c = c_0 \quad \text{on } \partial\Omega_{in} \quad (4.63)$$

$$c_g \frac{c}{c_g} = c_0 \quad \text{on } (\partial\Omega_0)_{in} \quad (4.64)$$

$$\tilde{c} = \frac{c_0}{c_g} \quad \text{on } (\partial\Omega_0)_{in} \quad (4.65)$$

and we can set $\tilde{c}_0 = \frac{c_0}{c_g}$.

In the case of a flux imposed by non-homogeneous Neumann conditions, as in equation (4.44), we have:

$$\begin{aligned} \epsilon_{min} \frac{-\epsilon_{turb}}{\epsilon_{min}} \frac{d}{L_g d \frac{x}{L_g}} \left(c_g \frac{c}{c_g} \right) \cdot \vec{n}_z &= c_g \frac{F_N}{c_g} \\ -E_{turb} \nabla c \cdot \vec{n}_z &= S_N \end{aligned} \quad (4.66)$$

where E and ∇c correspond to the general dimensionless form in equation (4.61), and $S_N = \frac{F_N}{c_g \epsilon_{min}}$.

Our variational formulation of (4.61) reads as follows: find $c \in V$ such that

$$a_g(c, d) = l_g(d) \quad \forall d \in V, \quad (4.67)$$

where

$$a_g(c, d) = \int_{\Omega_0} (\vec{V} \cdot \nabla c) d + \frac{1}{\rho} \int_{\Omega_0} E \nabla c \cdot \nabla d + \int_{\Omega_0} \tau_k \left(\vec{V} \cdot \nabla c - \frac{1}{\rho} \Delta(Ec) \right) (\vec{V} \cdot \nabla d) \quad (4.68)$$

$$\ell_g(d) = \int_{\Omega_0} S d + \int_{\Omega_0} \tau_k(S) (\vec{V} \cdot \nabla d) \left[+ \overbrace{\int_{\Gamma_N} S_N d \, d\Gamma}^{\text{if non-hom. Neu.}} - \underbrace{a_g(r_{\tilde{c}_0}, d)}_{\text{if non-hom. Dir.}} \right] \quad (4.69)$$

4.2.3 Advection-Diffusion-Reaction

We will discuss briefly here a modification to equation (4.39) to account for reaction phenomena. In the interest of a simple modification, we will treat the reaction term linearly for a known coefficient R representing a sum of the production and destruction terms in equation (4.37). This model will be used in chapters 5, 6, and 7 as a shifted model \mathcal{P}^{trial} to simulate model error in numerical tests of PBDW state estimation.

$$\rho \vec{v} \cdot \nabla c - \text{div}((\epsilon_{mol} + \epsilon_{turb}) \nabla c) + \rho R c = \rho F_{src} \quad (4.70)$$

In dimensionless formulation this gives us:

$$\frac{c_g v_{max}}{L_g} \tilde{v} \cdot \tilde{\nabla} \tilde{c} - \frac{1}{\rho} \frac{c_g \epsilon_{min}}{L_g^2} \tilde{\text{div}}(\tilde{\epsilon}_{tot} \tilde{\nabla} \tilde{c}) + c_g R \tilde{c} = c_g \tilde{F}_{src} \quad (4.71)$$

$$\frac{L_g v_{max}}{\epsilon_{min}} \tilde{v} \cdot \tilde{\nabla} \tilde{c} - \frac{1}{\rho} \tilde{\text{div}}(\tilde{\epsilon}_{tot} \tilde{\nabla} \tilde{c}) \frac{L_g^2}{\epsilon_{min}} R \tilde{c} = \frac{L_g^2}{\epsilon_{min}} \tilde{F}_{src} \quad (4.72)$$

Simplifying we have:

$$\vec{V} \cdot \nabla c - \Delta(Ec) + \tilde{R}c = S \quad (4.73)$$

where with $\vec{V} = P e_{max} \tilde{v}$, $E = \frac{1}{\rho} \tilde{\epsilon}_{tot}$, $\tilde{R} = \frac{L_g^2}{\epsilon_{min}} R$, and $S = \frac{L_g^2}{\epsilon_{min}} \tilde{F}_{src}$.

In variational formulation with homogeneous boundary conditions, adding the SUPG stabilization, we have:

$$\begin{aligned} \int_{\Omega_0} (\vec{V} \cdot \nabla c) d + \frac{1}{\rho} \int_{\Omega_0} E \nabla c \cdot \nabla d + \int_{\Omega_0} (\tilde{R} c d) + \int_{\Omega_0} \tau_k \left(\vec{V} \cdot \nabla c - \frac{1}{\rho} \Delta(Ec) + \tilde{R}c \right) (\vec{V} \cdot \nabla d) \\ = \int_{\Omega_0} S d + \int_{\Omega_0} \tau_k(S) (\vec{V} \cdot \nabla d) \end{aligned} \quad (4.74)$$

Part III

Numerical Results: RB and PBDW

Chapter 5

Application and Analysis in Exterior Air Quality Modeling: a 2D Case Study

Résumé :

Ce chapitre est consacré à la mise en place et l'étude numérique de la PBDW sur un problème bi-dimensionnel. Ce cas d'étude consiste en un site de $75\text{ m} \times 120\text{ m}$ qui comprend une maison, un bâtiment et une aire de jeu à proximité d'une route. On s'intéresse à la concentration de particules fines $PM_{2.5}$ provenant du trafic de la rue. La direction de vent sur le bord du domaine est fixe et connue. Les paramètres qui peuvent varier dans notre modèle sont l'intensité de la vitesse sur le bord du domaine et celle des émissions de polluant. Le champ de vitesse \vec{v} et la diffusion ϵ_{turb} sont solutions des equations de Navier-Stokes couplés et du modèle de turbulence $k - \epsilon$.

On étudie la stabilité et la convergence de la méthode en fonction du positionnement (optimal ou au hasard) des capteurs de concentration et du choix de la norme utilisée dans la formulation PBDW. La méthode PBDW est ensuite comparée à la méthode d'interpolation GEIM. Pour chacune des deux méthodes, nous étudions leur capacité à reconstruire correctement une carte de concentration à partir de mesures en prenant en compte i) l'erreur due à la variabilité paramétrique, ii) l'erreur de modèle. On remarque que dans le cas sans erreur de modèle, la GEIM est la plus performante. Par contre dans le cas d'erreur de modèle plus significative, la PBDW est plus performante.

Pour finir, une comparaison est faite avec une méthode inverse de type problème adjointe. Dans cette comparaison le champ de vitesse est solution des equations de Stokes et la diffusion est fixe.

5.1 Introduction to the Numerical Case Study

In this chapter we consider a simple case study in outdoor air quality modeling with our advection-diffusion model \mathcal{P}^{bk} given by (4.39). Below we give the practical considerations for these case studies, including the realistic choice of parameters based on air pollutant reports.

We consider the discrete finite element space V_h defined in section 4.2.2.2 over our calculation domain Ω .

5.1.1 Velocity Field

We first compute a wind field as described in section 4.2.1 using *Code_Saturne*.

In order to employ steady-state transport models on a pre-computed wind field, we chose to use aggregated CFD simulations to create a quasi-steady velocity field over N time steps of an unsteady fluid simulation which has reached a stationary state, denoted as discrete velocity solutions $u_h(t_n, \cdot)$ and viscosity solutions $\nu_h(t_n, \cdot)$. We can compute a single average solution for the wind field:

$$\bar{u}_h(\cdot) = \frac{1}{N} \sum_{n=1}^N u_h(t_n, \cdot) \quad (5.1)$$

Similarly we compute an average viscosity, $\bar{\nu}_t = \frac{1}{N} \sum_{n=1}^N \nu(t_n)$.

We will note that since *Code_Saturne* is a finite volume based software, the solutions u_h and ν_h are initially constant by element. The velocity and viscosity fields can be kept as constant-by-element functions (to be considered \mathbb{P}_0 FEM functions in *FreeFem++*) for use in calculating $\|\bar{u}\|_{\infty, K}$. This avoids adding additional interpolation error in converting to \mathbb{P}_1 or \mathbb{P}_2 FEM functions.

5.1.2 Parameters

The first study domain considered in chapters 5.1 and 6 represents a neighborhood with a house, an apartment building, and pollution sources of a street or various combustion sources. These choices were made to give a simplified case study representing a residential area with major pollution sources of traffic and wood burning.

In the interest of coherence with application over Fresno exposed in chapter 7, we would like to consider the transport of $PM_{2.5}$, and therefore consider main sources to be traffic and combustion (e.g. wood fires).

The choice of source intensity parameters should represent emissions from wood or charcoal burning.

For combustion sources interior to the calculation domain, we treat them as functions of the form presented in equation (4.42).

For wood fire sources [85] we found that a household oak fire burning at a rate of $\sim 3 \frac{kg}{hr}$ ($3kg$ of wood per hour) emits approximately $48 \frac{g}{h}$ in $PM_{2.5}$. This was taken as a general order of magnitude to inform the combustion source intensities c_{src} . We need to convert the total emissions rate $E_{src} \frac{g}{h}$ to an appropriate source intensity

in $\frac{kg}{m^3 \cdot s}$, using the fact that $c_{src} = \frac{1}{|\Omega_{src}|} E_{src}$, where Ω_{src} is the emission domain. If we consider that the combustion source is of size $50cm$ -cubed, so $|\Omega_{src}| = \frac{1}{8}m^3$ (an approximate, albeit exaggerated, representation of a home fire combustion source), then we have $c_{src} = 8E_{src}$. If we set $E_{src}^{fire} = 48 \frac{g}{hr}$, we have $c_{src} = 1.07e^{-4} \frac{kg}{m^3 \cdot s}$.

To cover the case of a significantly larger or more polluting fire, we will consider $c_{src} \in [0; 4]e^{-4} \frac{kg}{m^3 \cdot s}$. This is an order of magnitude used in initial case studies considering wood-fire combustion sources for exterior air quality modeling.

In the case of a three-dimensional combustion source treated as an area source (as opposed to a point source), with $|\Omega_{src}^{st}| = 25m^3$, we set $c_{src} = 5.32e^{-7} \frac{kg}{m^3 \cdot s}$ and a range of $[1e^{-7}; 1e^{-6}]$.

We then need to determine orders of magnitude for a residential street source. We considered an EPA report [188]. A summary of the data in the report which is taken into consideration for our purposes can be found in table 5.1.

Temperature - Vehicle Speed	Vehicle Category	Emission Types	Retained Emissions Factor
40mph - 22°C	2.2 ton mean weight	$PM_{10} \frac{g}{\sqrt{K\bar{T}}}$ of which $PM_{2.5} = 27\% - 34\%$	$PM_{2.5} = [0.08, 0.1] \frac{g}{\sqrt{K\bar{T}}}$
45mph - 20°C	2.2 ton mean weight	$PM_{10} \frac{g}{\sqrt{K\bar{T}}}$ of which $PM_{2.5} = 44\%$	$PM_{2.5} = 0.86 \frac{g}{\sqrt{K\bar{T}}}$
45mph - 20°C	2.2 ton mean weight - fleet average	$PM_{2.5}$ from exhaust, brake-wear, tire-wear	$PM_{2.5} = 0.1 \frac{g}{\sqrt{K\bar{T}}}$
45mph - 20°C	light duty	$PM_{2.5}$	$PM_{2.5} = [0.0425; 0.115] \frac{g}{\sqrt{K\bar{T}}}$
20mph	3.1 tons - 0.054 heavy-duty vehicle fraction	PM_{10} engine/braking/tire	$0.091 PM_{10} \frac{g}{\sqrt{K\bar{T}}}$
45mph	2.2 tons - 0.017 heavy-duty vehicle fraction	PM_{10} engine/braking/tire	$0.021 PM_{10} \frac{g}{\sqrt{K\bar{T}}}$

Table 5.1 – Table summarizing data used from [188]: general information from various tables in the document.

An initial order of magnitude for traffic emissions of EC (or $PM_{2.5}$) will be $E_{src}^{traffic} \in [0.02; 0.86] \frac{g}{\sqrt{K\bar{T}}}$.

To determine source emission rate in $\frac{kg}{s}$ we need to estimate VKT (vehicle kilometers traveled) on a small city road. For lack of easily accessible data on Fresno, we considered a document on the city of Calgary (Canada) [45]. Table 7 of [45] gives us 2009 daily VKT for skeletal roads over a $20km$ stretch. The estimated weekday $24h$ aggregated VKT is 137,000. We will neglect night-time traffic (considering most traffic is during daytime), and take this as a $12h$ average, we can consider this

implies an average of 685VKT per 100m stretch over 12h, then we have an average of $0.016 \frac{\text{VKT}}{s}$. Let us (somewhat arbitrarily) consider $\text{VKT}/s \in [0.01, 0.1]$ over a 100m stretch, giving a highly generalized, very broad estimate on a $100m \times 5m$ road, then we will have a street emission rate

$$E_{src}^{\text{street}} \in [2 \times 10^{-7}; 8.6 \times 10^{-5}] \frac{kg}{s}$$

and

$$c_{src}^{\text{street}} \in [4 \times 10^{-10}; 1.72 \times 10^{-7}] \frac{kg}{m^2 s}$$

since $|\Omega|_{src}^{\text{street}} = 500m^2$. In our study we will take $c_{src}^{\text{street}} \in [0; 2 \times 10^{-7}] \frac{kg}{m^2 s}$.

We also need to estimate a background concentration: clearly not all pollutants in a given area come from sources within that area. We consider that, excluding the case of a significant pollutant source just outside the domain of interest, a relatively uniform background concentration will already cover the area. We implement this with the non-homogeneous Dirichlet condition in equation (4.41). To determine an appropriate value of c_0 , we use average ambient concentrations of $PM_{2.5}$ posted by the U.S. EPA (www3.epa.gov) for the Western U.S. of the order $1 \times 10^{-8} \frac{kg}{m^3}$. At a smaller scale, we have LUR model predictions of EC over Fresno provided by Dr. Noth [138], ranging from $[3.23; 5.6] \times 10^{-9} \frac{kg}{m^3}$.

5.1.3 2D Case Study

We consider first a simple two-dimensional domain of study of dimensions $75m \times 120m$ seen in Figure 5.1, and chose a particulate pollutant, $PM_{2.5}$, which on the short term can be considered to have negligible reaction.

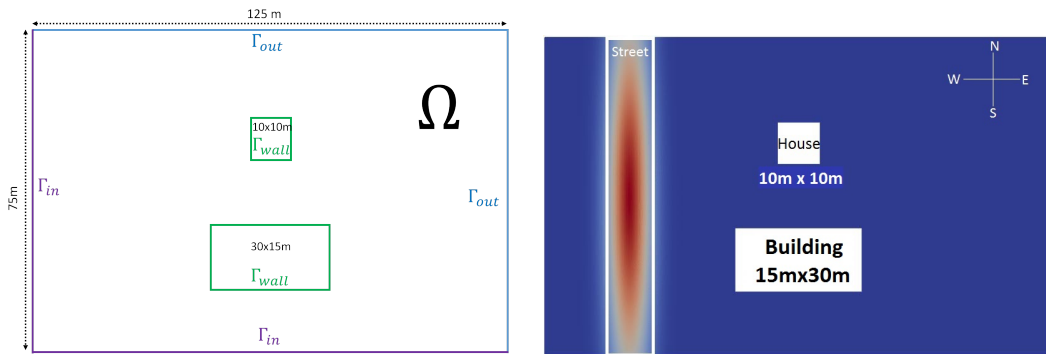


Figure 5.1 – 2D test domain with boundaries corresponding to the velocity field (left) and traffic pollution source (right).

Here the inlet boundaries Γ_{in} correspond to Γ_D from equation (4.41), and outlet boundaries Γ_{out} correspond to Γ_N . We take wind velocity (in a fixed direction $(1, 1)^T$) and pollutant source intensity as varying parameters $(\mathbf{p}_v, \mathbf{p}_s)$ in the best-knowledge parameter space $\mathcal{D}^{bk} \subset \mathcal{D}$, where the parameter space \mathcal{D} here represents the inputs to the problem: the wind fields \vec{v} and the source term F_{src} .

Wind velocities span the *calm* and *light air* categories of the Beaufort scale (from $0.1 \frac{m}{s}$ to $1.3 \frac{m}{s}$) and source intensity represents varying traffic, from $1 \times 10^{-3} \frac{mg}{m^3 s}$ to $1 \times 10^{-2} \frac{mg}{m^3 s}$. $\mathcal{D}^{bk} = \{(\mathbf{p}_v, \mathbf{p}_s) \in [0.1; 1.3 \frac{m}{s}] \times [0.1; 0.3 \frac{mg}{m^3}]\}$.

In this case study we chose to represent the source term not as a boundary condition, but as a source function

$$f_{src} = \exp\left(-\left(\frac{(x-x_c)^2}{r_x^2} + \frac{(y-y_c)^2}{r_y^2}\right)\right); \quad (5.2)$$

where (x_c, y_c) represents the center of the source domain, and r_x and r_y represent the radius in the x - and y - directions, respectively.

In figure 5.2 we can see concentration fields for lowest and highest wind velocity and emission rates, along with vectors representing the velocity fields.

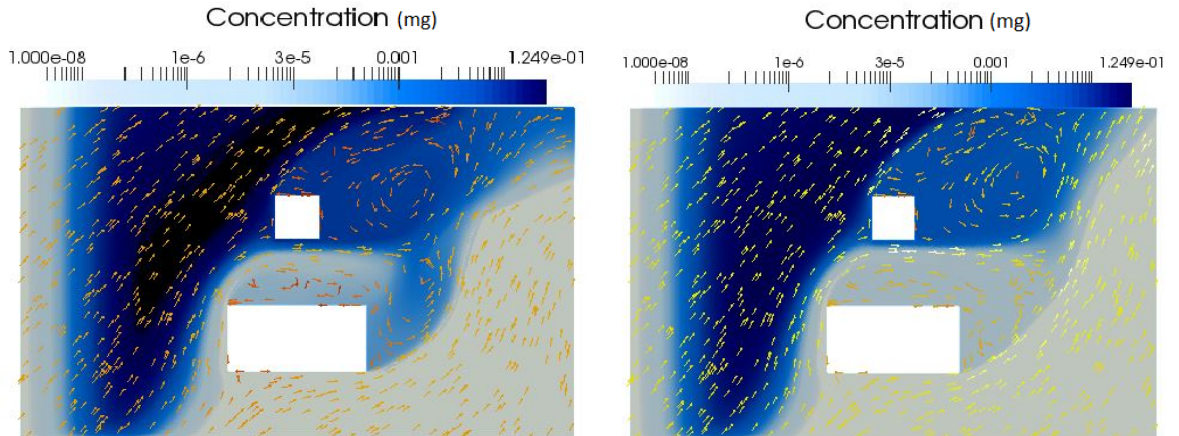


Figure 5.2 – Concentration solution (logarithmic scale) over velocity field with $(\mathbf{p}_v, \mathbf{p}_s) = (0.1 \frac{m}{s}, 1 \times 10^{-3} \frac{mg}{m^3})$ (left), and $(\mathbf{p}_v, \mathbf{p}_s) = (1.3 \frac{m}{s}, 1 \times 10^{-2} \frac{mg}{m^3})$ (right).

POD Analysis We began by studying the dimension of the solution manifold: we calculated a large *training* set of solutions to \mathcal{P}^{bk} for $\mathbf{p} \in \mathcal{D}^{bk}$, and constructed a POD basis (refer to section 2.1.2.2) of the concentration fields over the 2D domain. To do this we varied the intensity of the wind from $0.1 \frac{m}{s}$ to $1.3 \frac{m}{s}$ and fixed the intensity of the source at $10^{-2} \frac{mg}{m^3 s}$. The concentration depends linearly on the intensity of the source, meaning this parameter of the model does not need to be varied in the construction of a reduced basis.

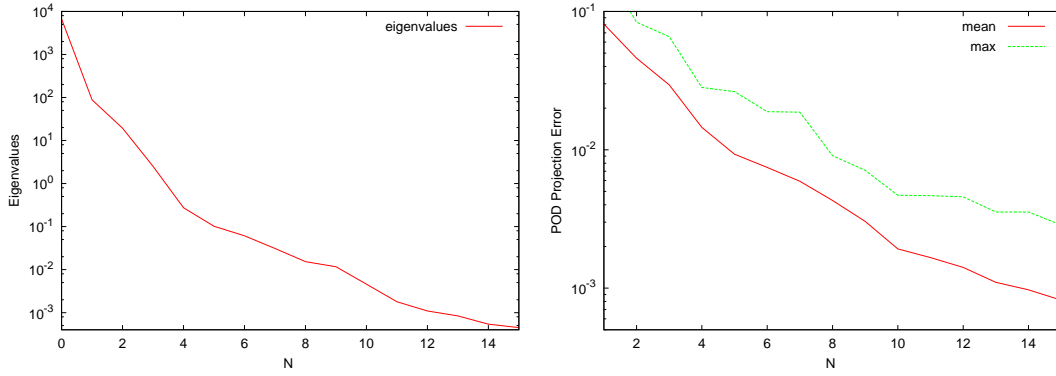


Figure 5.3 – Eigenvalues of the POD mass matrix \mathbf{M} (2.9) (left) ; Relative L^2 -norm POD projection (2.11) errors for pollutant concentration simulations (right)

Figure 5.3 shows the POD analysis of the concentration fields in the *training* set to study the feasibility of reduced basis methods on our model \mathcal{P}^{bk} . We show the rapid decay of the eigenvalues of the mass matrix associated to the solutions for $\mathbf{p} \in \mathcal{D}^{bk}$, and the maximal and mean relative projection errors of the concentration solutions onto the space spanned by the POD reduced basis.

5.2 Implementation of the PBDW method

The goal of this application is to serve as an initial test of the feasibility of the PBDW method in the air quality context. In the interest of coherence with real-world air quality studies, we thus want to consider a relatively small number of sensors over the domain (we'll consider up to 20) and test various sensor locations. We will consider PBDW results in the (academic) case of a perfect best-knowledge model, and in the case of unmodeled physics such as a reaction term or a true solution calculated with a different computational model.

5.2.1 Background RB space

The construction of a RB background space \mathcal{Z}_N for the 2D case study was done using the weak Greedy algorithm in the H^1 -norm (see algorithm 3 with $\mathcal{X} = H^1(\Omega)$) on a training set of dimension N_{train} of particular solutions for varying wind velocity parameters $\mathbf{p}_v \in \Xi_{train}^{bk}$, in the parameter set $\mathcal{D}^{bk} = \{\mathbf{p}_v \in [0.1; 1.3 \frac{m}{s}]\}$ and a fixed source intensity of $\mathbf{p}_s = 10^{-2} \frac{mg}{m^3 s}$.

A sign of a good reduced basis and small Kolmogorov n-width is rapid decay of projection errors of these training solutions onto the N -dimensional RB space. We denote $\Pi_{\mathcal{Z}_N}^1$ the H^1 -projection operator (corresponding to equation (4.24)) such that for all $f \in H^1(\Omega)$

$$\Pi_{\mathcal{Z}_N}^1 f = \sum_{k=1}^N \langle f, \zeta_k \rangle_{H^1} \zeta_k, \quad (5.3)$$

where $(\zeta_k)_{1 \leq k \leq N}$ are H^1 -orthonormal basis functions of \mathcal{Z}_N , and $E_N(c(\mathbf{p}))$ the projection error as defined in equation (4.25).

We want to represent the small Kolmogorov n -width of the solution manifold for \mathcal{D}^{bk} by studying the mean and maximal projection errors $E_N(c(\mathbf{p}_i))$, equations (4.26) and (4.27) respectively, of the training set of N_{train} solutions onto the N -dimensional RB spaces during the Greedy construction of the RB background space \mathcal{Z}_N . Relative projection errors over the calculation domain,

$$E_N^\Omega(c^{bk}(\mathbf{p}_i)) = \frac{|E_N(c^{bk}(\mathbf{p}))|}{\|c^{bk}(\mathbf{p}_i)\|_{L^\infty}} \in \mathcal{X}_h, \quad (5.4)$$

corresponding to a pointwise error on the calculation mesh, will be used to plot projection error maps spatially. In figure 5.4 we see the mean and maximal relative projection errors in H^1 norm as a function of N , given by equations (4.26) and (4.27).

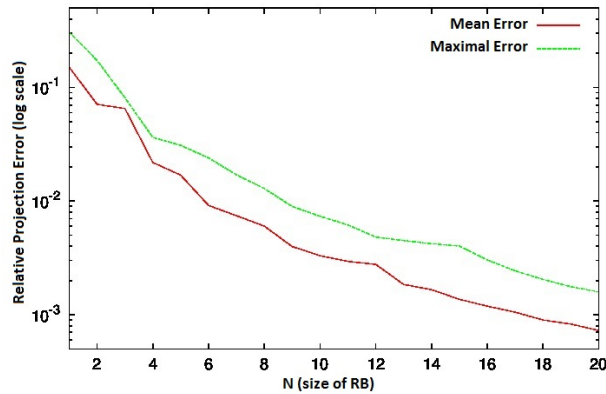


Figure 5.4 – Relative mean and maximal projection errors in H^1 norm, equations (4.26) and (4.27) respectively, during the greedy construction of the RB space \mathcal{Z}_N , as a function of N .

In figure 5.5 we see mean relative errors over the domain, as in equation (5.4), for $N = 1$ (top left), $N = 5$ (top right), $N = 10$ (bottom left), and $N = 15$ (bottom right).

We can see that the discretization error of the RB background space rapidly converges to under 1%. Given the complexity of reducing convection-dominated problems, we consider this wholly satisfactory. In addition, in air quality applications, model input errors are commonly much larger, in the range of 30 – 70% if not higher, as seen in section 1.2.3 ; an additional 1% error (with respect to the best-knowledge model) from the dimensional reduction of the approximation space

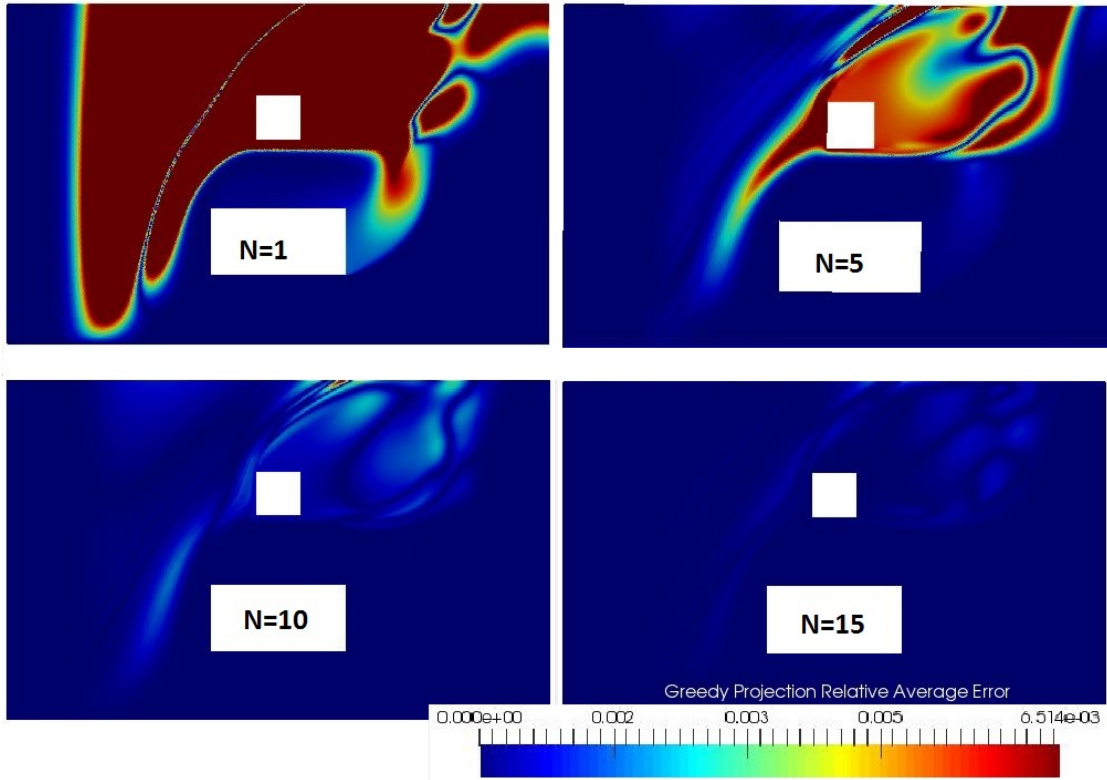


Figure 5.5 – Mean projection error over domain Ω , equation (5.4), during the greedy construction of the RB space \mathcal{Z}_N , for $N = 1$ (top left), $N = 5$ (top right), $N = 10$ (bottom left), $N = 15$ (bottom right).

from a finite element space to a RB space would thus be considered negligible. We will note from the RB discretization error maps over the domain, that for RB dimension $N \geq 10$, we have nearly eliminated the error, excepting small but unavoidable "shocks" from varying convection fields.

5.2.2 Sensor locations and Update Space

We will compare two cases of sensor locations in these case studies: the case of sensor locations chosen randomly, and the case of sensor locations chosen simultaneously with the background RB space generation particular solutions by a weak Greedy method.

In figure 5.6 we can see a set of sensor locations chosen randomly in 2D. The PBDW system was constructed from equation (3.14) using the RB background space discussed in section 5.2.1 and an Update space built from these sensor locations.

In figure 5.7 we can see the set Σ of possible sensor locations chosen for this application and those selected by a greedy algorithm minimizing the GEIM interpolation error, as described in section 4.1.2.1.

In figure 5.8 we see the values of the stability constant $\beta_{N,M}$ from equation (3.17), with $\|\cdot\|_{\mathcal{X}} = \|\cdot\|_{H^1}$, for various N -values as a function of M , comparing the PBDW

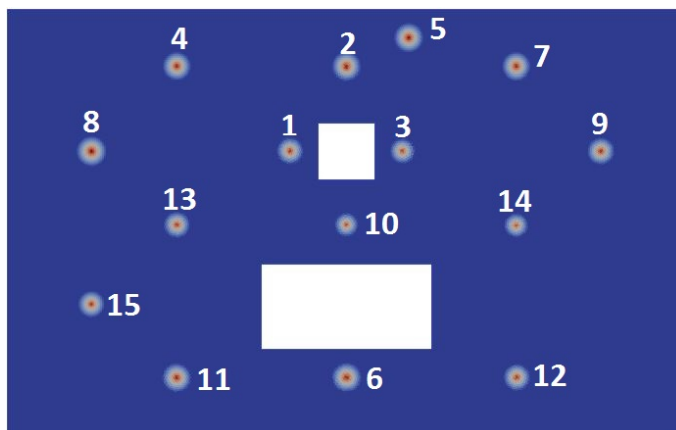


Figure 5.6 – Sensor locations chosen randomly.

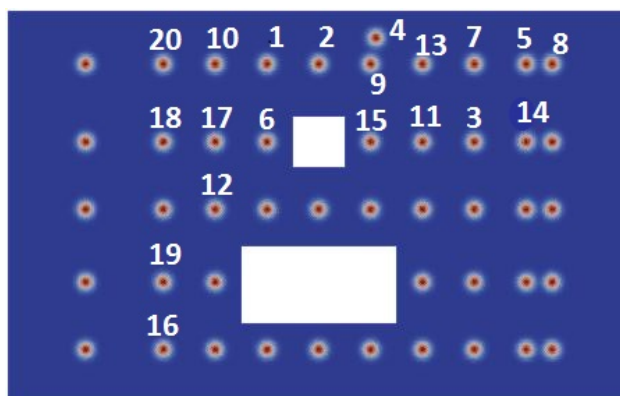


Figure 5.7 – Sensor locations chosen by a GEIM-based greedy algorithm (section section 4.1.2.1).

system corresponding to random sensor locations from figure 5.6 and greedily-placed sensors in figure 5.7.

As $\beta_{N,M}$ is a non-decreasing function of M , we see improvement in the stability constants for larger numbers of data points, for each fixed background RB dimension N . We note that in general for $N \simeq M$ the formulation is less stable, as evidenced by very low values of $\beta_{N,M}$ and discussed in [114]. Given this knowledge, we can make the choice to disregard PBDW results for $N \simeq M$ (as we will see in section 5.3). If we compare the stability constants in figure 5.8 for randomly chosen sensor locations (left) to those for sensor locations chosen by a greedy algorithm (right), we can see that in the 2D case we've improved by up to $\mathcal{O}(10^5)$ for some M and N values, and at least by a factor of 2 for smaller background dimensions.

In figure 5.9 we can see the values of the condition numbers of the PBDW matrices, for $N = 5, 6, 8,$ and 12 as a function of M , with $\|\cdot\|_{\mathcal{X}} = \|\cdot\|_{H^1}$, comparing the PBDW system corresponding to random sensor locations from figure 5.6 and greedily-placed sensors in figure 5.7.

If we compare the condition numbers in figure 5.9 for randomly chosen sensor

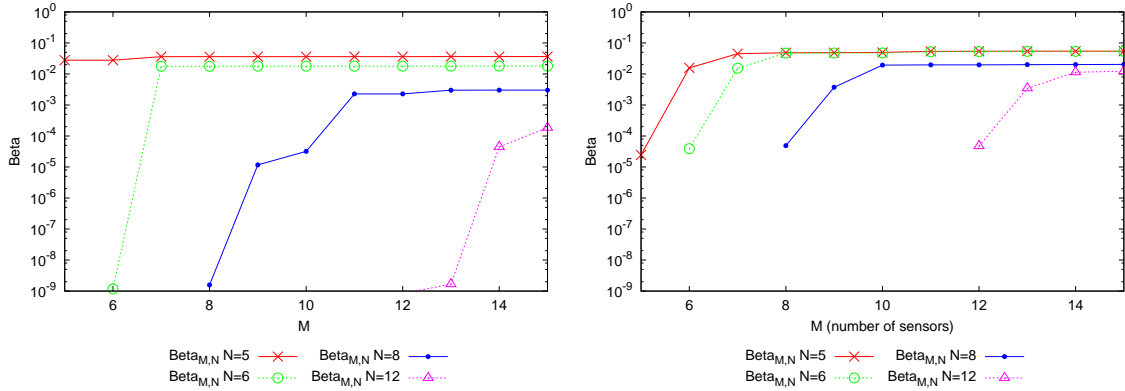


Figure 5.8 – Stability constant $\beta_{N,M}$ (3.17) with $\|\cdot\|_{\mathcal{X}} = \|\cdot\|_{H^1}$, as a function of M for $N = 5, 6, 8, 12$. PBDW system corresponding to sensor locations in figure 5.6(left) ; PBDW system corresponding to sensor locations chosen by a GEIM-based greedy algorithm (section 4.1.2.1).

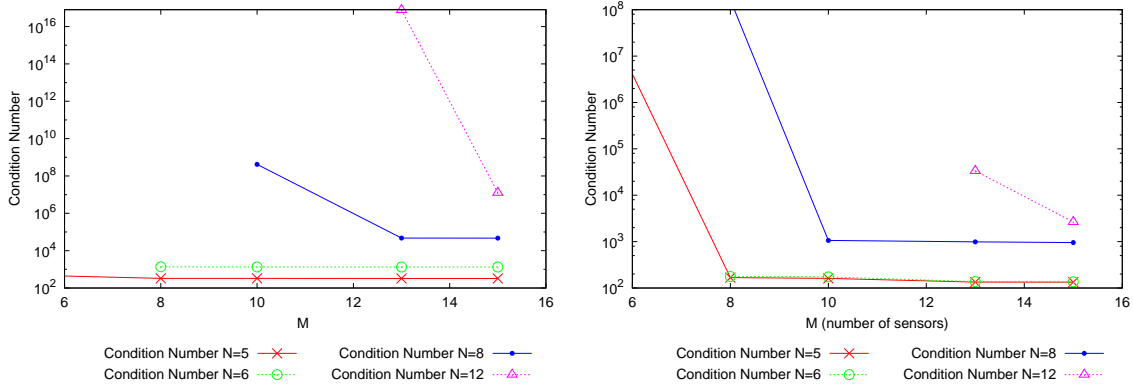


Figure 5.9 – Condition number of PBDW matrices, with $\|\cdot\|_{\mathcal{X}} = \|\cdot\|_{H^1}$, as a function of M for $N = 5, 6, 8, 12$. PBDW system corresponding to random sensor locations from figure 5.6 (left) ; PBDW system corresponding to sensor locations chosen by a GEIM-based greedy algorithm (section 4.1.2.1) (right).

locations (left) to those for sensor locations chosen by a greedy algorithm (right), we can see that in the 2D case with few sensors and $N = 5$, the random-sensor system is better conditioned, but this advantage is quickly lost as M and N increase. For $N = 8$ we have improved the condition number by $\mathcal{O}(10^2)$.

5.3 State Estimation Results : PBDW

In this section we will present the numerical results of the PBDW method on the 2D case study. We will present the PBDW state estimation results over the full domain and over a domain of interest, considering the variations in sensor choice discussed in paragraph 5.2.2. We will also compare the results of the PBDW method in 2D to those obtained by the GEIM, in both precision and computational time.

In order to test and validate the PBDW method for our case study, we have computed *trial* solutions to the shifted model \mathcal{P}^{trial} given by equation (4.70), for $N_{trial} = 6$ parameter values. We denote by Ξ^{trial} the parameter set for the group of trial solutions, each parameter corresponding to a parameter $\mathbf{p}_{trial} \in \mathcal{D}^{bk} \setminus \Xi_{train}^{bk}$. For these N_{trial} trial parameters, three sets of FEM approximations representing c^{true} , using three different models, are computed to construct synthetic data for the PBDW method. One set consists of solutions to equation (4.39) representing the (unrealistic) case of a perfect best-knowledge model \mathcal{P}^{bk} , with the goal of demonstrating the error inherent to the MOR approach of the PBDW method. The remaining trial sets consist of solutions to an advection-diffusion-reaction problem \mathcal{P}^{trial} (4.70) with linear reaction coefficients of $R = 0.001$ and $R = 0.0001$. These sets are used to demonstrate how the method handles two levels of model error, with an average error of 8% (and up to 17%) and 1%, respectively.

In figure 5.10 we see the relative mean projection errors onto the background RB space \mathcal{Z}_N over each of these trial sets defined by

$$\frac{1}{N_{trial}} \sum_{i=1}^{N_{trial}} \frac{\|E_N(c^{trial}(\mathbf{p}_i))\|_{H^1}}{\|c^{trial}(\mathbf{p}_i)\|_{H^1}}, \quad (5.5)$$

from the set of $N_{trial} = 6$ parameters $\mathbf{p}_i \in \Xi^{trial}$, where $E_N(c)$ is defined in (4.25). We consider that these errors demonstrate how well our background space \mathcal{Z}_N can approximate the trial solutions, both for parametric variation and the case of an imperfect model.

We define the trial solution corresponding to maximal error $c^{trial}(\mathbf{p}_{max})$, where $\mathbf{p}_{max} \in \Xi^{trial}$ is defined by equation (5.6):

$$\mathbf{p}_{max} = \underset{\mathbf{p} \in \Xi^{trial}}{\text{ARGMAX}} \frac{\|c^{trial}(\mathbf{p}) - c_{N,M}(\mathbf{p})\|_{\mathcal{X}}}{\|c^{trial}(\mathbf{p})\|_{\mathcal{X}}} \quad (5.6)$$

In figure 5.11 we can see the FEM approximations $c^{trial}(\mathbf{p}_{max})$ (left), solution to \mathcal{P}^{trial} (4.70), compared with the PBDW approximations $c_{N,M}(\mathbf{p}_{max})$ using random sensor locations (figure 5.6) and greedy selected sensors (figure 5.7).

Both PBDW state estimates provide close reconstruction of the physical state with only $N = 6$ background RB functions. However, the greedy-placed sensors better capture the lower peak in concentration than the randomly-placed sensors.

In figure 5.12 we represent again the FEM solution and PBDW state approximation, but with synthetic data from solutions to \mathcal{P}^{trial} with more significant model error, $R = 0.001$, to study how the PBDW method handles non-negligible model error. Again we see reasonable reconstruction of the physical state, but this time the randomly-placed sensors have an advantage. The greedy-placed sensors were chosen to best capture information on the advection-diffusion solutions, which vary more further from the source. The reaction term however has strongest effect where concentrations are highest: at the source. Our "greedy" sensors have less information on this region and thus misrepresents the concentration. The under representation of

the concentration remains relatively small however. Additionally we can expect that when applied to case studies with more variation in the physical state, the "greedy" sensors will be chosen to capture more variation.

In figure 5.13 we see PBDW best-fit error corresponding to equation (4.17) for the sets of trial solutions with significant model error in both the H^1 and L^∞ norms. These errors represent the best possible approximation of the trial solutions for $\mathbf{p} \in \Xi^{trial}$ by the approximation spaces \mathcal{Z}_N and \mathcal{U}_M . We see that while the number of background basis functions N improves the approximation quality in H^1 -norm, we see no improvement for added sensors M . This tells us that while in practice all the information in the PBDW system on the true solution $c^{true}(\mathbf{p})$ for some parameter configuration \mathbf{p} comes from the M sensors, the corresponding update basis q_m functions do not enlarge the span of the approximation space $\mathcal{Z}_N \oplus (\mathcal{U}_M \cap \mathcal{Z}_N^\perp)$. This means the update spaces we see here are doing little to correct for unmodeled physics. However, we will see that increasing M data points does improve the quality of the PBDW approximation for a given N background dimension. This can be attributed to the improved local approximations and increase in information on the physical state informing the system resolution.

If we consider the PBDW approximation error in the L^∞ norm, we can quantify this pointwise error improvement:

$$\frac{1}{N_{trial}} \sum_{i=1}^{N_{trial}} \frac{\|E_{M,N}^{PBDW}(c(p_i))\|_{L^\infty}}{\|c^{bk}(\mathbf{p}_i)\|_{L^\infty}} \quad (5.7)$$

We see this in the pointwise maximal errors (5.7) (averaged over the trial set) plotted in the same figure.

We define the PBDW state estimation error as follows

$$E_{M,N}^{PBDW}(c(p)) = c^{trial}(p) - c_{N,M}(p), \quad (5.8)$$

and calculate mean relative error in the PBDW state estimation of the trial set of solutions to \mathcal{P}^{trial} for $\mathbf{p} \in \Xi^{trial}$ pointwise over the calculation domain:

$$E_{M,N}^{PBDW,\Omega}(p) = \frac{|E_{M,N}^{PBDW}(c(p))|}{\|c^{trial}(p)\|_{L^\infty}} \in \mathcal{X}_h \quad (5.9)$$

The mean and maximal relative error in the PBDW state estimation with respect to the trial solutions, in H^1 are

$$\frac{1}{N_{trial}} \sum_{i=1}^{N_{trial}} \frac{\|E_{M,N}^{PBDW}(c(p_i))\|_{\mathcal{X}}}{\|c^{trial}(\mathbf{p}_i)\|_{\mathcal{X}}} \quad (5.10)$$

$$\text{MAX}_{\mathbf{p} \in \Xi^{trial}} \frac{\|E_{M,N}^{PBDW}(c(p))\|_{\mathcal{X}}}{\|c^{trial}(\mathbf{p})\|_{\mathcal{X}}} \quad (5.11)$$

In figures 5.14, 5.16, and 5.17 we represent relative mean and maximal error curves for the PBDW approximation, corresponding to equations (5.10) and (5.11) respectively, as a function of N RB basis functions for fixed M number of sensors.

We want to show the influence of the size of the RB space on the quality of the PBDW approximation using random sensor locations, on each of the three trial sets.

In figure 5.14 the observations used in the PBDW system are synthetic data obtained from a perfect best-knowledge model \mathcal{P}^{bk} , such that $c^{true} = c^{bk}$. In figures 5.16 and 5.17, observations used in the PBDW system are synthetic data from the shifted model \mathcal{P}^{trial} such that $c^{true} \neq c^{bk}$, with a reaction term of $R = 0.0001$ and $R = 0.001$ respectively, to represent a model error in the computation of synthetic data. We can see that with little or no model error with $N = 6$ background basis functions we achieve about 1% error (mean error measure in the H^1 -norm), and about 3% error with significant model error (\mathcal{P}^{trial} with reaction $R = 0.001$). We note that the non-monotone error curves are to be expected: there is no mathematical argument for strictly decreasing error, as the error depends not only on the best-fit of the PBDW approximation space, but also on the stability and conditioning of the system. We can observe that the instability for N approaching M (seen in the stability coefficient $\beta_{M,N}$ of equation (3.17)) has an amplified effect on the error in the case of more significant model error. This is consistent with equation (3.18).

In figure 5.15 we can see PBDW approximation relative mean errors mapped over the domain, as in equation (5.9), for trial solutions with no model error. We see significant change between $N = 2$ and $N = 6$, as can be expected given the dimension of the background space. We see less improvement with an increase in M , unsurprising in the case of a perfect model \mathcal{P}^{bk} .

In figure 5.18 we again see relative mean errors mapped over the domain but for the case of significant model error. Again we see significant improvement between $N = 2$ and $N = 6$, but negligible change when adding more data points. This suggests that our Update space does not add significantly to the span of the PBDW approximation space $\mathcal{Z}_N \oplus \mathcal{U}_M$. In this simple test, $M = 8$ is sufficient data for the PBDW system to approximate the state over the $N = 6$ background basis functions, and adding more update basis functions does not enlarge the approximation space, and so does not improve the approximation.

In figures 5.19, 5.21, and 5.22 we see relative mean and maximal error curves for the PBDW approximation, corresponding to equations (5.10) and (5.11) respectively, for each of the three trial sets, using sensors chosen by a greedy procedure. In figure 5.19 the observations used in the PBDW system are synthetic data obtained from a perfect best-knowledge model \mathcal{P}^{bk} , such that $c^{true} = c^{bk}$. In figures 5.21 and 5.22, observations used in the PBDW system are synthetic data from the shifted model \mathcal{P}^{trial} such that $c^{true} \neq c^{bk}$, with a reaction term of $R = 0.0001$ and $R = 0.001$ respectively, to represent a model error in the computation of synthetic data. We can see that with little or no model error with $N = 6$ background basis functions we again achieve $\sim 1\%$ mean error, and $\sim 3\%$ error with significant model error. We note that we have more consistent error results, with fewer peaks in the error, as compared to sensors chosen randomly. We can attribute this to the increased stability and conditioning of the PBDW linear system. We also note that we did not significantly improve the error in the best case (of N - and M -values), but did

in the worst cases. We could thus draw the preliminary conclusion that using data from sensors placed using a greedy procedure is no guarantee of improved precision in the PBDW approximation (here it depends on N - and M -values), but seems to improve the stability of the system and consistency of the results, which would be a non-negligible advantage in the online stage when precise error analysis is not feasible.

In figures 5.20 and 5.23 we see relative mean PBDW approximation errors mapped over the domain, as in equation (5.9), using synthetic data from sensors selected via a greedy procedure. In figure 5.20 the synthetic data were computed with no model error from \mathcal{P}^{bk} . Here we see a bit more improvement between $M = 8$ and $M = 15$, which can be attributed to better-placed sensors. If we compare to the random-sensor case, we can see the effect of sensor placement: in general, the randomly chosen sensor system better approximated concentration near the source, as multiple data points are placed here. By contrast, the greedy-selected sensors are well-suited to capturing convective effects of varying wind fields, and we can see this in improved approximation furthest from the source.

In figure 5.23 the synthetic data were computed from the shifted model \mathcal{P}^{trial} with a reaction term of $R = 0.001$ to represent significant model error. Here we see more significant improvement with added data points. We again note that this PBDW state estimation is less precise at the source, but more precise in determining convective transport further from the source, again attributable to sensor locations. We see that with $N = 6$ and $M = 15$ the error is under 6% everywhere, and often under 1%. Compare to corresponding case with randomly placed sensors, where the error surpasses 6% in a small region. Again we see significant improvement between $N = 2$ and $N = 6$, but negligible change when adding more data points. This suggests that our Update space does not add significantly to the span of the PBDW approximation space $\mathcal{Z}_N \oplus \mathcal{U}_M$. In this simple test, $M = 8$ is sufficient data for the PBDW system to approximate the state over the $N = 6$ background functions, and adding more update basis functions does not enlarge the approximation space, and so does not improve the approximation.

In RBM applications it is often unnecessary to reconstruct the approximated solution over the full domain Ω ; instead the solution of some output value on the solution over a smaller domain of interest $\Omega_{out} \subset \Omega$ is approximated. This is highly compatible with air quality studies, as often the physical *quantity of interest* (QoI) is a concentration peak in an area or the average concentration over a period of time in an area. This renders RBMs much more advantageous (no online complexity is dependent on the mesh dimension \mathcal{N}_h). In this case study we will consider the quantity of interest to be the average concentration over a subdomain of interest, which could represent, for example, a playground.

We define the QoI PBDW state estimation error as follows

$$E_{M,N}^{PBDW_{out}}(c(\mathbf{p})) = \ell^{out}(c(\mathbf{p})) - \ell^{out}(c_{N,M}(\mathbf{p})), \quad (5.12)$$

where

$$\ell^{out}(c(\mathbf{p})) = \frac{1}{|\Omega_{out}|} \int_{\Omega_{out}} c(\mathbf{p}) d\Omega. \quad (5.13)$$

In figure 5.24 we can see a representation of a domain of interest in the computational domain Ω , and in figure 5.25 the PBDW relative mean errors (5.12) in H^1 norm over this domain:

$$\frac{1}{N_{trial}} \sum_{i=1}^{N_{trial}} \frac{|E_{M,N}^{PBDW_{out}}(c(\mathbf{p}_i))|}{\|c(\mathbf{p}_i)\|_{H^1(\Omega_{out})}} \quad (5.14)$$

We see that while the errors over our chosen domain of interest (chosen to represent for example a childrens' playground) suffer the same instabilities as a function of M and N , the overall error committed is of the order $\mathcal{O}(10^{-5})$ with no model error or with significant model error.

In figures 5.26 and 5.27 we can see relative mean PBDW approximation errors and bounds over $\mathbf{p} \in \Xi^{trial}$. In figure 5.26 the observations used in the PBDW system are synthetic data obtained from a perfect best-knowledge model \mathcal{P}^{bk} , such that $c^{true} = c^{bk}$, and In figure 5.27, observations used in the PBDW system are synthetic data from the shifted model \mathcal{P}^{trial} such that $c^{true} \neq c^{bk}$, with a reaction term of $R = 0.001$, to represent a model error in the computation of synthetic data. Plots show:

- The best-fit error from equation (4.17), projection error of the trial solutions to \mathcal{P}^{trial} onto approximation space $\mathcal{Z}_N \oplus (\mathcal{U}_M \cap \mathcal{Z}_N^\perp)$
- PBDW approximation error (5.8) (i.e. the left-hand-side of equation (3.18)), and
- An a priori error bound given by (the right-hand-side of) equation (3.18),

all in relative mean with respect to $\|c^{trial}(\mathbf{p}_i)\|_{H^1}$ over the trial set, as described by equation (5.10) for relative mean PBDW approximation error. We choose to fix the background basis size at $N = 6$, as would be chosen in the online implementation of this study. We can see that the PBDW method provides nearly identical approximation precision in both cases, with and without model error. We also notice that in this case with N chosen well after offline study of results, the improvement by greedy-placed sensors is negligible.

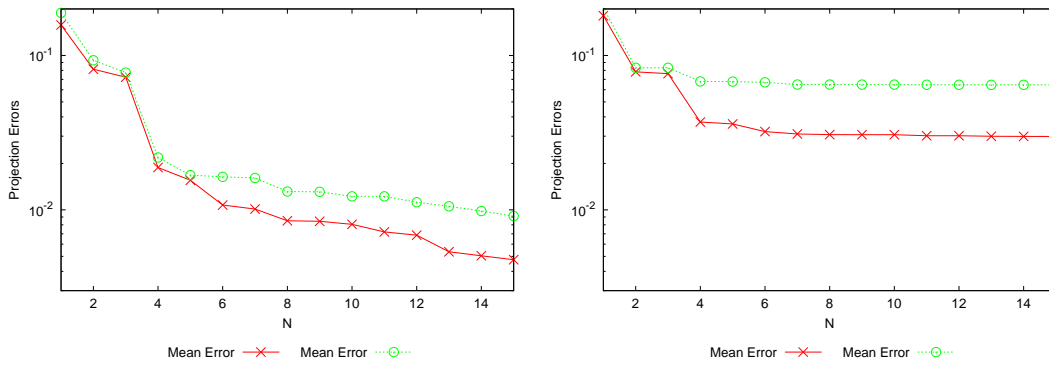


Figure 5.10 – Relative mean projection error (5.5) in H^1 -norm, projection Π_{Z_N} defined by (4.24), of each of the sets of trial solutions for parameter set Ξ^{trial} . Left: no model error (model \mathcal{P}^{bk}). Right: added reaction term $R = 0.001$ (model \mathcal{P}^{trial}).

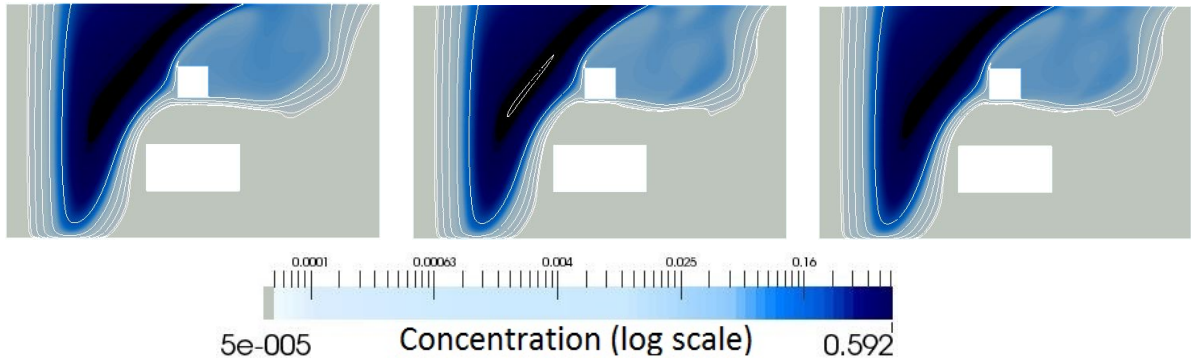


Figure 5.11 – Approximation of the concentration for $\mathbf{p} = \mathbf{p}_{max}$, logarithmic scale. Trial solution to \mathcal{P}^{trial} with model error simulated by a reaction term of $R = 0.0001$. True FEM solution (left), PBDW approximation using simulated measurement data, with random sensors (middle), PBDW approximation with greedy selected sensors (right).

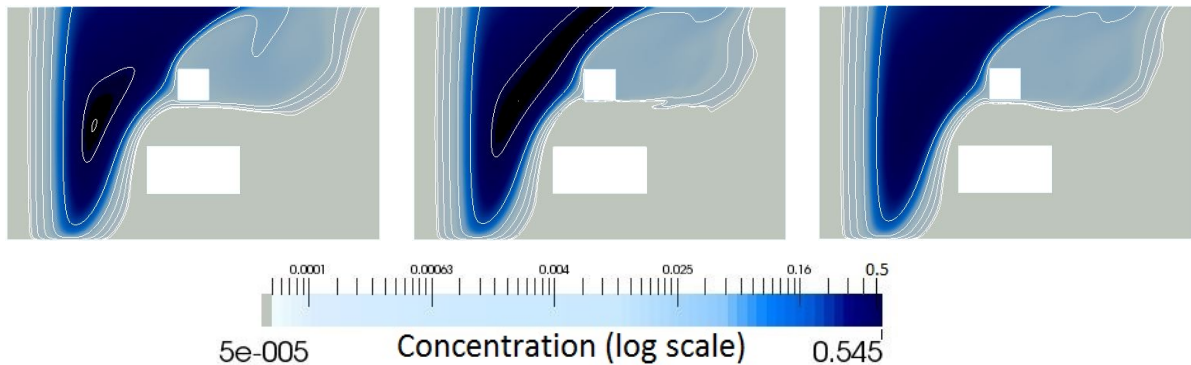


Figure 5.12 – Approximation of the concentration for $\mathbf{p} = \mathbf{p}_{max}$, logarithmic scale. Trial solution to \mathcal{P}^{trial} with model error simulated by a reaction term of $R = 0.001$. True FEM solution (left), PBDW approximation using synthetic data, with random sensors (middle), PBDW approximation with greedy selected sensors (right).

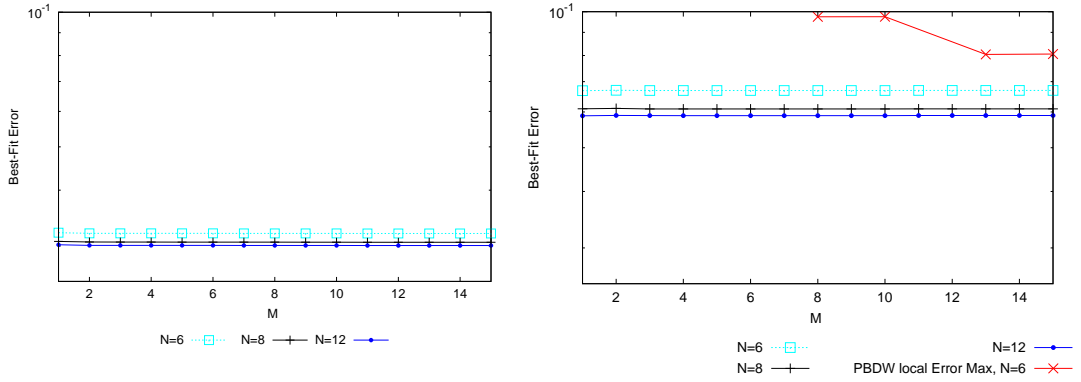


Figure 5.13 – Best-fit error, equation (4.17), of the set of trial solutions over $\mathbf{p} \in \mathcal{D}^{trial}$ and model error with an added reaction term of $0.001c$, projected onto the approximation space $\mathcal{Z}_N \oplus (\mathcal{U}_M \cap \mathcal{Z}_N^\perp)$ as a function of M . H^1 -norm (left) and L^∞ -norm (right). Compared to mean error (5.7) over trial solutions of relative PBDW approximation error in the L^∞ norm (right). Sensors chosen by GEIM.

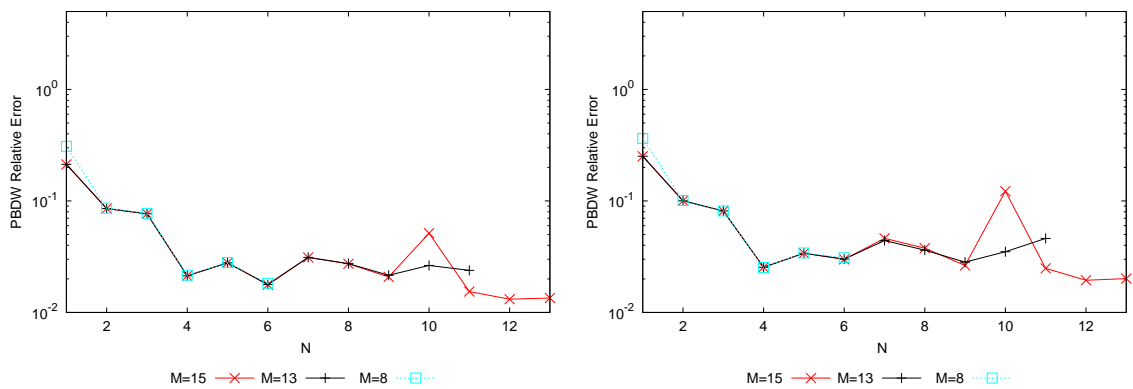


Figure 5.14 – Relative mean (5.10) (left) and maximal (5.11) (right) PBDW approximation error as a function of N for fixed M values. Using synthetic trial data for parameter set Ξ^{trial} with no model error (model \mathcal{P}^{bk}). Sensor locations chosen randomly.

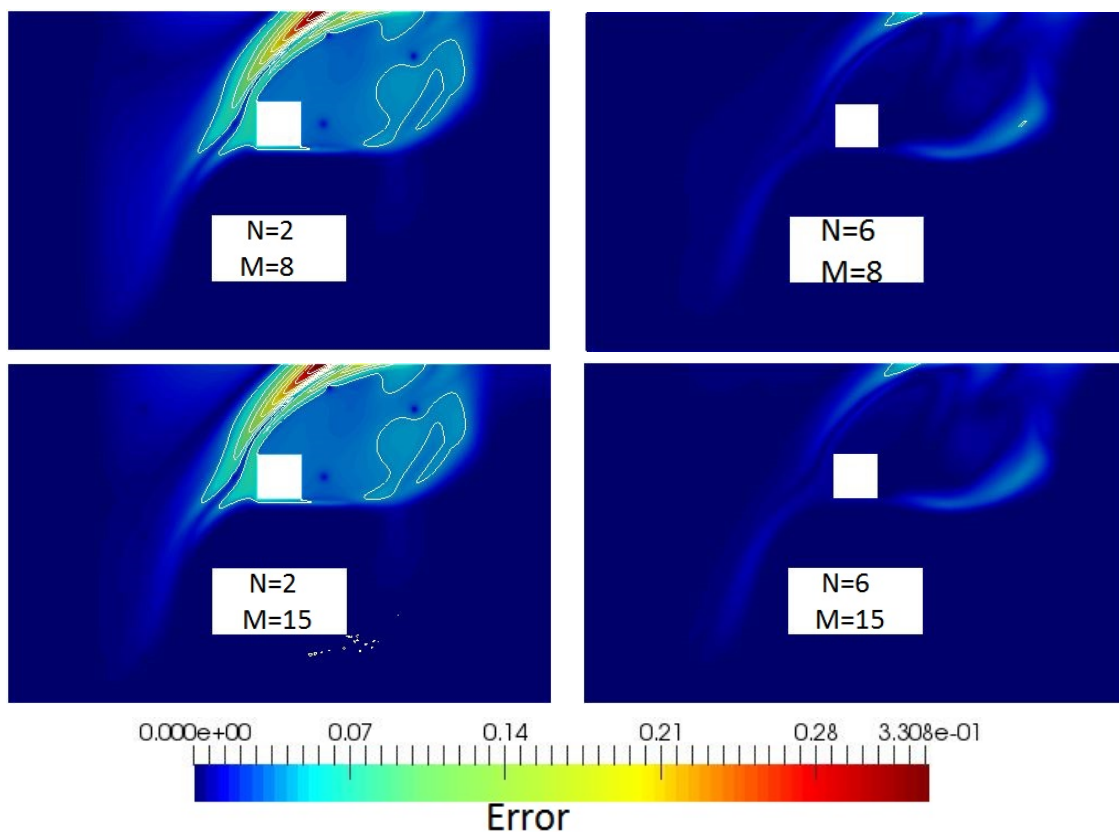


Figure 5.15 – Relative mean PBDW approximation error maps for $N = 2$ (left), $N = 6$ (right), and for $M = 8$ (top) and $M = 15$ (bottom). Using synthetic trial data for parameter set Ξ^{trial} with no model error (model \mathcal{P}^{bk}). Sensor locations chosen randomly.

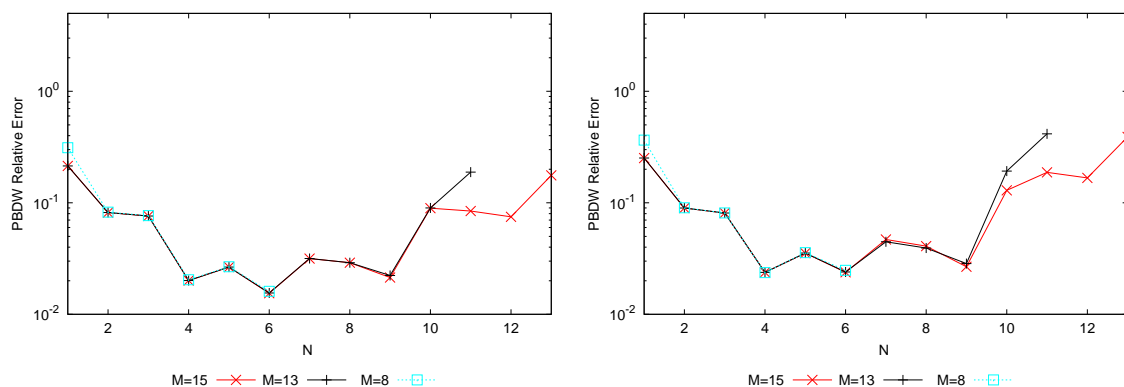


Figure 5.16 – Relative mean (5.10) (left) and maximal (5.11) (right) PBDW approximation error as a function of N for fixed M values. Using synthetic trial data for parameter set Ξ^{trial} with added reaction term $R = 0.0001$ (model \mathcal{P}^{trial}). Sensor locations chosen randomly.

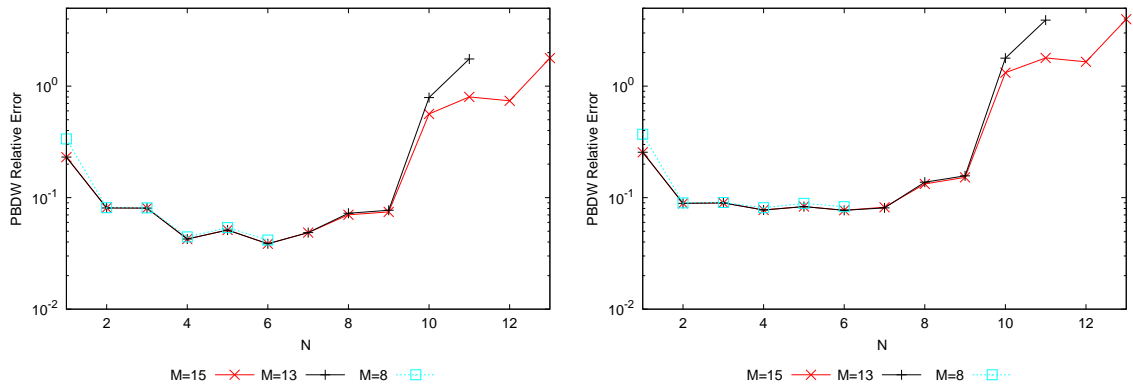


Figure 5.17 – Relative mean (5.10) (left) and maximal (5.11) (right) PBDW approximation error as a function of N for fixed M values. Using synthetic trial data for parameter set Ξ^{trial} with added reaction term $R = 0.001$ (model \mathcal{P}^{trial}). Sensor locations chosen randomly.

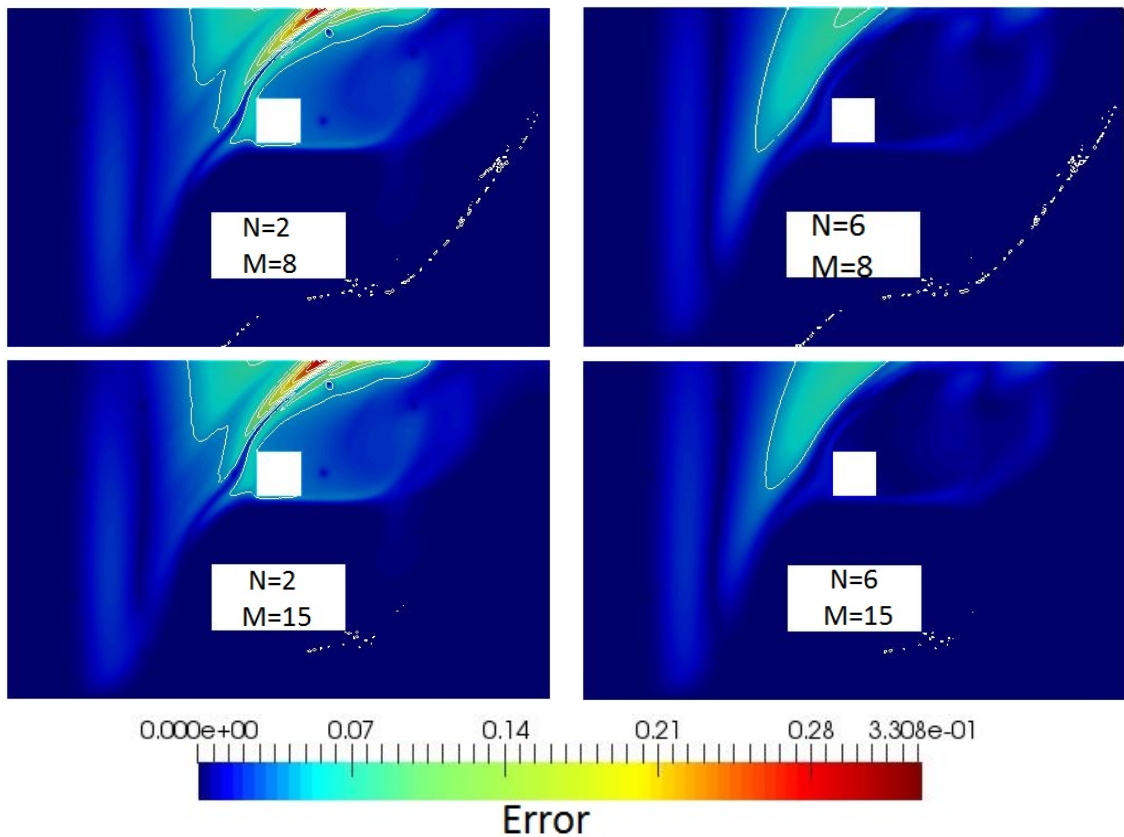


Figure 5.18 – Relative mean PBDW approximation error maps for $N = 2$ (left), $N = 6$ (right), and for $M = 8$ (top) and $M = 15$ (bottom). Using synthetic trial data for parameter set Ξ^{trial} with added reaction term $R = 0.001$ (model \mathcal{P}^{trial}). Sensor locations chosen randomly.

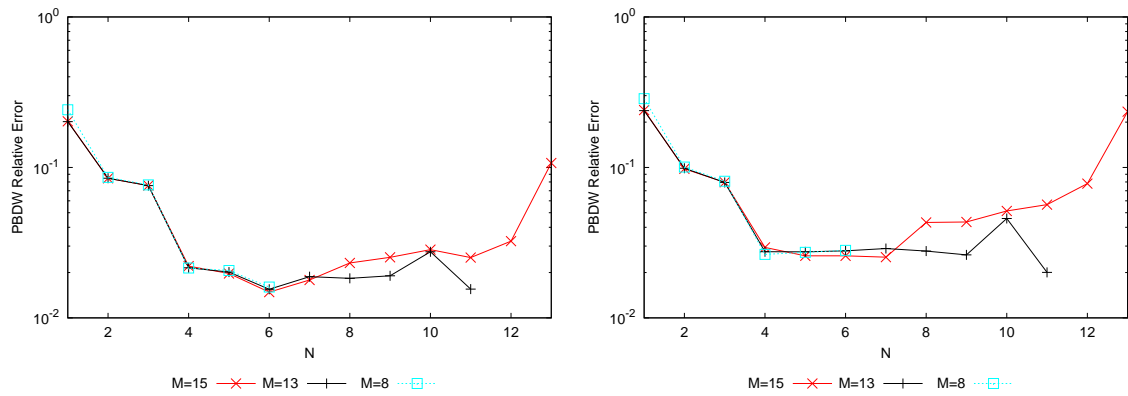


Figure 5.19 – Relative mean (5.10) (left) and maximal (5.11) (right) PBDW approximation error as a function of N for fixed M values. Using synthetic trial data for parameter set Ξ^{trial} with no model error (model \mathcal{P}^{bk}). Sensor locations chosen by a greedy procedure.

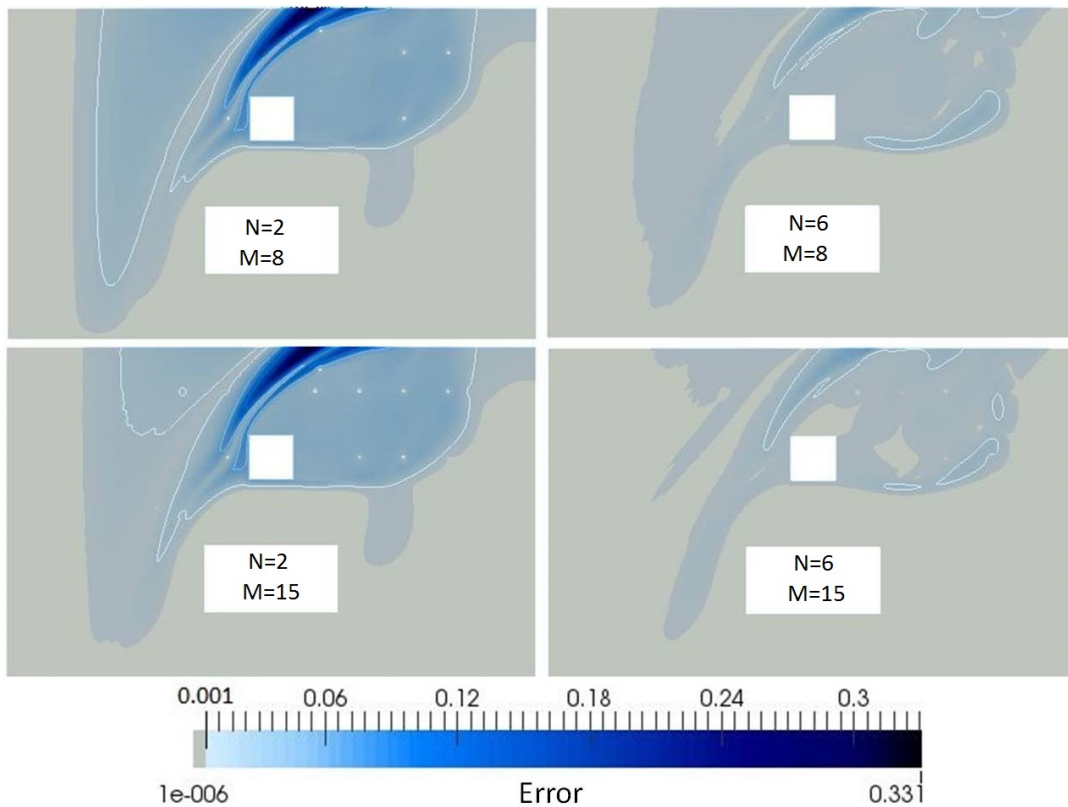


Figure 5.20 – Relative mean PBDW approximation error maps for $N = 2$ (left), $N = 6$ (right), and for $M = 8$ (top) and $M = 15$ (bottom). Using synthetic trial data for parameter set Ξ^{trial} with no model error (model \mathcal{P}^{bk}). Sensor locations chosen by a greedy procedure.

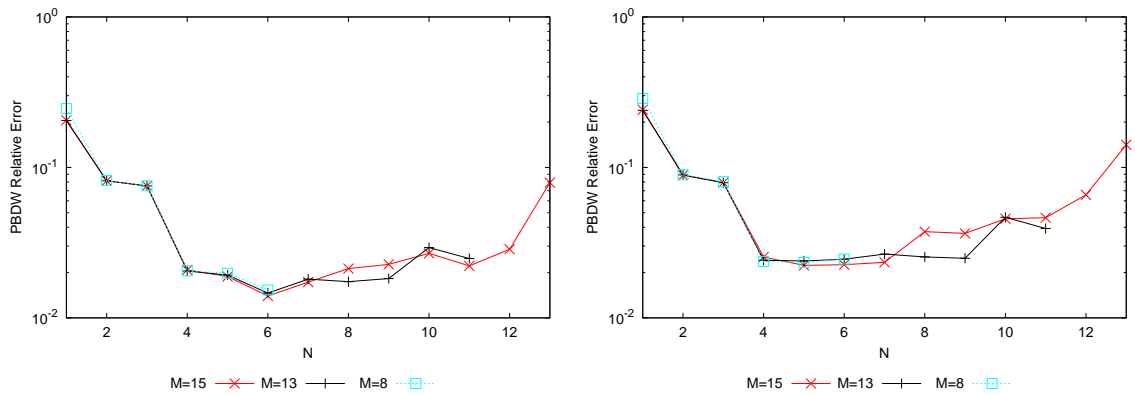


Figure 5.21 – Relative mean (5.10) (left) and maximal (5.11) (right) PBDW approximation error as a function of N for fixed M values. Using synthetic trial data for parameter set Ξ^{trial} with added reaction term $R = 0.0001$ (model \mathcal{P}^{trial}). Sensor locations chosen by a greedy procedure.

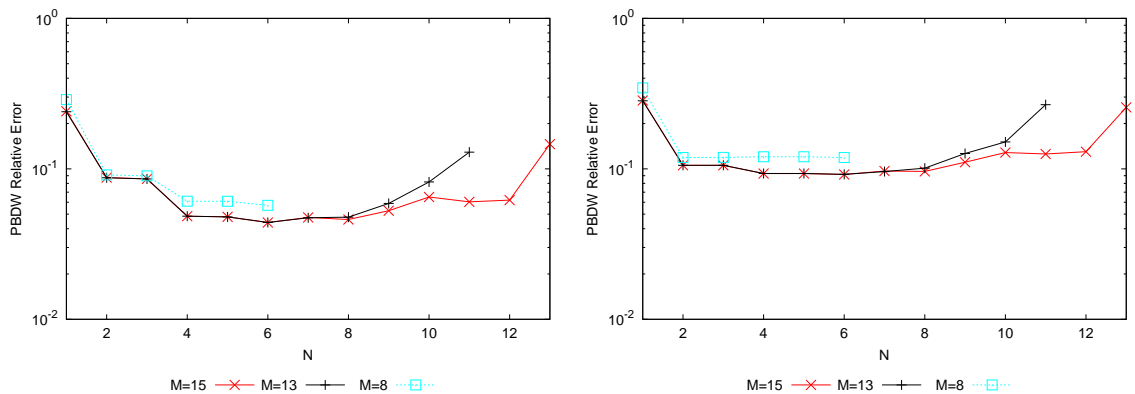


Figure 5.22 – Relative mean (5.10) (left) and maximal (5.11) (right) PBDW approximation error as a function of N for fixed M values. Using synthetic trial data for parameter set Ξ^{trial} with added reaction term $R = 0.0001$ (model \mathcal{P}^{trial}). Sensor locations chosen by a greedy procedure.

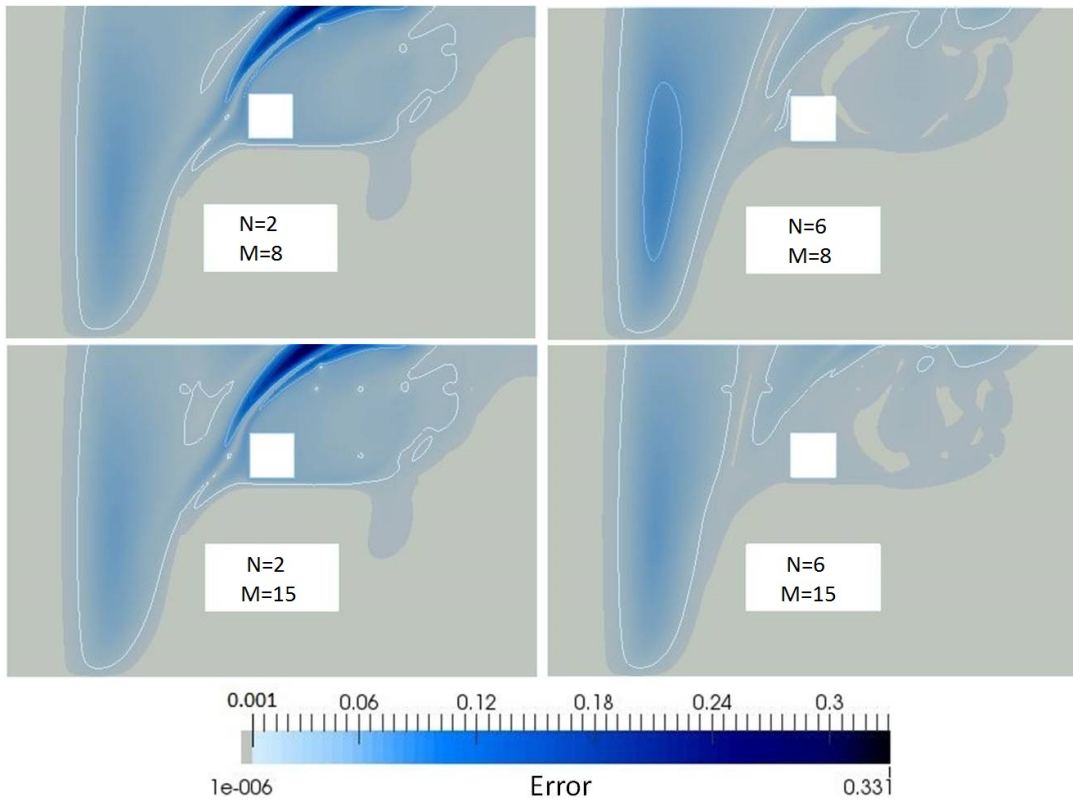


Figure 5.23 – Relative mean PBDW approximation error maps for $N = 2$ (left), $N = 6$ (right), and for $M = 8$ (top) and $M = 15$ (bottom). Using synthetic trial data for parameter set Ξ^{trial} with added reaction term $R = 0.001$ (model \mathcal{P}^{trial}). Sensor locations chosen by a greedy procedure.

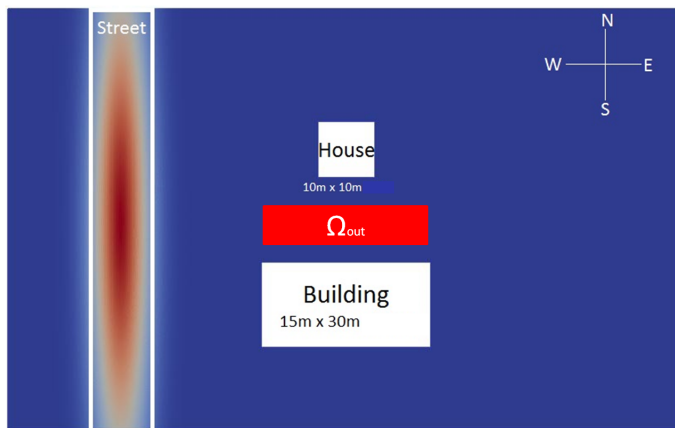


Figure 5.24 – Representation of a domain of interest Ω_{out} in the full computational domain Ω .

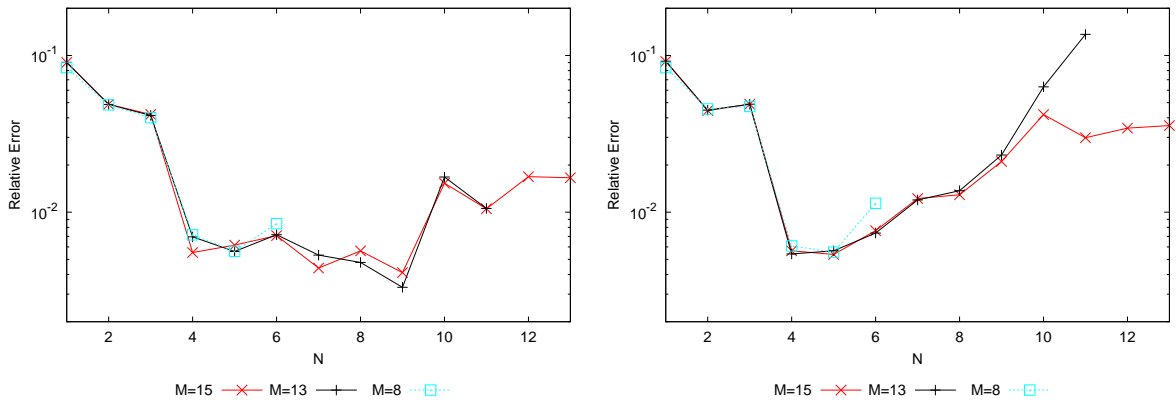


Figure 5.25 – Relative mean error of the PBDW approximation (5.14) over a domain of interest as a function of N for various M values. Using synthetic trial data for parameter set Ξ^{trial} with no model error (model \mathcal{P}^{bk} , left), and with added reaction term $R = 0.001$ (model \mathcal{P}^{trial} , right). Sensor locations chosen by a greedy procedure.

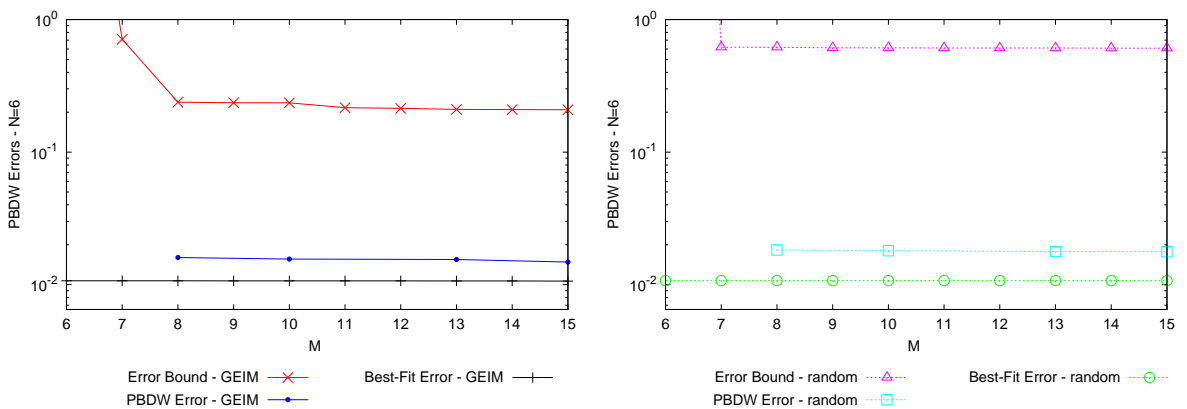


Figure 5.26 – Relative mean PBDW results as a function of number of data points M for background basis dimension $N = 6$ values. Using synthetic trial data for parameter set Ξ^{trial} with no model error (model \mathcal{P}^{bk}). Sensor locations chosen by a greedy procedure (left), and randomly (right).

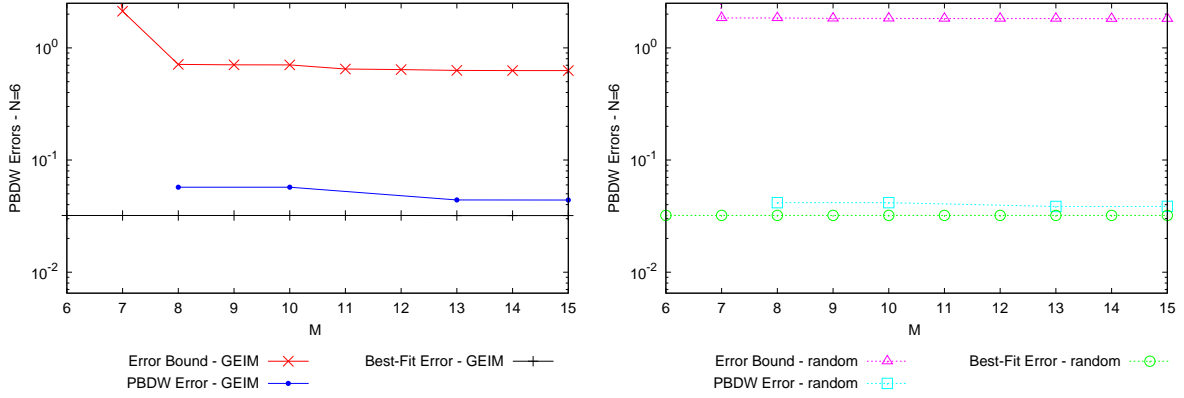


Figure 5.27 – Relative mean PBDW results as a function of number of data points M for background basis dimension $N = 6$ values. Using synthetic trial data for parameter set Ξ^{trial} with added reaction term $R = 0.001$ (model \mathcal{P}^{trial}). Sensor locations chosen by a greedy procedure (left), and randomly (right).

5.4 PBDW Norm modifications

In this section we present the state estimation results on our 2D case study using a modified norm presented in section 4.1.1.3, defined by equation (4.21). We set $L_g = 75m$ the characteristic length associated to the 2D domain of study. In figures 5.28 and 5.29, we compare stability coefficients (3.17) for the PBDW formulation in the H^1 -norm ($L_g = 1$) and the \tilde{H}^1 -norm with $L_g = 75$, the system using random sensor locations and sensor locations chosen by a greedy procedure, respectively. We see that in these cases we have no significant difference in $\beta_{N,M}$ induced by the changed norm.

In figures 5.30 and 5.31, we compare the matrix conditioning for the PBDW formulation in the H^1 -norm ($L_g = 1$) and the \tilde{H}^1 -norm with $L_g = 75$, the system using random sensor locations and sensor locations chosen by a greedy procedure, respectively. We see here a slight improvement in the case of sensor locations chosen by a greedy procedure induced by the \tilde{H}^1 norm for $L_g = 75$, but some deterioration in the case of randomly-placed sensors.

In figures 5.32 and 5.33, we compare the relative mean PBDW approximation error (5.10) over the set of trial solution for $\mathbf{p} \in \Xi^{trial}$ and model \mathcal{P}^{bk} , in the H^1 -norm, for the PBDW formulation in the H^1 -norm ($L_g = 1$) and the \tilde{H}^1 -norm with $L_g = 75$, for each set of sensor locations, respectively. In these figures we see no significant improvement from the \tilde{H}^1 norm.

In figures 5.35 and 5.36, we compare the relative mean PBDW approximation error (5.10) over the set of trial solution for $\mathbf{p} \in \Xi^{trial}$ and model \mathcal{P}^{trial} with reaction $R = 0.001$, in the H^1 -norm, for the PBDW formulation in the H^1 -norm ($L_g = 1$) and the \tilde{H}^1 -norm with $L_g = 75$, for random sensor locations and sensors chosen by a greedy procedure. In these figures we see no improvement from the \tilde{H}^1 norm, and a slight loss of stability in the case of sensors chosen by the greedy procedure.

We next compare these relative mean PBDW errors mapped over the calculation

domain, as in (5.9). In figures 5.34 and 5.37 we consider $\mathbf{p} \in \Xi^{trial}$ with model \mathcal{P}^{bk} , and model \mathcal{P}^{trial} with reaction $R = 0.001$, respectively. Here, we see a more significant difference between the choices of norm, and actually find that the \tilde{H}^1 norm deteriorates the quality of our solution.

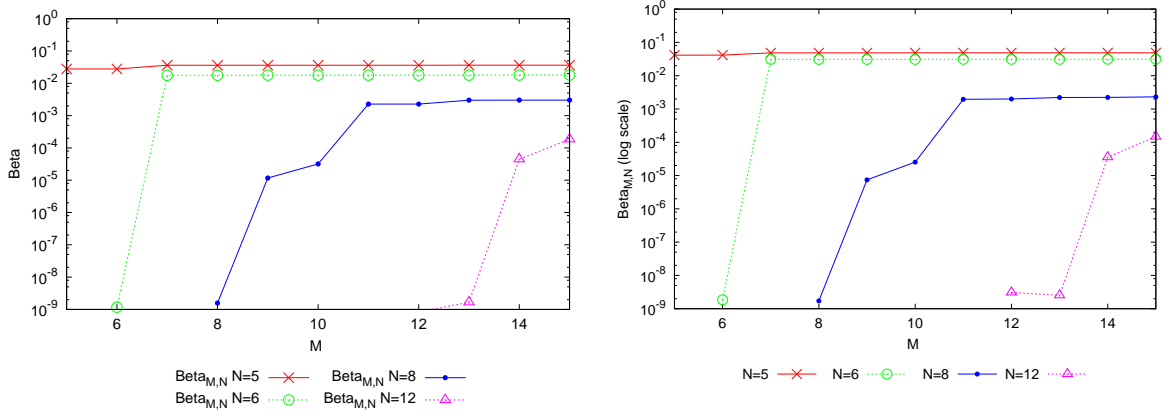


Figure 5.28 – Stability constant $\beta_{N,M}$ (3.17) in \tilde{H}^1 norm, for $L_g = 1$ (left), and $L_g = 75$ (right) as a function of M , for sensor locations chosen randomly.

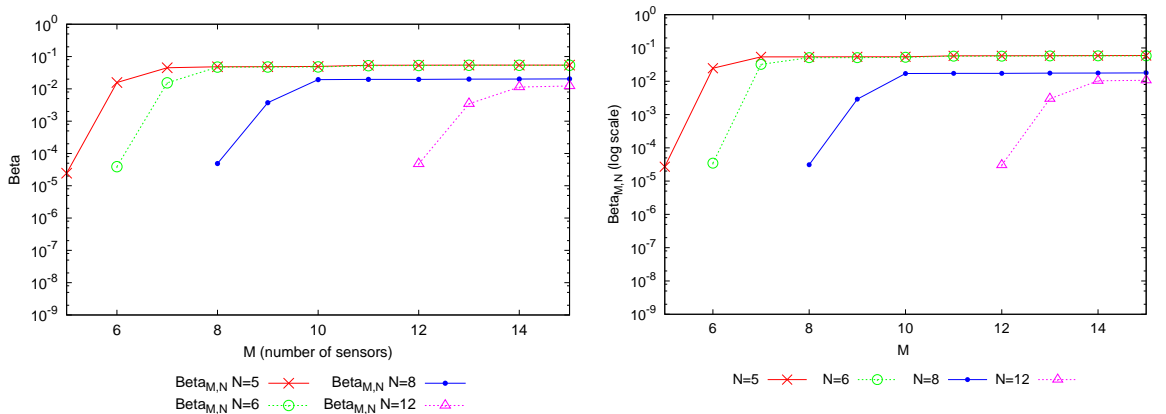


Figure 5.29 – Stability constant $\beta_{N,M}$ (3.17) in \tilde{H}^1 norm for $L_g = 1$ (left), and $L_g = 75$ (right) as a function of M , for sensor locations chosen by a greedy procedure.

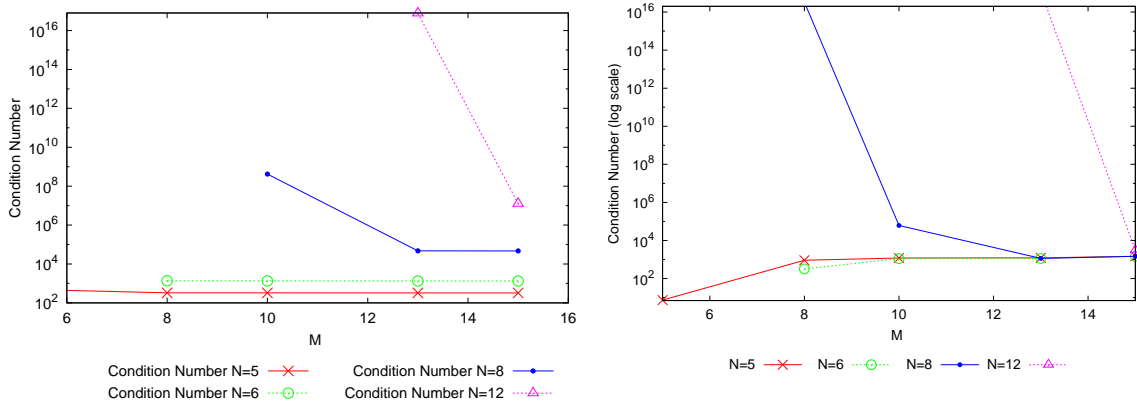


Figure 5.30 – PBDW matrix conditioning number in \tilde{H}^1 norm for $L_g = 1$ (left), and $L_g = 75$ (right) as a function of M , for sensor locations chosen randomly.

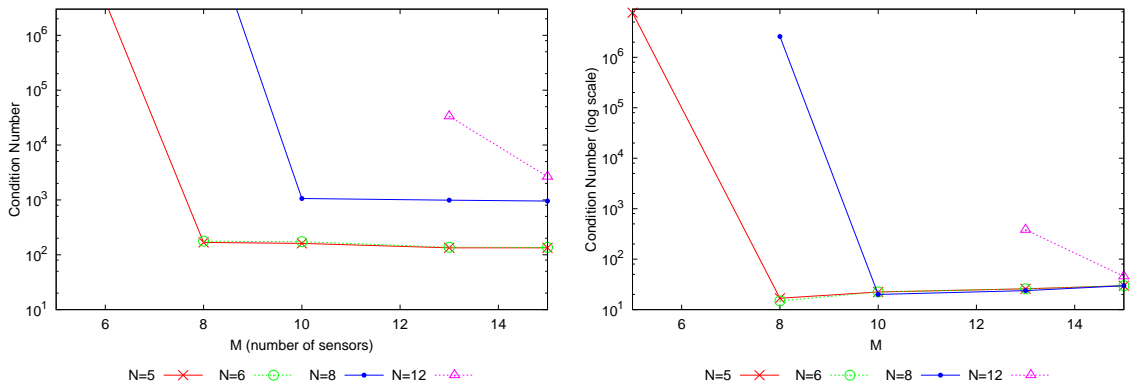


Figure 5.31 – PBDW matrix conditioning number in \tilde{H}^1 norm for $L_g = 1$ (left), and $L_g = 75$ (right) as a function of M , for sensor locations chosen by a greedy procedure.

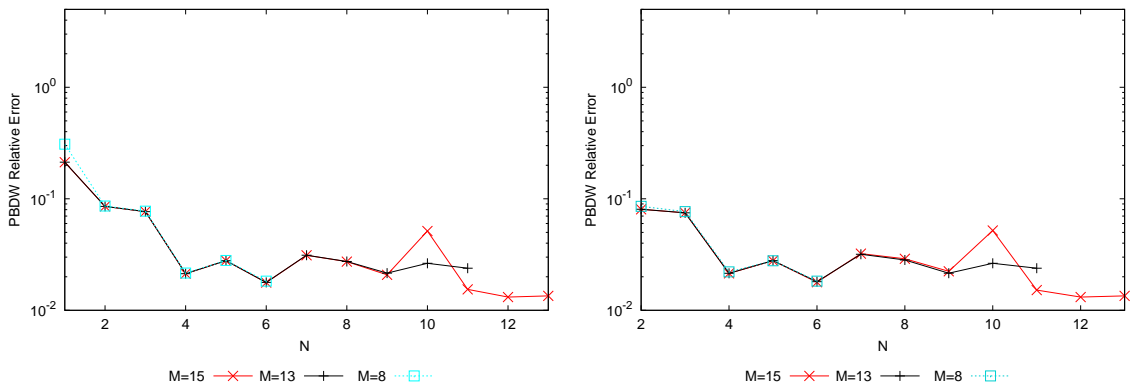


Figure 5.32 – Relative mean PBDW approximation errors, calculated in the H^1 norm (left) vs. the \tilde{H}^1 norm (right), with random sensor locations. Using synthetic trial data for parameter set Ξ^{trial} with no model error (model \mathcal{P}^{bk}).

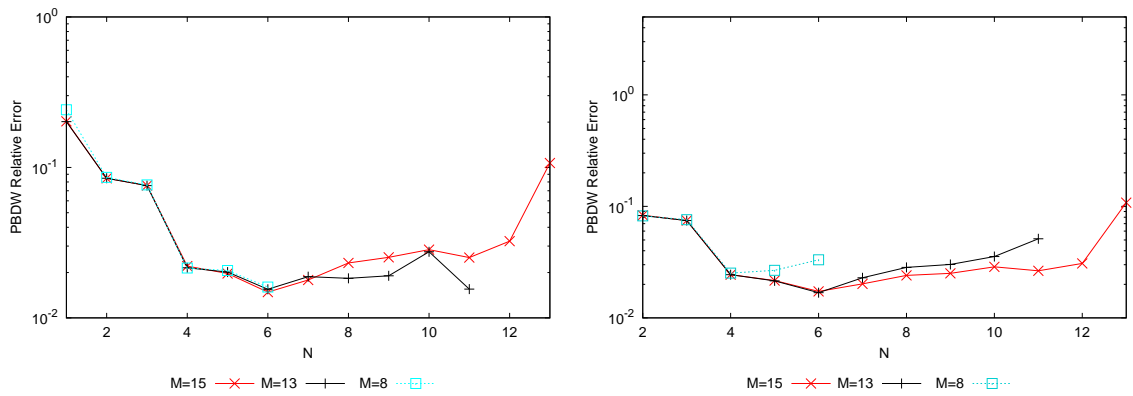


Figure 5.33 – Relative mean PBDW approximation errors, calculated in the H^1 norm (left) vs. the \tilde{H}^1 norm (right), with sensor locations chosen by a greedy procedure. Using synthetic trial data for parameter set Ξ^{trial} with no model error (model \mathcal{P}^{bk}).

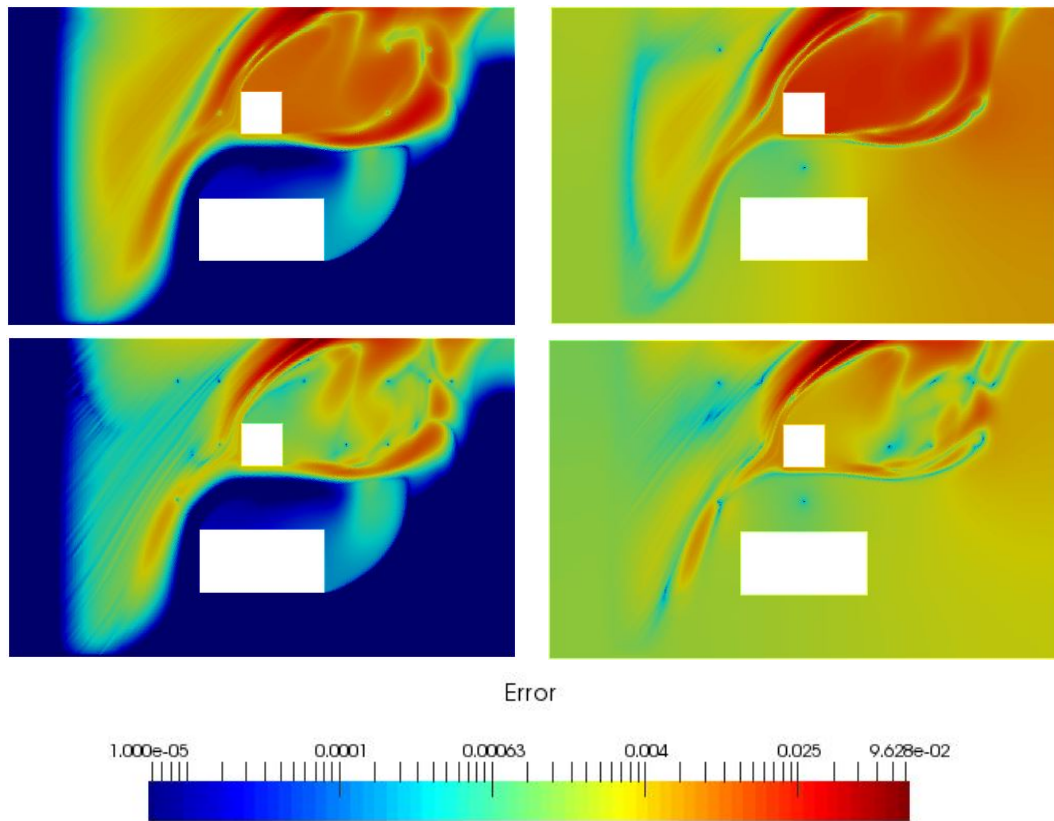


Figure 5.34 – Relative mean PBDW approximation errors, mapped over the domain, for the PBDW system using the H^1 norm (left column) vs. the \tilde{H}^1 norm (right column), with $M = 8$ and $N = 5$ (top row) and with $M = 13$ and $N = 8$ (bottom row). Using synthetic trial data for parameter set Ξ^{trial} with no model error (model \mathcal{P}^{bk}), and sensor locations chosen by a greedy procedure.

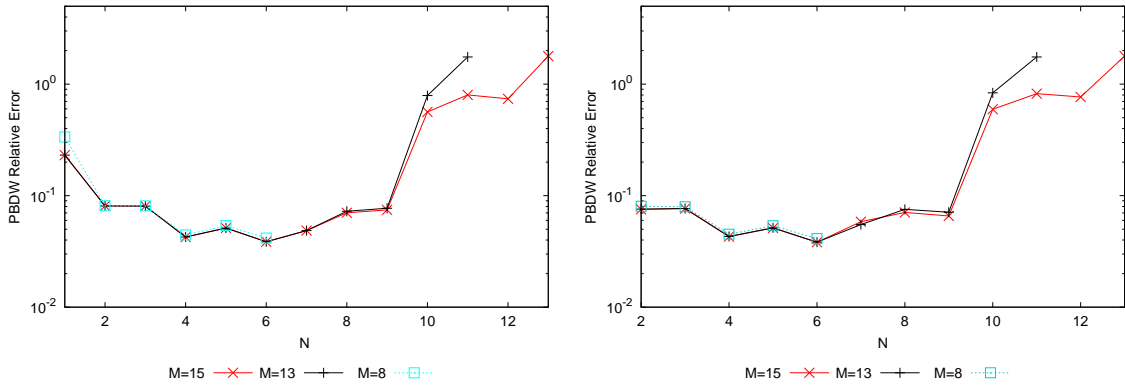


Figure 5.35 – Relative mean PBDW approximation errors, calculated in the H^1 norm (left) vs. the \tilde{H}^1 norm (right), with random sensor locations. Using synthetic trial data for parameter set Ξ^{trial} with added reaction term $R = 0.001$ (model \mathcal{P}^{trial}).

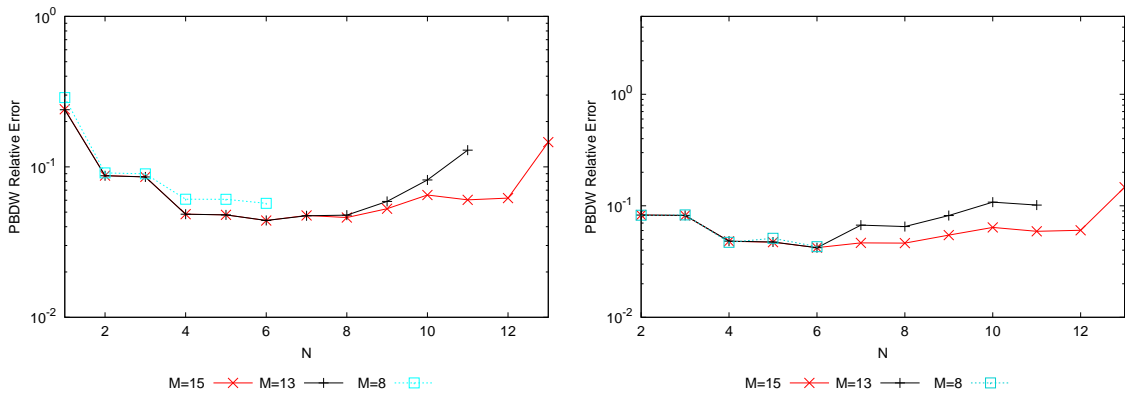


Figure 5.36 – Relative mean PBDW approximation errors, calculated in the H^1 norm (left) vs. the \tilde{H}^1 norm (right), with sensor locations chosen by a greedy procedure. Using synthetic trial data for parameter set Ξ^{trial} with added reaction term $R = 0.001$ (model \mathcal{P}^{trial}).

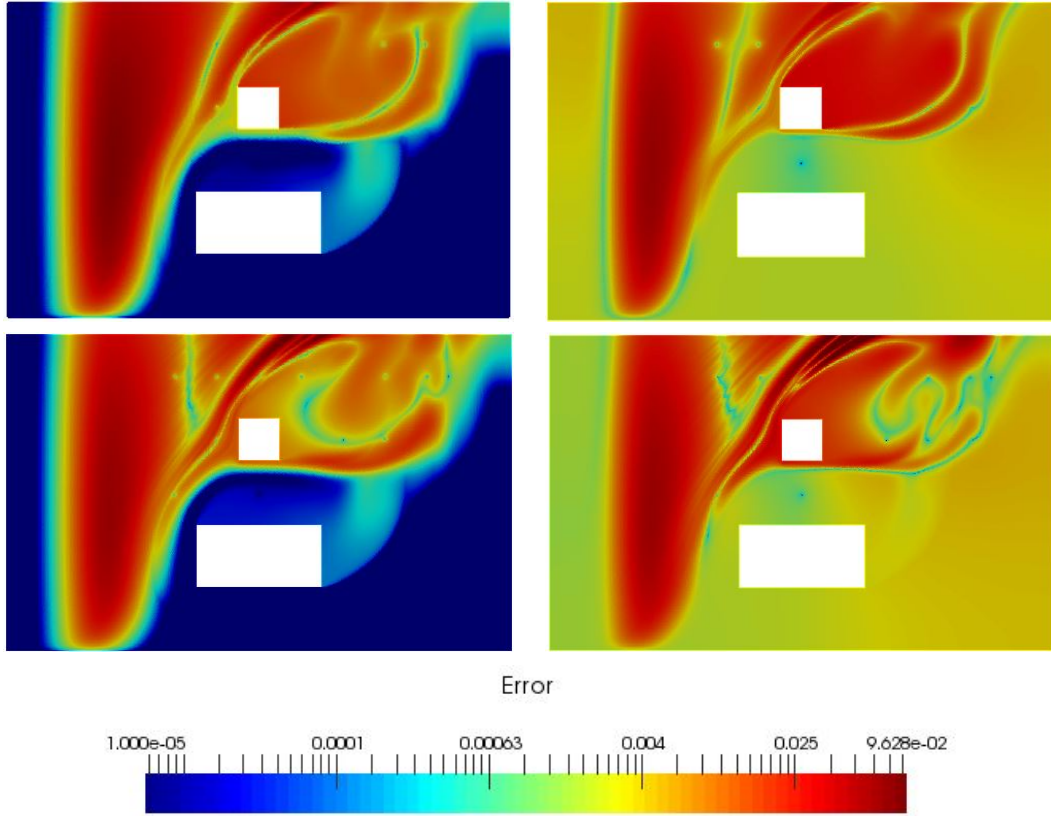


Figure 5.37 – Relative mean PBDW approximation errors, mapped over the domain, for the PBDW system using the H^1 norm (left column) vs. the \tilde{H}^1 norm (right column), with $M = 8$ and $N = 5$ (top row) and with $M = 13$ and $N = 8$ (bottom row). Using synthetic trial data for parameter set Ξ^{trial} with added reaction term $R = 0.001$ (model \mathcal{P}^{trial}), and sensor locations chosen by a greedy procedure.

5.4.1 Adapted sensor placement

Upon reflection we decided to reconsider the optimal sensor selection in the case of the \tilde{H}^1 -norm. In fact, the GEIM-based Greedy algorithm as presented in section 4.1.2.1 used to construct the optimal sensor set defined the GEIM set of functionals Σ to the set of linear functionals $\ell_m \in \mathcal{X}'$ from equation (3.5). This does not take into account the increased support of each Update basis function q_m , $1 \leq m \leq M$, defined by equation (3.8) with the norm \tilde{H}^1 . Here we replaced the linear functionals ℓ_m in the Greedy algorithm by the corresponding basis functions q_m (which we computed over all the possible sensor locations on the grid in figure 5.7).

In figure 5.38 we see the \tilde{H}^1 adapted Greedy sensor locations.

In figure 5.39 we compare the FEM solution to \tilde{H}^1 PBDW state estimates for trial solutions with significant model error of $R = 0.001$. We can see the trial solution corresponding to maximal error, $c^{trial}(\mathbf{p}_{max})$, as defined by equation (5.6), compared with the \tilde{H}^1 PBDW approximations from manually-chosen sensor locations and the newly adapted Greedy sensors, similarly to figure 5.12 in section 5.3. We see

reasonable reconstruction of the physical state with both sensor sets. While the Greedy sensors add a very small phantom concentration in some regions, this error is negligible. The Greedy system has more accurately reconstructed the concentration peak near the source, however both PBDW approximations underestimate the peak. The under-representation of the concentration remains relatively small.

In figure 5.40 we can see relative mean the best-fit errors from equation (4.17) corresponding to the \tilde{H}^1 PBDW approximation spaces. The projection error is computed over a set of trial solutions with significant model error ($R = 0.001$) in the H^1 norm. Here we see a significant difference induced by the change in Update space due to the \tilde{H}^1 norm. We notice that in the case of a perfect model, for each N -value the relative best-fit error is nearly constant with respect to M . This implies that, as was the case in figure 5.13, our Update basis functions q_m do not provide new information outside the span of the background approximation space \mathcal{Z}^N . This effect is again to be expected, however for a different reason as in section 5.3. The trial solutions were computed with the same bk model as the reduced basis, which is meant to approximate the associated solution space, meaning the information on these trial solutions should be in the background space. However, we see improvement of the best-fit error in the case of an imperfect model, thanks to our new Update basis with larger support. The added update basis functions now enlarge the span of the PBDW approximation space $\mathcal{Z}^N \oplus (\mathcal{U}^M \cap \mathcal{Z}^{N\perp})$ to capture information on the trial solutions from the shifted model not spanned by the background space. We also note that additional background basis functions do not greatly improve the approximation, as the trial solutions do not lie on the same solution manifold.

In figures 5.41 and 5.42 we see relative mean and maximal error curves for the \tilde{H}^1 PBDW approximation with sensor locations in figure 5.38 for each of two trial sets. We can see that with no model error with $N = 6$ Background functions we again achieve $\sim 1\%$ mean error, and $\sim 3\%$ error with significant model error. We note that we see more consistent error results with respect to figures 5.33, 5.32 5.36, and 5.35.

In figure 5.43 for adapted Greedy sensors we see relative mean errors mapped over the domain in the case of no model error, for the \tilde{H}^1 PBDW system. Here we see a bit more improvement between $M = 8$ and $M = 15$, which can be attributed to better-placed sensors. However, the background space alone can represent these trial solutions, so as expected the most improvement is provided by N .

In figure 5.44 we consider adapted Greedy sensors for the case of significant model error. Here we see more significant improvement with added data points. We again note that the correction by the update basis functions can add non-physical error to the approximation, however this is generally of negligible order. Again we see significant improvement between $N = 2$ and $N = 6$. We see that with $N = 6$ and $M = 15$ the error is under 7% everywhere, and often under 1%.

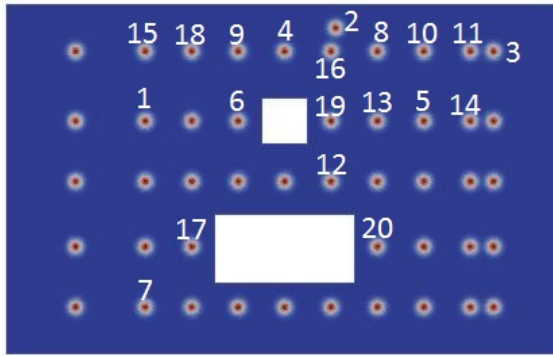


Figure 5.38 – Sensors locations chosen by a GEIM-based Greedy algorithm over \tilde{H}^1 Update basis functions q_m defined by equation (3.8).

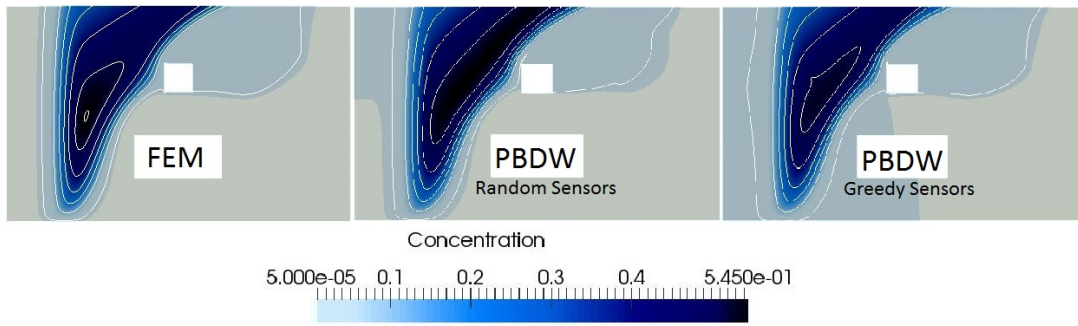


Figure 5.39 – Approximation of the concentration for $\mathbf{p} = \mathbf{p}_{max}$. Trial solution with model error simulated by a reaction term of $R = 0.001$. FEM solution c^{true} (left), \tilde{H}^1 PBDW approximation using synthetic data, with random sensors (middle), \tilde{H}^1 PBDW approximation with greedy selected sensors of figure 5.38 (right). We set $M = 13$ and $N = 6$ here.

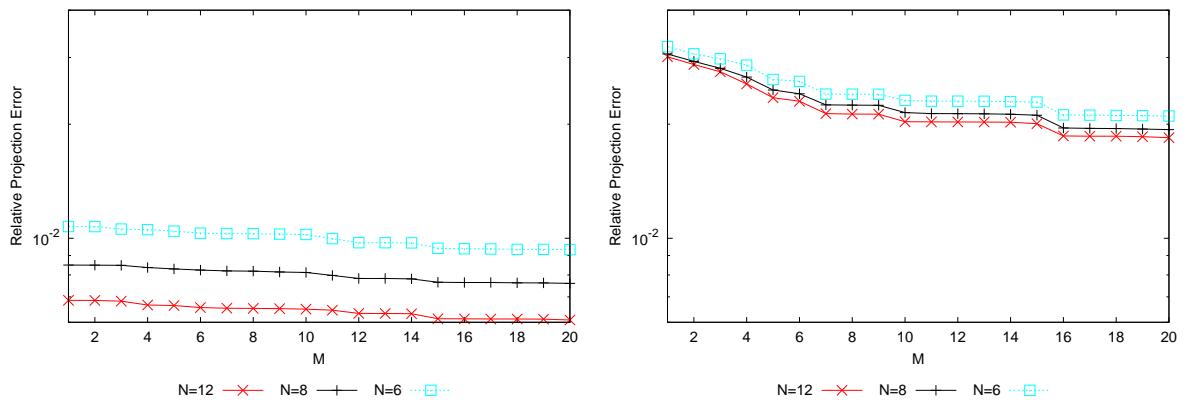


Figure 5.40 – Relative mean best-fit error onto the \tilde{H}^1 PBDW approximation spaces, equation (4.17). Set of trial solutions over $\mathbf{p} \in \mathcal{D}^{trial}$, as a function of M in H^1 -norm. No model error (left), and model error with an added reaction term of $0.001c$ (right). Greedy selected sensors of figure 5.38.

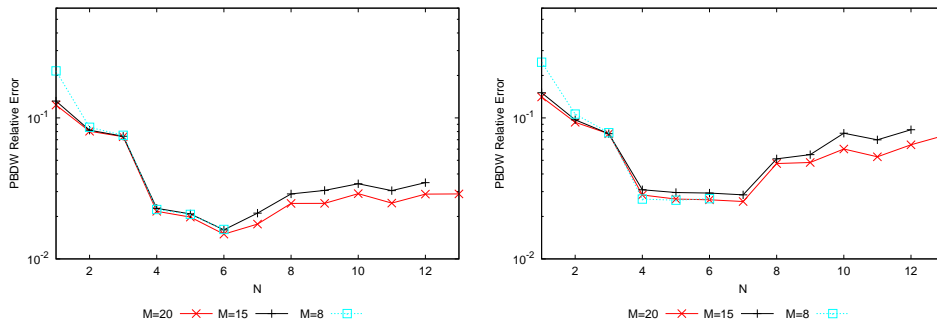


Figure 5.41 – Relative mean (equation (5.10), left) and maximal (equation (5.11), right) \tilde{H}^1 PBDW approximation error in H^1 -norm as a function of Background RB dimension N for various numbers of data points M , over $\mathbf{p} \in \mathcal{D}^{trial}$ with no model error. Greedy selected sensors of figure 5.38.

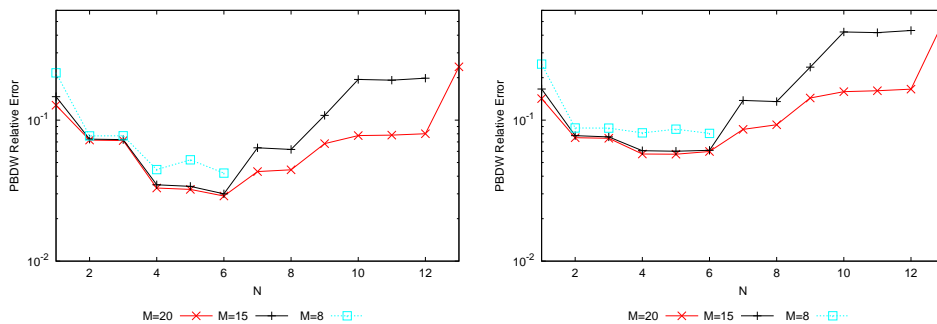


Figure 5.42 – Relative mean (equation (5.10), left) and maximal (equation (5.11), right) \tilde{H}^1 PBDW approximation error in H^1 -norm as a function of Background RB dimension N for various numbers of data points M , over $\mathbf{p} \in \mathcal{D}^{trial}$, model error with an added reaction term of $R = 0.001$. Greedy selected sensors of figure 5.38.

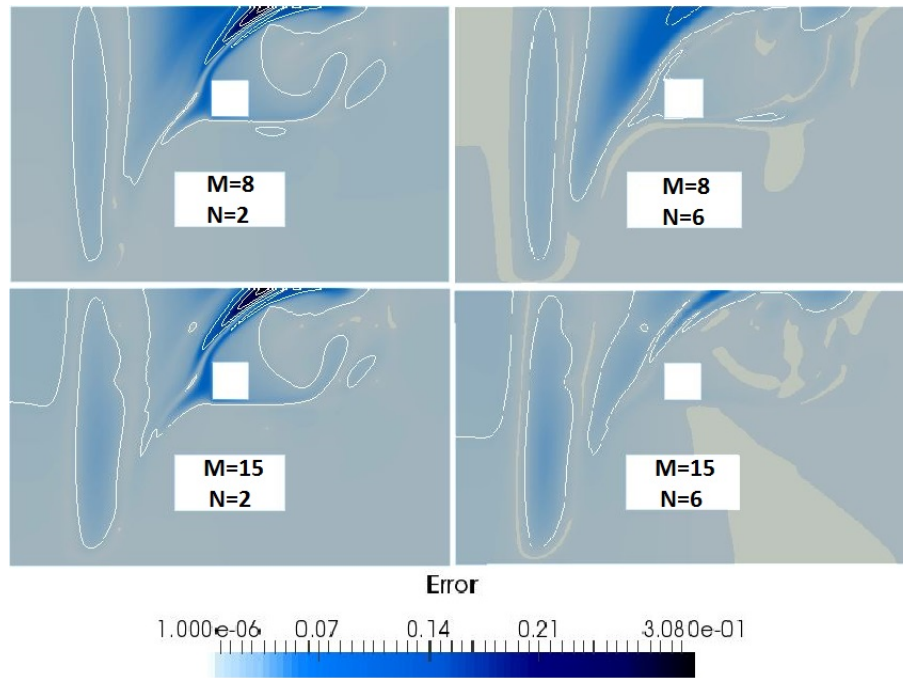


Figure 5.43 – Relative mean pointwise \tilde{H}^1 PBDW approximation error maps, equation (5.9), for $N = 2$ (left), $N = 6$ (right), and for $M = 8$ (top) and $M = 13$ (bottom), over $\mathbf{p} \in \mathcal{D}^{trial}$ with no model error. The lowest contour line shows 1% error. Greedy selected sensors of figure 5.38.

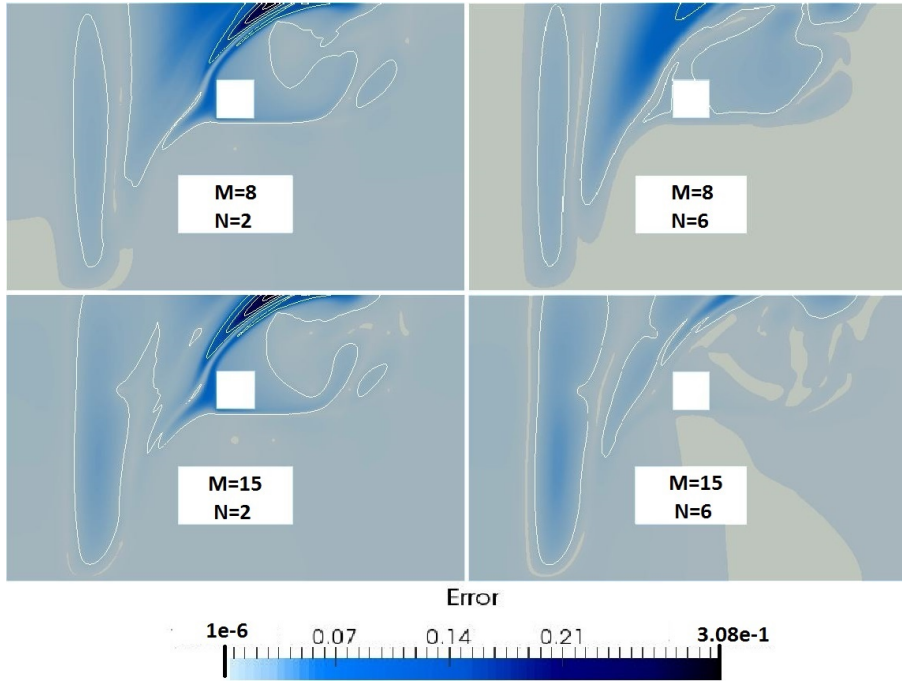


Figure 5.44 – Relative mean pointwise \tilde{H}^1 PBDW approximation error maps, equation (5.9), for $N = 2$ (left), $N = 6$ (right), and for $M = 8$ (top) and $M = 13$ (bottom), over $\mathbf{p} \in \mathcal{D}^{trial}$ with model error by an added reaction term of $0.001c$. The lowest contour line shows 1% error. Greedy selected sensors of figure 5.38.

5.5 Comparison to other methods: GEIM

In this section we want to compare the results of the PBDW state estimation on this two-dimensional case study to those obtained by the GEIM interpolation method discussed in previous sections. The GEIM method is implemented with $M = N$, equal number of basis functions and data points. Below we can see the results of the two methods, both of which we implemented offline from the same set of training solutions and sensors, and applied to the same set of 6 trial solutions of varying parameters and with added model error.

We can see that the GEIM method performs similarly, and even surpasses for $M = 10$, to the PBDW method in the case of little model error. However in the case of significant model error and $M > 10$, the PBDW method provides a significantly better estimation. In this particular case study, we seem to have more consistent error results for varying M -values, and aspect that could be valuable in online studies without feasible error analysis.

In figures 5.46, and 5.47 we compare relative mean error maps of the GEIM and PBDW approximations using synthetic data with little or significant model error. We consider the case of $M = 10$, the best case of the GEIM approximation according to figure 5.45. We can see similar results for little model error, with only a small region over 1% error in both approximations, while the GEIM approximation eliminates a region of error with respect to the PBDW estimation. In the case of

significant model error, however, we see a clear advantage in the PBDW estimation, with no peak above 14% and only a small under representation of the source intensity.

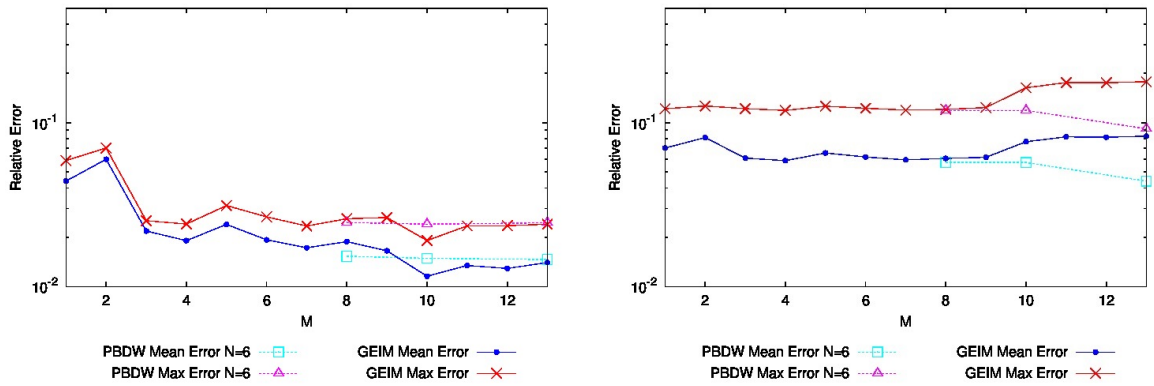


Figure 5.45 – Relative mean (5.10) and maximal (5.11) PBDW approximation error as a function of number of data points M for background basis dimension $N = 6$, and GEIM interpolation errors as a function of $M = N$. Using synthetic trial data for parameter set Ξ^{trial} from model \mathcal{P}^{trial} with a small added reaction term of $R = 0.0001$ (left), and significant model error from $R = 0.001$ (right). Sensor locations chosen by a greedy procedure.

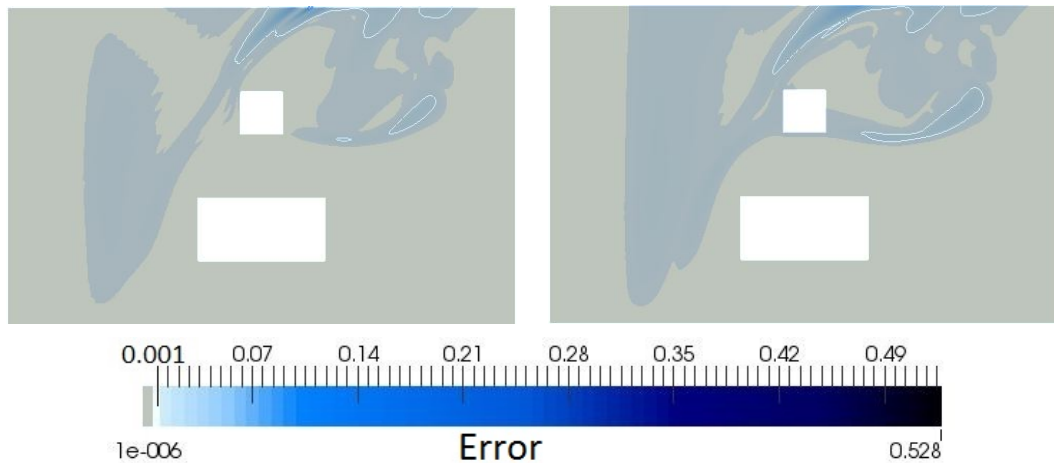


Figure 5.46 – Relative mean errors of the GEIM (left) with $M = 10$ and the PBDW (right) with $M = 10$, $N = 6$, approximations, mapped over the calculation domain. Using greedy selected sensors and synthetic trial data over parameters Ξ^{trial} on model \mathcal{P}^{trial} , with model error added by a reaction term of $R = 0.0001$. Mapping of the errors is truncated at 1×10^{-6} , and the lowest contour line shows 1% error.

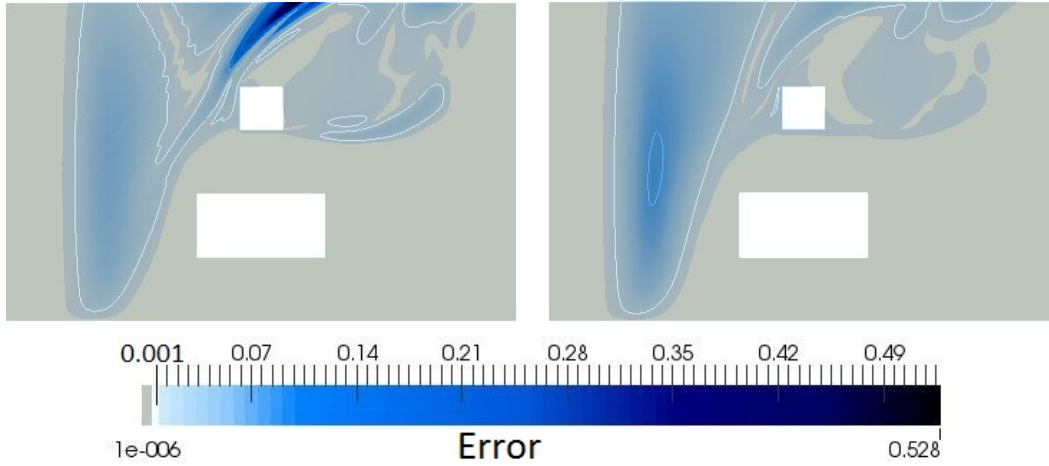


Figure 5.47 – Relative mean errors of the GEIM (left) with $M = 10$ and the PBDW (right) with $M = 10$, $N = 6$, approximations, mapped over the calculation domain. Using greedy selected sensors and synthetic trial data over parameters Ξ^{trial} on model \mathcal{P}^{trial} , with model error added by a reaction term of $R = 0.001$. Mapping of the errors is truncated at 1×10^{-6} , and the lowest contour line shows 1% error.

5.5.1 Norm modifications

This section describes an update to the PBDW and GEIM comparison in light of improved implementation of the \tilde{H}^1 norm in section 5.4.1 with $L_g = 75m$. In figure 5.48 we see that in the case of significant model error and $M > 10$, the \tilde{H}^1 PBDW method provides a significantly better estimation than the GEIM. In this particular case study, we seem to have more consistent error results for varying M -values, and aspect that could be valuable in online studies without feasible error analysis.

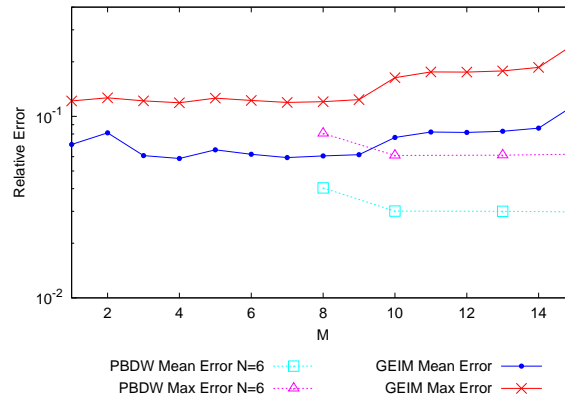


Figure 5.48 – Relative mean and maximal \tilde{H}^1 PBDW errors as a function of number of data points M for PBDW Background basis dimension $N = 6$, and GEIM interpolation errors as a function of $M = N$, over $\mathbf{p} \in \mathcal{D}^{trial}$. Model error by an added reaction term $0.001c$. Greedy selected sensors of figure 5.38 for the PBDW estimation, and of figure 5.7 for the GEIM approximation.

In figure 5.49 we compare relative mean error maps for the GEIM and \tilde{H}^1 PBDW

approximations over trial sets with little ($R = 0.0001$) or significant ($R = 0.001$) model error. We consider the case of $M = 10$. We again see similar results for little model error, with only a small region over 1% error in both approximations, while the GEIM approximation reduces a region of error with respect to the \tilde{H}^1 PBDW estimation. In the case of significant model error, however, we see a clear advantage in the \tilde{H}^1 PBDW estimation, with no peak near or above 15% and only a small misrepresentation of the source intensity.

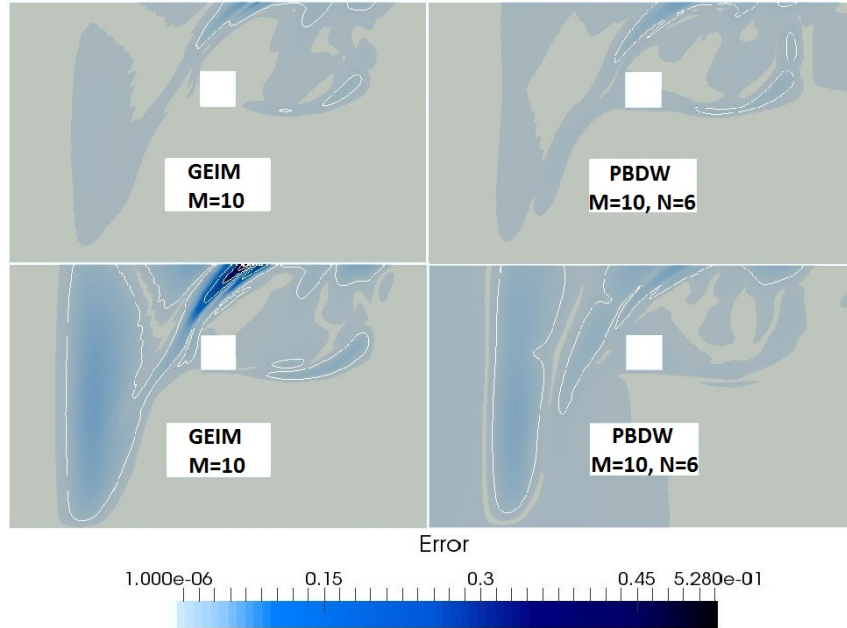


Figure 5.49 – Relative mean pointwise GEIM (left) and \tilde{H}^1 PBDW (right) approximation error maps for $M = 10$ and $N = 6-M = 10$, respectively, over $\mathbf{p} \in \mathcal{D}^{trial}$. Model error of $0.0001c$ (top) and $0.001c$ (bottom). Mapping of the errors is truncated at 1×10^{-6} , and the lowest contour line shows 1% error. Greedy selected sensors of figure 5.38 for the PBDW estimation, and of figure 5.7 for the GEIM approximation.

5.6 Comparison to other methods: the adjoint problem

In this section we would like to compare the PBDW method not to the similar GEIM method for non-intrusive reduced-order data assimilation, but to the more classical adjoint method (section 2.2.3.1) to treat data assimilation with a parameterized PDE model for urban fluxes. We chose to work with a simplified version of our case study. Instead of using CFD velocity fields computed with *Code_Saturne*, we used velocity fields given by the Stokes equations, and we also replaced the turbulent viscosity field by a single aggregated turbulence field from *Code_Saturne*. This decision was made because one of the parameters to calibrate by the adjoint problem is actually the wind field, meaning the adjoint method would be applied, in addition to the concentration equation (4.52), to both the fluid model from Navier-Stokes (4.31) and the $k - \epsilon$ turbulence model (4.33). Not only would this feat, which has been investigated in [193] for water networks using Navier-Stokes with no turbulence

closure, be far from trivial to implement, but would require measurement data on the wind field (which we assume *a priori* is not among the data available). We thus consider the Stokes formulation for our wind velocity over the computational domain, given by equation (5.21), and that the direction \vec{v}_d of the inflow is fixed but the intensity v_{in} is a parameter.

5.6.1 Adjoint Transport Problem: problem definition

Here we first we expose the details of the adjoint problem and associated Lagrangien and gradient descent method, used in the application of the adjoint inverse method (section 2.2.3.1) for the estimation of optimal parameters of the best-knowledge transport problem given by (4.52).

If we've defined the M sensors as in equation (3.5), then we have that the mismatch function as described in equation (2.55), for sensor function φ_m from equation (3.4) and data y_m^{obs} , is written:

$$e_m(c) = \int \varphi_m c \, d\Omega - y_m^{obs}(c) \quad (5.15)$$

Considering the cost functional given by equation (2.56), the associated Lagrangien is defined by

$$\begin{aligned} \mathcal{L}(p, c, \phi, \psi) = & I(c) - \left(\int_{\Omega} \epsilon(x) \nabla c \cdot \nabla \phi + \int_{\Omega} \vec{v} \cdot \nabla c \phi - \int_{\Omega} F_{src} \phi \right) \\ & - \int_{\Gamma_{in}} (c - c_0) \psi, \end{aligned} \quad (5.16)$$

where $I(c)$ is given by equation (2.57), and ϕ and ψ are the Lagrange multipliers associated to the following constraints:

- $\phi \in X'$: multiplier associated to the constraint “ c is a solution of (4.52)”
- $\psi \in \mathbb{R}$: multiplier associated to the constraint “ $c = c_0$ on Γ_D ”

Differentiating (5.16) along an element $w \in X_0$ with respect to c we have:

$$\begin{aligned} \left\langle \frac{\partial \mathcal{L}}{\partial c}, w \right\rangle &= \sum_{k=1}^M e_k(c) \ell_k(w) - \int_{\Omega} \epsilon(x) \nabla w \cdot \nabla \phi - \int_{\Omega} \vec{v} \cdot \nabla w \phi - \int_{\Gamma_{in}} w \psi \\ &= \sum_{k=1}^M e_k(c) \int_{\Omega} \sigma_k(w) d\Omega - \int_{\Omega} \epsilon(x) \nabla w \cdot \nabla \phi + \int_{\Omega} \vec{v} \cdot \nabla \phi w \\ &\quad - \int_{\partial\Omega} \phi w (\vec{v} \cdot \vec{n}) - \int_{\Gamma_{in}} w \psi \end{aligned} \quad (5.17)$$

If we set equation (5.17) to zero we get the variational formulation of the adjoint problem of which the solution is given by:

$$\begin{cases} -\operatorname{div}(\epsilon(x)\nabla\phi(\mathbf{p})) - \vec{v} \cdot \nabla\phi(\mathbf{p}) = \sum_{k=1}^M \varphi_k e_k(c(\mathbf{p})) & \text{in } \Omega \\ \phi(\mathbf{p}) = 0 & \text{on } \Gamma_{in} \\ -\epsilon(x)\nabla\phi(\mathbf{p}) \cdot \vec{n} + \phi(\mathbf{p}) \vec{v} \cdot \vec{n} = 0 & \text{on } \partial\Omega \setminus \Gamma_{in} \end{cases} \quad (5.18)$$

and $-\epsilon(x)\nabla\phi \cdot \vec{n} = \psi$ on Γ_{in} because

$$\int_{\Gamma_{in}} (\psi - \epsilon(x)\nabla\phi \cdot \vec{n} + \phi \vec{v} \cdot \vec{n}) w = 0$$

The derivative of the Lagrangian $\mathcal{L}(\mathbf{p}, c, \phi, \psi)$ with respect to c is null in $(\mathbf{p}, c(\mathbf{p}), \phi, \psi)$ with $c(\mathbf{p})$ the solution of (4.52), and for any (ϕ, ψ) we have

$$J(\mathbf{p}) = \mathcal{L}(\mathbf{p}, c(\mathbf{p}), \phi, \psi)$$

In this adjoint problem, we see the advection and diffusion terms present, but along an opposite-direction velocity field $\vec{v}_{adj} = -\vec{v}$, and with the source terms replaced by $\sum_{k=1}^M \varphi_k e_k(c(\mathbf{p}))$. We thus will see the same instability problems as in the direct transport problem and need to implement numerically with a stabilization. As such, we define the SUPG-stabilized adjoint transport problem:

$$\begin{cases} a_{adj}^{SUPG}(\phi_h, w_h) \equiv a_{adj}(\phi_h, w_h) + \sum_k \tau_k (\mathcal{L}^{adj} \phi_h, \vec{v}_{adj} \cdot \nabla w_h)_k \\ l_{adj}^{SUPG}(w_h) \equiv l_{adj}(w_h) + \sum_k \tau_k (\sum_{k=1}^M \varphi_k e_k(c(\mathbf{p})), \vec{v}_{adj} \cdot \nabla d_h)_k \end{cases} \quad (5.19)$$

where $\mathcal{L}^{adj} \phi_h = -\operatorname{div}(\epsilon(x)\nabla\phi(\mathbf{p})) + \vec{v}_{adj} \cdot \nabla\phi(\mathbf{p})$, $a_{adj}(\phi_h, w_h) = \int_{\Omega} \epsilon(x)\nabla w \cdot \nabla\phi - \int_{\Omega} \vec{v}_{adj} \cdot \nabla w \phi$, and $l_{adj}(w_h) = \sum_{k=1}^M e_k(c)\ell_k(w_h)$.

5.6.2 Definition of the parameters

We consider that the direction \vec{v}_d of the inflow wind is fixed but the intensity v_{in} is a parameter.

In this study, we will thus have two parameters :

- intensity of the pollution : α_i
- intensity of the inflow wind : v_{in}

The source of pollution is of the form

$$F_{src} = \sum_{i=1}^{N_s} \alpha_i f_i \quad (5.20)$$

where N_s is the number of possible sources, α_i are intensities, and f_i represents the source i (e.g. as in equation (4.43) or (4.42)).

In this case we have $F_{src}(x) = \alpha f_{src}(x)$ where $\alpha \in [0, 10^{-2}] \frac{mg}{m^3 \cdot s}$, but we will start with α constant. In the interest of maintaining linear constraints and reasonable computational times for a more direct comparison of methods, the velocity field for inflow wind direction \vec{v}_d and intensity v_{in} can be approximated by the solution of the following Stokes equation

$$\left\{ \begin{array}{ll} -\nu \Delta \vec{v}(x, \mathbf{P}) + \nabla p(x, \mathbf{P}) = 0 & \text{in } \Omega, \\ \operatorname{div} \vec{v}(x, \mathbf{P}) = 0 & \text{in } \Omega, \\ \vec{v}(x, \mathbf{P}) = v_{in} \vec{v}_d & \text{on } \Gamma_{in}, \\ \vec{v}(x, \mathbf{P}) = \vec{0} & \text{on } \Gamma_{wall}, \\ -\nu \frac{\partial v_i}{\partial n}(x, \mathbf{P}) + p(x, \mathbf{P}) = 0 & \text{on } \Gamma_{out}, \end{array} \right. \quad (5.21)$$

where v_i , $i = 1, 2$ are the x_i -component of the velocity field. Using a superposition principle, the solution $\vec{v}(x, \mathbf{P})$ of the problem (5.21), for any value of v_{in} , can be obtained by

$$\vec{v}(x, \mathbf{P}) = v_{in} \vec{v}_0(x)$$

where $\vec{v}_0(x)$ is the solution of (5.21) with $v_{in} = 1$.

As for the turbulent viscosity, we will use an aggregated viscosity defined by

$$\nu_t = \frac{1}{N_{train}} \sum_{k=1}^{N_{train}} \bar{\nu}_t(v_{in}^k) \quad \text{with} \quad v_{in}^k \in \Xi_{train}^{bk} \subset [0.1; 1.3] \frac{m}{s}, \quad (5.22)$$

and $\bar{\nu}_t(v_{in}^k)$ is the turbulent viscosity given by a *Code_Saturne* simulation where we imposed the inlet boundary condition such that $|v_{max}| = v_{in}^k$ at the boundary.

Suppose that $\mathbf{P} = (p_1, \dots, p_{N_p})$ where N_p is the number of parameters of our model. Then,

$$\frac{\partial J(x, \mathbf{P})}{\partial p_i} \lambda_i = \frac{\partial \mathcal{L}}{\partial p_i}(\mathbf{P}, c(x, \mathcal{P}), \phi(x, \mathbf{P})) \lambda_i \quad (5.23)$$

where $\lambda_i \in \mathbb{R}$ and $1 \leq i \leq N_p$. For $p_i = \alpha_i$, we have

$$\frac{\partial J(p)}{\partial p_i} \lambda = \frac{\partial \mathcal{L}}{\partial \alpha_i}(\alpha, c(\alpha), \phi(\alpha)) \lambda = \int_{\Omega} \lambda f_i \phi(p), \quad (5.24)$$

and

$$\frac{\partial T(p)}{\partial p_i} \lambda = \frac{\partial T(p)}{\partial \alpha_i} \lambda = \xi (\alpha_i - \alpha_i^0) \lambda, \quad (5.25)$$

For $p_i = v_{in}$, we have

$$\frac{\partial J(x, \mathbf{P})}{\partial p_i} \lambda_i = -\lambda_i \int_{\Omega} \vec{v}_0 \cdot \nabla c(\mathbf{P}) \phi(\mathbf{P}).$$

With Tikhonov regularization we have also

$$\frac{\partial T(x, \mathbf{P})}{\partial p_i} \lambda_i = \xi(p_i - p_i^0) \lambda_i, \quad \forall \lambda_i \in \mathbb{R}.$$

We will see the implementation of this inverse method in the case studies considered in sections 5.6.

5.6.3 State estimation results

In order to estimate the Kolmogorov dimension of \mathcal{M}_h the manifold of all the solutions of \mathcal{P}^{bk} (4.52) when the parameters vary, we resort to a POD analysis. In our study, the parameter α (intensity of the pollution) being linear, we only need to compute a set of concentration when the velocity intensity v_{in} varies. Let $\Xi_{train} \subset \mathcal{D} = [0.1 : 1.3]m/s$ be the set of parameter used to compute a POD basis. This POD analysis consist in a singular value decomposition method to the correlation matrix of H^1 -norm scalar products $\langle c_h(\mathcal{P}_i), c_h(\mathcal{P}_j) \rangle_{H^1(\Omega), 1 \leq i, j \leq N_{train}}$, for different values of the parameters $\mathcal{P} \in \Xi_{train}$.

An H^1 -orthonormalized POD basis (2.10) was constructed, as described in section 2.1.2.2, and we define P_N^{POD} be the H^1 -orthogonal projection operator from X_h into the space X_N^{POD} – spanned by the N first POD basis functions w_k , as defined by equation (2.11). Let $\mathcal{D}^{trial} \subset \mathcal{D} = [0.1 : 1.3]m/s$ be a set of parameters such that $\mathcal{D}^{trial} \cap \mathcal{D}^{training} = \emptyset$. Each training solution $\{c_h(\mathcal{P}_i), \mathcal{P}_i \in \Xi_{train}\}$ and trial solution $\{c_h(\mathcal{P}_i), \mathcal{P}_i \in \Xi_{trial}\}$ were projected onto $X_h^{k,POD}$ to analyze the ability of the POD basis to approach the manifold \mathcal{M}_h , depending on the number of POD modes. In figure 8.5 we can see the associated errors plotted. We observe that the projection errors decay rapidly and are quite small.

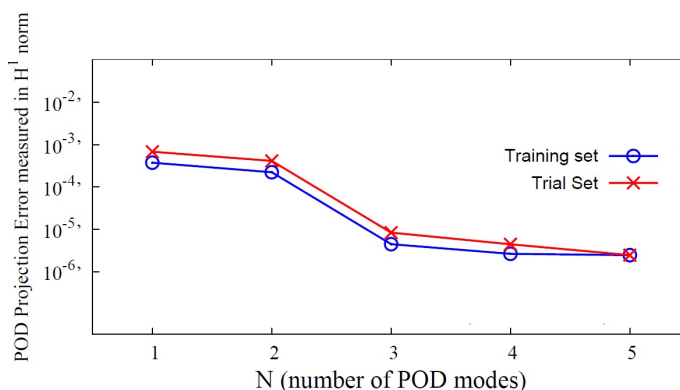


Figure 5.50 – Relative error of the POD projection measured in H^1 norm for several sets of concentration

We first selected sensors by a Greedy GEIM-based algorithm from a sparse grid of 15 possible locations, seen in figure 5.51.

In figure 5.52 we see the selected sensors.

Let c^{bk} be the solution from the best knowledge model, \mathbf{p}_{adj} the set of parameters obtained by the adjoint method and $c^{bk}(\mathbf{p}_{adj})$ the corresponding concentration, c^{true}

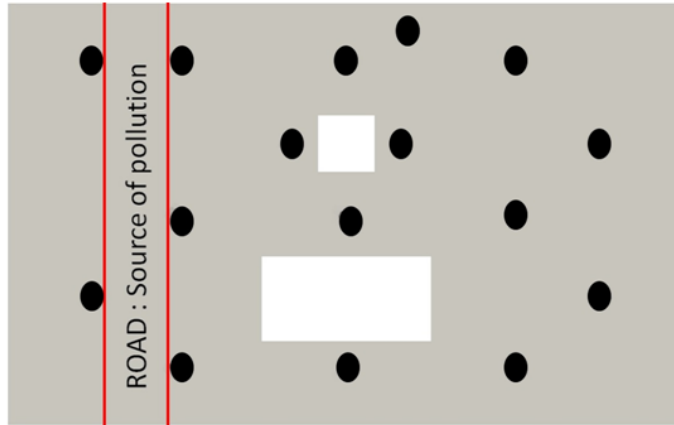


Figure 5.51 – Sensor locations considered for the Adjoint vs. PBDW comparison, sparse grid on which we performed a Greedy selection.

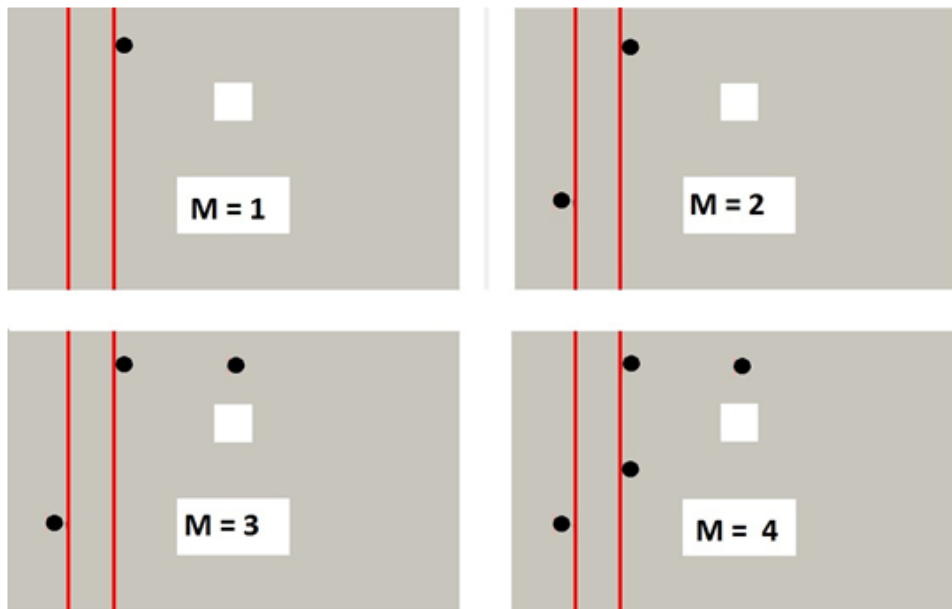


Figure 5.52 – Sensor locations considered for the Adjoint vs. PBDW comparison. Selected sensors for $M = 1, 2, 3, 4$.

be the true concentration, \mathcal{I}_M be the "best-knowledge"-based GEIM interpolation operator and c^{pbdw} the PBDW approximation. In table 5.2 we have compared relative error on the reconstructed concentration, measured in H^1 -norm, with no model error and $M = 2$ measurements. We can see that the adjoint and PBDW methods perform similarly in terms of precision, but the adjoint method requires 26 iterations (i.e. 26 approximations each of the direct and adjoint problem by classical discrete methods), while the PBDW requires the solution of a 3×3 linear system. We also note that the GEIM method outperforms both the adjoint method by one order of precision, which is unsurprising given the better performance of the GEIM in the case of a perfect model in seen in section 5.5.

Adjoint method with $M = 2$ $c^{true} - c^{bk}(\mathbf{p}_{adj})$	GEIM with $M = 2$ $c^{true} - \mathcal{I}_M(c^{true})$	PBDW with $M = 2, N = 1$ $c^{true} - c^{pbdw}$
0.00161454 (26 iterations)	0.000264946	0.00180676

Table 5.2 – Global Error measured in H^1 -norm (relative error) using greedy sensor position (1 iteration = 1 FEM direct approximation + 1 FEM adjoint approximation)

In table 5.3 we have compared error on the reconstructed concentration, measured in the H^1 -norm, when there is model error and $M = 2$ measurements. We consider two sources of model error: a reaction term R as in section 5.3, or error in the calculation of the wind field by (5.21). In the latter case the "true" wind field \vec{v}^{true} is simulated by Navier-Stokes (4.31) with $k - \epsilon$ turbulent closure. We recall here that the GEIM operator \mathcal{I}_M was built using solution from the "best-knowledge" model.

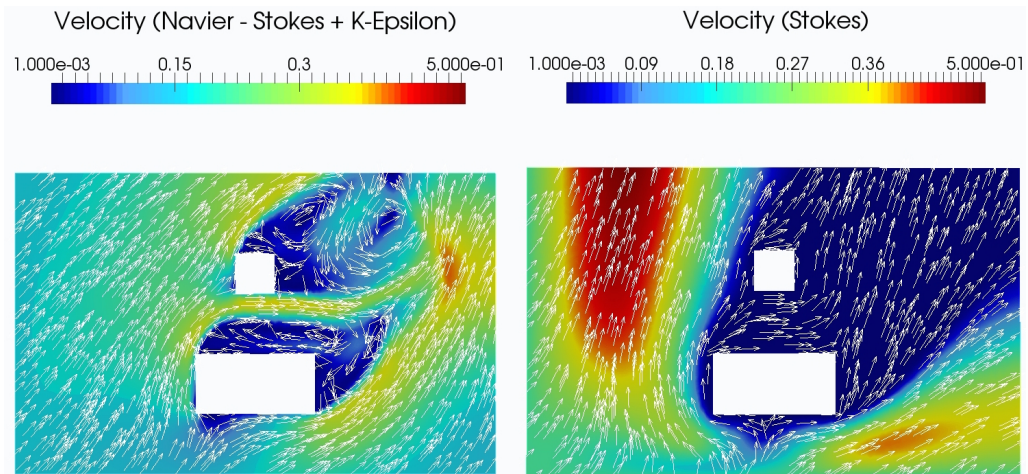


Figure 5.53 – Wind field computed by Navier-Stokes with $k - \epsilon$ turbulence closure (left), compared to a wind field computed by Stokes (right).

We can in figures 5.53 and 5.54 that this model error in the velocity field is quite severe, in stark contrast to the the levels of model error induced by the added reaction terms in section 5.3.

We can see that in the case of a shifted model \mathcal{P}^{trial} by a linear reaction term $R = 0.001$, the PBDW method performs the best, with under 6% of error, and the adjoint and GEIM methods follow closely behind. However the adjoint method needs 34 iterations to achieve these results, a computationally costly procedure. In the case of model error in the velocity field none of the methods manages to

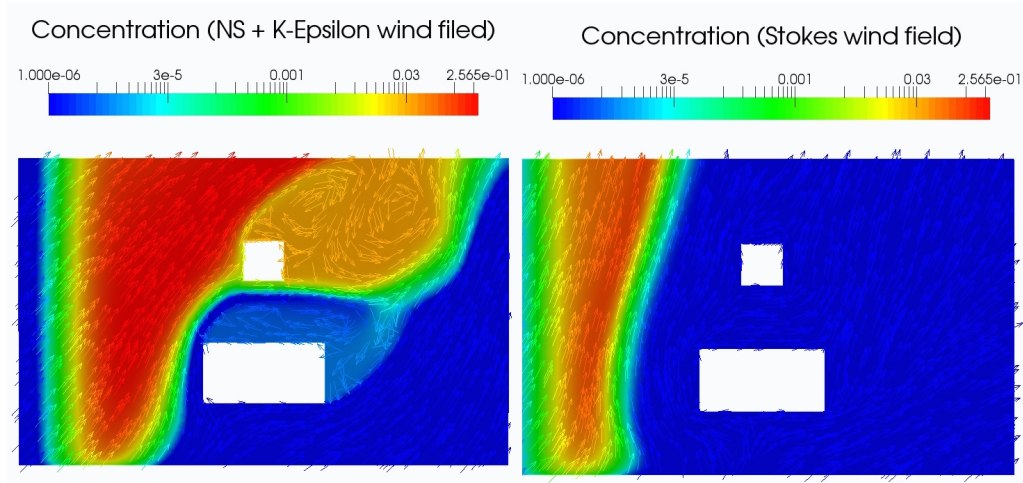


Figure 5.54 – Concentration field from \mathcal{P}^{bk} over a Navier-Stokes wind/turbulence field (left), compared to a concentration field over a Stokes wind field with a single aggregated Navier-Stokes turbulence field (right).

	Model Error	Adjoint method ($M = 2$)	GEIM ($M = 2$)	PBDW ($M = 2, N = 1$)
True model: $R = 1 \times 10^{-3}$	$c^{true} - c^{bk}(\mathbf{p}^{true})$ 0.089632	$c^{true} - c^{bk}(\mathbf{p}_{adj})$ 0.0598593 (34 iterations)	$c^{true} - \mathcal{I}_M(c^{true})$ 0.0646513	$c^{true} - c^{pbdw}$ 0.0558197
True model: Navier-Stokes	1.44017	0.918449 (49 iterations)	0.808705	0.815477

Table 5.3 – Global Error measured in H^1 -norm (relative error) using greedy sensor position (1 iteration = 1 FEM direct approximation + 1 FEM adjoint approximation)

effectively reconstruct the pollution field, however the GEIM and PBDW perform slightly better than the adjoint method.

In the tables 5.4, 5.5, and 5.6 we compare the reconstructed concentration obtained with the PBDW and the GEIM with $M = 2$ to $M = 4$ measurements, in each of the three trial cases.

In table 5.4 we can see that the GEIM outperforms the PBDW consistently by approximately one order of precision.

In table 5.5 the GEIM performs better for only $M = 2$ sensors, but the PBDW achieves slightly higher precision for $M \geq 3$, thanks to its model error correction in the update term.

		PBDW		GEIM
M	N	Measured in L^2 -norm	Measured in H^1 -norm	Measured in H^1 -norm
2	1	0.00167063	0.00180676	0.000264946
2	2	0.00225851	0.00221687	
3	1	0.00167056	0.00180672	5.66303×10^{-6}
3	2	0.00172873	0.00169383	
3	3	1.33289×10^{-5}	1.90045×10^{-5}	
4	1	0.00167056	0.00180671	1.19627×10^{-7}
4	2	0.00145774	0.00143721	
4	3	1.32982×10^{-5}	1.89733×10^{-5}	
4	4	3.40861×10^{-5}	5.52569×10^{-5}	

Table 5.4 – Global Error (relative error) using greedy sensors position with no Model Error

		PBDW		GEIM
M	N	Measured in L^2 -norm	Measured in H^1 -norm	Measured in H^1 -norm
2	1	0.0554883	0.0558197	0.0646513
2	2	0.135202	0.138185	
3	1	0.0554883	0.0558197	0.0624035
3	2	0.102717	0.104952	
3	3	0.051463	0.0599434	
4	1	0.0554883	0.0558198	0.0860289
4	2	0.0842945	0.0860841	
4	3	0.0514849	0.0599753	
4	4	0.0551605	0.0739137	

Table 5.5 – Global Error (relative error) using greedy sensor position with Model Error: true solution with linear reaction $r = 10^{-3}$

		PBDW		GEIM
M	N	Measured in L^2 -norm	Measured in H^1 -norm	Measured in H^1 -norm
2	1	0.808053	0.814611	0.808705
2	2	1.07974	1.09336	
3	1	0.808048	0.814609	0.755544
3	2	0.847354	0.853547	
3	3	0.767675	0.77688	
4	1	0.807876	0.814501	96.9648
4	2	0.803784	0.810851	
4	3	0.735551	0.74329	
4	4	289.299	499.063	

Table 5.6 – Global Error (relative error) using greedy sensors position with Model Error: true solution with Navier-Stokes with $k - \epsilon$ turbulence closure wind field

In table 5.6, both methods perform poorly and provide unstable results, no better than around 75% error.

We next study the results of the PBDW method when sensors are chosen by a greedy procedure from a much less sparse set of locations, seen in figure 5.55. Figure 5.56 shows the selected sensors for up to $M = 6$ sensors.

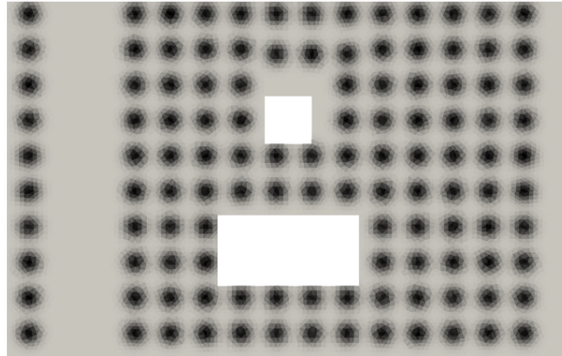


Figure 5.55 – Sensor locations considered for the PBDW method, a grid of 100 possible sensors on which we perform a Greedy selection.

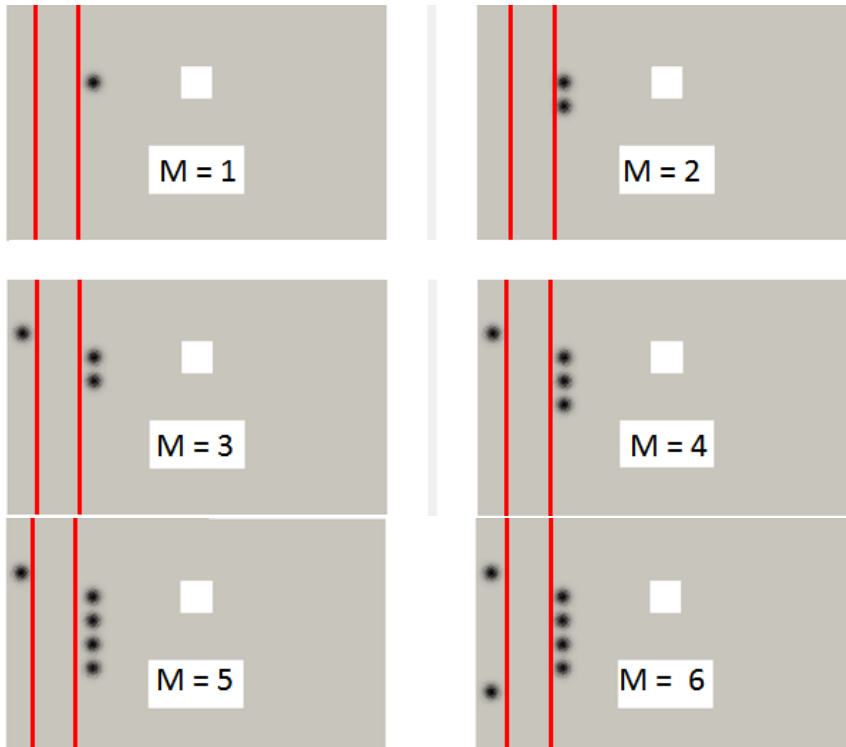


Figure 5.56 – Grid of sensor locations considered for the PBDW method. Selected sensors for $M = 1$ through $M = 6$.

In table 5.7 we see the relative error results of the PBDW method for the three trial cases, considering up the $M = 6$ and $N = 4$. We can see that in the case of a perfect model \mathcal{P}^{bk} only $N = 3$ background basis functions are required to approximate the solution manifold \mathcal{M}^{bk} , and the addition of supplementary basis functions, which are of very small norm after the Gram-Schmidt orthonormalization process, renders the method less stable. We see excellent reconstruction of the state in the case of a perfect model, and wholly satisfactory reconstruction in the case of \mathcal{P}^{trial} with a linear reaction term of $R = 0.001$. However in the case of model error in the velocity field, we see instability from $N > 1$, which we attribute to the strong differences in the Stokes vs. Navier-Stokes fields.

M	N	No model error	Model Error : linear reaction	Model Error : velocity NS + $k - \epsilon$
2	1	0.00143845	0.0541295	0.953214
2	2	0.00833031	0.068833	8.92753
3	1	0.00143806	0.0541278	0.953208
3	2	0.00111454	0.0540292	1.07518
3	3	$2.37966e - 05$	0.0538432	1.24394
4	1	0.00143961	0.0540795	0.96318
4	2	0.00124217	0.0542685	1.18722
4	3	$2.36478e - 05$	0.0538542	1.22608
4	4	0.000223533	0.0571449	84.2731
5	1	0.00143934	0.0540764	0.954574
5	2	0.00126515	0.0542688	1.68631
5	3	$2.37248e - 05$	0.0538322	1.37484
5	4	0.000209717	0.055371	94.0984
6	1	0.00143892	0.0540742	0.954564
6	2	0.00125894	0.0542696	1.32241
6	3	$2.39223e - 05$	0.0538388	1.26228
6	4	0.000108483	0.0538581	92.6699

Table 5.7 – Global relative error (measured in H1 norm) of the PBDW method

We conclude from this comparison that in the case of little to no model error, the GEIM method outperforms the PBDW in terms of precision, and outperforms the adjoint method in terms of computational time, while the PBDW only outperforms the adjoint method in computational time. However, in the case of more significant model error, such as \mathcal{P}^{trial} as in equation (4.70), the PBDW method gives the most precise results and significantly reduces computational cost as compared with the adjoint method. However, each of these methods has limitations, and none was robust enough to treat the case of severe model error in the transporting wind field. We note that in the case of PBDW and GEIM, nothing prevents us from using the more accurate velocity fields from Navier-Stokes with $k - \epsilon$ turbulent closure (excepting

offline computation time), whereas the adjoint method for problems parameterized by Navier-stokes velocity with $k - \epsilon$ turbulent closure remains an open problem.

5.7 Computational times

In table 5.8 we compare computational times for the classic FEM approximation of equation (4.39) (with no model order reduction or data assimilation) for reference, and the PBDW state estimation and GEIM approximation. In the case of full reconstruction of the physical state the PBDW method reduces by nearly 20 times the calculation time, and the GEIM method saves even a few more seconds, given the smaller linear system size. We also compare computational times for the PBDW estimation and the GEIM approximation of an output quantity, considering the average pollution concentration over subdomain Ω_{out} as shown in figure 5.24. In the case of a QoI rendering full reconstruction of the physical state unnecessary, we see a reduction by a factor of over 500 for both the PBDW method and the GEIM method, leaving nearly negligible calculation times. These differences could be taken into consideration in the case of full reconstruction of the pollution field along with the precision and peaks in error results when determining which MOR data assimilation method is most pertinent and advantageous to the application. However the improved model error correction provided by the PBDW method for relatively equivalent calculation times gives a clear advantage to PBDW state estimation.

CPU Times 74GB RAM desktop	Offline Stage	Online Stage (average CPU times)	
		State Estimate $\Omega : 125m \times 75m$	Quantity of Interest $\Omega_{out} : 20m \times 10m$
FEM-SUPG $c^{bk}(\mathbf{p})$ $\mathcal{N}_h \sim 323,000$	-	$7.4h + 61s$ (fluid) (disp.)	$85\text{min} + 1.3s$ (fluid) (disp.)
MOR Methods			
Training set $N_{train} = 40$	$296.6h$	-	-
PBDW ($M = 10, N = 6$)	10.26min	$5.35s$	$0.18s$
GEIM ($M = 10$)	42.7min	$3.32s$	$0.17s$

Table 5.8 – Computational times of two MOR-data assimilation methods over the full calculation domain and estimation of average concentration over a subdomain Ω_{out} (see figure 5.24), compared to FEM approximation. Average over the set of trial solutions considered here.

In table 5.9 we compare computational times in the case of a simplified Stokes wind field for the three methods, PBDW, GEIM, and adjoint. We again give the time required to compute a training set by FEM approximation for reference. We note that no MOR technique was applied in the adjoint method here. The use of

RBMs for the direct and adjoint problem would significantly reduce these calculation times, but add an offline phase (corresponding to the construction of the PBDW background space in addition to a RB space for the adjoint problem), and the online approximation would remain iterative and thus (slightly) more costly than both the PBDW and GEIM.

CPU Times	Offline Stage	Online Stage (average CPU times)
Training set $N_{train} = 40$	43min	-
PBDW ($M = 2, N = 2$)	2.1min	1.4s
GEIM ($M = 2$)	36.4s	0.8s
Adjoint Method ($M = 2$)	-	38.3min

Table 5.9 – Computational times of the adjoint method compared to the PBDW and GEIM for the state estimate of the Stokes-based 2D case study.

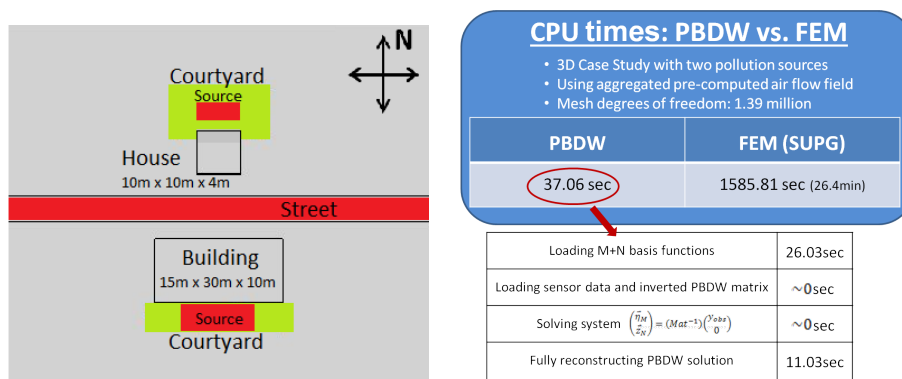
Chapter 6

Application in Exterior Air Quality Modeling: a 3D Case Study

Résumé :

Dans ce chapitre, nous étendons notre étude numérique à un problème tridimensionnel. Comme précédemment, on s'intéresse à la concentration de particules fines $PM_{2.5}$ dans un petit quartier résidentiel. Il existe plusieurs sources de pollution possible : la route, des sources de combustion autour de la maison et du bâtiment. Dans cette étude l'intensité du vent n'est plus un paramètre qui varie, seule l'intensité des différentes sources d'émissions peut varier.

Comme dans le cas 2D, nous étudions la stabilité et la convergence de la méthode PBDW en fonction du positionnement des capteurs (au hasard, sur une grille uniforme ou donné par un algorithme de type greedy), et de la norme choisie dans la formulation PBDW. La convergence de la méthode a également été étudiée en fonction de l'erreur de modèle. Dans la seconde partie de ce chapitre nous nous intéresserons à la convergence de la formulation PBDW lorsque le modèle a été a-dimensionné.



Représentation du domaine 3D avec les zones d'émission de pollution en rouge (à gauche). Tableau récapitulatif des temps de de calcul de la phase *en-ligne* de la PBDW (à droite).



In this section we extend the two-dimensional case study from chapter 5 to a three-dimensional domain of dimensions $60m \times 60m \times 20m$, seen in Figure 6.1.

Here we will show two separate cases of study: first, we will consider only combustion sources of $PM_{2.5}$ representing residential backyard fires or grills. In this case we have 10 possible source locations, and consider solutions with one in each yard of varying and independent intensities. This is an interesting study because RBMs are generally not suited to cases of moving sources, however here we have a finite set of possible locations, with some very close to each other, and we explore how the PBDW method can reconstruct the concentration field under these conditions.

In the second case, we will modify the parameters to be better suited to RBMs with only three possible source locations. Here we add a street pollution source and background concentration as parameters, and treat the combustion sources as area sources rather than point sources.

We will again use the practical aspects discussed in the two-dimensional case in section 5.1

6.1 Initial study

The three-dimensional case study on the domain represented in figure 6.1 was considered for 10 varying parameters of source intensity, in the parameter set $\mathcal{D}_{train}^{bk} = \{\mathbf{p}_i \in [0 : 5 \times 10^{-4} \frac{kg}{m^3}]\}$.

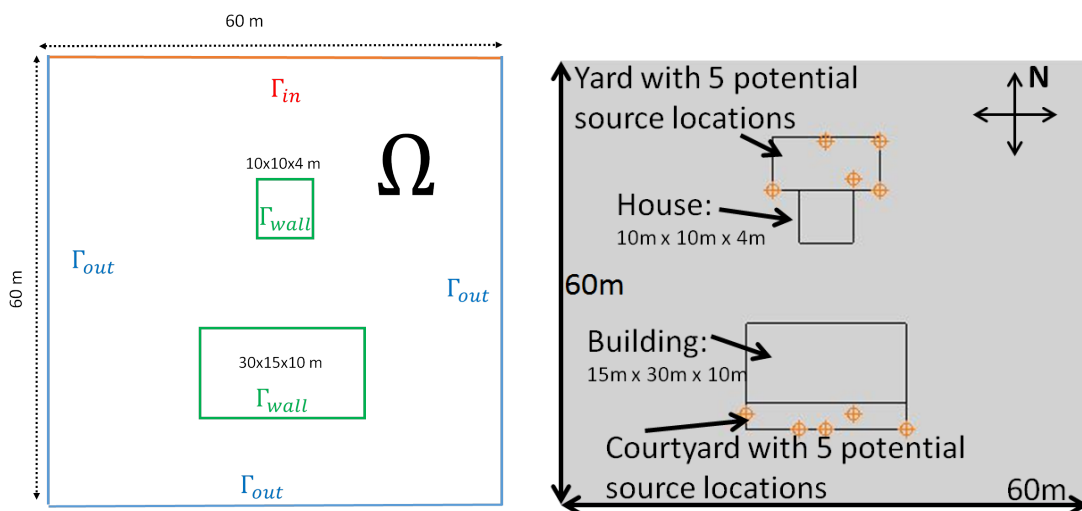


Figure 6.1 – 3D test domain with boundaries corresponding to the velocity field (left), and with various combustion pollution sources (right).

A single turbulent velocity field was considered, represented in figure 4.6 on a larger velocity domain with a mesh of $\sim 600,000$ nodes. We computed the wind

field as described in section 4.2.1, with a vertical inflow profile given by equation (4.36), with $v_0 = 2$ and $z_0 = 1$. The inlet BC was set to $\|\vec{u}\| = 2z^\alpha$ and direction $(x^*, y^*)^T$ in practice we set $\alpha = 0.4$. We then computed a quasi-steady velocity field as described in section 5.1.1.

The transport domain was meshed with ~ 1.39 million nodes, giving a global Peclet number (4.50) of approximately 212.6 with $L_g = 60m$. At a height of $1m$ the wind velocity was set to $7.2 \frac{km}{h}$ in a due south direction. Here the inlet boundaries Γ_{in} correspond to Γ_D from equation (4.41), and outlet boundaries Γ_{out} correspond to Γ_N . In figure 6.2 we can see concentration fields for two parameter sets.

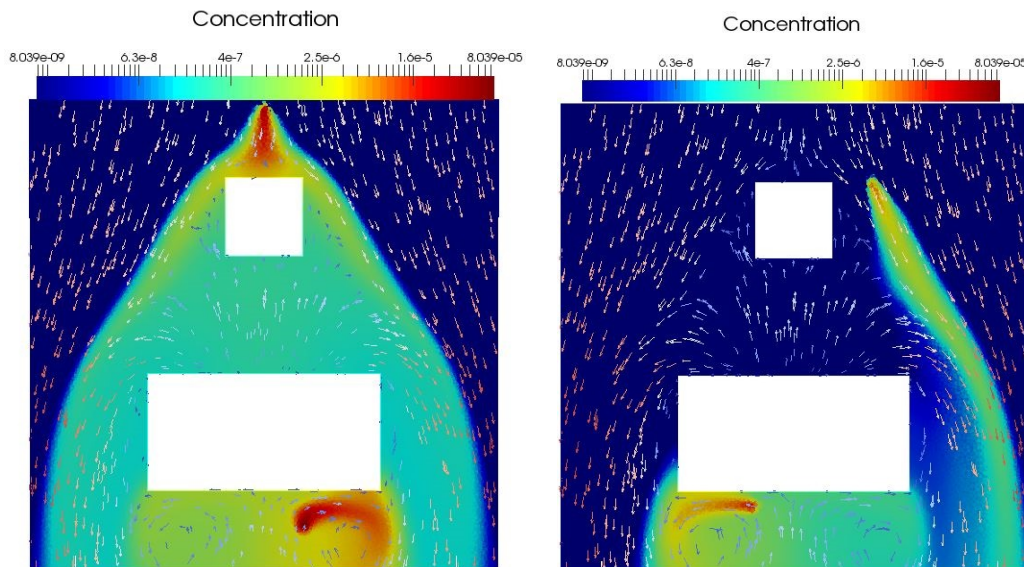


Figure 6.2 – Concentration solution over velocity field with parameters $(3.33 \times 10^{-4} \frac{kg}{m^3}, 3.33 \times 10^{-4} \frac{kg}{m^3})$ (left), and $(1.11 \times 10^{-4} \frac{kg}{m^3}, 1.11 \times 10^{-4})$ (right), for two sets of source locations. Horizontal slice taken at $z = 1m$.

While we could assume the dimension of the solution manifold to be 10 (the number of source locations), we chose to treat the problem in the framework of RBMs for two reasons. First, we wanted to study the effect of numerical instabilities in our solutions by studying RB projection errors to investigate whether the actual dimension is greater than 10. Secondly, we wanted to investigate the possibility that the source locations nearest each other would provide concentration fields resembling each other, and we'd be able to represent the solution manifold with fewer than $N = 10$ solutions.

In figure 6.3 we see the projection errors (4.26) during the construction of a RB background space using a greedy procedure as in chapter 5 (see algorithm 3).

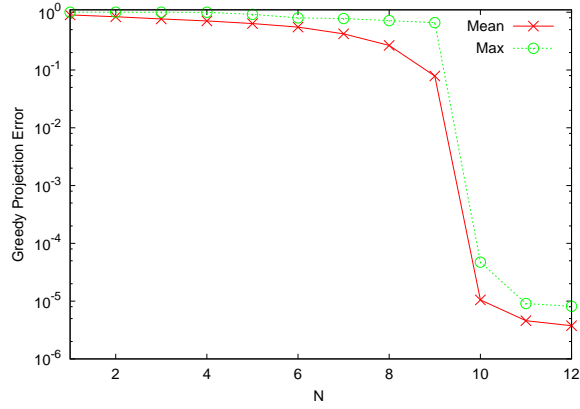


Figure 6.3 – Greedy H^1 projection errors of a training set of solutions.

As in the two-dimensional case study, we consider that given the physical complexity of the problem and the tendency for some numerical error to persist after stabilization of the model \mathcal{P}^{bk} , this level of precision offered by a reduced basis space to approximate the solution manifold \mathcal{M}^{bk} satisfactory.

6.1.1 Sensor locations and update space

We again want to study the PBDW formulation in the case of various sensor configurations Σ . Σ_1 is a randomly selected set (figure 6.4 left), Σ_2 sensors are placed on a quasi uniform grid at $z = 0.75m$ height (figure 6.4 right), and Σ_3 sensors were chosen on a quasi uniform grid at heights $z = 0.5m$, $z = 1m$, and $z = 1.5m$ (figure 6.5) by a Greedy-based procedure to optimally select sensors.

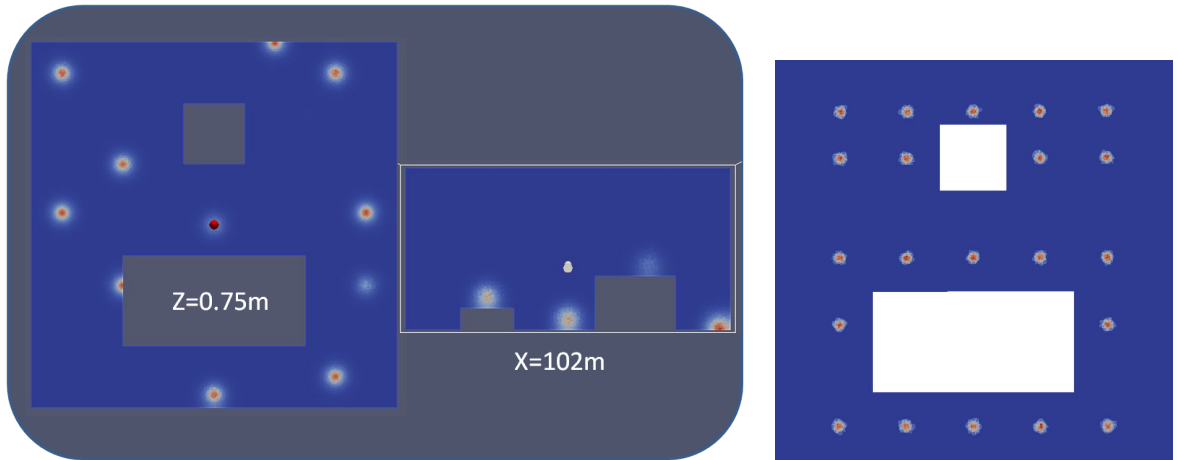


Figure 6.4 – Sensor locations Σ_1 (left-middle), and Σ_2 (right).

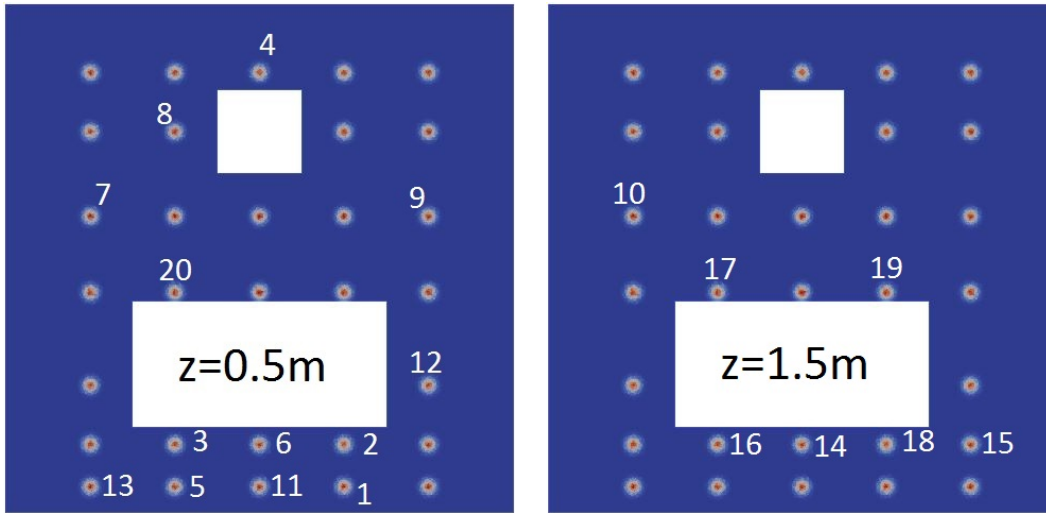


Figure 6.5 – Sensor locations Σ_3 chosen by a greedy algorithm. Left: sensors at height $z = 0.5m$. Right: sensors at height $z = 1.5m$.

In figure 6.6 we compare the stability constant $\beta_{N,M}$ (3.17) for the different sets of sensor locations Σ . We can see that the best stability is given by the sensors chosen by a greedy procedure Σ_3 , and sensors Σ_2 attain equivalent stability for higher M -values, while sensors Σ_1 induce overall less stable systems.

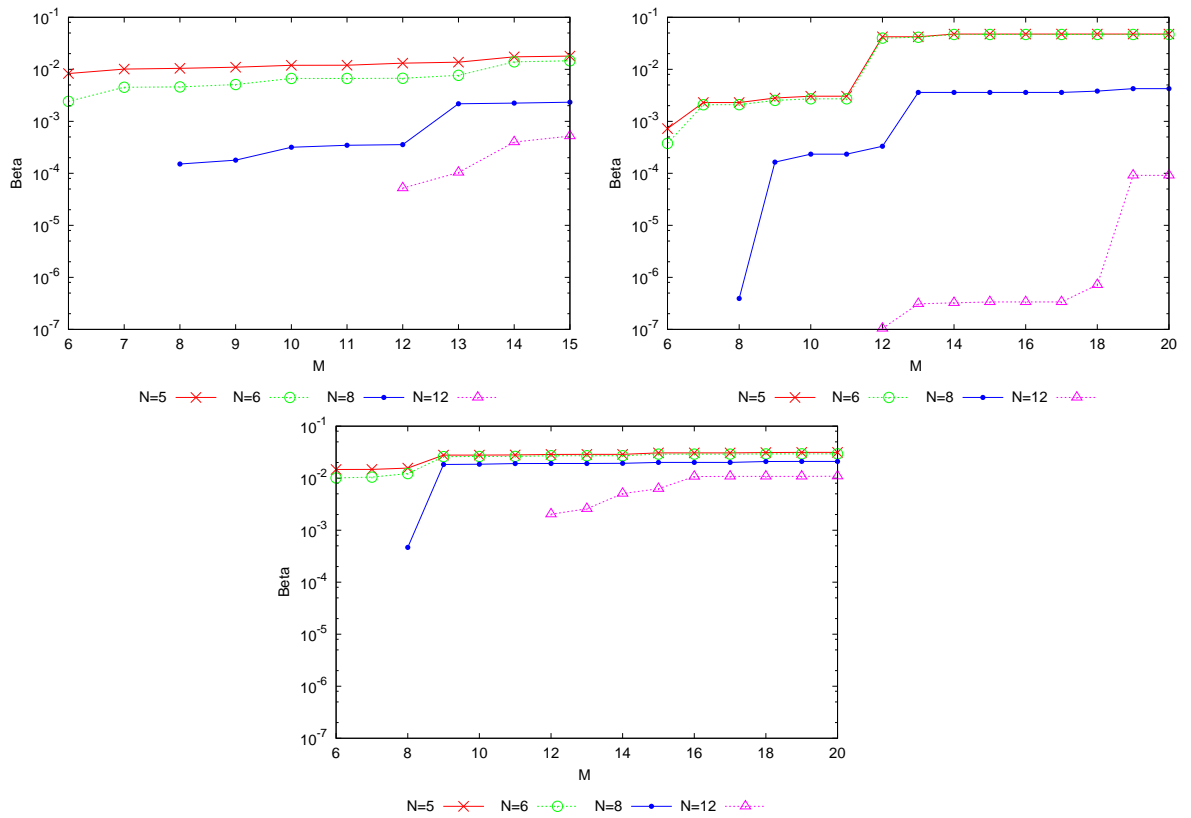


Figure 6.6 – Stability constant $\beta_{N,M}$ in H^1 norm as a function of M for various N values, for sensor locations Σ_1 (top left), and Σ_2 (top right), and for sensor locations Σ_3 chosen by a greedy procedure (bottom).

In figure 6.7 we compare the condition numbers of the PBDW matrix for the different sets of sensor locations. We see the same pattern as with the stability constants here, with the greedy-placed sensors Σ_3 inducing an overall best-conditioned system (even if we do see slight improvement from the grid locations Σ_2 for low values of N and high values of M), and poor conditioning in systems induced by Σ_1 .

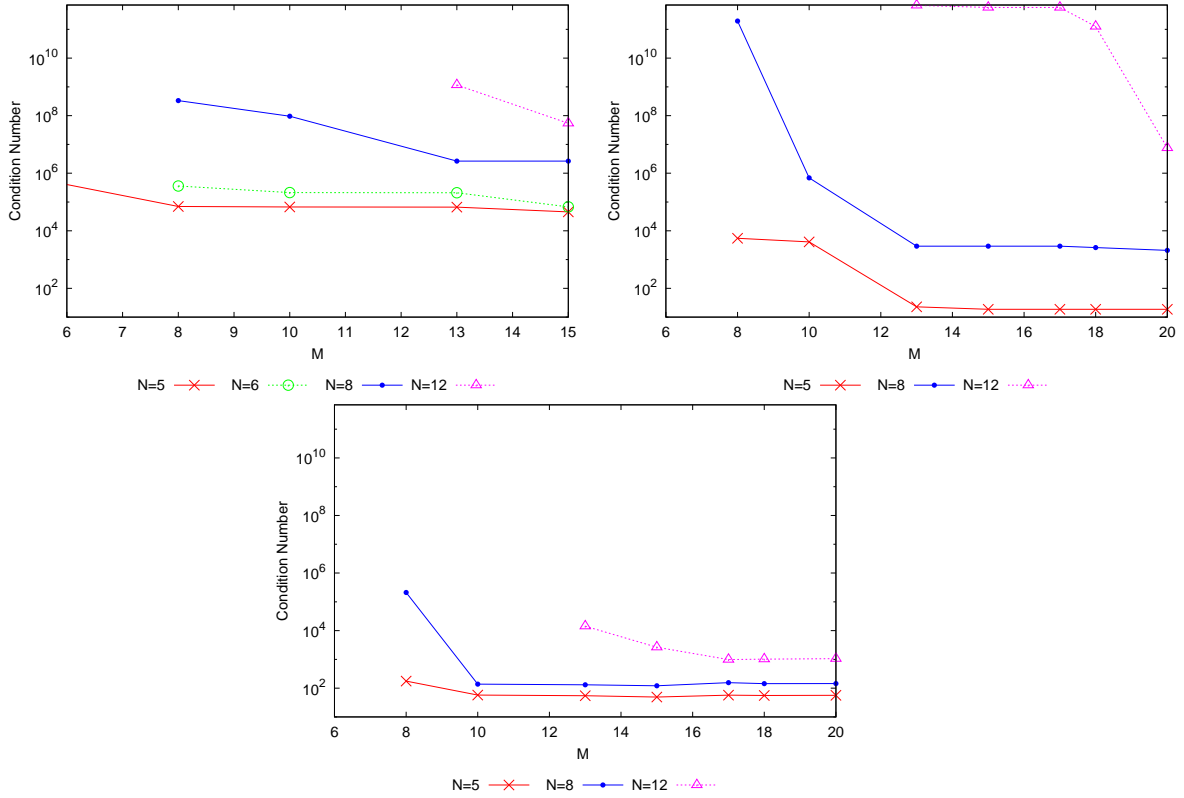


Figure 6.7 – Condition Number of PBDW matrices in H^1 norm as a function of M for various N values, for sensor locations Σ_1 (top left), Σ_2 (top right), and for Σ_3 chosen by a greedy procedure (bottom).

6.1.2 PBDW state estimation

Given the different nature of this case study configuration as compared to our 2D study in chapter 5.1, we first study during an offline stage the compatibility of this configuration with the PBDW method on a set of 10 training solutions Ξ_{test}^{bk} for $\mathbf{p} \in \Xi_{train}^{bk}$, not included in the background basis. We select these solutions carefully to represent those which are both closely dependent on the basis functions of \mathcal{Z}_N (training solutions with low projection error) and those which are least well approximated by the basis (training solutions with maximal projection error for $N = 15 - 20$).

While the full dimension of \mathcal{M}^{bk} is $N = 10$, we do not rule out a background basis of dimension $N = 8$ because two of the source locations are relatively close to others, and we wish to see if this small spatial shift can be relatively well represented in overall state estimation on Ω with a smaller background "basis".

In figure 6.8 we consider the PBDW approximation of a training solution for $\mathbf{p} \in \Xi_{test}^{bk}$, using background spaces \mathcal{Z}_N built by a Greedy algorithm or a POD method. We can see that both background spaces resulted in some "phantom" pollution being added, but to a lesser extent with the Greedy basis.

Figure 6.9 compares PBDW errors (5.9) to simple projection errors (5.4) in logarithmic scale for this same solution. We can see that both background spaces resulted in some "phantom" pollution being added at each of the source positions represented in the background spaces \mathcal{Z}_N , but to a lesser extent with the Greedy basis.

In what follows we chose to use RB background spaces \mathcal{Z}_N constructed by a Greedy algorithm. In figure 6.10 we see the PBDW approximations of two training solutions, one which is very well-approximated by the background space and one which is less-well approximated. We see good reconstruction of the solution in each case.

We next considered sets of trial solutions to a shifted model \mathcal{P}^{trial} for parameters $\mathbf{p} \in \Xi^{trial} \subset \mathcal{D}^{bk} \setminus \Xi_{train}^{bk}$, as seen in chapter 5.1. Here the variations of the parameters $\mathbf{p} \in \Xi^{trial}$ are the intensities of the 10 sources, and we used sensor sets Σ_2 and Σ_3 .

In figures 6.11 and 6.12, we see relative mean and maximal PBDW approximation errors, as defined in equations (5.10) and (5.11), using the sensor set Σ_2 6.4, over a trial set of solutions with $\mathbf{p} \in \Xi^{trial}$ with no model error and with a reaction coefficient $R = 0.0001$, respectively. We see in both figures a significant drop in error from $N = 10$, and degraded approximation quality as N approaches M , particularly in the case of the imperfect model \mathcal{P}^{trial} , consistent with the stability coefficients shown in figure 6.6.

In figures 6.13, 6.14, and 6.15 we consider the optimal sensor set Σ_3 6.5 chosen by a greedy procedure. We again see relative mean and maximal PBDW approximation errors over $\mathbf{p} \in \Xi^{trial}$ with no model error and with a reaction coefficients of $R = 0.0001$ and $R = 0.001$. We again see a significant drop in approximation error from $N = 10$, particularly in the case of a perfect model \mathcal{P}^{bk} , in which case we have negligible error both in mean and maximal. In the case of smaller model error 6.14, we attain about 1% error in the PBDW approximation, and in the case of significant model error 6.15, we attain about 10% approximation error.

In figures 6.16 and 6.17 we see relative mean approximation errors plotted over the calculation domain, as defined in (5.9), for $M = 20$ and $N = 12$ or $N = 10$. We see negligible error in the case of a perfect model, only visible in the intensity of the sources. In the case of model error by a reaction term of $R = 0.0001$, we see more significant error, but still under 1% almost everywhere for sensor set Σ_2 , and everywhere for sensor set Σ_3 . We notice that for $N = 10$, sensor set Σ_2 has lower error peaks than the greedy-selected sensor set Σ_3 , however the Σ_2 solution is significantly degraded for $N = 12$. This coincides with the instability with respect to M and N values which we see in figures 6.11 and 6.12, where as the Σ_3 solutions remain satisfactory for various N values.

In figure 6.18 we see the mean approximation error in the case were we neglect to span the entire solution manifold, and only consider $N = 8$ background basis func-

tions. If two locations are very close to one another, we see that we can reasonably reconstruct the pollution field (but would not expect the new source location to be identified unless we have a sensor very close by), and in this case of trial solutions for parameter set Ξ^{trial} we did not correctly identify the intensity of the sources. We do not consider this result surprising given the dimension of the solution space. The correction provided by the update space allows for incorporation of the M data points, but does not make up for an under-represented solution manifold. We note, however, that relative PBDW approximation error is under 1% over the majority of the domain, and the majority of the error is committed in the identification of source intensity.

We conclude from this study that given a finite (and relatively small) set of possible source locations, the PBDW method is capable of identifying the intensity of the sources (including the non-existence of the source as zero-intensity), provided the background space \mathcal{Z}_N represents each of the possible source locations.

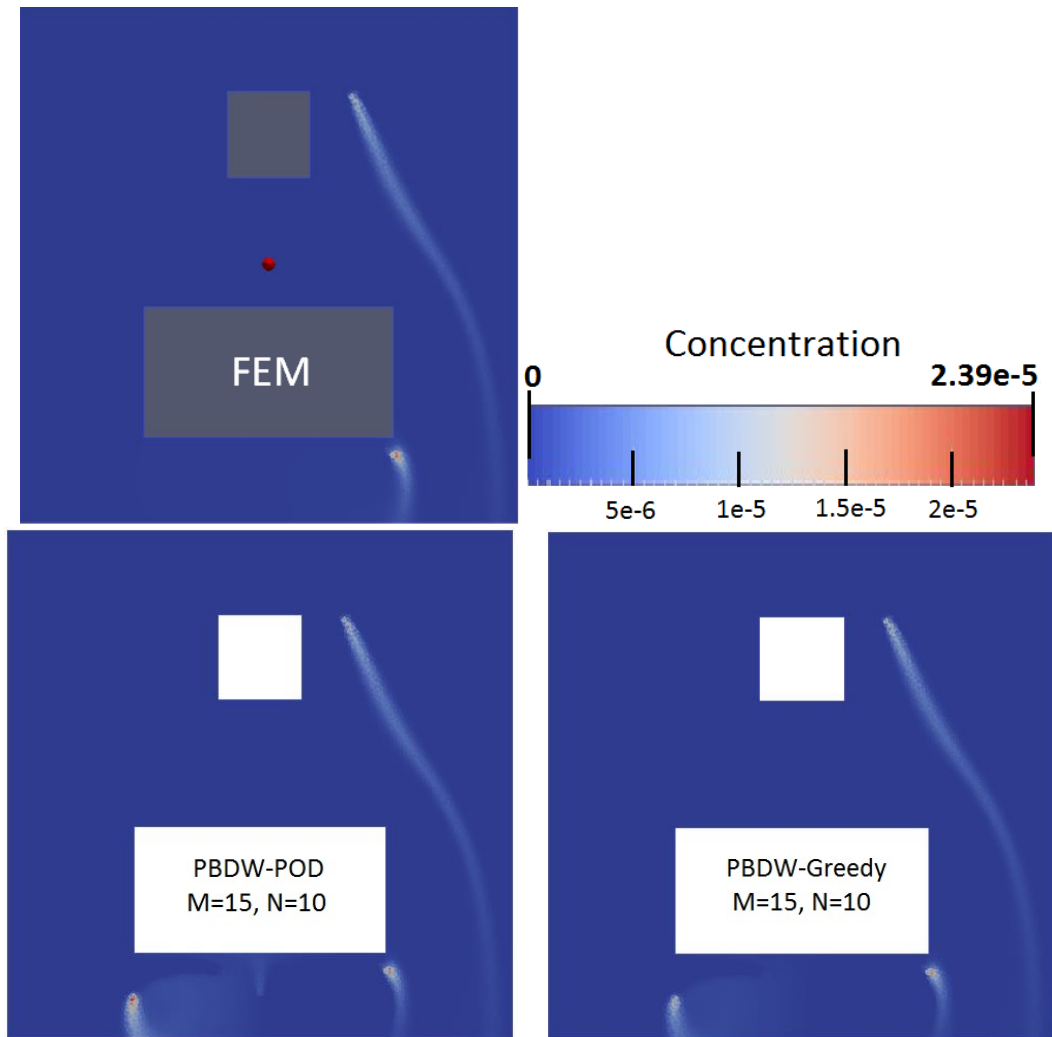


Figure 6.8 – PBDW approximated concentration using non-noisy synthetic data as compared with the FEM concentration solution with source intensity $\mathcal{I} = 1.11 \times 10^{-4}$. FEM solution (top), POD-PBDW approximation (bottom left), Greedy-PBDW approximation (bottom right).

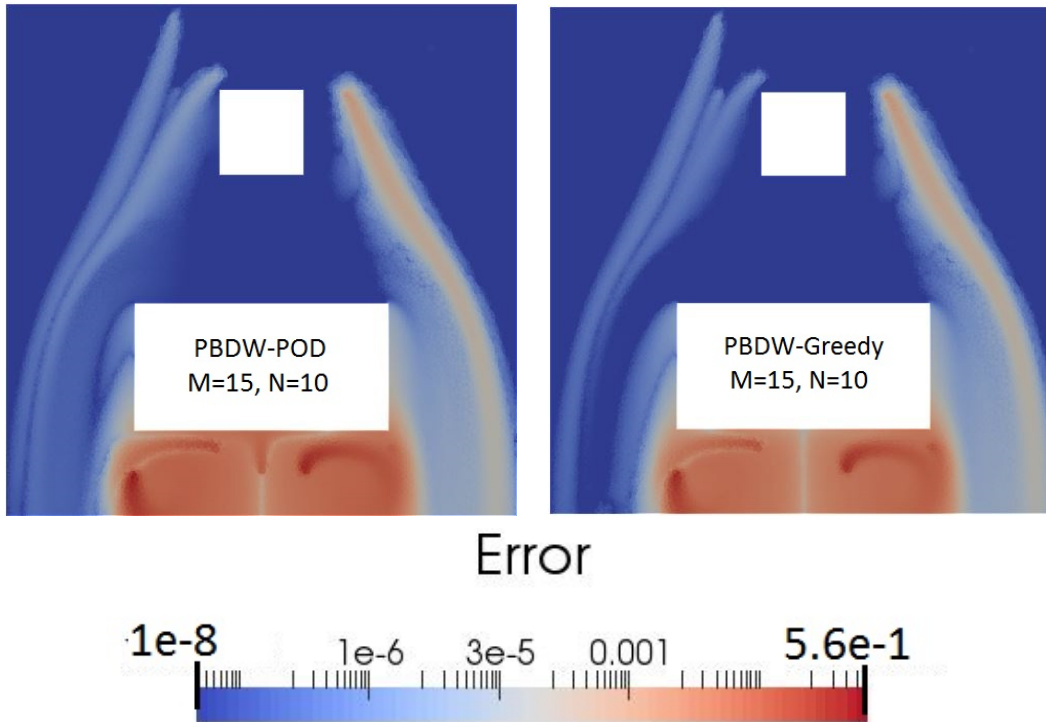


Figure 6.9 – Relative PBDW approximation error using non-noisy synthetic data in log scale. Solution with intensity $\mathcal{I} = 1.11 \times 10^{-4}$.

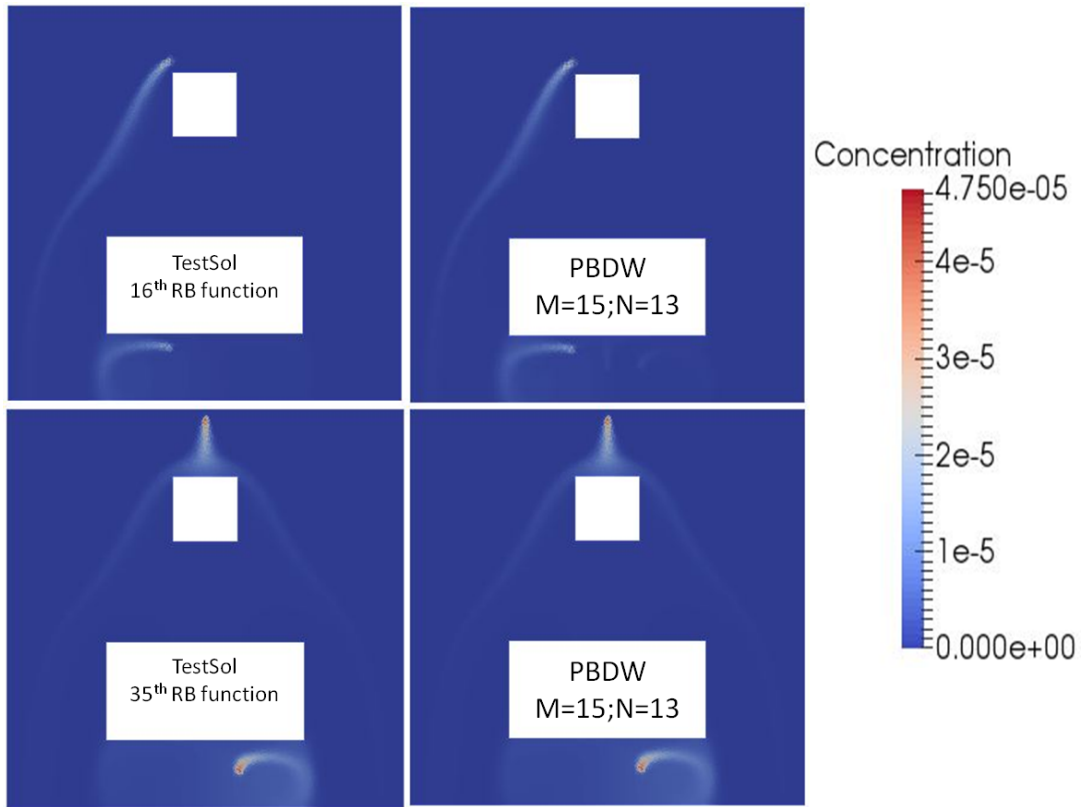


Figure 6.10 – FEM concentration simulation (left) ; relative PBDW approximated concentration using non-noisy synthetic data (right).

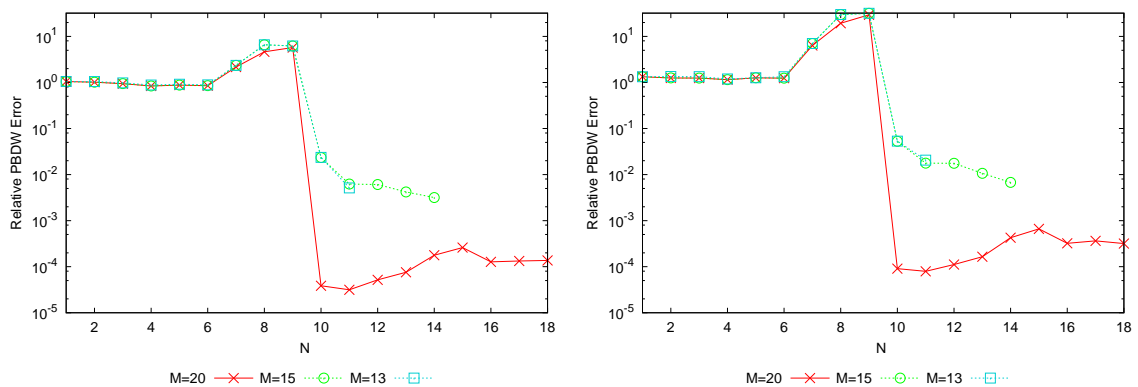


Figure 6.11 – Relative mean (5.10) (left) and maximal (5.11) (right) PBDW approximation errors in the H^1 -norm as a function of N for various M -values, using synthetic trial data for parameter set Ξ^{trial} with no model error (model \mathcal{P}^{bk}), and sensor locations Σ_2 .

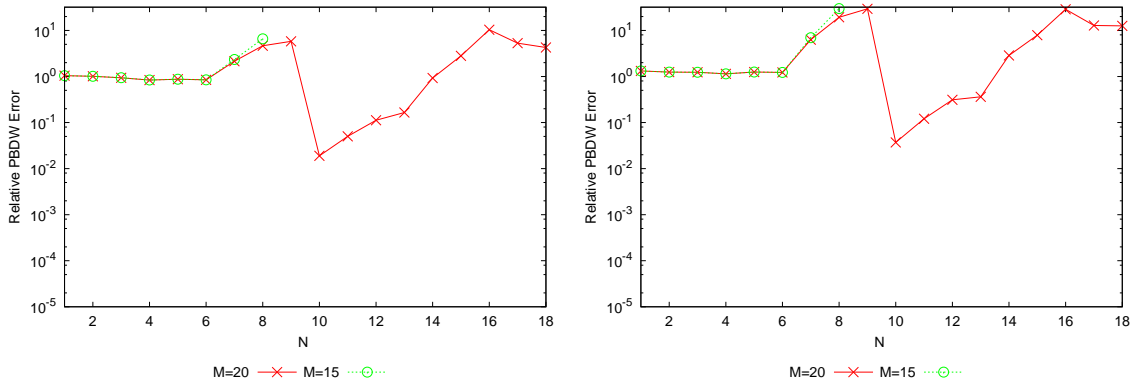


Figure 6.12 – Relative mean (5.10) (left) and maximal (5.11) (right) PBDW approximation errors in the H^1 -norm as a function of N for various M -values, using synthetic trial data for parameter set Ξ^{trial} with reaction coefficient $R = 0.0001$ (model \mathcal{P}^{trial}), and sensor locations Σ_2 .

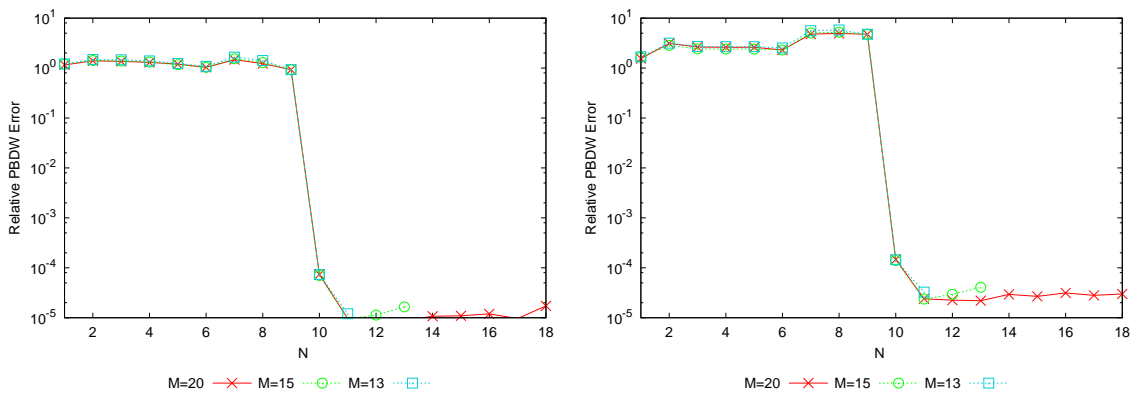


Figure 6.13 – Relative mean (5.10) (left) and maximal (5.11) (right) PBDW approximation errors in the H^1 -norm as a function of N for various M -values, using synthetic trial data for parameter set Ξ^{trial} with no model error (model \mathcal{P}^{bk}), and sensor locations Σ_3 .

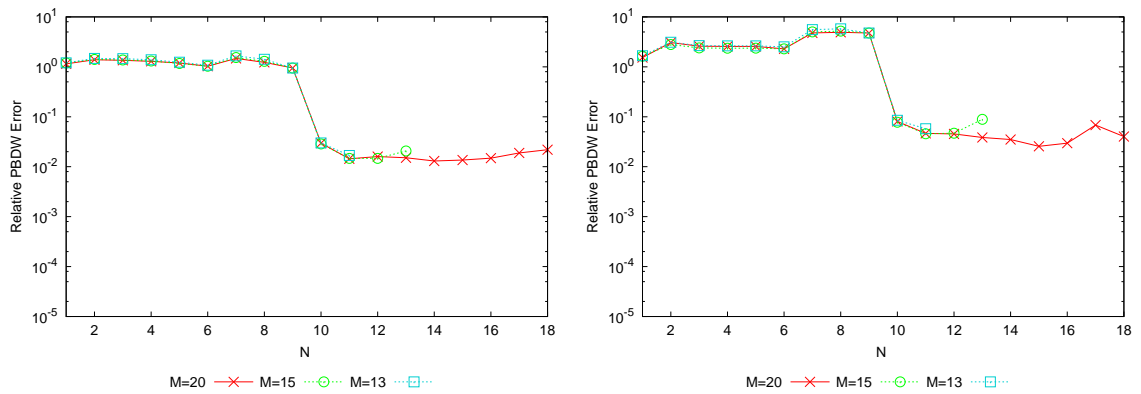


Figure 6.14 – Relative mean (5.10) (left) and maximal (5.11) (right) PBDW approximation errors in the H^1 -norm as a function of N for various M -values, using synthetic trial data for parameter set Ξ^{trial} with reaction coefficient $R = 0.0001$ (model \mathcal{P}^{trial}), and sensor locations Σ_3 .

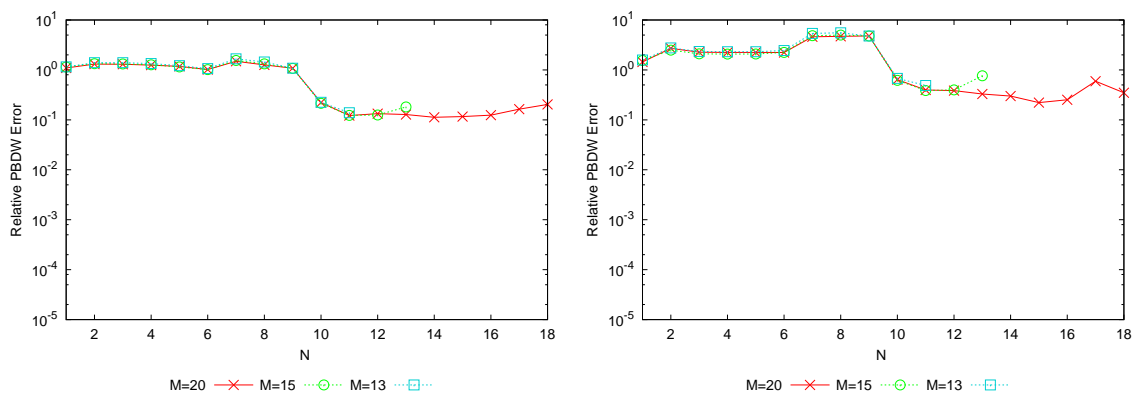


Figure 6.15 – Relative mean (5.10) (left) and maximal (5.11) (right) PBDW approximation errors in the H^1 -norm as a function of N for various M -values, using synthetic trial data for parameter set Ξ^{trial} with reaction coefficient $R = 0.001$ (model \mathcal{P}^{trial}), and sensor locations Σ_3 .

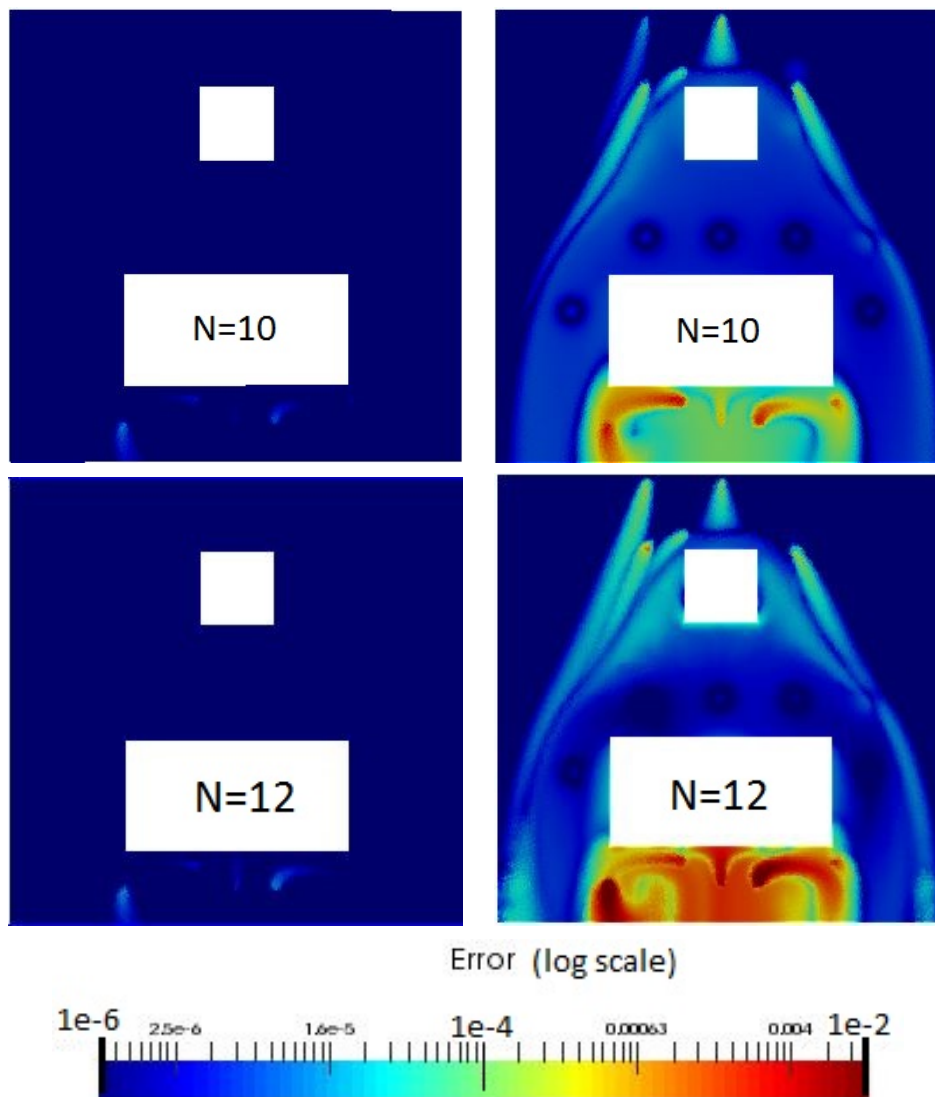


Figure 6.16 – Relative mean PBDW errors (5.9) for $M = 20$, using synthetic trial data for parameter set Ξ^{trial} and sensor locations Σ_2 . Left: no model error. Right: reaction coefficient $R = 0.0001$ (model \mathcal{P}^{trial}).

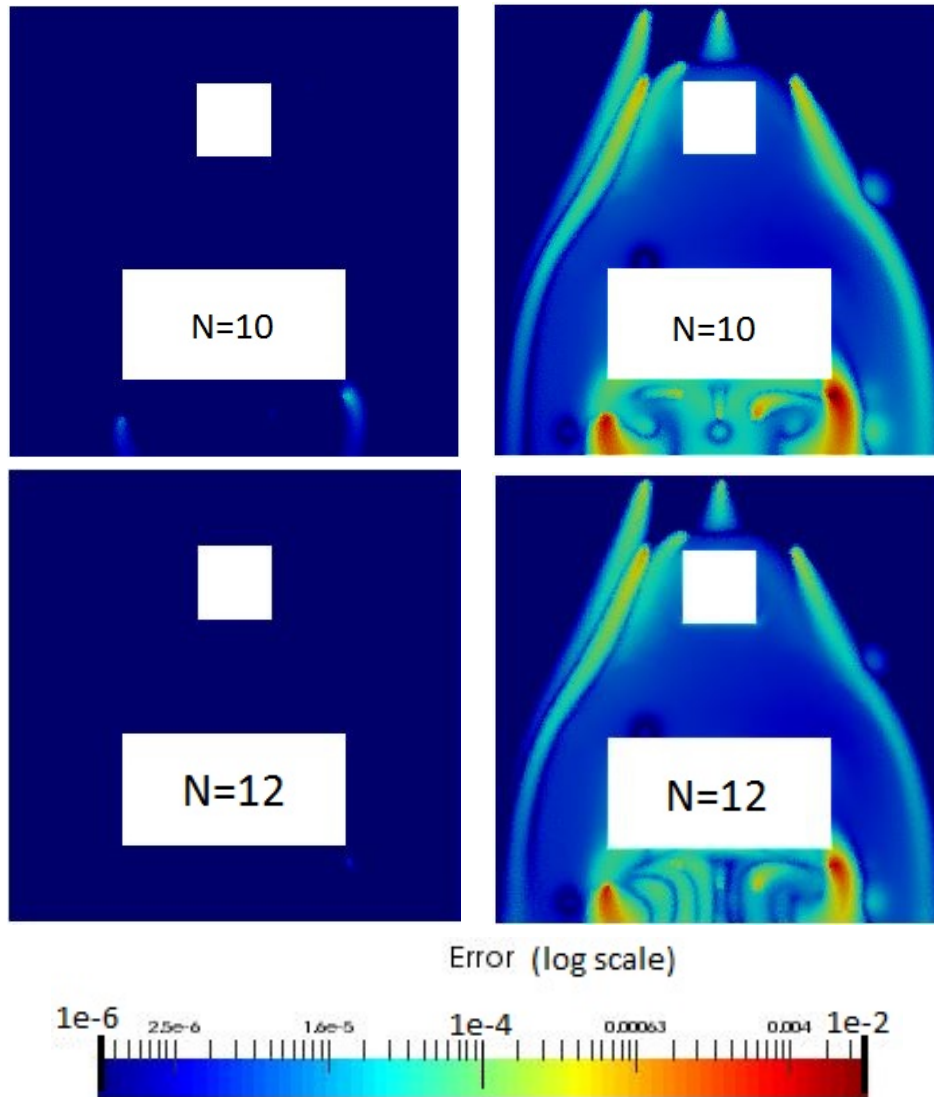


Figure 6.17 – Relative mean PBDW errors (5.9) for $M = 20$, using synthetic trial data for parameter set Ξ^{trial} and sensor locations Σ_3 . Left: no model error. Right: reaction coefficient $R = 0.0001$ (model \mathcal{P}^{trial}).

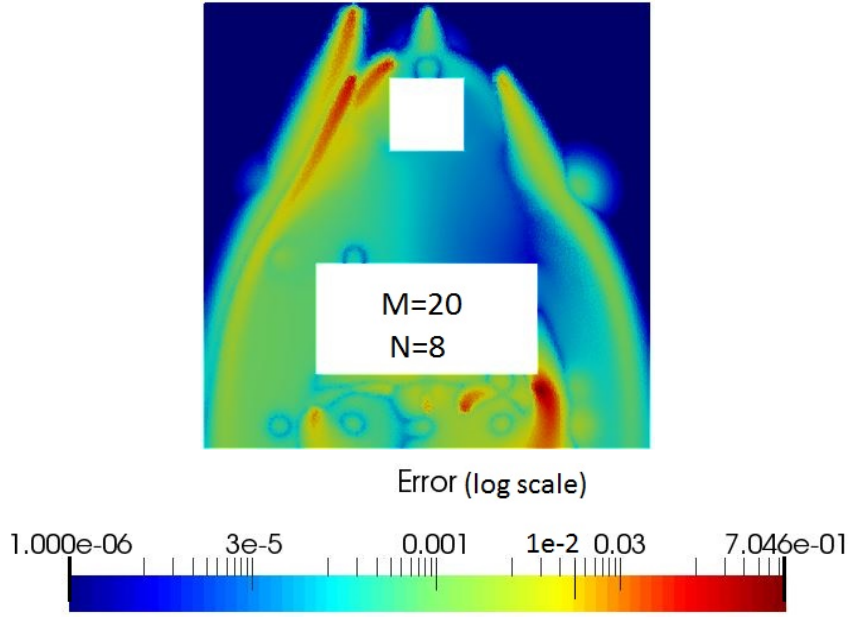


Figure 6.18 – Relative mean PBDW error (5.9) for $M = 20$ and $N = 8$, using synthetic trial data for parameter set Ξ^{trial} , sensor locations Σ_3 , and reaction coefficient $R = 0.0001$ (model \mathcal{P}^{trial}).

CPU times: For this three-dimensional case study we considered a fixed wind field which took just over 3 days to compute using *Code_Saturne* with 1500 iterations on a 74GB desktop machine with 8 cores. We considered a training set of 74 concentration solutions (32.6h of concentration calculations), for a total time of nearly 5 days for the computation of a training ensemble. Table 6.1 gives offline computation times for the construction of the approximation spaces and PBDW system for $M = 15$ and $N = 10$.

CPU Times	Offline Stage
74GB RAM desktop	
Training set $N_{train} = 74$	< 5days
PBDW ($M = 15, N = 10$)	$\sim 8h$

Table 6.1 – Offline computational times of the PBDW method over the 3D calculation domain.

Figure 6.19 shows online calculation times of the online phase for the FEM solution with SUPG, as compared to the PBDW method online phase.

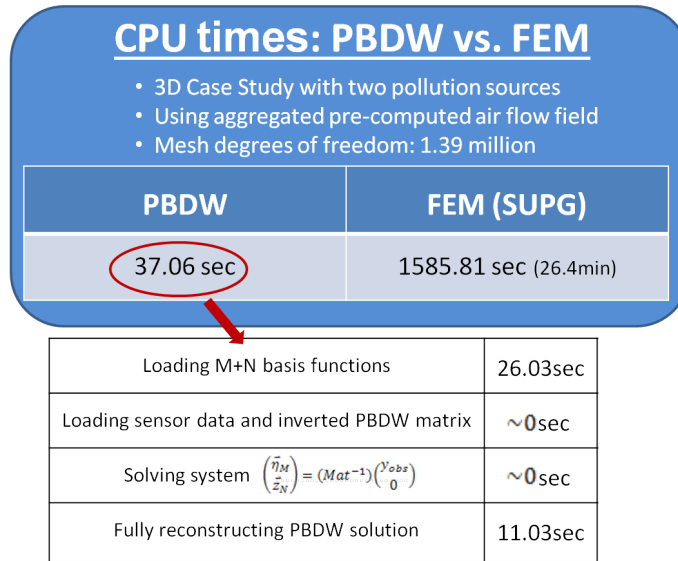


Figure 6.19 – Computational times for the PBDW method online for this case study.

Once the computationally-heavy offline stages has been accomplished for our PBDW configuration, we have the possibility of state estimation in quasi-real-time, with more than a 100-fold time gain with respect to classical approximation by finite elements for the reconstruction of the PBDW approximation over the full computational domain.

6.1.3 PBDW Norm Modifications

In section 5.4 we briefly considered the merits of the alternative \tilde{H}^1 -norm (4.21) introduced in section 4.1.1.3. Here we want to again make the comparison. In figure 6.20 we see update basis functions computed in the \tilde{H}^1 -norm for sensor locations Σ_2 . We can see that the norm change has enlarged the support of each functions and lowered the maximal values, essentially smoothing the functions.

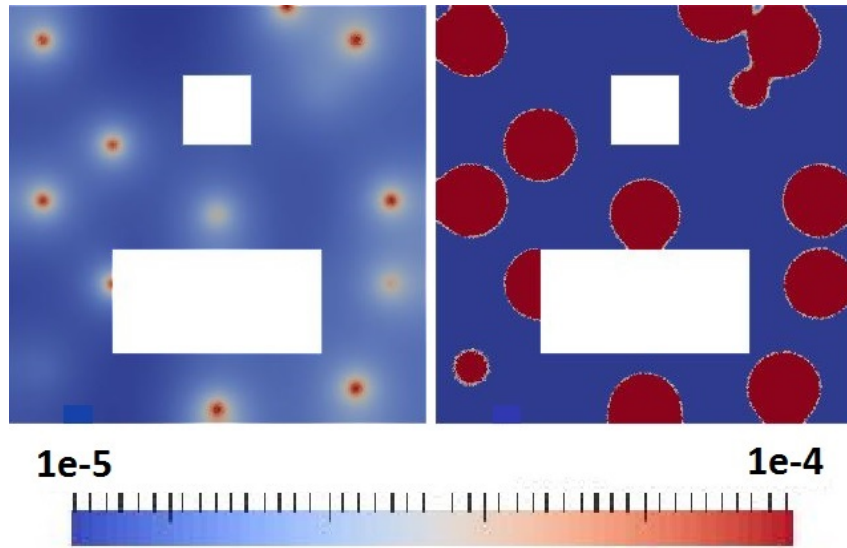


Figure 6.20 – Update basis functions constructed by Riesz representation (3.7) in the H^1 -norm (left), as compared to those constructed in the \tilde{H}^1 -norm (4.21) (right), presented on a common scale.

In figure 6.21 we compare PBDW relative mean approximation errors over the computational domain on a set of trial solutions to \mathcal{P}^{trial} with $R = 0.001$ approximated by a PBDW system in the H^1 or \tilde{H}^1 norms. We can see that while the error maps take similar forms, the errors are generally more elevated in the \tilde{H}^1 PBDW formulation.

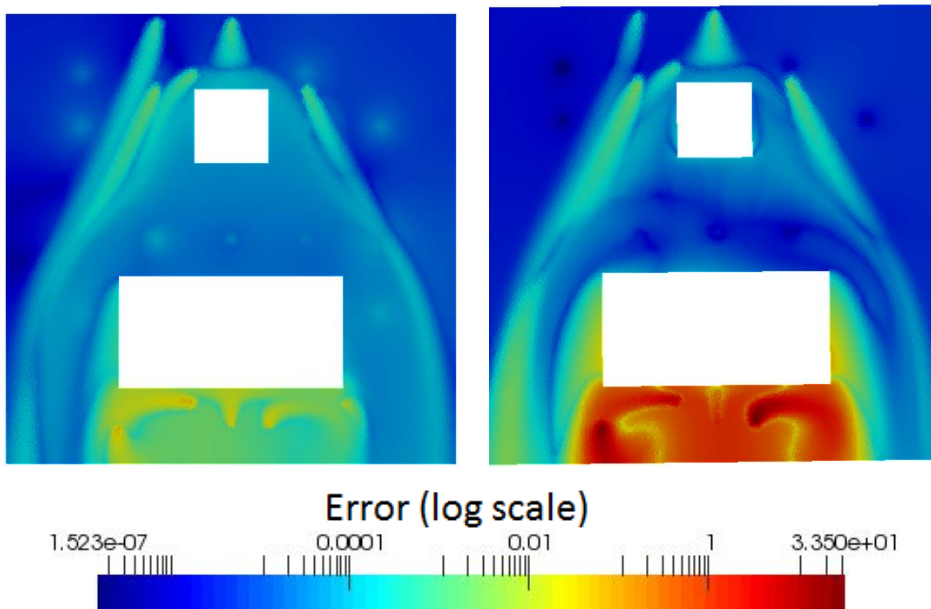


Figure 6.21 – Relative mean PBDW errors (5.9) for $M = 20$ and $N = 12$, using synthetic trial data for parameter set Ξ^{trial} with reaction coefficient $R = 0.001$ (model \mathcal{P}^{trial}), and sensor locations Σ_2 . PBDW approximation in H^1 norm (left), and \tilde{H}^1 norm (right). Relative errors computed in the H^1 -norm.

In figure 6.22 we compare PBDW relative mean approximation errors in H^1 -norm on the same set of trial solutions to \mathcal{P}^{trial} with $R = 0.001$ approximated by a PBDW system in the H^1 or \tilde{H}^1 norms. Here we see clear instability in the approximation results offered by the \tilde{H}^1 norm. The climb in approximation error seen in the H^1 -norm is to be expected as N nears M , as seen in our discussion on stability. However the large peak in approximation error for the \tilde{H}^1 PBDW system is not optimal.

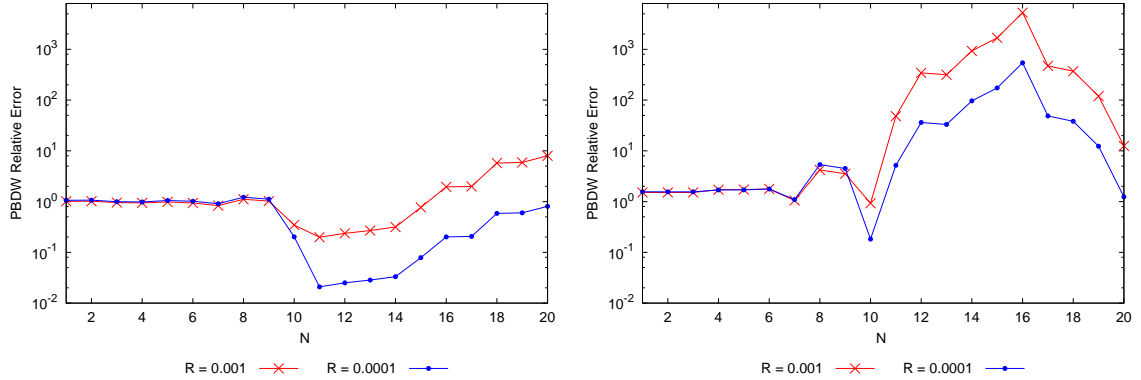


Figure 6.22 – Relative mean PBDW errors in the H^1 -norm as a function of N for $M = 20$, using synthetic trial data for parameter set Ξ^{train} (model error only) with reaction coefficients $R = 0.001$ and $R = 0.0001$ (model \mathcal{P}^{trial}), and sensor locations Σ_2 . In H^1 norm (left), and \tilde{H}^1 norm (right).

This initial study of the \tilde{H}^1 norm using previously chosen sensor locations leads us to the same initial conclusion we took in the previous study in section 5.4. While the \tilde{H}^1 norm does successfully smooth our update basis functions, for the sensor set Σ_2 we see no evidence of improvement of PBDW state estimation results, which we attribute to a loss in stability of the system. In what follows we will continue to consider the H^1 -norm. However, in light of the more recently improved results after reflection upon sensor placement for the \tilde{H}^1 Update space described in section 5.4.1, we add the three-dimensional extension of this \tilde{H}^1 adapted study to the perspectives for this work.

In this case study configuration we employed the PBDW method to reconstruct the pollution field from various sources of varying intensities. The method reasonably well reconstructed the pollution fields, even when nearby sources were represented by a single basis function. However, the reconstruction from point sources at discrete locations is not the most adapted application for RBMs, and we chose to modify the configuration in what follows.

6.2 Adapted dimensionless case study

In this section we consider an application of the dimensionless formulation from equation (4.67) presented in section 4.2.2.3. We consider the same three-dimensional domain in figure 6.1, but here we modify the pollutant source representation. In-

stead of considering what (for our purposes represent) point sources of combustion, we consider area sources over a small emission domain. The justification for this is twofold: in a residential neighborhood we cannot know exactly where backyard combustion would take place, and in-home wood-burning combustion would be a fixed source, hence the moving of small combustion sources is not necessarily realistic. Secondly, identifying the location of point sources is not always adapted to MOR methods. Below we see a representation of the emissions domains.

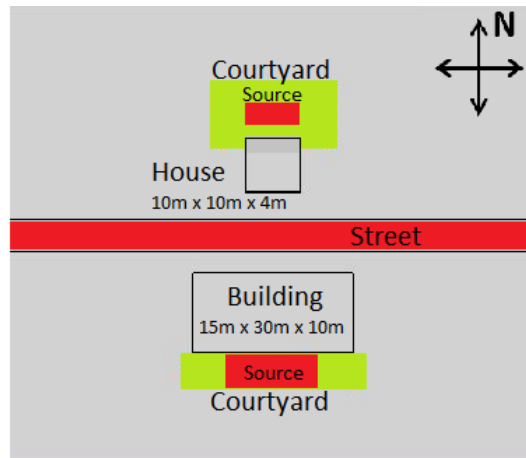


Figure 6.23 – 3D test domain with combustion and traffic pollution sources.

We consider the same wind field shown in figure 4.6. We define the model \mathcal{P}^{bk} as equation (4.67), with parameters being the intensity of the three pollutant sources and the background concentration c_{in} . We define the parameter space \mathcal{D}^{bk} as follows.

$$\mathcal{D}^{bk} = \{(c_{in}, c_h, c_b, c_r) \in \mathcal{D}_{in}^{bk} \times \mathcal{D}_y^{bk} \times \mathcal{D}_y^{bk} \times \mathcal{D}_r^{bk}\} \quad (6.1)$$

where

$$\mathcal{D}_{in}^{bk} = [1 \times 10^{-12} : 1 \times 10^{-8}]$$

$$\mathcal{D}_y^{bk} = [0 : 1 \times 10^{-6}]$$

$$\mathcal{D}_r^{bk} = [0 : 1 \times 10^{-7}]$$

The emission quantities correspond to those in paragraph subsection 5.1.2, adjusted for the larger source region. The background concentrations are based on EPA air quality standards for a three-year average over California (www3.epa.gov). We consider our characteristic length for the dimensionless equations $L_g = 60m$, and characteristic concentration of 1×10^{-6} .

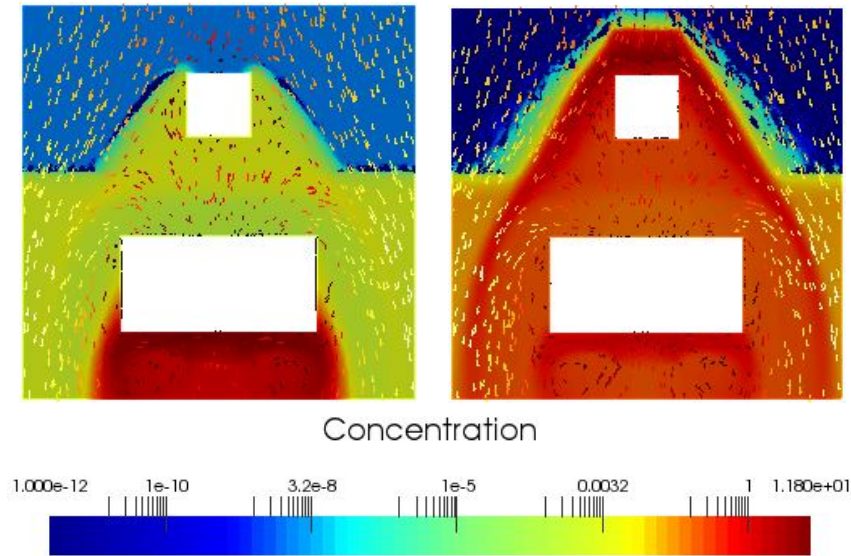


Figure 6.24 – Concentration solution (logarithmic scale) over velocity field with $\mathbf{p} = (1 \times 10^{-8}, 0, 1 \times 10^{-6}, 5 \times 10^{-10}) \frac{kg}{m^3}$ (left), and $\mathbf{p} = (1 \times 10^{-12}, 1 \times 10^{-6}, 1 \times 10^{-7}, 1 \times 10^{-7}) \frac{kg}{m^3}$ (right).

6.2.1 A Simpler Background Space

In this study configuration, the varying parameters are the source terms and boundary terms of a linear equation. We are thus not in the framework of RBMs, as each solution affinely depends on just 4 solutions to \mathcal{P}^{bk} . We see these "basis" functions in figure 6.25, including the "zero" solution as the fourth function, serving to treat varying background concentrations as a parameter, while each of the other three functions were computed with the same background concentration for stability of the numerical FEM problem.

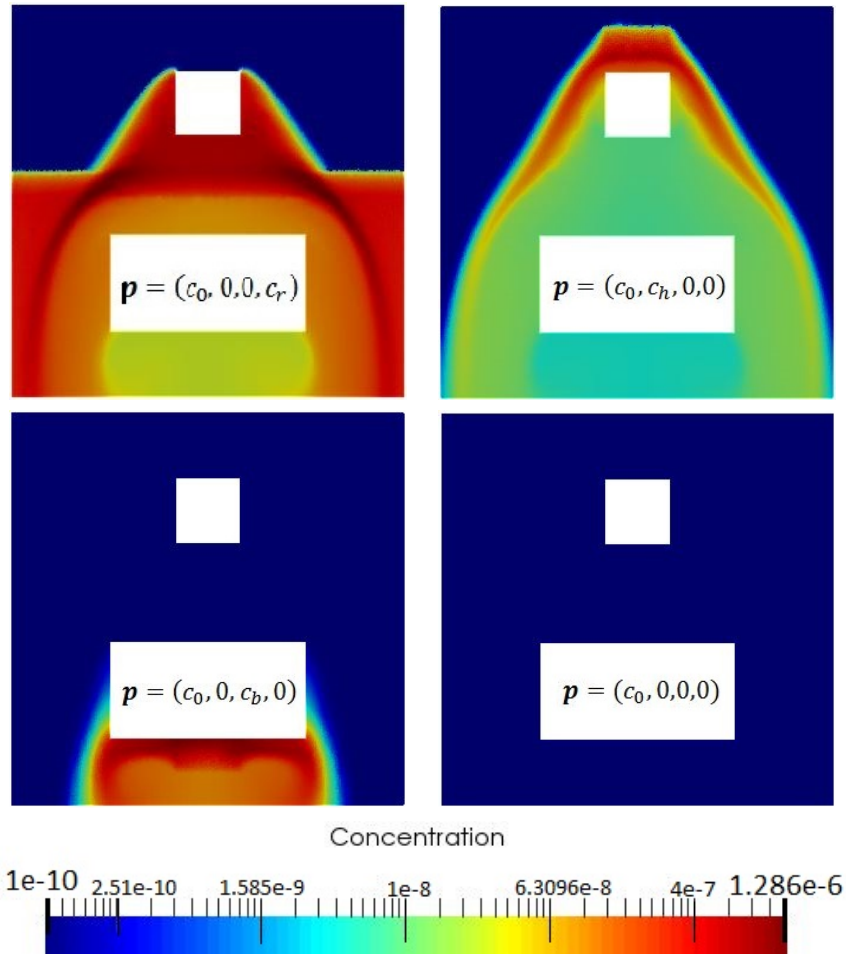


Figure 6.25 – Set of $N = 4$ solutions to \mathcal{P}^{bk} for $\mathbf{p} \in \mathcal{D}^{bk}$, spanning the solution manifold \mathcal{M}^{bk} .

In figure 6.26 we see the mean and maximal relative projection errors in H^1 norm as a function of N of a training set of particular solutions for varying parameters in \mathcal{D}^{bk} of equation (6.1) onto a set of up to 4 solutions as seen in figure 6.25. We can see a sharp drop in error up to $N = 4$, as expected.

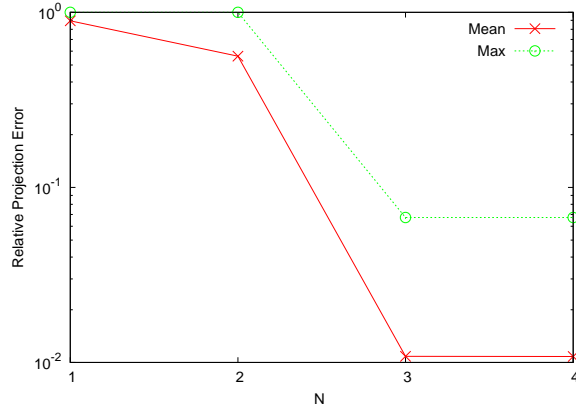


Figure 6.26 – Projection errors of a training ensemble of solutions to \mathcal{P}^{bk} onto the set of up to 4 solutions shown in figure 6.25 . Relative mean and maximal errors in H^1 norm as a function of N .

6.2.2 Sensor locations and Update space

We considered here the GEIM-inspired selection of sensor locations presented in section 4.1.2 over the set Σ of possible locations given in subsection 6.1.1, seen in figure 6.5.

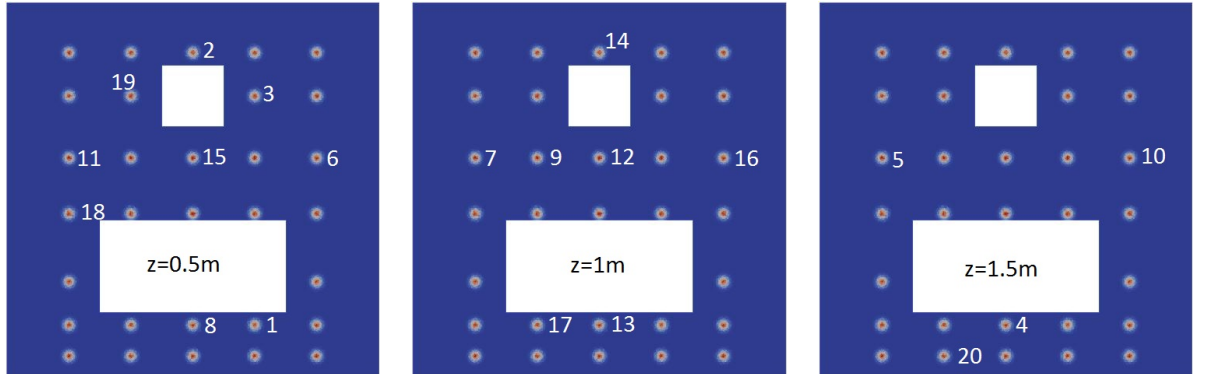


Figure 6.27 – Sensor locations chosen by GEIM algorithm over the training set in section 6.2. Left: sensors at height $z = 0.5m$. Middle: sensors at height $z = 1m$. Right: sensors at height $z = 1.5m$

In figure 6.28 we can see the stability constant $\beta_{N,M}$ (3.17) associated to the PBDW system. We can see that the stability constant is relatively high, which is unsurprising given the low value of N .

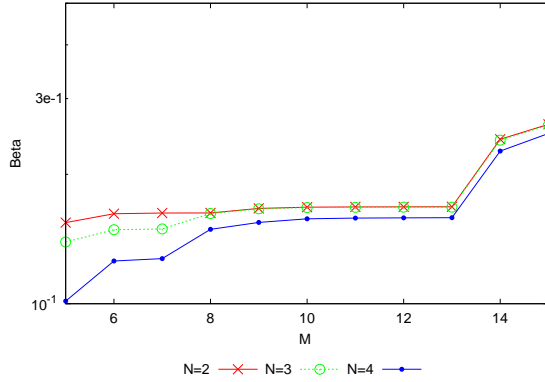


Figure 6.28 – Stability constant $\beta_{N,M}$ in H^1 norm as a function of M for various N values, for sensor locations chosen by a greedy procedure.

6.2.3 PBDW state estimation

In the following we will consider three sets of $N_{trial} = 20$ trial solutions to test the method. Each of the trials corresponds to parameters within \mathcal{D}^{bk} but different from the values used in the training set for the RB space. One set consists of solutions to equation (4.67) representing the (unrealistic) case of a perfect model \mathcal{P}^{bk} , with the goal of demonstrating the error inherent to the PBDW MOR method. The remaining trial sets consist of solutions to the dimensionless advection-diffusion-reaction problem (4.73) as in section 4.2.3 with reaction coefficients (be adimensionalizing) of $0.001c$ and $0.0001c$. These sets are used to demonstrate how the method handles two levels of model error.

In figures 6.29 and 6.30 we compare the "true" solution to \mathcal{P}^{trial} to the PBDW approximation, for $\mathbf{p} = \mathbf{p}_{max}$ defined as in (5.6), where $\mathbf{p}_{max} = (c_{in}, c_h, c_b, c_r) = (1 \times 10^{-12}, 5 \times 10^{-7}, 0, 5 \times 10^{-11})$.

On the left of figure 6.29 we see the FEM solution to \mathcal{P}^{bk} for \mathbf{p}_{max} , and on the right we see the associated PBDW approximation for $M = 8$ and $N = 3$. We can see that the dominant source and advected pollution is very well represented, as is the less-intense street source. However our PBDW approximation fails to reconstruct the correct background concentration, missing its mark by one order of precision. The instability seen in the PBDW approximation represents an over-shot correction at a sensor location, corresponding to the subtraction of an update basis function to match the measurement of the background concentration and some numerical instability. Given the different orders of the concentration sources and the background concentration, it is unsurprising that the minimization posed in equation (3.11) does not correct for this term which is up to 6 orders smaller than the others.

In figure 6.30 we compare the FEM solution to \mathcal{P}^{trial} with $R = 0.001$ for \mathbf{p}_{max} to the associated PBDW approximation for $M = 8$ and $N = 3$. We again see that the dominant source and advected pollution is very well represented, however in this case with significant model error present in the best-knowledge model, our PBDW

approximation apparently has not reconstructed the background concentration or the secondary source. Again we attribute this to the dimensionality of the dominant source term, being up to 6 orders larger than the other parameters.

In figures 6.31 and 6.32 we see relative mean and maximal PBDW approximation errors in the H^1 norm, and plotted over the computation domain, respectively, for trial solutions to \mathcal{P}^{bk} with $\mathbf{p} \in \Xi^{trial}$. We can see that from $N = 3$ we have quite good precision of the PBDW approximation, around 1% mean and under 10% maximal error. When we map the relative mean PBDW approximation errors over the computation domain, we can see numerical instability in the peaks of the errors, and that the majority of the error is in a high recirculation zone.

In figure 6.33 we see relative mean and maximal PBDW approximation errors in the H^1 norm for trial solutions to \mathcal{P}^{trial} with $R = 0.001$ and parameters $\mathbf{p} \in \Xi^{trial}$. Here we see less precision in the PBDW state estimation, but still relatively good considering the non-negligible level of model error, and that we consider we have numerical instabilities adding to our model error. In figure 6.33 we see that with this added model error $M = 5$ is not enough sensors for optimal global precision, but adding over $M = 10$ data points gains no improvement.

We see promising results here, but remark that the PBDW method is not exempt from the dimensionality problems which can affect data assimilation methods. A formulation with weights on the terms corresponding to smaller-dimension in the selection of sensors by GEIM could be considered in future study.

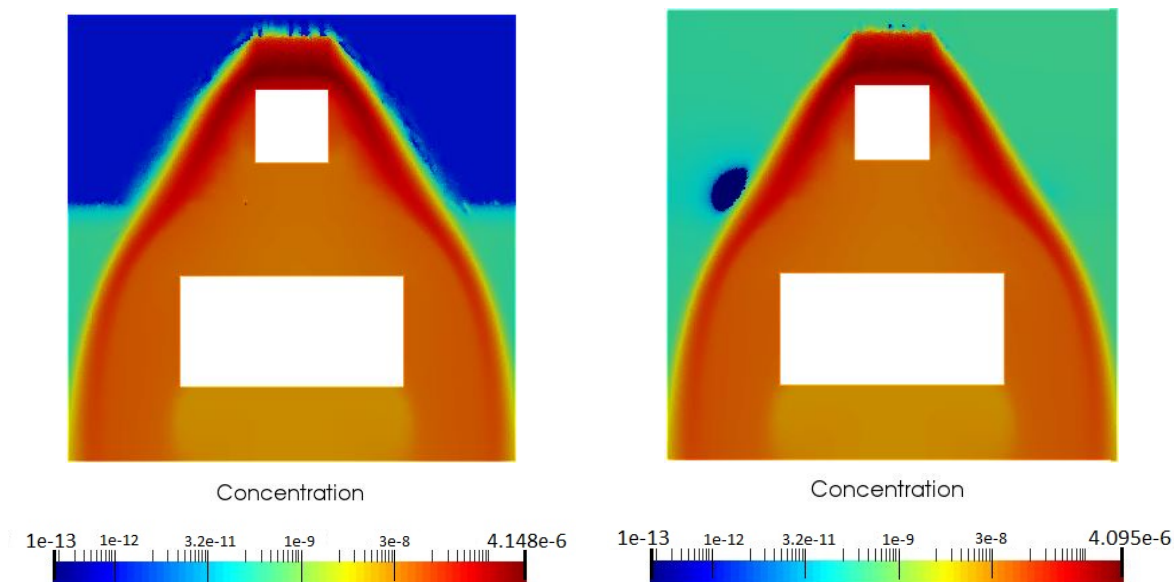


Figure 6.29 – Trial solution corresponding to maximal error, $p_{max} \in \mathcal{D}_{trial}^{bk}$ (5.6), logarithmic scale. Using synthetic trial data for parameter set Ξ^{trial} with model error with no model error. FEM solution (left), PBDW approximation (right). We set $M = 8$ and $N = 3$ here.

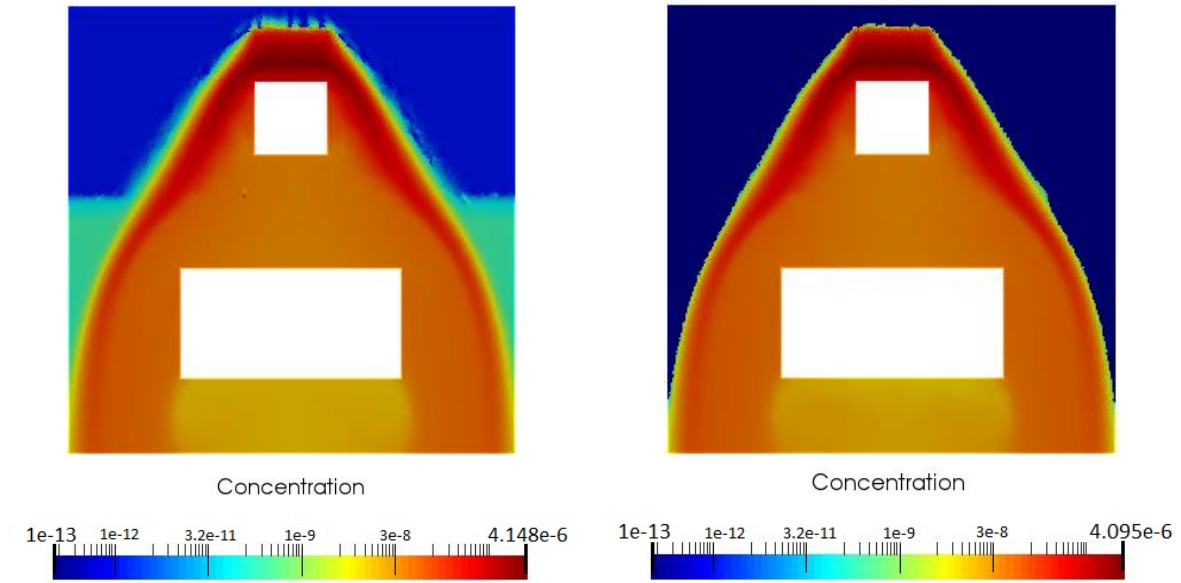


Figure 6.30 – Trial solution corresponding to maximal error, $p_{max} \in \mathcal{D}_{trial}^{bk}$ (5.6), logarithmic scale. Using synthetic trial data for parameter set Ξ^{trial} with model error with an added reaction term of $R = 0.001$. FEM solution (left), PBDW approximation (right). We set $M = 8$ and $N = 3$ here.

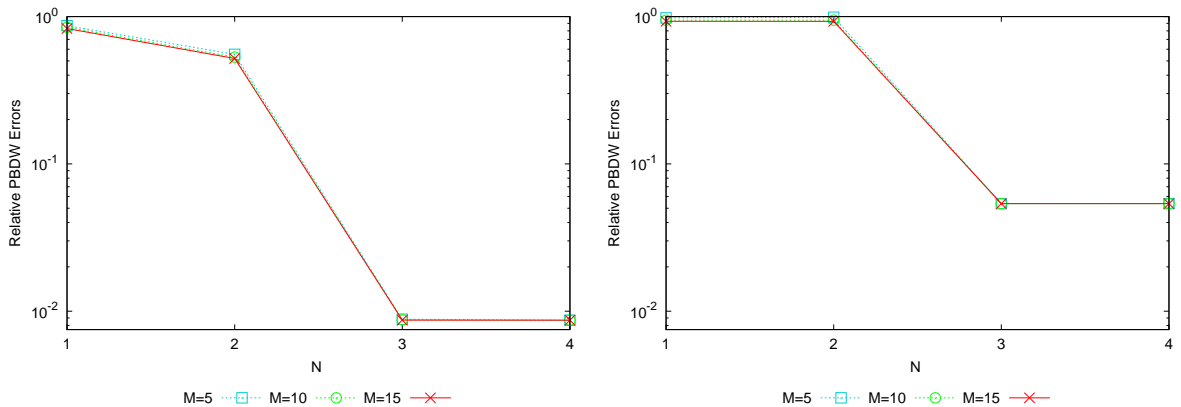


Figure 6.31 – Relative mean (5.10) (left) and maximal (5.11) (right) PBDW approximation error as a function of N for fixed M values. Using synthetic trial data for parameter set Ξ^{trial} with no model error (model \mathcal{P}^{bk}). Sensor locations chosen by a greedy procedure.

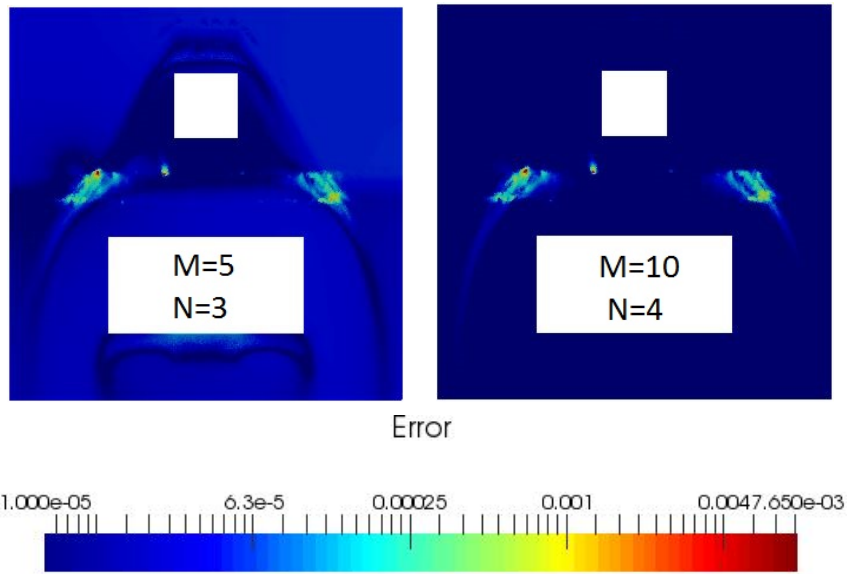


Figure 6.32 – Relative mean PBDW approximation error maps for $M = 4$ and $N = 3$ (left), and $M = 10$ and $N = 4$ (right). Using synthetic trial data for parameter set Ξ^{trial} with no model error (model \mathcal{P}^{bk}). Sensor locations chosen by a greedy procedure.

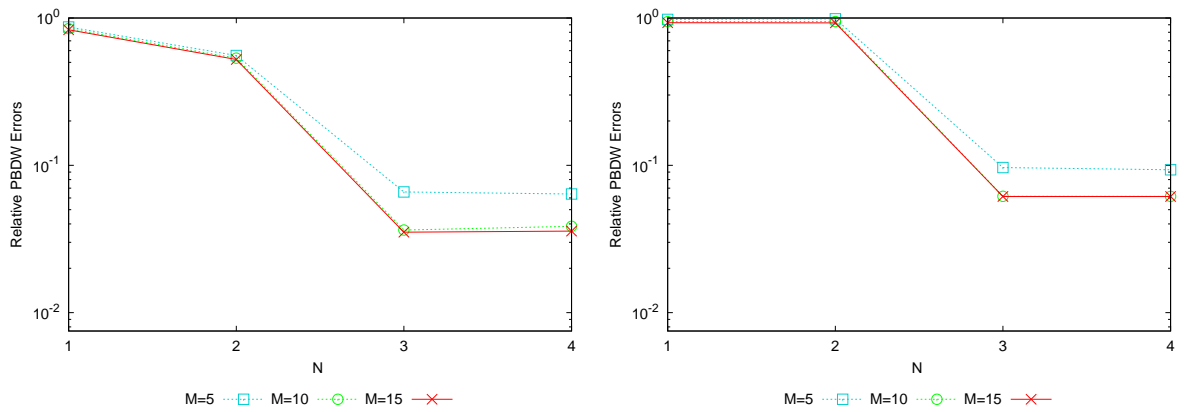


Figure 6.33 – Relative mean (5.10) (left) and maximal (5.11) (right) PBDW approximation error as a function of N for fixed M values. Using synthetic trial data for parameter set Ξ^{trial} with $R = 0.001$ (model \mathcal{P}^{trial}). Sensor locations chosen by a greedy procedure.

Chapter 7

A Real-World Application: Air Quality Modeling for Fresno

Résumé :

Ce chapitre porte sur la mise en place de la méthode PBDW pour une application *in-situ* sur un quartier de $800\text{ m} \times 800\text{ m}$ à Fresno en Californie. Cette ville est particulièrement touchée par de fortes concentrations de pollution. Cette application est en vue de l'évaluation d'exposition menée par une équipe de recherche en épidémiologie à l'Université de Californie Berkeley (UCB). Le but à long terme est d'améliorer les méthodes pour estimer des expositions individuelles. L'écoulement d'air sur le domaine a été calculé sur la base des données météorologiques du 1 avril 2001. On considère que les sources de pollutions sont deux larges rues. Le positionnement des capteurs est choisi par un algo de type greedy parmi un ensemble de 2250 positions. On étudie la stabilité et la convergence de la méthode en fonction du nombre de point de mesure et de l'erreur de modèle (aucune, petite ou moyenne). On remarque que l'on arrive à reconstruire le champ de concentration jusqu'à 1% de précision presque partout dans le domaine.

PBDW CPU Times	Online Stage
$M = 8, N = 3$	7.1s
$M = 15, N = 3$	12.2s
$M = 15, N = 5$	13.3s

Tableau récapitulatif des temps de calcul de la phase *en ligne* de la PBDW.

On conclut le chapitre avec une discussion sur les implications de ces résultats, et des perspectives pour de futurs travaux.

In this chapter we present a collaboration between two disciplines, the mathematical methods presented in this thesis and the epidemiology exposure assessments employed by a research team at UC Berkeley (UCB). The long-term goal is to improve the methods for estimating individual exposures and expand the ability of current UCB epidemiologic studies to evaluate the association of these exposures to various health conditions from allergies and asthma to birth defects and glucose dysfunction. As scientific measures of health outcomes have become more refined, the need for more accurate evaluation of exposure has grown.

7.1 Introduction

In California, the San Joaquin Valley (SJV) air basin is particularly impacted by high concentrations of ambient particulate matter (PM) and other pollutants. Fresno, one of the largest cities within the SJV, has been the study area for over a decade of air pollution epidemiology studies examining the impact of air pollution on children's health. The rich UCB measurement data (15 years of hourly data for multiple air pollutants at numerous locations in one city) provide input data for both model refinement by PBDW implementation and validation of results. The results of this method could prove helpful to the research team at UC-Berkeley, and provide the groundwork for application of these methods in studies closer to home, to serve the French environmental health program for example.

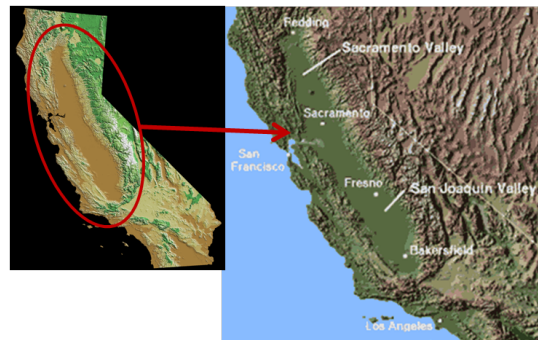


Figure 7.1 – Geographical location of interest: San Joaquin Valley.

An advantage of this collaboration with UCB is that the state of California is a leader in air quality studies, with a wealth of data (e.g. emissions) and modeling expertise.

The collaboration with the team led by Dr. Noth and Professor K. Hammond began in the framework of a grant application for the France Berkeley Fund, and continued with a visit to UCB as a Visiting Student Researcher in Fall of 2015. The results from these initial works will be presented here. Dr. Noth and Pr K. Hammond are currently involved in the on-going Children's Health and Air Pollution Study (CHAPS), a collaboration of UC Berkeley, Stanford University, UC San Francisco, and California State University, Fresno, funded as a Children's Environmental Health Center by NIEHS and USEPA, designed to study the effects of

pollutant gases, PM, black carbon (BC) and elemental carbon (EC), and polycyclic aromatic hydrocarbons (PAHs) on health outcomes in a cohort of children. These studies have employed statistical models for exposure prediction using either spatial interpolation or linear regression to account for temporal and spatial trends in air pollution [138, 139].

Since 2001, the UCB team has collected hourly data on the criteria air pollutants (ozone, PM_{2.5}, PM₁₀, carbon monoxide (CO), nitrogen oxides (NO₂, NO_x), and sulfur dioxide), and standard meteorology measures (e.g. wind direction and speed, temperature, relative humidity) from routine air quality measurement networks (run by the California Air Resources Board, the San Joaquin Valley Air Pollution Control District and the US EPA). In addition to these routine measurements, hourly data has also been collected for particle-bound PAH and BC for the past 14 years at 1-4 sites (e.g., 3 sites for 2002-3; 4 sites from 2014-2018). During two periods of time extensive spatial sampling was conducted, when data were collected at a larger number of sites (see figure 7.2).

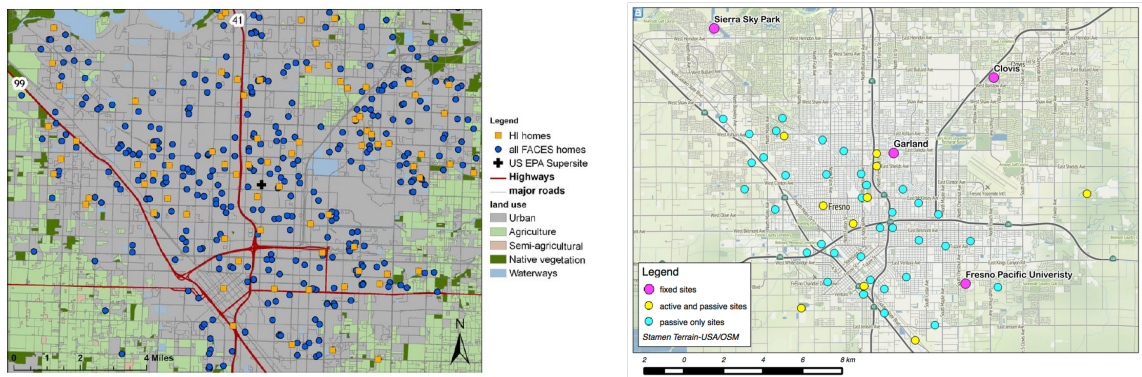


Figure 7.2 – Maps of sensor locations and subjects’ homes in Fresno. Left: FACES spatially-rich monitoring. Homes with sampling sites are marked by orange squares, other subjects’ homes by blue dots. 8 schools were also monitored. Right: CHAPS spatially-rich monitoring sites, in yellow and magenta. [197]

The goal of this collaboration is to apply the PBDW method to air quality modeling over the city of Fresno, beginning by studying a small neighborhood in Fresno with simulated data from the LUR model implemented by EM Noth [138]. This provides a first near-real-world application of the PBDW MOR and data assimilation method, and lays the groundwork for extension to a larger domain using real measurement data on air pollution and meteorological conditions collected in Fresno from 2001 through present (see figure 7.3).



Figure 7.3 – Pollution and meteorological sensors in Fresno [139]

Challenges and Difficulties

This project is exceptionally challenging, and we hoped our initial work would be the first steps toward a larger collaboration.

A significant hurdle necessary before beginning any modeling effort is to construct a three-dimensional geometry representing the domain of study. It is then necessary to select a model, and determine whether an operational model could be incorporated. Furthermore meteorology and emissions data are necessary, to select a database, understand the format of the data, and integrate it with the model. A method of validating the simulations and final state estimation is also crucial.

7.2 Fresno Case Study: a central neighborhood

We began by selecting a neighborhood in Fresno measuring approximately $2km^2$, represented in map view in figure 7.4.

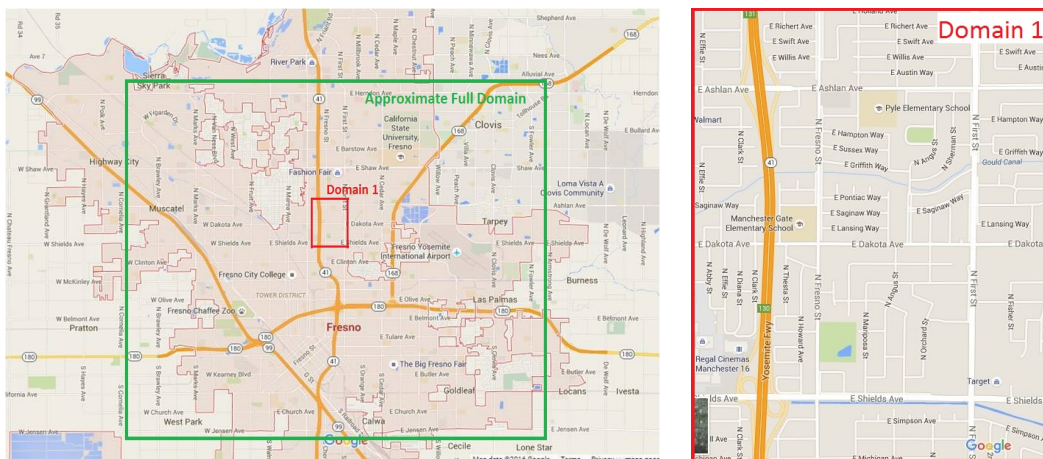


Figure 7.4 – Maps of calculation domains in Fresno. Left: Full view. Right: Zoom on reduced domain (Map data: Google 2015)

This neighborhood was chosen strategically to include a data measurement headquarters where meteorological data is available as well as a second data point for multiple criteria pollutants. The neighborhood is mostly residential and contains two elementary schools and a park, making it a relatively simple urban geometry including multiple potential regions of interest for air quality studies.

7.2.1 Geometry and Mesh

The first step toward pollution modeling over Fresno was the construction of a 3D geometrical representation of the neighborhood using data available online. We note that this step is often reduced to the selection of a 3D urban model available. In fact in many European cities, urban models are readily available, and more are being made available. This was not the case over Fresno.

We started with downloadable layers of Fresno in shapefiles available on the Fresno city website (<https://www.fresno.gov/publicworks/developer-doorway/technical-library>), which provided two-dimensional GIS (geographic information system) data on the streetplan, locations of addresses, parks, and 2D building footprints. These can be read in GIS software such as QGIS [183] (free two-dimensional GIS software) or ArcGIS [68] (more sophisticated GIS software).

We detailed the geographical data more using GoogleEarth (www.google.com/earth/download) to create three-dimensional representations of the remaining buildings in the neighborhood. A simplified approximation can be made by adding a polygon to *MyPlaces* resembling the building, and saving the place as a .kmz file. The painstakingly created individual building files can then be imported into ArcGIS as a vector layer, then added to the map, and eventually merged with other shapefiles as desired. Once the buildings were added, we removed approximately half the address points (address numbers are skipped in most cities), and used the "buffer" feature of the software to build a rectangular shape around each address point. We then extruded the rectangles to make simple 3D representations of a single-story house of similar size to those in the neighborhood.

In figure 7.5 we see the original shapefiles, along with the trimmed-down address shapefile and an additional shapefile containing (sparse) 2D building footprints.



Figure 7.5 – Representations of the domain in QGIS [183]. Left: available GIS data over Domain 1. Right: supplemented and formatted GIS data.

In figure 7.6 we can see the full 3D geometry in ArcGIS, after complementing available data using GoogleEarth.



Figure 7.6 – ArcGIS [68] representation of the neighborhood from geographical data, with constructed residential homes at locations of addresses.

We then exported the GIS data to SolidWorks [2], from which we converted the file to *.step* format in 3D with an atmospheric height of $30m$, chosen from literature estimates of a $30m$ boundary layer. We chose to set the origin at ground level of the measurement headquarters, and thus converted 2D GIS data into a 3D cartesian geometrical calculation domain. In figure 7.7 we see this three-dimensional

geometry in Salome-Platform [32], software used to construct a mesh, in which we defined boundary labels for use in simulation. We also illustrate a zoom on the three-dimensional mesh of over 6 million nodes in Salome.

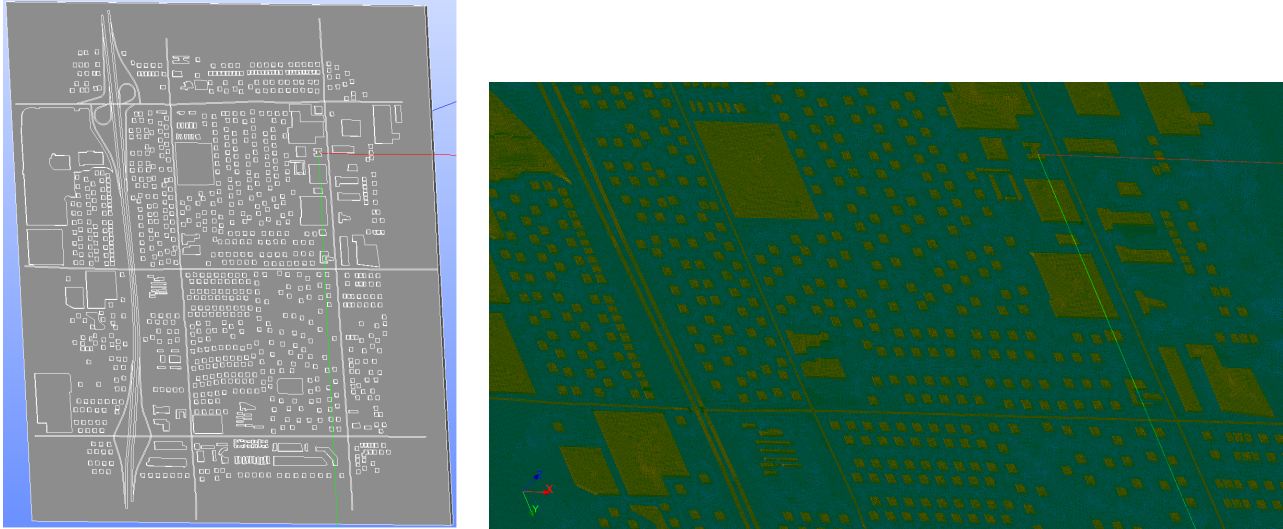


Figure 7.7 – Salomé [32] representation of a 3D geometrical domain made by extrusion of the 2D data, centered at a chosen data point (left). Zoom on the 3D calculation mesh (right).

These figures represent the neighborhood of Fresno during the various steps of creating a calculation mesh for our CFD and CTM studies, first step toward urban-scale modeling of air quality over Fresno. In case studies over cities where this data is publicly or privately available, this time-consuming step is unnecessary, as urban digital maps can be coupled with external softwares to provide the urban geometry for the code of our choice.

7.2.2 A CFD wind field

Once we disposed of a computation domain and appropriate conforming mesh, we used historical meteorological data from the measurement headquarters (conveniently placed at $(0, 0, 0)$) to select a time for our study.

Here we employed *Code_Saturne* as described in section 4.2.1 (and appendix C) to calculate a CFD wind field over the domain constructed to represent Fresno (figure 7.6). We note that our domain includes an appropriate "buffer" zone of $15L$ where L is the dimension of the most exterior obstacle.

Figure 7.8 represents the velocity field over the calculation domain (a cut at $z = 1m$ and a vertical cut to represent the logarithmic inflow profile) after 3500 time steps of $0.1s$. Boundary conditions correspond to those described in section 4.2.1 and section 6 for a South-Easterly wind (direction 308° at $11.4 \frac{km}{h}$). This wind direction and speed was chosen based on meteorological data from April 1, 2001,

when we found a 12-hour period during which wind direction fluctuated less than 30° . We averaged the hourly wind directions and velocities to set our aggregated inflow conditions. We then consider that the measurement was taken at approximately $10m$, to determine the appropriate coefficient $c = 1.3$ from equation (4.36).

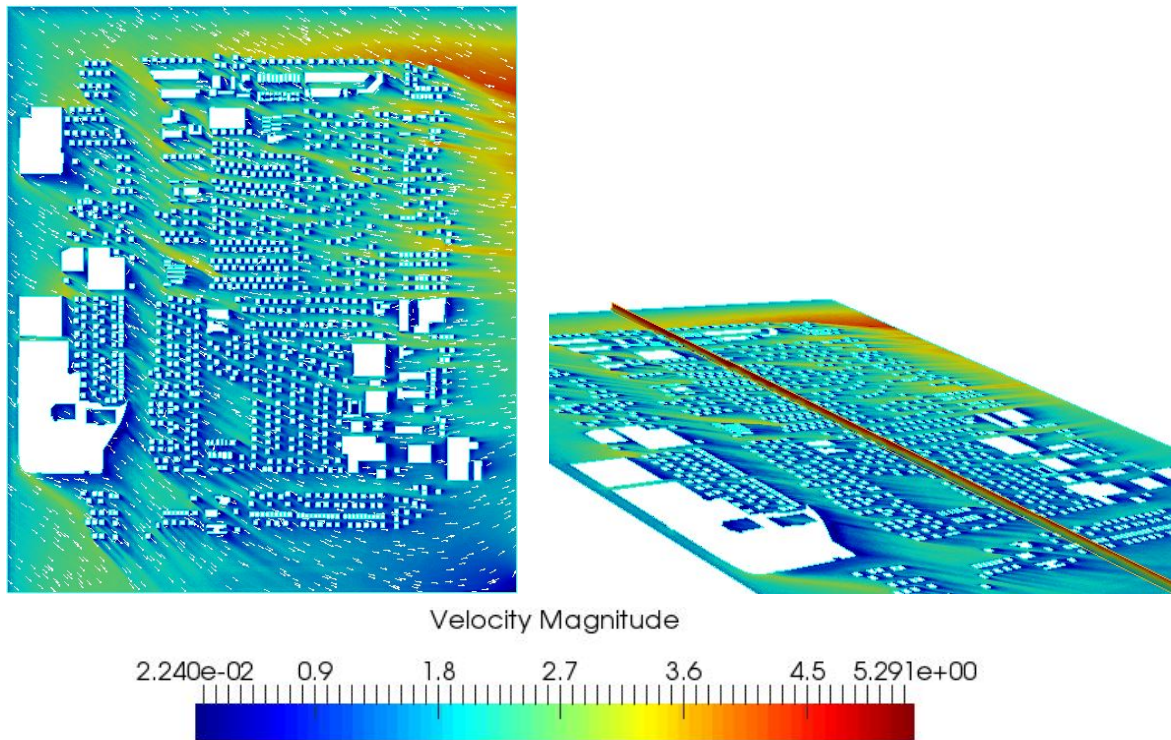


Figure 7.8 – Wind field over a neighborhood of Fresno for $\vec{v}_{in} = 1.3 * z^{0.4}$ in **SE** direction (308 deg), corresponding to conditions over Fresno on 1/4/2001. Left: a horizontal cut at $z = 1m$. Right: illustration of the vertical flow profile with an added vertical cut.

As in the 3D case study presented in section 6, the CFD velocity field was aggregated over 50 time steps in order to treat it as stationary for this first implementation. This was computed on a desktop machine with $74GB$ of RAM using 8 cores, and calculation time necessary to reach a stabilized velocity field took 37 days for 3750 time iterations over nearly 6 minutes of simulation time window.

7.2.3 Pollutant concentration fields

In Fresno, home heating by wood burning is common, contributing to the high concentrations of PM. We thus chose to first study $PM_{2.5}$. Factors taken into consideration in this choice are the numerous measurement sites available for this criteria pollutant, and the relatively negligible reaction (as opposed to gaseous species).

Given the size of this large residential neighborhood of Fresno and the level of mesh refinement necessary for transport simulations over an advection-dominated realistic wind field, the accurate simulation of pollutant dispersion by PDE's with-

out the employment of more robust codes and powerful calculation machines was determined to be impractical. The concentration calculation domain was thus taken to be a subdomain of the geometry in figure 7.6, as seen in figure 7.9.

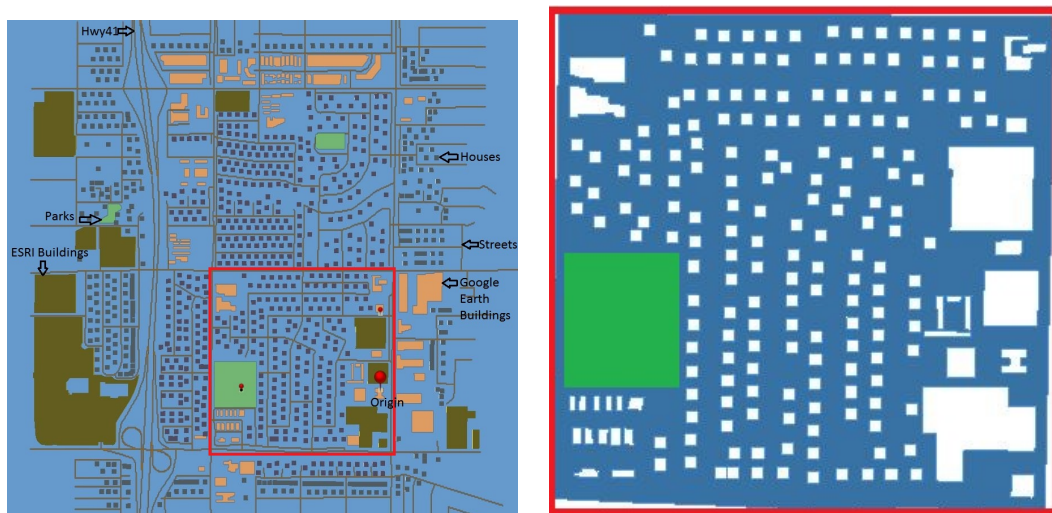


Figure 7.9 – Representation (ArcGIS) of a neighborhood in Fresno over which a wind field was computed using *Code_Saturne* (left). Representation of a subdomain of the fluid domain used to study pollutant concentrations (right).

This domain is approximately $800m \times 800m \times 30m$, and we considered a mesh of 1.64 million nodes. We translated the full-sized domain by a characteristic length of $L_g = 100m$ as in section 4.2.2.3 and used dimensionless equations, where $c_g = 1 \times 10^{-12} \frac{kg}{m^3}$. We used a reduced velocity field with $\vec{v} = \vec{v}^{true}/5$ for computational stability without drastically refining the mesh; in future applications mesh adaptation should be considered to construct an appropriately (but not excessively) refined mesh for concentration transport computations on the full velocity. Solution of the stabilized finite element model \mathcal{P}^{bk} given by (4.61) in FreeFem++ took approximately 31 minutes.

In figure 7.10 we see a *trial* solution to \mathcal{P}^{trial} given by equation (4.73) with $R = 0.001$, where pollution sources are taken to be two streets with intensities $5 \times 10^{-7} \frac{kg}{m^3} s^{-1}$ and $5 \times 10^{-9} \frac{kg}{m^3} s^{-1}$, chosen as described in section 5.1.2, and a background concentration of $5 \times 10^{-11} \frac{kg}{m^3}$.

We computed a set of 8 trial solutions for source intensities and background concentrations not represented by the basis functions of the background space \mathcal{Z}^N constructed from \mathcal{P}^{bk}

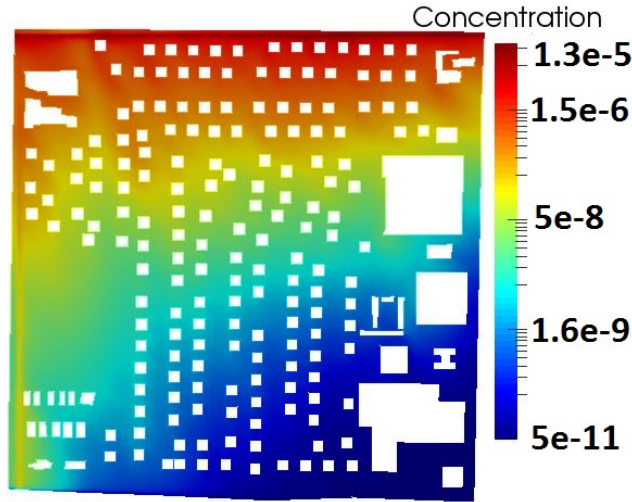


Figure 7.10 – A concentration solution to \mathcal{P}^{bk} with two street pollution sources.

In order to study the dimension of the solution manifold, which we expect to be $N = 3$ given the linearity of the problem \mathcal{P}^{bk} , we perform a POD analysis. We computed an ensemble solutions with these three parameters $\mathbf{p} = (p_0, p_1, p_2) \in \Xi_{train}^{bk}$ such that the background concentration $p_0 \in [1 \times 10^{-12}; 1 \times 10^{-8}]$, and the street source intensities $p_1, p_2 \in [0; 1 \times 10^{-7}]$.

In figure 7.11 we see the eigenvalues of the H^1 norm correlation matrix (2.9) associated to solutions to \mathcal{P}^{bk} for $\mathbf{p} \in \Xi_{train}^{bk}$, along with the H^1 POD projection errors as a function of N , as described by (2.10) and (2.11). These images demonstrate the relatively small dimension of the solution manifold for the parameter space we considered, however we can see that the dimension is larger than 3. In fact, the rank of the stiffness matrix is 13. We attribute this to numerical instabilities in the computational code for our model \mathcal{P}^{bk} . We could choose to neglect this aspect, however if we want to account for cases of imperfect best-knowledge models, the imperfection could very well include numerical instabilities which we can't always remove by hand (not to mention that in automatic processes we do not make by-hand modifications). We thus chose to accept this imperfection in our model and treat the solution as higher dimension than 3.

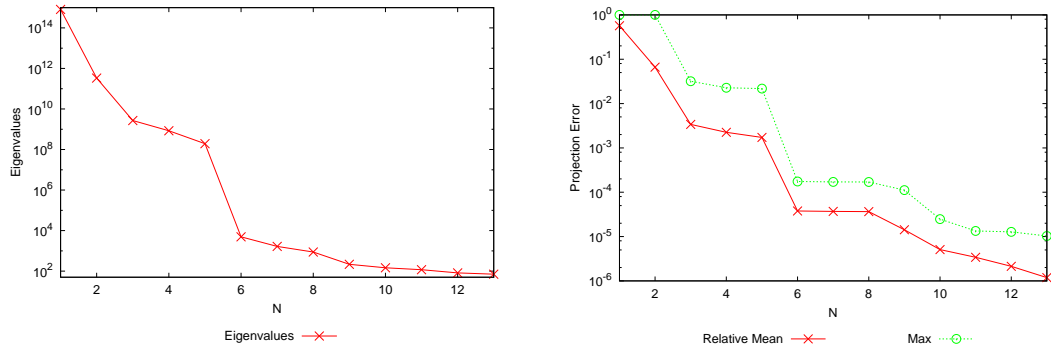


Figure 7.11 – Left: Eigenvalues of H^1 -norm correlation matrix associated to the ensemble of solutions to \mathcal{P}^{bk} for $\mathbf{p} \in \mathcal{D}^{bk}$. Right: Mean and max relative POD projection errors of these solutions.

7.2.4 PBDW state estimation

We want to test a first implementation of the PBDW method with this significantly more complex domain.

In order to compute our Update space we need to select sensor locations in the domain. We defined a set of 2254 possible locations over the domain and performed a greedy procedure of selection. In figure 7.12 we see a selection of potential sensor locations among the relatively dense grid, and we see the set of 25 sensors selected by a greedy procedure. We can see that many of these sensors are on the very edge of the domain.

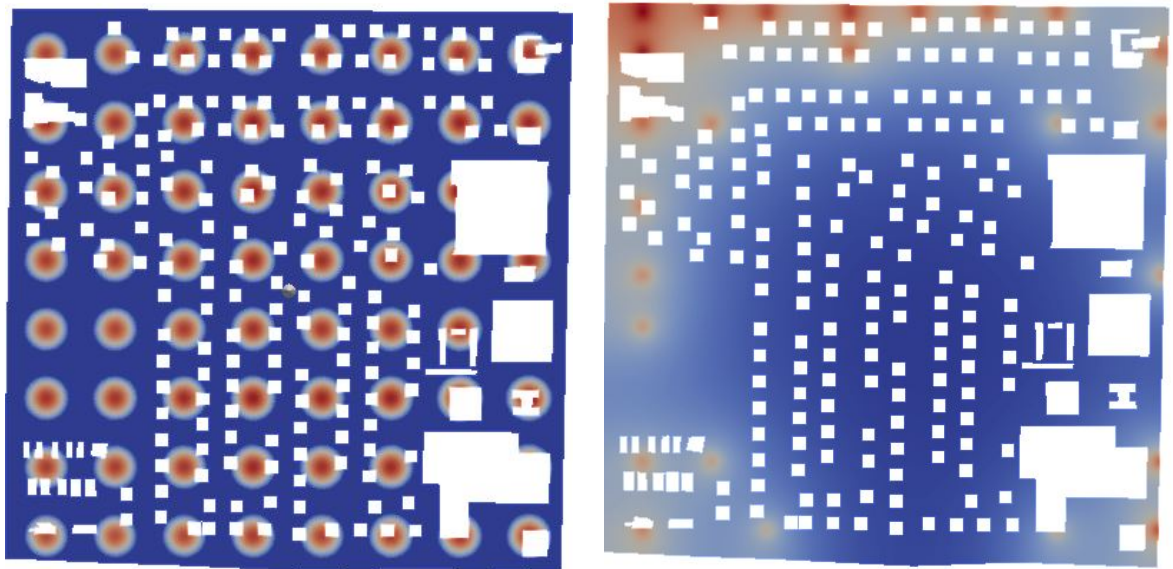


Figure 7.12 – Potential sensor locations, from a set of 2250 at varying heights (left), and 25 Greedy-selected sensors (right).

In figure 7.13 we see the stability constant $\beta_{N,M}$ (3.17) for the PBDW system, as well as the condition numbers of the PBDW matrices. We can see that we greatly lose stability from $N = 6$, and the matrix is poorly conditioned.

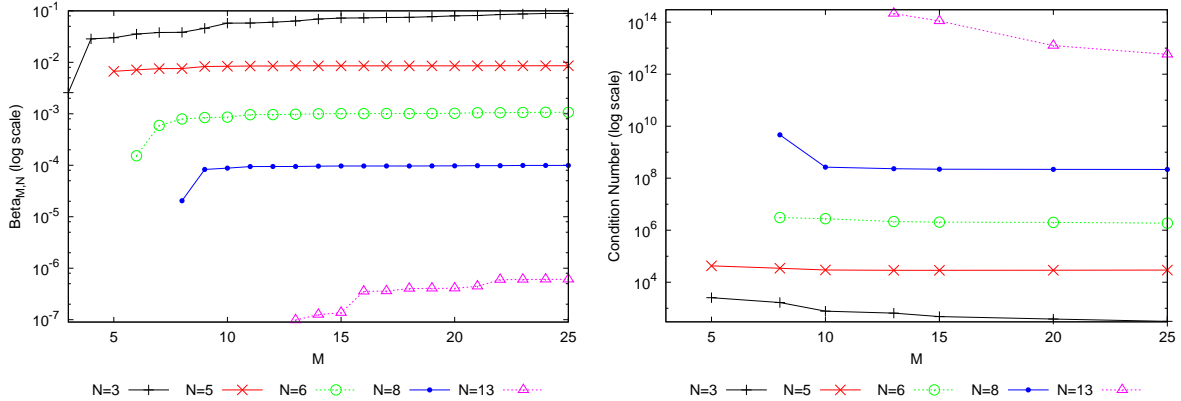


Figure 7.13 – Left: stability constant $\beta_{N,M}$ (3.17) with $\|\cdot\|_{\mathcal{X}} = \|\cdot\|_{H^1}$. Right: condition number of PBDW matrices, with $\|\cdot\|_{\mathcal{X}} = \|\cdot\|_{H^1}$. As a function of M for $N = 3, 5, 8, 13$. Sensor locations chosen by a greedy algorithm

We denote by Ξ^{trial} the parameter set for the group of trial solutions, each parameter corresponding to a parameter $\mathbf{p}_{trial} \in \mathcal{D}^{bk} \setminus \Xi_{train}^{bk}$. In order to test the PBDW method in accuracy and stability on our large and complex domain (with no more sensors than over the smaller domains), we will use synthetic data from these trial solutions in order to simulate measurement data and model error, and compute approximation errors of the PBDW method. The goal is to determine whether the PBDW method is robust enough for this application before attempting to implement with real data and no way of precise validation by calculation of true error.

In figure 7.14 we compare the FEM solution to model \mathcal{P}^{trial} with $R = 0.0001$ to the associated PBDW approximation for parameter p_{max} (5.6). We can see that the PBDW state estimate closely resembles the "true" solution, even for this configuration in which we see an effect of pollutant accumulation in a zone of high recirculation near a traffic source.

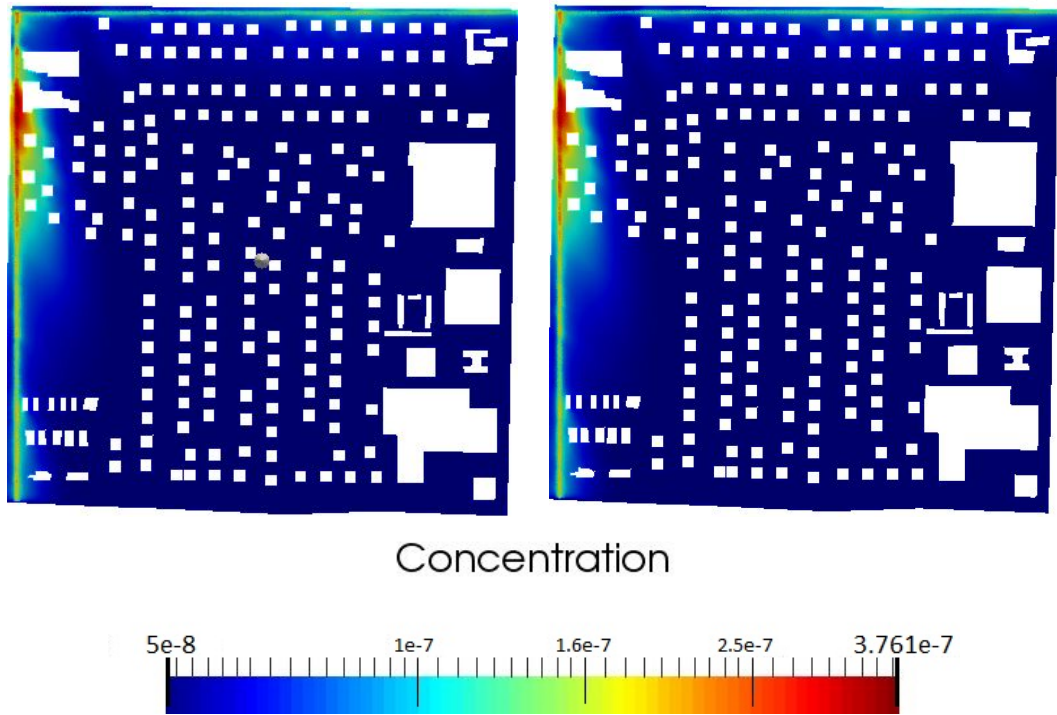


Figure 7.14 – FEM solution (left), PBDW approximation for $M = 8$ and $N = 3$ (right) with $p_{max} \in \mathcal{D}_{trial}^{bk}$ (5.6) and synthetic data with reaction term of $R = 0.0001$ (model \mathcal{P}^{trial}).

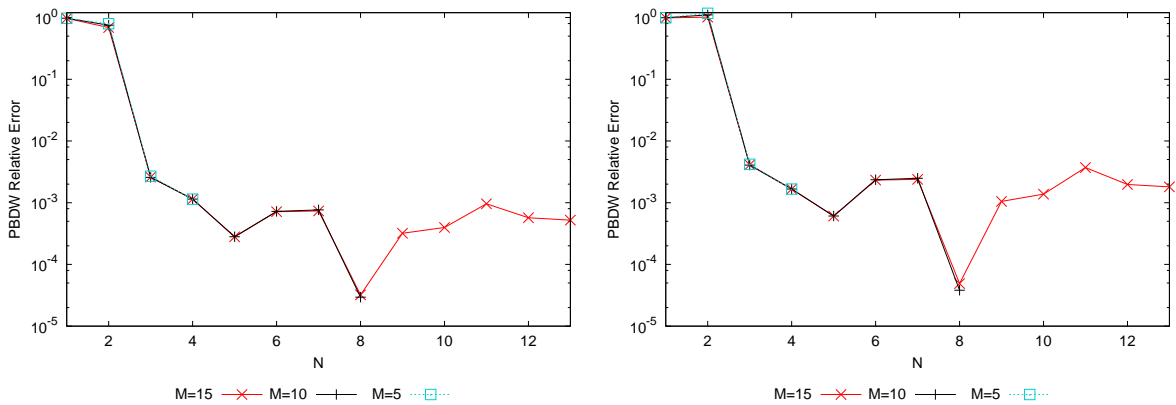


Figure 7.15 – Relative mean (5.10) (left) and maximal (5.11) (right) PBDW approximation error as a function of N for fixed M values. Using synthetic trial data from \mathcal{P}^{bk} , $\mathbf{p} \in \Xi^{trial}$, no model error. Sensor locations chosen by a greedy procedure.

In figure 7.15 we can see Relative mean (5.10) and maximal (5.11) PBDW approximation errors as a function of N for fixed M values. We see peaks in the approximation error correlated the stability and conditioning plots and with N -values. We determine that the improved span of the solution manifold with numerical instabilities after $N = 5$ no longer compensates for the instability of adding solutions which, aside from numerical instabilities, are already included in the span of the

background space \mathcal{Z}^N . In figure 7.16 we see these mean and maximal PBDW approximation errors over a trial set of solutions to model \mathcal{P}^{trial} with a $R = 0.0001$. In this case we can see that the model error renders the formulation less stable, particularly for higher numbers of measurement points M . We saw this trend in section 6 as well, and speculated that the poorly-conditioned system may be over-determined, but this effect calls for more investigation.

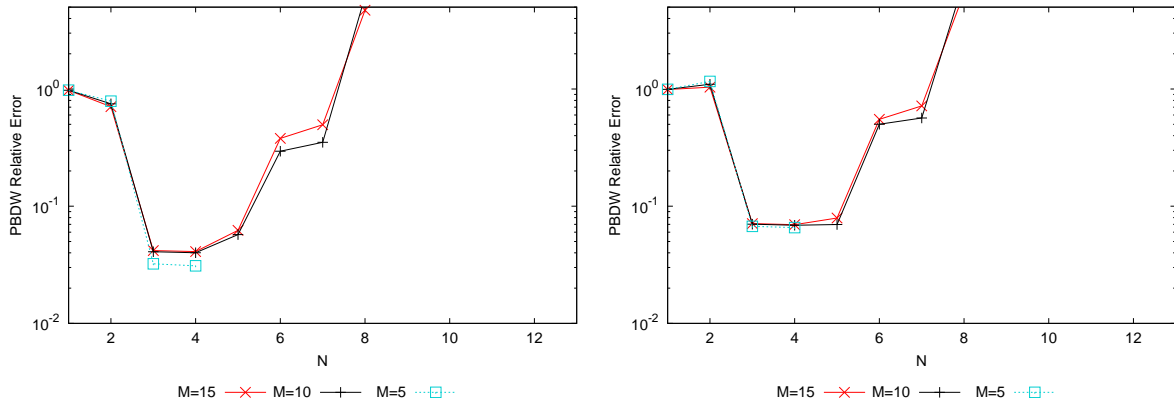


Figure 7.16 – Relative mean (5.10) (left) and maximal (5.11) (right) PBDW approximation error as a function of N for fixed M values. Using synthetic trial data from \mathcal{P}^{trial} , $\mathbf{p} \in \Xi^{trial}$, reaction term $R = 0.0001$. Sensor locations chosen by a greedy procedure.

In figure 7.17 we compare the PBDW approximation quality for two levels of model error, $R = 0.0001$ and $R = 0.0005$, in the model \mathcal{P}^{trial} . We see that, as expected, errors for a higher level of model error are higher, up to one order of precision, but that the curves take the same shape.

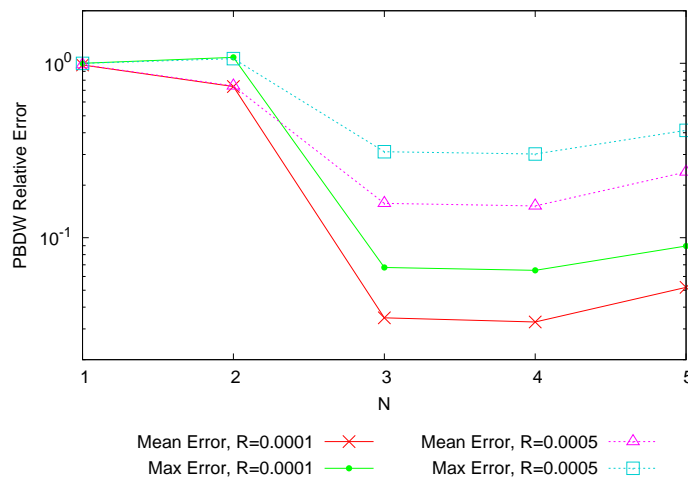


Figure 7.17 – Relative mean (5.10) and maximal (5.11) PBDW approximation error as a function of N for $M = 8$. Using synthetic trial data with added reaction terms of $R = 0.0001$ and $R = 0.0005$ in model \mathcal{P}^{trial} . Sensor locations chosen by a greedy procedure.

In figures 7.18 and 7.19 we show relative mean PBDW approximation errors plot-

ted over the calculation domain, as defined by (5.9), for two sets of 8 trial solutions with $\mathbf{p} \in \Xi^{trial}$, solutions to \mathcal{P}^{bk} and to \mathcal{P}^{trial} with for $R = 0.0001$, respectively. We can see that for this example with a background space perfectly representing the physical phenomena and parameter space (the case of trial solutions to \mathcal{P}^{bk} with no reaction term), we have entirely negligible error. With model error by an added reaction term, we can reconstruct the concentration field to at least 1% precision almost everywhere in the domain, a promising result for future application of these methods. We also note that the choice of a reaction term in the shifted model \mathcal{P}^{trial} was motivated by the desire to represent a physical phenomena not accounted for in the model \mathcal{P}^{bk} . In the case of $PM_{2.5}$ over Fresno, we can reasonably consider reaction to be less significant than the other physical phenomena accounted for in \mathcal{P}^{bk} , and thus a small error on reaction modification is not unlikely.

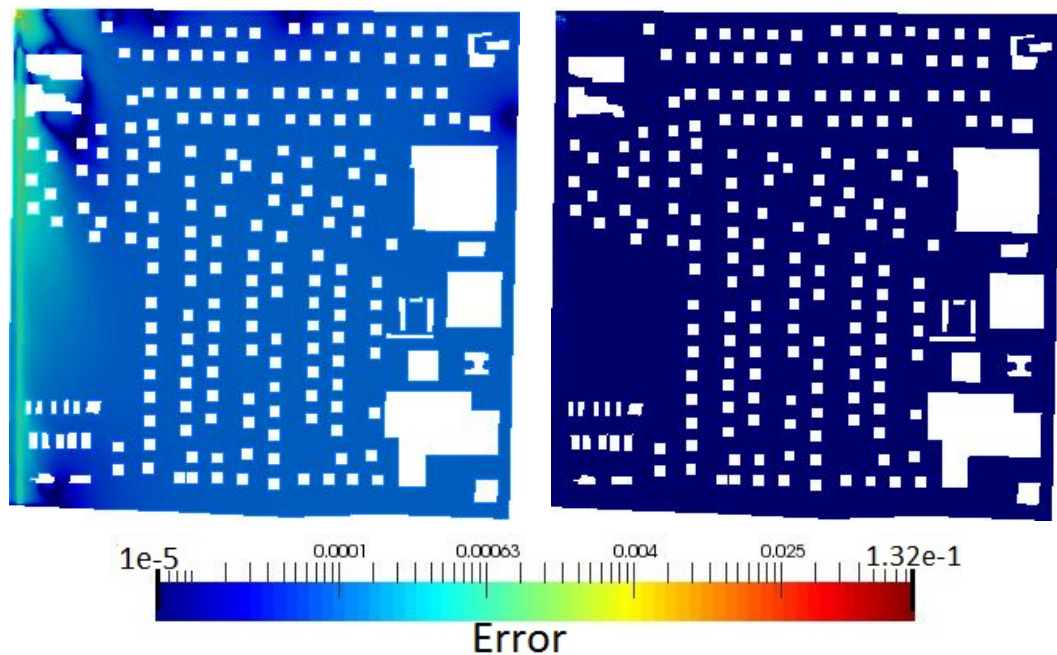


Figure 7.18 – Relative mean PBDW approximation error over a set of 8 trial solutions to \mathcal{P}^{bk} for $\mathbf{p} \in \Xi^{trial}$ with no model error. Left: $M = 8$, $N = 3$. Right: $M = 10$ and $N = 5$.

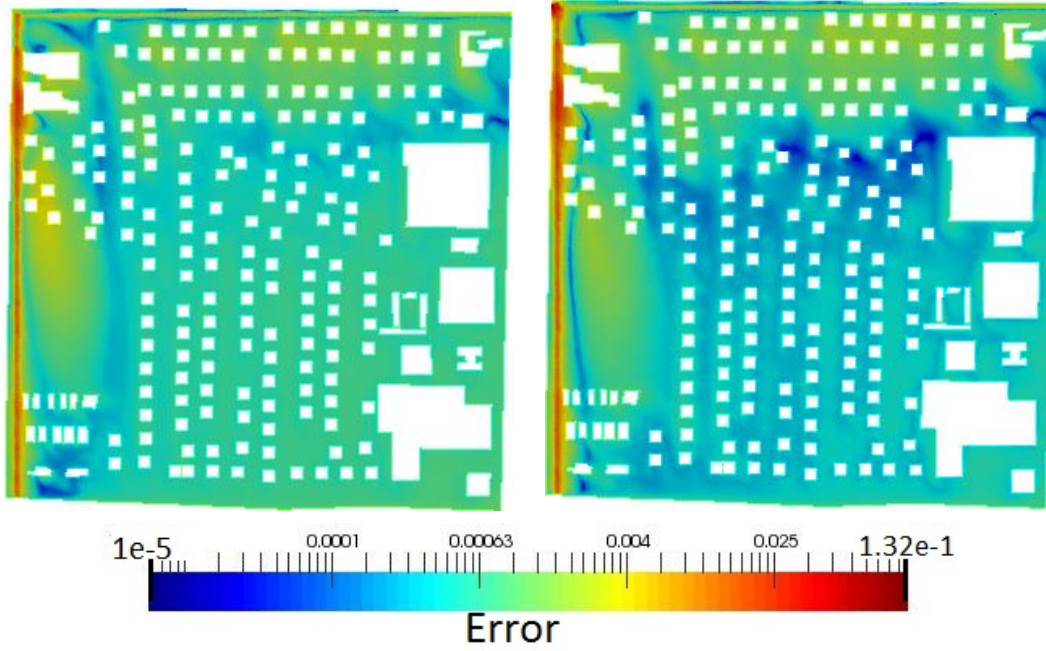


Figure 7.19 – Relative mean PBDW approximation error over a set of 8 trial solutions to \mathcal{P}^{trial} for $\mathbf{p} \in \Xi^{trial}$ with $R = 0.0001$. Left: $M = 8$, $N = 3$. Right: $M = 10$ and $N = 5$.

In table 7.2 we give computational times required for this first study over our real-world computational domain. We give offline computational time only in table 7.1 for the calculation of a concentration solution given the CFD wind field, as the CFD field cost depends on computational power of the machine, and input from meteorological models may be substituted in future studies.

FEM CPU Times	
FEM \mathbb{P}_1 - SUPG	31min

Table 7.1 – Computational times of the FEM approximation of \mathcal{P}^{bk} . Average over the set of training solutions considered here.

PBDW CPU Times	Online Stage (average CPU times)
	Reconstruction of the full solution $c_{M,N}$
$M = 8, N = 3$	7.1s
$M = 15, N = 3$	12.2s
$M = 15, N = 5$	13.3s

Table 7.2 – Computational times of the PBDW state estimation for various M and N values. Average over the set of trial solutions considered here.

7.3 Conclusion and Perspectives

In this chapter we studied the implementation of the PBDW using our own best-knowledge model (4.61) with source terms and boundary conditions informed by literature. We examined the results of the PBDW method using synthetic data from our *trial* solutions to (4.73) and a shifted parameter set Ξ^{trial} to study the stability of and validate this first test.

These results show promise in the expansion of the PBDW reduced basis data assimilation method from relatively small domains with simple geometry, as has been studied in previous works and in chapters 5 and 6, toward a large domain with highly complex geometry, and over complex physical phenomena depending on turbulent velocity fields. While the extension to application over the full city of Fresno and use with real observational data will require more study, we believe this first step demonstrates the feasibility of non-intrusive reduced order variational data assimilation methods as the PBDW in urban-scale real-world scenarios.

The next step we hope to take is to utilize available operational models, such as the larger-scale model WRF-Chem [167], combined with meteorological measurement data to inform boundary conditions and background concentration for both airflow and pollutant transport modeling, and implement more precise pollutant emissions data available in online data bases. This strategy could greatly improve the quality of the background space \mathcal{Z}^N and better inform our model on a more appropriate parameter space \mathcal{D}^{bk} . We could also hope to replace our simplistic CTM (4.61) with a more sophisticated urban-scale model. Expansion towards larger domains will also be necessary in order to implement this method with more sparse measurement data, as is available over Fresno. This will require domain decomposition and geometrical parameters in order to handle large domains with urban-scale pollution modeling.

Part IV

A Study in Tunnel Engineering

Chapter 8

A non-intrusive reduced basis method for elastoplasticity problems in geotechnics

R. Chakir ¹ and J.K. Hammond¹

Article under review for publication by the Journal of Computational and Applied Mathematics.

Abstract

This work aims at investigating the use of reduced basis (RB) methods to diminish the cost of numerical simulation of elastoplasticity problems arising from geotechnics modeling, and involving parameter-dependent partial differential equations (PDEs). Computation times for large three-dimensional analysis commonly take tens of hours, making optimization procedures or sensitivity analysis, relying on repeated simulations, hardly feasible. In many cases the geotechnical analysis requires very specific features such as highly non-linear constitutive laws, making the necessary modification of the FE calculation code for a standard RB method impossible. An approach making it possible to use the reduced basis framework without having to modify the code gives the so-called non-intrusive reduced basis method a versatility of great practical interest. Our approach involves the computation of less expensive (but less accurate) FE approximation during the online stage and improvement of those solutions using a RB-based rectification method.

Keywords : Reduced Basis method; Finite Element method; Parametric studies; Elastoplasticity; Soils.

8.1 Introduction

Numerical modeling has met growing success over the last decades, becoming indispensable in the field of geotechnical engineering, leading to the numerical simulation

¹Université Paris Est, IFSTTAR, 10-14 Bd Newton, Cité Descartes, 77447 Marne La Vallée Cedex, France.

by finite elements of even larger nonlinear problems. This trend stems from the need to account for the influence of constructing new structures, such as deep foundations of high-rise buildings or shallow tunnels for transport infrastructures, on neighboring structures (e.g. sewers, existing buildings, etc.) in dense urban areas. Computation times for large three-dimensional analysis commonly take tens of hours, making sensitivity analysis relying on repeated simulations hardly feasible. A common approach is to develop simplified models, such as metamodels, to approximate the model without significant loss of accuracy. In [25] a metamodel based on Proper Orthogonal Decomposition (POD) with radial basis functions (RBF) was applied to test problems in material mechanics with the goal of illustrating the capability of these metamodels to reproduce mechanical responses to the loading of complex non-linear material systems. An extended version of the POD-RBF metamodel was proposed in [98] to surrogate a 3D finite element simulation of a tunnel using a Hardening Soil model.

Another approach to rapidly compute reliable approximations of solutions of complex problems with many parameters is the use of reduced basis (RB) methods [153]. These methods rely on the parametric structure of the model and that when the parameters vary, the manifold of all possible solutions can be approximated by n -dimensional spaces. The performance and efficiency of the reduced basis methods are governed by the Kolmogorov n -width of the manifold of all the possible solutions [46] – which measures how well the manifold of all the possible solutions can be approximated by n -dimensional linear spaces. Thus, when the Kolmogorov n -widths decay rapidly with the space dimension, the manifold of all possible solutions can be approximated by a low-dimensional space, the reduced basis space. This reduced basis space is made of particular solutions of the parametrized problem with well-chosen parameter values.

Application of the reduced basis method to linear elastic solid mechanics problems with parameters of different natures (either physical or geometrical) has been proposed in [83, 92, 110, 129, 191]. One of the keys of RB techniques is the decomposition of the computational work into offline and online stages. During the offline stage the reduced basis functions are computed, as well as all parameter-independent quantities. This is done only once, whereas parameter-dependent quantities are computed during the online stage. The efficiency of reduced basis or POD-based reduction methods relies on liberating online calculation costs from dependency on the discretization, in order to only perform calculations with very low complexity. However in elasto-plastic problems with highly nonlinear behavior, not uncommon in the field of soil mechanics, the computational complexity of the local integration of nonlinear constitutive laws is not reduced.

Several alternative ways to carry out the standard POD-based reduction method for problems with nonlinear behavior have been investigated. For example in [48, 158] a partial reduction is performed over the region of the domain with elastic behavior, while the plastified region remains unreduced. This selective POD-based model reduction was extended by an adaptive method of sub-structuring POD(A-SPOD) in which the subdomain where model reduction is applied is determined automatically.

In [164–166] a hyper-reduction approach was proposed by Ryckelynck to treat the problem of local dependency and extended by Zhang [204] to a thermo-elasto-plastic model. The hyper reduction method consists in introducing reduced integration domains for internal variables.

However these methods require modification of the finite element calculation code leading to an intrusive procedure, which is particularly restrictive in the case of the considered geotechnics modeling applications. Analysis of the displacement field around a tunnel opening using numerical techniques is quite sensitive to the constitutive models of the soil used to describe the fundamental behavior of the materials involved. In many cases the analysis requires very specific features which are not available in all finite element software, such as highly non-linear constitutive laws, involving a complex description of hardening phenomena in soils. Given a well-adapted software for the problem considered, an approach making it possible to use reduced basis methods without modifying the code, and considering it as a "black box", gives the so-called non-intrusive reduced basis method a versatility of great practical interest. Our approach involves the computation of less expensive (but less accurate) FE approximations with a black-box FE software, and the improvement of these solutions using a reduced basis during the online stage.

In order to understand this so-called non-intrusive reduced basis approach, let us specify that the idea of reduced basis methods is, for a given parameter value, to compute an inexpensive approximation of the projection of the truth FE solution onto the reduced basis space. This consists in finding a good approximation of the coefficients of the decomposition of the truth FE solution in a basis made of particular solutions for well-chosen parameters values. Our non-intrusive approach aims at computing inexpensive, yet sufficiently accurate, approximations of the optimal coefficients by using a "coarse" FE as a substitute to the truth FE solution, since "coarse" FE approximations can be computed quickly enough to be used in model reduction techniques. The goal of our technique is to recover the accuracy of the truth FE approximation by doing a simple rectification which ensures that, for the set of parameters used in the construction of the reduced basis, our method returns exactly the corresponding truth FE solutions. In [34, 35], we have shown on simple examples the potential of this non intrusive reduced basis approach. In [133] a theoretical understanding to this so-called "rectification method" was given. In this work, we aim to demonstrate the feasibility of this approach in geotechnics modeling.

This paper is organized as follows. In Section 2, we formulate the elastoplastic problem providing a brief description of the physical system, the material behavior laws, the governing equations and boundary conditions. In Section 3, we provide a brief introduction to reduced basis methods, and discuss a preliminary analysis of the feasibility and reliability of RB approximations of the elastoplastic problem. In Section 4 the problem is solved with a non-intrusive reduced basis method. Finally Section 5 presents our conclusions.

8.2 The elastoplastic problem

The chosen application belongs to the field of tunnel engineering. In urban areas, it is necessary to consider the possible impact of the construction of a shallow tunnel on existing structures (buildings, foundations, etc.). In many cases, the first step consists of evaluating the settlements that would be induced by the construction of a tunnel in a "greenfield" environment, i.e. with no structure at the surface. Our first case of study is a circular tunnel built through a 50-m horizontal ground layer. The tunnel diameter is $D=10$ m and the axis depth is $H=25$ m. The analysis is carried out under the plane strain assumption. If the ground is homogeneous and isotropic, only half of the ground layer needs to be considered. For practical reasons, the analysis is limited to a distance of $L=100$ m from the tunnel axis (see figure 8.1a). Our second case of study is a twin tunnel built under an existing tunnel through a 75-m horizontal ground layer (see figure 8.1b).

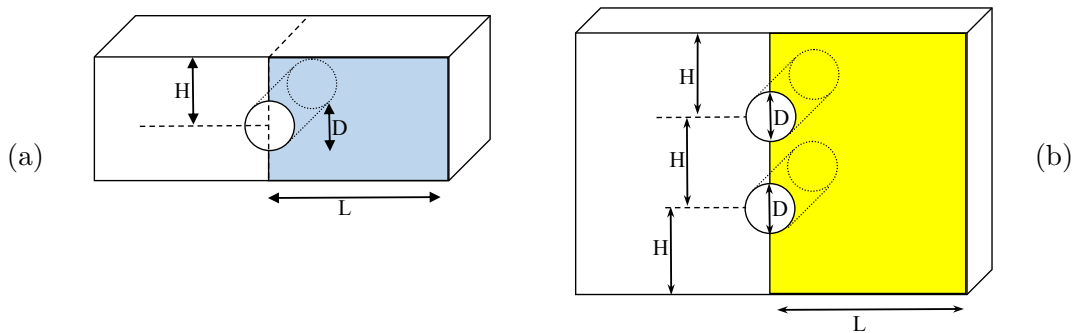


Figure 8.1 – Geometry of the physical domains : single tunnel (left) and twin tunnels (right)

8.2.1 From material behavior laws to the governing equations

In design calculations, materials (soil, concrete, rock, metal, liquid, gas) are considered as continuous mediums (or continua). These materials are thus considered to obey certain general physical and mechanical principles, such as the conservation of energy and momentum. While everyday experience can tell us that different materials do not behave in the same way under the same forces, general physics laws do not allow us to make the distinction between different sorts of materials. We therefore want to characterize the specific behavior of the continuum equivalent to the material under consideration. This is the goal of the constitutive laws associated to a material; the laws must characterize the evolution caused by given exterior forces and be specific to the material in question. When switching from one material to another, the laws must translate the differences in practically observed behavior. The constitutive law associated to a material is necessary to complete the system of equations of any mechanics problem of continua or structural design. The behavior of the soils in our problem is represented by an elastoplastic model used for pul-

verulent soils (sands) and for long-term coherent soils (clay and silt). Observations show that irreversible deformations appear when the stress exceeds a certain level. Let u be the displacement vector; the deformation is assumed to be infinitesimal so that the strain tensor can be written as $\epsilon(u) = \frac{1}{2}(\nabla u + {}^t\nabla u)$. The framework of plasticity is based on the assumption that the strains can be split into the sum of two terms :

$$\epsilon = \epsilon^e + \epsilon^p, \quad (8.1)$$

where ϵ^e is the elastic strain tensor and ϵ^p is the plastic part of the total strain tensor ϵ , which corresponds to the irreversible part of the strain. The elastic part of the behavior of the soil is linear² and isotropic and described by Hooke's law (characterized by Young's modulus E and Poisson's coefficient ν). The plastic part of the soil's behavior is considered nonlinear and is obtained via the Mohr-Coulomb model [47] (characterized by the cohesion c , the friction angle φ , and the dilatancy angle ψ).

8.2.1.1 Linear elastic behavior : Hooke's Law

Hooke's law (8.2) describes the relationship between the stress tensor $\sigma(u) \in \mathbb{R}^{d \times d}$ and the elastic strain tensor $\epsilon^e(u) \in \mathbb{R}^{d \times d}$.

$$\begin{aligned} \sigma(u) - \sigma^0 &= \frac{E\nu}{(1+\nu)(1-2\nu)} \text{tr}(\epsilon^e(u)) \mathbf{I}_d \\ &+ \frac{E}{(1+\nu)} \epsilon^e(u) \end{aligned} \quad (8.2)$$

with σ^0 the initial stress tensor, E and ν soil's parameters.

8.2.1.2 Nonlinear plastic behavior : Mohr Coulomb's model

It is assumed that the plastic strain does not evolve as long as the stress tensor remains in the interior of a region of the stress space, called the elastic domain [47,128]. The elastic domain is generally defined by a condition of the type $f(\sigma_{ij}) < 0$, where f is called the yield function. The yield surface is the boundary of the elastic domain and thus defined by $f(\sigma) = 0$. For sands, the yield function can be expressed as follows.

$$f(\sigma_{ij}) = (\sigma_\ell - \sigma_s) - (\sigma_s + \sigma_\ell) \sin \varphi - 2c \cos \varphi, \quad (8.3)$$

where σ_ℓ and σ_s represent the largest and smallest eigenvalues of the stress tensor σ (often called principal stresses in mechanics). The parameters φ and c are the friction angle and the cohesion characterizing the soil. In this study, we focus on the case of elastic-perfectly plastic models, in which the yield surface does not evolve

²Let us note that here the term "linear" or "nonlinear" refers to the behavior of the material, not necessarily to a linear or nonlinear equation.

with loading. Let us consider the stress tensor σ_{ij} corresponding to a given load. If $f(\sigma_{ij}) < 0$, then σ_{ij} is in the elastic domain, we have that the deformation variation is described simply by

$$d\epsilon = d\epsilon^e.$$

If $f(\sigma_{ij}) = 0$, then σ_{ij} is on the boundary of the elastic domain. To describe the behavior at this point, we need to know if the material is in loading, in which case the deformation variation is described by

$$d\epsilon = d\epsilon^p + d\epsilon^e.$$

or if the material is unloading and has an elastic behavior. At a regular point σ_{ij} of the elasticity boundary, the plastic deformation can be described by the so-called "plastic flow rule"

$$d\epsilon^p = d\hat{\lambda} \frac{\partial g}{\partial \sigma},$$

where $d\hat{\lambda} \geq 0$ is a scalar called the plastic multiplier and g is given by

$$g(\sigma_{ij}) = (\sigma_\ell - \sigma_s) - (\sigma_s + \sigma_\ell) \sin \psi - 2c \cos \psi. \quad (8.4)$$

The problem is closed by the "consistency condition"

$$df d\hat{\lambda} = 0. \quad (8.5)$$

8.2.1.3 Equilibrium equation

We consider a static process, and the equilibrium describing our system is:

$$\text{div}(\sigma) + \rho F = 0, \quad (8.6)$$

where $\rho F = \begin{pmatrix} 0 \\ -\gamma \end{pmatrix}$ is the external body force and γ is the volumetric weight of the soil.

The elastic deformation is linked to the variation of the stress by a linear relation:

$$\sigma - \sigma^0 = C : \epsilon^e. \quad (8.7)$$

From (8.2) one can see that C_{ijkl} (representing the elasticity tensor of the material) is constant, symmetrical ($C_{ijkl} = C_{jikl} = C_{ijlk} = C_{klij}$) and depends only on E and ν .

8.2.1.4 Single tunnel case

In this paper, we consider 2D problems on bounded domains. We denote by $\Omega_a \subset \mathbb{R}^2$ the computational domain used in the "single tunnel" study case (see figure 8.2).

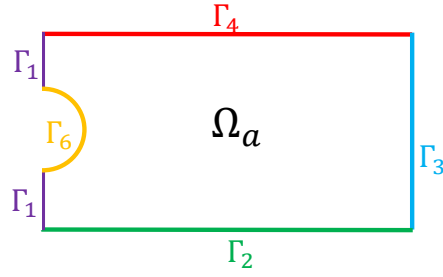


Figure 8.2 – Boundaries of domain Ω_a

We impose zero horizontal displacement on Γ_1 and Γ_3 and zero horizontal and vertical displacement on Γ_2 . The load consists of a surface density of force I applied on the wall of the tunnel (Γ_6) calculated from the initial stress tensor (which we assumed geostatic):

$$I = \lambda \sigma^0 \cdot \vec{n}, \quad \text{with} \quad \sigma^0 = \begin{pmatrix} x_2 K_0 \gamma & 0 \\ 0 & x_2 \gamma \end{pmatrix},$$

where λ represents the confinement loss caused by the excavation of the tunnel, and $K_0 = 1 - \sin(\varphi)$ the coefficient of the earth's pressure at rest. Let $(u_{i,i=1,\dots,d})$ be the displacement components in the x_i -directions. The boundary conditions of our problem read as follows:

$$\begin{cases} \sigma \cdot \vec{n} = -\lambda \sigma^0 \cdot \vec{n} & \text{on } \Gamma_6, \\ (\sigma \cdot \vec{n})_2 = 0 & \text{on } \Gamma_1 \text{ and } \Gamma_3, \\ \sigma \cdot \vec{n} = \vec{0} & \text{on } \Gamma_4, \\ u_1 = 0 & \text{on } \Gamma_1, \Gamma_2 \text{ and } \Gamma_3, \\ u_2 = 0, & \text{on } \Gamma_2. \end{cases} \quad (8.8)$$

8.2.1.5 Twin tunnel case

We denote by $\Omega_b \subset \mathbb{R}^2$ the computational domain used in the "twin tunnel" study (see figure 8.3) .

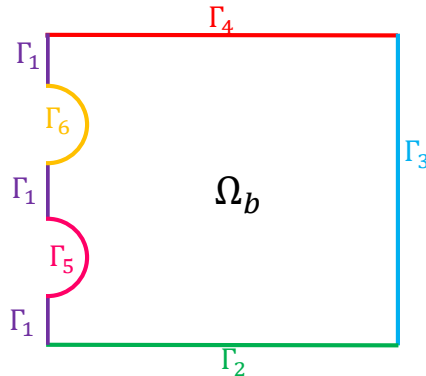


Figure 8.3 – Boundaries of domain Ω_b

In this case, the simulation is decomposed into two stages. During the first stage we compute the stress tensor after the excavation of a single tunnel on boundary Γ_6 , by solving the same problem as in case 8.2.1.4. We denote by σ_a the resulting stress tensor. Starting from this state, we compute the stress tensor and displacement after the excavation of the twin tunnel on the boundary Γ_5 . Thus, during the second stage of our calculation equation (8.7) is replaced by

$$\sigma - \sigma_a = C : \varepsilon^e \quad (8.9)$$

and the boundary conditions read as follows

$$\left\{ \begin{array}{l} \sigma \cdot \vec{n} = -\lambda \sigma^0 \cdot \vec{n} \quad \text{on } \Gamma_5, \\ \sigma \cdot \vec{n} = \sigma_a \cdot \vec{n} \quad \text{on } \Gamma_6, \\ \sigma \cdot \vec{n} = \vec{0} \quad \text{on } \Gamma_4, \\ (\sigma \cdot \vec{n})_2 = 0 \quad \text{on } \Gamma_1 \text{ and } \Gamma_3, \\ u_1 = 0 \quad \text{on } \Gamma_1, \Gamma_2 \text{ and } \Gamma_3, \\ u_2 = 0, \quad \text{on } \Gamma_2. \end{array} \right. \quad (8.10)$$

8.2.1.6 F.E. approximation

In what follows, Ω represents a generic computational domain such that $\Omega = \Omega_a$ in the "single tunnel" simulations, and $\Omega = \Omega_b$ in the second stage of the "twin tunnel" simulations. Associated to the physical domain Ω , we define the following functional space

$$X = \left\{ v \in (H^1(\Omega))^2 \left| \begin{array}{l} v_1 = 0 \text{ on } \Gamma_1, \Gamma_2, \Gamma_3 \\ v_2 = 0 \text{ on } \Gamma_2 \end{array} \right. \right\} \quad (8.11)$$

In addition, we decompose the left-hand side of the weak form of our elastoplastic problem, arising from (8.6) into a linear term:

$$a_e(u, v) = \int_{\Omega} \varepsilon(u) : C : \varepsilon(v) d\Omega$$

and a nonlinear term

$$a_p(\varepsilon^p(u), v) = \int_{\Omega} \varepsilon^p(u) : C : \varepsilon(v) d\Omega,$$

and denote by $\mathcal{L}(v)$ the right-hand-side term.

In "single tunnel" simulations the right-hand-side term is

$$\int_{\Omega} \rho F v d\Omega - \int_{\Omega} \sigma^0 : \varepsilon(v) d\Omega - \int_{\Gamma_6} \sigma^0 \vec{n} \cdot v d\Gamma.$$

In the second stage of the "twin tunnel" simulation, the right hand side term is

$$\int_{\Omega} \rho F v d\Omega - \int_{\Omega} \sigma_a : \varepsilon(v) d\Omega - \int_{\Gamma_5} \sigma^0 \vec{n} \cdot v d\Gamma - \int_{\Gamma_6} \sigma_a \vec{n} \cdot v d\Gamma.$$

The weak form of our elastoplastic problem is: find $u \in X$ such that, $\forall v \in X$,

$$a_e(u, v) - a_p(\epsilon^p(u), v) = \mathcal{L}(v). \quad (8.12)$$

Let $\{\mathcal{T}_h\}_h$ be a family of regular triangulations of Ω and denote by X_h the following \mathbb{P}_k finite element space

$$X_h = \{v = (v_1, v_2) \in X, \forall K \in \mathcal{T}_h, v_i|_K \in \mathbb{P}_k(K)\}.$$

The finite element discretization of (8.12) is as follows : find $u_h \in X_h$ such that,

$$a_e(u_h, v_h) - a_p(\epsilon^p(u_h), v_h) = \mathcal{L}(v_h). \quad (8.13)$$

CESAR-LCPC [91], a FEM-based software, was used to solve (8.13), employing a fixed-point strategy to approximate the displacement u_h , the stress tensor σ_h , the strain tensor ϵ_h , and the plastic strain tensor ϵ_h^p . For more details on the computational procedure see [47, 128].

In what follows we fix the Poisson coefficient at $\nu = 0.3$, the volumetric weight of the soil at $\gamma = 20kN/m^3$, and assume that the dilatancy angle is equal to the friction angle ($\psi = \varphi$)³.

We want to apply reduced basis methods within this framework to compute the displacement u_h corresponding to different values of $E \in [100; 300] MPa$, $\varphi \in [22; 34]$ degrees, $\lambda \in [0.2; 0.4]$ and $c \in [20; 40] kPa$ for the cases introduced in sections 8.2.1.4 and 8.2.1.5.

In the remaining sections we denote by $\mu = (E, \lambda, \varphi, c)$ our parameter set, by $\mathcal{D} \subset \mathbb{R}^4$ our parameter domain, and denote by $u_h(\mu)$ the solutions of the parametrized problem (8.13).

8.3 Methodology

The numerical simulation of the problems introduced in the sections 8.2.1.4 and 8.2.1.5 can prove to be costly, particularly in the many-query context, due to the parametric nature, making in an ideal candidate for reduced basis methods. The reduced basis method relies on the fact that when the parameters vary, the set of solutions may be of small Kolmogorov dimension, implying that $\mathcal{M}_h = \{u_h(\mu) \in X_h \mid \mu \in \mathcal{D}\}$, the manifold of all solutions, can be approximated by a finite set of well-chosen FE solutions of the parametrized PDE. One can identify a set of parameters, $S_N = (\mu_1, \mu_2, \dots, \mu_N) \in \mathcal{D}^N$ such that the particular solutions $(u_h(\mu_1), \dots, u_h(\mu_N))$ will generate this low dimension space. The idea of RB methods is to compute an inexpensive and accurate approximation, $u_h^N(\mu)$, of the solution to problem (8.12) for any $\mu \in \mathcal{D}$ by seeking a linear combination of the particular

³The question of the choice of the dilatancy angle ψ is a common issue in geotechnical engineering ; some authors also recommend to take $\psi = 0$, or $\psi = \phi - 30$. This question could be discussed in detail, but falls out of the scope of the present paper.

solutions $(u_h(\mu_1), \dots, u_h(\mu_N))$:

$$u_h^N(\mu) = \sum_{i=1}^N \alpha_i^h(\mu) u_h(\mu_i). \quad (8.14)$$

The low-dimensional space should be constructed so that for some tolerance $\epsilon > 0$, the RB approximations given by equation (8.14) are such that

$$\max_{\mu \in \mathcal{D}} \|u_h(\mu) - u_h^N(\mu)\|_X \leq \epsilon. \quad (8.15)$$

For a stable implementation of the reduced basis method, it is necessary to build a better basis than the one composed of the $\{u_h(\mu_i)\}_{1 \leq i \leq N}$, usually by a Gram-Schmidt method. In what follows, we denote by $\{\xi_1, \dots, \xi_N\}$ these L^2 -orthonormalized basis functions, and by X_h^N the approximation space which they span: the reduced basis space. During the implementation of the reduced basis method, the computational work is separated into two stages: *offline* and *online*. This decomposition is a key ingredient of the method. The reduced basis functions, $\{\xi_1, \dots, \xi_N\}$, as well as all expensive parameter-independent terms are computed once during the *offline* stage and stored, whereas during the online stage – for each new value of the parameters – inexpensive parameter-dependent quantities are evaluated, together with the computation of the coefficients $\alpha_i^h(\mu)$.

The usual RB method is a Galerkin method on the space X_h^N , which is of much smaller dimension than the original approximation space X_h , so solving the problem (8.13) in X_h^N is less expensive than in the truth FE space X_h . However, to perform the online stage efficiently, one must isolate the parametric contribution to the corresponding linear system, allowing all parameter-independent matrices and vectors to be built only once and saved during the offline stage. In the case of Mohr-Coulomb's model used in CESAR-LCPC, a parameter-dependent term must be calculated at each integration point of the mesh during the iterative procedure implemented to solve (8.13); it is hence impossible to free the online stage of the FE complexity (i.e. the degrees of freedom in the mesh). This entirely nullifies the advantages of the RB method applied to our model. To overcome this flaw, we propose to use an alternative, less intrusive method, introduced in [34, 35], where coarse FE approximations are computed during the online stage, then projected into the reduced basis space and improved by a rectification technique.

We will begin by considering an analysis of the feasibility of RB methods for our problem (section 8.3.1), and will then discuss the non-intrusive method in more detail in section 8.3.2.

CESAR-LCPC was used as a black-box software to compute the FE approximation of equation (8.13). FreeFem++ [79] was used for the POD analysis, the implementation of the two-grid FE/RB method and analysis of the results. Three meshes were considered: a coarse mesh \mathcal{T}_H for the inexpensive computation of coarse solutions, a fine mesh \mathcal{T}_h for the computation of satisfactory solutions used in the

construction of the reduced basis, and a reference mesh \mathcal{T}_{ref} considered fine enough to provide truth solutions used for error calculation. See figure 8.4 below.

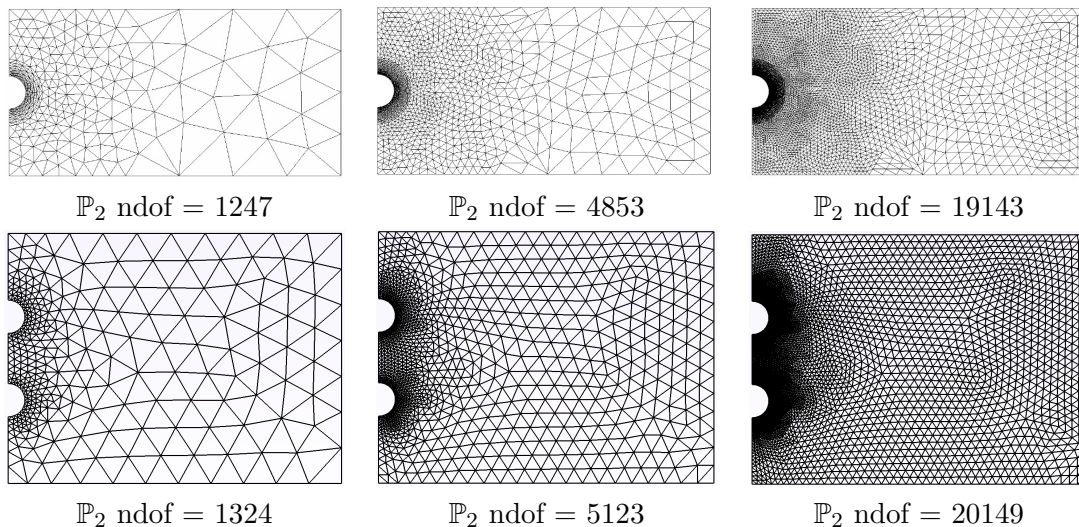


Figure 8.4 – Top: Embedded meshes used in case study 8.2.1.4 – coarse (left), fine (middle) and reference (right) – Bottom : embedded meshes in case study 8.2.1.5 – coarse (left), fine (middle) and reference (right).

8.3.1 POD analysis

In order to determine if model reduction approaches, such as reduced basis methods or proper orthogonal decomposition, can be applied to this problem, we will try to evaluate the complexity of the manifold \mathcal{M}_h of all possible solutions induced by varying parameters. This analysis consists in a singular value decomposition method applied to the correlation matrix of solutions of (8.13) computed for different values of the parameters. Once the rapid decay rate of the singular values is confirmed, one can assume that RB method is worth implementing. Using CESAR-LCPC with mesh \mathcal{T}_h to compute \mathbb{P}_1 and \mathbb{P}_2 -FE solutions of (8.13) for varying values of $\mu \in \Xi_{test}$ — a parameter set with sample size of $N_{test} = 525$ selected over the parameter domain \mathcal{D} — we computed a correlation matrix of L^2 -norm scalar products $(u_h(\mu_i), u_h(\mu_j))_{L^2(\Omega), 1 \leq i, j \leq N_{test}}$. An L^2 -orthonormalized POD basis was constructed using the following eigenfunctions

$$w_k = \frac{1}{\sqrt{\lambda_k}} \sum_{\ell=1}^{N_{test}} v_k(\ell) u_h(\mu_\ell) \quad 1 \leq k \leq N_{test}, \quad (8.16)$$

where $v_k(\ell)$ represents the ℓ^{th} component of the k^{th} eigenvector of the correlation matrix when ordered by decreasing eigenvalues.

Let P_k^{POD} be the L^2 -orthogonal projection operator from X_h into the space $X_h^{k,POD}$, spanned by the k first POD basis functions w_k . Each test solution $\{u_h(\mu_i), \mu_i \in \Xi_{test}\}$ was projected onto $X_h^{k,POD}$ to analyze the ability of the POD basis to approach the

manifold \mathcal{M}_h , depending on the number of POD modes. In figure 8.5 we can see the associated errors plotted along with the eigenvalues of the matrix, where the average error is

$$\frac{1}{N_{test}} \sum_{i=1}^{N_{test}} \|u_h(\mu_i) - P_k^{POD} u_h(\mu_i)\|_{L^2}$$

and the maximal error is

$$\|u_h(\mu_{max}^k) - P_k^{POD} u_h(\mu_{max}^k)\|_{L^2} \text{ with } \mu_{max}^k = \underset{\mu_i \in \Xi_{test}}{\operatorname{argmax}} \|u_h(\mu_i) - P_k^{POD} u_h(\mu_i)\|_{L^2}.$$

We observe that the eigenvalues decay rapidly and that the projection errors are quite small. Figure 8.6 shows the average POD projection errors of so-called reference solutions, computed on a reference mesh \mathcal{T}_{ref} (see figure 8.4) for parameter values not included in the sample space solutions. These errors are plotted with the fine FEM error for comparison. Figure 8.7 displays the corresponding maximal errors.

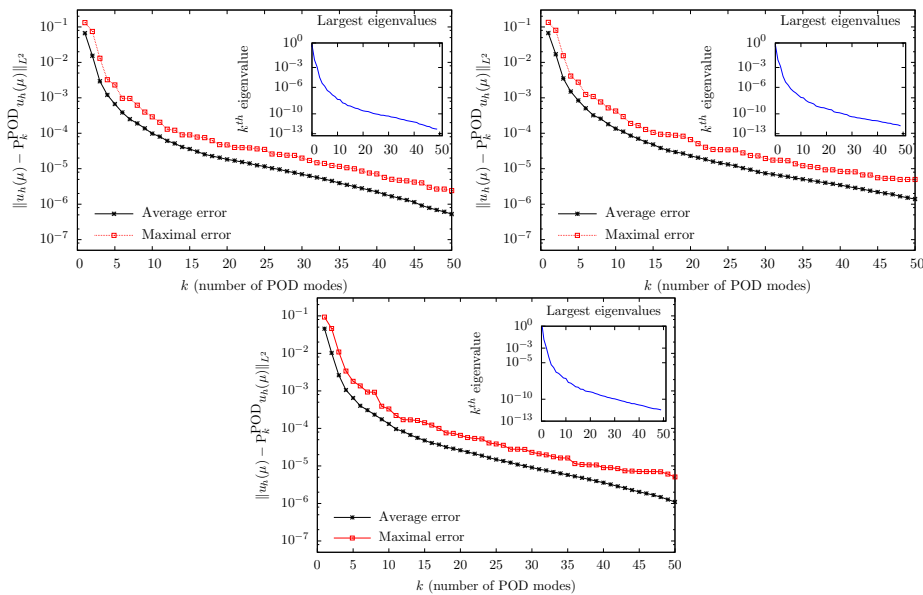


Figure 8.5 – Relative errors of the POD projection. Top: study case 8.2.1.4 using \mathbb{P}_1 (left) and \mathbb{P}_2 (right) FE snapshots ; Bottom: study case 8.2.1.5 using \mathbb{P}_2 -FE snapshots

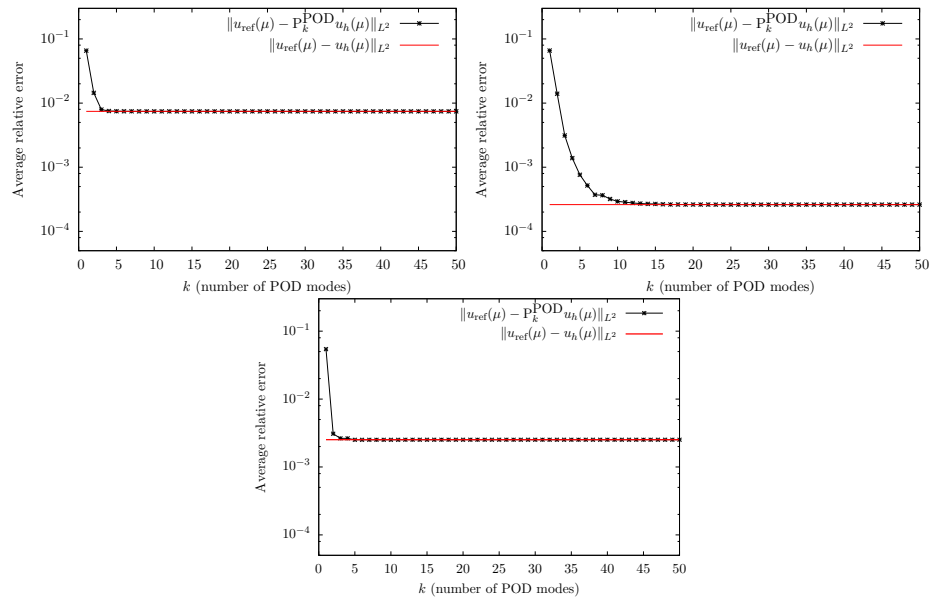


Figure 8.6 – Average error of the POD projection vs FEM error. Top: study case 8.2.1.4 using \mathbb{P}_1 (left) and \mathbb{P}_2 (right) FEsnapshots ; Bottom: study case 8.2.1.5 using \mathbb{P}_2 -FE snapshots

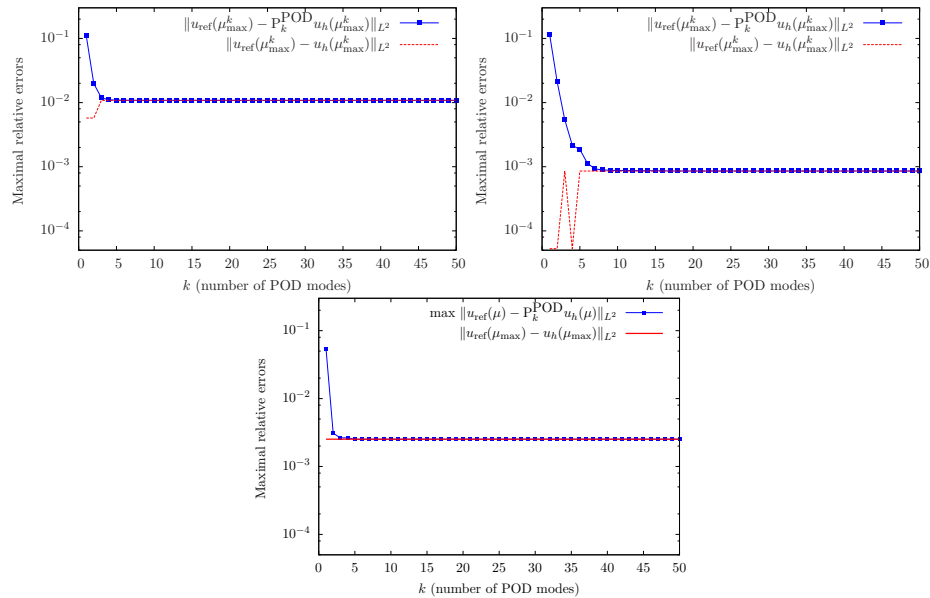


Figure 8.7 – Maximal error of the POD projection vs FEM error. Top: study case 8.2.1.4 using \mathbb{P}_1 (left) and \mathbb{P}_2 (right) FEsnapshots ; Bottom: study case 8.2.1.5 using \mathbb{P}_2 -FE snapshots

We can see for case 8.2.1.4 that with only $k = 5$ POD modes, the POD projection errors reach the same level of accuracy as the \mathbb{P}_1 FEM errors. As for the \mathbb{P}_2 FE errors, we only need about $k = 10$ POD nodes. For case 8.2.1.5 with only $k = 5$ POD modes, the POD projection errors reach the same level of accuracy as the \mathbb{P}_2

FEM errors. This suggests that a reduced basis approach is worth implementing for both case studies.

8.3.2 A non-intrusive reduced basis method : two-grid FE/RB method with a rectification approach

A popular strategy for constructing a reduced basis in the case of parameter-dependent problems is to use Greedy algorithms, based on the idea of selecting the locally optimal element at each step. This option can be seen as an alternative to the POD strategy of the previous section. If we have an appropriate a priori error estimator to avoid fully solving the problem to compute the test solutions, the Greedy algorithm can be very low-cost. Knowing the Kolmogorov dimension of the solution space is relatively small, we can fix a maximum number N_g of basis functions to be computed by the Greedy algorithm (given below, algorithm 2). Additionally, for stable implementation the chosen basis functions are L^2 -orthonormalized with a Gram-Schmidt method.

Algorithm 2 : Greedy algorithm to build the reduced basis space

```

1: Initialization:   GIVEN
    $\Xi_{test} = (\mu_1, \dots, \mu_{n_{test}}) \in \mathcal{D}^{n_{test}}, n_{test} \gg 1$ 
2: CHOOSE RANDOMLY  $\mu_1 \in \mathcal{D}$ 
3: SET  $S_1 = \{\mu_1\}$  and  $X_h^1 = \text{span}(u_h(\mu_1))$ .
4: for  $N = 2$  to  $N_g$  do
5:    $\mu_N = \underset{\mu \in \Xi_{test}}{\text{argmax}} \frac{\|u_h(\mu) - P_{N-1} u_h(\mu)\|_{L^2}}{\|u_h(\mu)\|_{L^2}}$ 
   (where  $P_{N-1}$  is the  $L^2$ -orthogonal projection operator from  $X_h$  into  $X_h^{N-1}$ )
6:    $S_N = S_{N-1} \cup \mu_N$ 
7:    $X_h^N = X_h^{N-1} + \text{span}(u_h(\mu_N))$ 
8: end for

```

For a given parameter value, RB methods aim to compute an inexpensive approximation of the projection of the truth FE solution onto the reduced basis space. This requires approximating the coefficients of the decomposition of the truth FE solution in the basis of the reduced basis space. As shown in [34, 35], the optimal coefficients

$$\beta_i^h(\mu) = (u_h(\mu), \xi_i)_{L^2} \quad (8.17)$$

intervening in the decomposition of the L^2 -projection of $u_h(\mu)$ into the space X_h^N , can be considered as the best linear combination of the reduced basis functions.

Let $\{\mathcal{T}_H\}_H$ be a family of ‘‘coarse’’ regular triangulations of Ω , such that $H \gg h$; we denote by X_H the coarse FE approximation space associated to this mesh, and by $u_H(\mu)$ the coarse FE approximation of (8.13) on X_H .

The two-grid FE/RB method consists in proposing a alternative to the coefficients $\beta_i^h(\mu)$ by using

$$\beta_i^H(\mu) = (u_H(\mu), \xi_i)_{L^2}, \quad (8.18)$$

the optimal coefficients intervening in the decomposition of the L^2 -projection of $u_H(\mu)$ into the space X_h^N . As the computation of $u_H(\mu)$, for $H \gg h$, is significantly less expensive than that of $u_h(\mu)$, coarse FE approximations can be computed quickly enough to be used in the *online* stage, although they may not be accurate enough for practical use. In [34, 35], we have shown on a simpler example that – with the mesh size H chosen adequately such that $h \sim H^2$ – this first NIRB approximation provides some improvement in accuracy with respect to the coarse solution. In what follows, we denote by P_N the projection operator such that

$$P_N v = \sum_{i=1}^N (v, \xi_i)_{L^2} \xi_i, \quad \forall v \in X_h.$$

Considering that we have used embedded FE spaces, namely $X_H \subset X_h$, we can write

$$P_N u_H(\mu) = \sum_{i=1}^N \beta_i^H(\mu) \xi_i$$

To further improve the accuracy of this first NIRB technique we propose to perform a rectification of the $P_N u_H(\mu)$.

This is so far an empirical approach, which leads to great improvements in practice. A first explanation of the successful post-processing strategy first presented in [34] and then used in [80] in the framework of reduced basis simulation of PDEs can be found in [133]. This treatment will ensure that for the parameters $\{\mu_i\}_{1 \leq i \leq N}$ used in the construction of the reduced basis, the method returns exactly $u_h(\mu_i)$. In practice, we want to identify a rectification matrix R^N associated to the transformation \mathcal{R}_N such that :

$$\mathcal{R}_N P_N u_H(\mu_i) = P_N u_h(\mu_i) \quad \forall 1 \leq i \leq N.$$

Since $\{\beta_j^h(\mu_i)\}_{1 \leq j \leq N}$ and $\{\beta_j^H(\mu_i)\}_{1 \leq j \leq N}$ are the optimal coefficients intervening in the decomposition of $P_N u_h(\mu_i)$ and $P_N u_H(\mu_i)$, the standard matrix, denoted by A_N , associated to the transformation \mathcal{R}_N is equal to

$$A_N = (\mathbf{B}_h^N) \times (\mathbf{B}_H^N)^{-1} \text{ with } A_N \in \mathbb{R}^{N \times N},$$

$$\text{where } \mathbf{B}_h^N = \left(\begin{array}{c|ccc} \beta_1^h(\mu_1) & \cdots & \beta_1^h(\mu_N) \\ \vdots & \vdots & \vdots \\ \beta_N^h(\mu_1) & \cdots & \beta_N^h(\mu_N) \end{array} \right) \text{ and } \mathbf{B}_H^N = \left(\begin{array}{c|ccc} \beta_1^H(\mu_1) & \cdots & \beta_1^H(\mu_N) \\ \vdots & \vdots & \vdots \\ \beta_N^H(\mu_1) & \cdots & \beta_N^H(\mu_N) \end{array} \right).$$

Let us note that, contrarily to the $u_h(\mu)$, which we don't want to compute for a large number of values of μ , the truth solutions $u_h(\mu_i)$ have already been computed to build the reduced basis, making the computation of A_N relatively cheap. For

each new value of μ , the coefficients $\beta_i^H(\mu)$ will be replaced by $\sum_{k=1}^N A_{ik}^N \beta_k^H(\mu)$, and

an improved two-grid FE/RB approximation to equation (8.13), for $R_N = A_N$, can be :

$$\mathcal{R}_N P_N u_H(\mu) = \sum_{i,j=1}^N A_{ij}^N \beta_j^H(\mu) \xi_i^N. \quad (8.19)$$

In our problem, we noticed that A_N was rather poorly conditioned, and propose here a pre-processing to improve the rectification. Instead of computing the coefficients from the fine and coarse RB solutions, we will consider the previously computed POD basis functions to construct another rectification matrix K_N . To do so, in addition to the POD basis function w_k introduced in the previous section, we introduced "coarse" POD basis function

$$w_k^H = \sum_{\ell=1}^{N_{test}} v_k(\ell) u_H(\mu_\ell) \quad 1 \leq k \leq N.$$

We defined a pre-processing matrix

$$D_N = (\mathbf{F}_h^N) \times (\mathbf{F}_H^N)^{-1},$$

where $\mathbf{F}_h^N = \left(\begin{array}{c|ccc} (w_1, \xi_1)_{L^2} & \cdots & (w_N, \xi_1)_{L^2} \\ \vdots & \vdots & \vdots \\ (w_1, \xi_N)_{L^2} & \cdots & (w_N, \xi_N)_{L^2} \end{array} \right)$ and $\mathbf{F}_H^N = \left(\begin{array}{c|ccc} (w_1^H, \xi_1)_{L^2} & \cdots & (w_N^H, \xi_1)_{L^2} \\ \vdots & \vdots & \vdots \\ (w_1^H, \xi_N)_{L^2} & \cdots & (w_N^H, \xi_N)_{L^2} \end{array} \right)$.

We then construct the new rectification matrix K_N as follows, for a suitable N_{max} .

$$K_N = \begin{pmatrix} D_{N_{max}} & 0 \\ 0 & T_N \end{pmatrix},$$

with $T_N = \frac{1}{N} \begin{pmatrix} 1 & & 0 \\ & \ddots & \\ 0 & & 1 \end{pmatrix} \in \mathbb{R}^{(N-N_{max}) \times (N-N_{max})}$. By "cutting off" the chosen

rectification before significant increases in the condition number (at N_{max}), we can prevent associated peaks in error, thus achieving the results of K_N .

Figure 8.8 shows condition numbers for the three proposed matrices: A_N , D_N , and K_N in case study 8.2.1.4. Figure 8.9 shows rectification errors for the three proposed rectification matrices in case study 8.2.1.4. We can see that the matrix D_N is better conditioned than the matrix A_N , and that the rectification process is improved. However the most significant improvements are seen with matrix K_N .

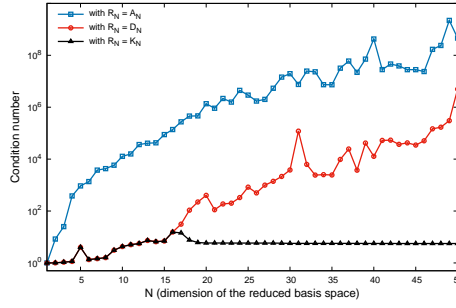


Figure 8.8 – Condition number of the different rectification matrices: A_N , D_N , and K_N during the offline stage (\mathbb{P}_2 FEM solutions) in case study 8.2.1.4

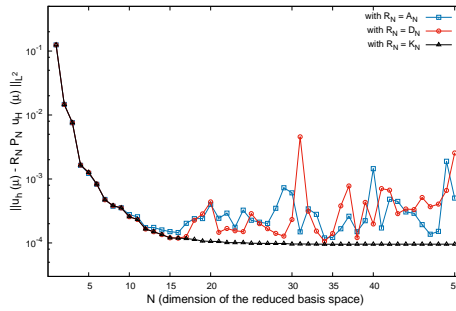


Figure 8.9 – Average rectification errors the offline stage (\mathbb{P}_2 FEM solutions) depending on the rectification matrix in case study 8.2.1.4

8.4 Numerical experiments

A parameter set Ξ_{trial} with sample size of $N_{trial} = 16$ was selected over $\mathcal{D} \setminus \Xi_{test}$ to test our method with \mathbb{P}_2 FEM grids represented in figure 8.4.

While in some applications, the simple rectification with $R_N = A_N$ will achieve the desired results, in this case the significant variation between coarse and fine solutions used to build the rectification matrix caused inadequate rectification results. We thus used matrix $R_N = K_N$ introduced in the previous section to improve the rectification.

8.4.1 Single tunnel study case

In this section, we present the results of numerical tests of the two-grid FE/RB method on case study 8.2.1.4.

Figure 8.10 shows rectification errors during the offline stage. In Figure 8.11, we can see the two-grid reduced basis method errors using rectification matrix $R_N = K_N$, for $N = 16$; the error reaches the same order of precision as the \mathbb{P}_2 -FEM fine solutions. We note that while rectification error in Figure 8.10 does not descend further for $N \geq N_{max}$, in contrast to the fine projection errors during the offline stage, Figure 8.11 shows that the rectification approximation online does attain the same precision as the fine FEM solution. Figure 8.12 shows the actual displacement for a given pa-

parameter, $\mu = \mu_{\max} = \underset{\mu \in \Xi_{\text{trial}}}{\text{argmax}} \|u_h(\mu) - R_N P_N u_H(\mu)\|_{L^2} = (125, 0.35, 23, 0.03)$. The application of this problem being to evaluate impact on surface structures, we can consider displacement at the surface to be a quantity of interest.

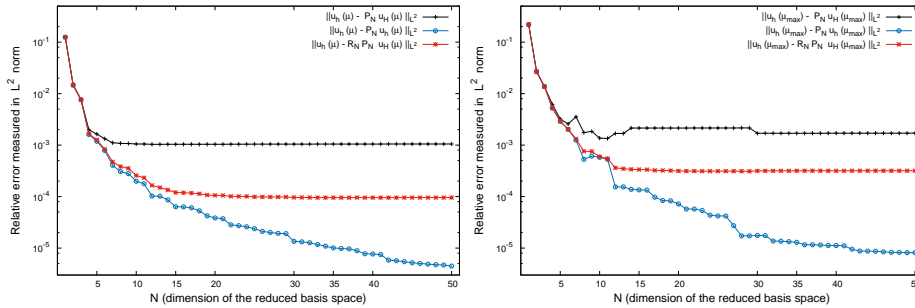


Figure 8.10 – Average (left) and maximal (right) errors during offline stage with $R_N = K_N$ and $N_{\max} = 16$

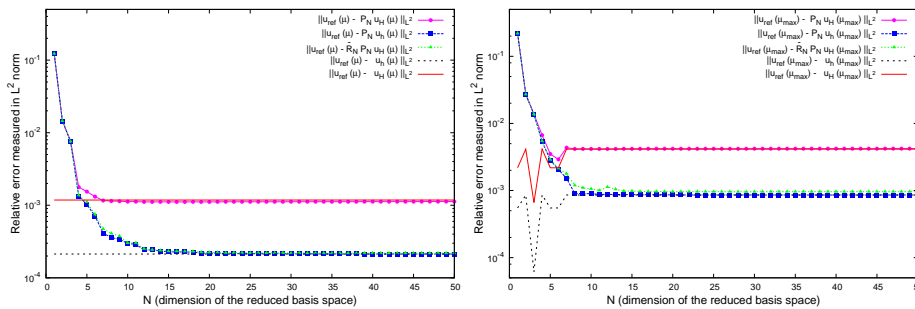


Figure 8.11 – Average (left) and maximal (right) rectified RB projection errors on trial space during the online stage with $R_N = K_N$ and $N_{\max} = 16$

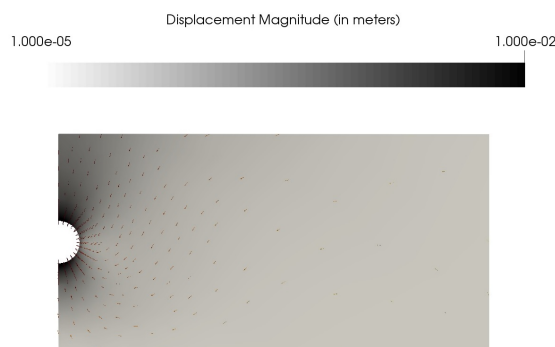


Figure 8.12 – Displacement value for $\mu_{\max} = (125, 0.35, 23, 0.03)$

Figure 8.13 shows error maps with respect to the \mathbb{P}_2 -FE approximation over the calculation domain at various N -values of the two-grid FE/RB method, with and without the rectification, where the parameter value $\mu_{\max} = (125, 0.35, 23, 0.03)$ corresponds to the solution with maximal error. We can see the errors of the rectified

solution with respect to the non rectified solution. Figure 8.14 shows errors over the calculation domain for $N = 15$ with respect to the very fine reference solution, again for $\mu_{\max} = (125, 0.35, 23, 0.03)$. We can see that the rectified solution errors closely resemble the fine FEM errors.

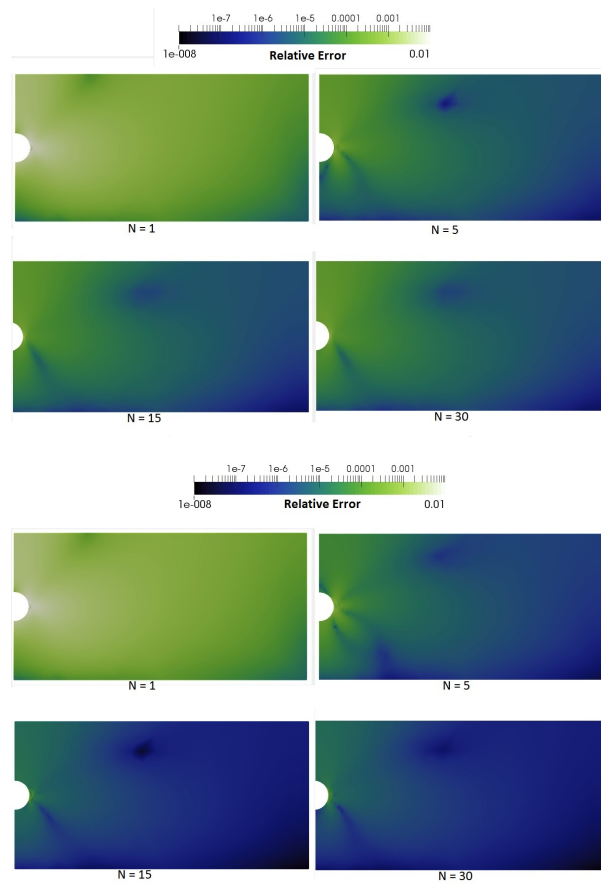


Figure 8.13 – Relative error maps of the two-grid FE/RB approximation without (left) and with (right) rectification as function of N for $\mu = \mu_{\max} = (125, 0.35, 23, 0.03)$

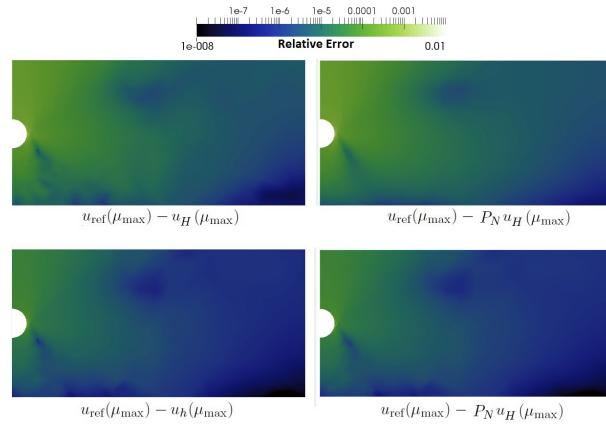


Figure 8.14 – Error maps for $N=15$ and $\mu_{\max} = (125, 0.35, 23, 0.03)$

In Figure 8.15 we can see a plot of the vertical displacement of the surface soil as a function of distance from the tunnel. The most significant displacement occurs, of course, nearest the tunnel.

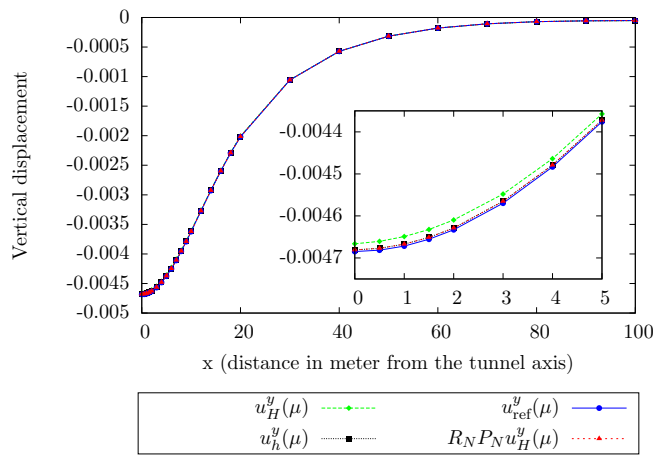


Figure 8.15 – Value of the vertical displacement on the surface for $\mu = \mu_{\max} = (125, 0.35, 23, 0.03)$

Figure 8.16 and Table 8.1 show computation times for finite element simulations and the proposed online reduced basis method. We can see that satisfactory results can be obtained in a total of 3.17s over the full domain, a reduction by 85% of computation time compared to a fine finite element approximation. In the case of many-query approximations – such as parametric studies, and possibly optimization procedures which are currently too computationally expensive for practical use – this reduction would prove to be significant.

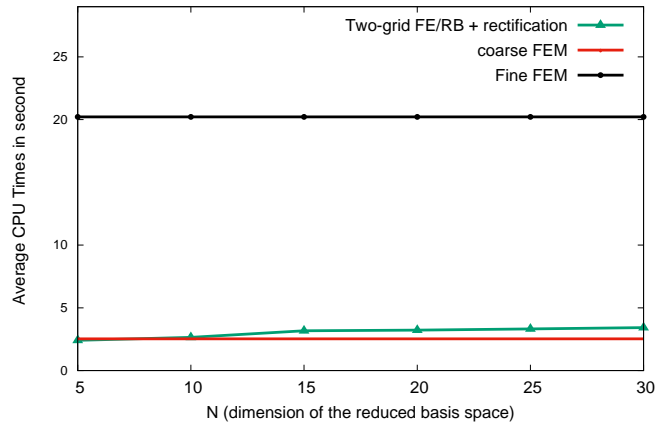


Figure 8.16 – Comparison of calculation times of \mathbb{P}_2 -FE and two-grid FE/RB Methods

	CPU Times
Coarse FEM	2.41s
Two-Grid RB/FE	3.17s
Fine FEM	20.22s

Table 8.1 – Comparison of calculation times of \mathbb{P}_2 -FE and two-grid FE/RB Methods (for $N = 15$, providing approximation error equivalent to the fine FEM solution).

8.4.2 Twin tunnel study case

In this section, we present the numerical test results of the two-grid FE/RB method on case study 8.2.1.5. Figure 8.17 represents the average errors using rectification matrix $R_N = K_N$ and $N_{max} = 21$. The error reaches the same order of precision as the P2-FEM fine solutions.

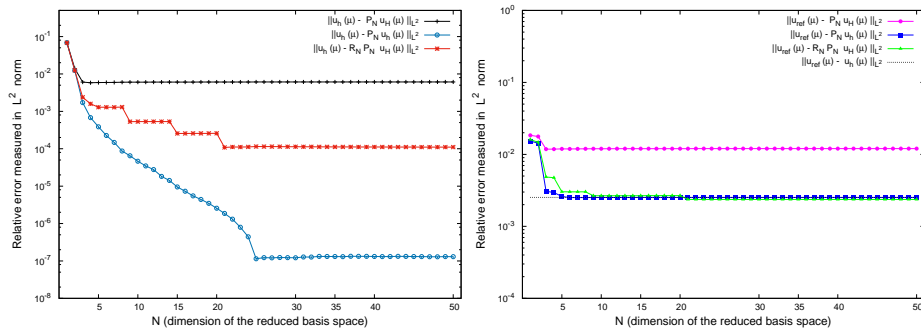


Figure 8.17 – Average errors during offline (left) and online (right) stage with $R_N = K_N$ and $N_{max} = 21$

Figure 8.18 shows the actual displacement for a given parameter, $\mu = \mu_{\max}$.

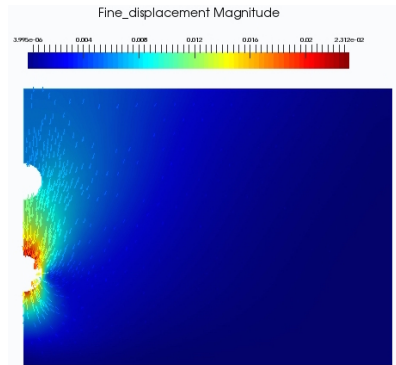


Figure 8.18 – Displacement value for $\mu_{\max} = (125, 0.35, 23, 0.03)$

Figure 8.19 shows errors over the calculation domain for $N = 15$ with respect to the reference solution, of the two-grid FE/RB method, with and without the rectification, with the parameter $\mu_{\max} = (125, 0.35, 23, 0.03)$. We can see the errors of the rectified solution with respect to the unrectified solution. We can also see that the rectified solution errors closely resemble the truth projection error.

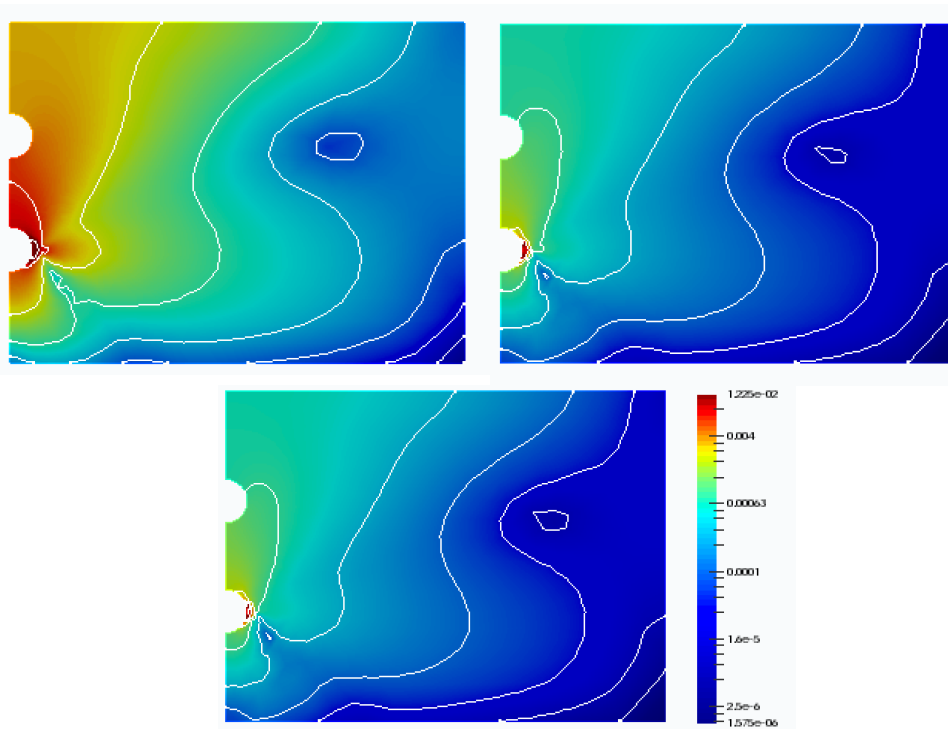


Figure 8.19 – Error maps for $N=15$ and $\mu_{\max} = (125, 0.35, 23, 0.03)$ Top left : $u_{ref} - P_N u_H$; Top right $u_{ref} - R_N P_N u_H$; Bottom $u_{ref} - P_N u_h$;

8.5 Conclusions

In this paper we proposed a non-intrusive reduced basis method for application to the parametrized PDEs governing an elastoplasticity problem which could not be solved using a standard reduced basis method. We demonstrated the small dimension of the solution space affiliated to the problem using POD analysis. We then proposed two rectification methods in the non-intrusive framework, and found that a modified rectification method was more adapted to the problem considered. In the first case study considered, the particular problem being the displacement of the soil around a shallow tunnel, the displacement at the surface approximated by the reduced model was considered, showing the successful approximation results held true when considering only the most important area of the domain. In the second case study the method was able to account for a second deeper tunnel, showing successful approximation results of displacement in the domain and around the first shallow tunnel.

The results of this study demonstrate the feasibility of the presented two-grid non-intrusive reduced basis method in geotechnics modeling, a domain for which reduced modeling techniques can provide great benefit. Specifically, this technique is well-adapted to the particular PDE problem studied considering its non-intrusive nature.

Acknowledgment

The authors would like to graciously thank Emmanuel Bourgeois for fruitful discussions and very valuable advice regarding our numerical simulations with CESAR-LCPC.

This research did not receive any specific grant from funding agencies in the public, commercial or not-for-profit sectors.

Conclusions and Perspectives

In this final chapter we reiterate the motivation, context, and goals of the research, discuss the contributions made in this thesis in adaptations of the PBDW and GEIM for air quality modeling, numerical results in case studies for exterior air quality modeling, and extension to a real-world application. We then discuss limitations and perspectives for future work, and draw our final conclusions.

What was the purpose of this work?

We began the discussion by providing examples of the grave effects of air pollution worldwide. Detailed air quality data is necessary in many types of studies, on the health effects of exposure to pollutants, in the identification sources of air pollutants, and on the fate of air pollution. The spatially dense predictions at adaptive scales offered by numerical simulation of AQMs, in addition to relatively sparse data measurements, can inform with great detail and precision such indispensable studies on air quality, the development of smarter urban operations, and crisis management.

Urban modeling problems are notoriously complex and costly for solution for varying parameters, and calibration of mathematical models to real-world problems adds a layer of complexity. It would be unrealistic to assume that even a highly informed and sophisticated mathematical model as are currently available can exactly represent the physics and chemistry of air pollution. Data assimilation methods are a very useful technique to improve the accuracy of air quality approximations, when combined with state-of-the-art modeling technology such as small-scale modeling chains, however require very costly computational work.

The need for model reduction is particularly pertinent in these applications, requiring ever smaller scales, more precision, and repeated solution for parametric variation and data assimilation. Robust, precise, reduced-order methods of data assimilation are of great interest in the field of air quality modeling.

In this thesis we aimed to demonstrate the necessity and feasibility of RB and data assimilation methods in the context of air quality modeling and even more broadly in urban modeling, and to advance the application of reduced basis and data assimilation to PDE-based simulation for pollutant concentration in air.

What contributions have we made?

Over the course of this thesis, we studied the use of RBMs for exterior air pollution, and in geotechnics modeling. We found promising results in appropriate implementation of the PBDW and GEIM methods on relatively simple 2D and 3D case studies in exterior pollution, and in a simplified implementation over a real-world problem of concentration estimation in Fresno, CA, which we summarize below.

- *Adaptations for Applications in Environmental Modeling*

In chapter 4 we discussed adaptations of the PBDW method for applications in pollutant modeling, and we provided an introductory discussion of PDE modeling for air quality. We covered practical considerations for the use of a PDE model for pollutant concentration by advection-diffusion-reaction including a SUPG stabilization for the solution by finite element methods and a dimensionless formulation for generalization of the problem and more clear understanding of the physical quantities involved. Contributions made in this chapter include the practical considerations of the PBDW method for air quality modeling, studying the stability of the system based on an inf-sup coefficient associated to the mathematical model and the Update space, and choice of locations for experimental measurements by a GEIM-based Greedy procedure. Special attention must be paid to the construction of the RB and Update spaces with relatively smooth solutions, and sensor placement for the stability of the system for successful application of these methods.

- *Case Studies in Exterior Air Quality*

We aimed in this study to demonstrate the feasibility of RBMs in the context of air quality modeling, and the ability of the PBDW to contribute to the use of parameterized PDE models for air quality by reducing computational costs and accounting for unmodeled physics.

The application of two non-intrusive reduced order variational data assimilation methods provided low-cost state estimation with data fit for imperfect mathematical models, inducing relatively low approximation errors generally under $\mathcal{O}(10^{-1})$ in relative error (very low when compared to errors inherent to many air quality models).

We began with a two-dimensional case study in chapter 5. We presented the results of the PBDW state estimation in the case of a perfect model \mathcal{P}^{bk} (and thus only parametric variation), as well as the cases of little or significant model error. We found that the PBDW method performed nearly equivalently in the cases of no or little model error, and in the case of significant model error the method was able to approximate the physical state with an overall error of $\sim 3\%$ and no more than 14% peaks. In the field of air quality modeling, approximation error under $\sim 20\%$ is slightly to significantly less than error levels of a state-of-the-art AQM due to complex conditions, unknown inputs, and poorly modeled physics and chemistry.

When compared to the GEIM approximation, results were similar with little model error, but the PBDW methods proves advantageous in the case of more significant model error. Computational times of the two reduction methods are similar, however the GEIM does have the slight advantage of a smaller linear system. This advantage is outweighed however by the PBDW's improved ability to correct from an imperfect model. These methods were compared to results by the more classical

data assimilation method of inverse problems, showing similar state estimation precision and greatly improved computational costs. In particular, the wind field was not reconstructed for the PBDW method, and neither air flow nor pressure sensors were necessary in the PBDW formulation for a given parameter range. The PBDW method also accommodates a potentially large number of sensors.

We compared our variational methods to the adjoint inverse method on a model with simplified Stokes velocity fields, and found that in the case of model error, the PBDW and GEIM performed similarly to the adjoint method, in terms of precision of the state estimation, for each of the model errors considered, while reducing computational costs. In the case of no model error and sensors selected by a greedy algorithm, the GEIM performs better by one order of precision. The PBDW method is non-intrusive in its use of the computational code, and better handles estimation using an imperfect model, which standard inverse methods do not generally treat. The analysis of PBDW effectiveness should be continued with a comparison to the weak constraint 3D-Var method for imperfect model.

When extended to a three-dimensional case study with either point or area sources in chapter 6, we found similar conclusions on the PBDW method.

The results presented above are encouraging, and show that this method may prove very useful in larger-scale air quality studies for the case of studies using a reasonably stable and precise model \mathcal{P}^{bk} .

- *A Real-World Application*

Chapter 7 treated the next step in application of urban-scale PDE models with model order reduction and data assimilation by expanding the previous case studies in exterior pollutant modeling to a larger-scale real-world application over a neighborhood of Fresno, California. Difficulties specific to this application include the construction of a simplified three-dimensional domain representing a neighborhood over Fresno from two-dimensional map data freely available online.

We simulated a decoupled concentration field over a velocity field representing real-world meteorology conditions over this domain, employing the stabilized dimensionless formulation from chapter 4, to obtain relatively stabilized concentration fields resulting from traffic pollution on two surface streets in the domain, which we considered to be our best-knowledge model. We obtained promising first results in cases with synthetic data from a shifted model, reconstructing with high precision the concentration field with relative PBDW approximation errors generally of the order $\mathcal{O}(10^{-2})$ in the case of a small model error. We were able to reconstruct the concentration fields in 7.1s, as compared to 31 minutes for a single solution of the direct problem \mathcal{P}^{bk} .

We consider these results very promising for future operational implementation, and this work has laid the groundwork for application with more precise real-world input data (specifically emissions data and meteorological data) and assimilation of real measurement data to use our RB data-assimilation method for large-scale quasi real-time air quality approximation.

- *RBM for Geotechnics Modeling*

Finally in chapter 8 we continued in the theme of non-intrusive reduced basis methods for urban modeling with a different application in the field of tunnel engineering. This work gives an example of the versatility of reduced basis methods and non-intrusive techniques in other urban modeling applications, providing a specific example in which the non-intrusivity is essential and RBMs can be used for geotechnics modeling in urban development projects. The two-grid NIRB method applied with a black-box code for tunnel engineering allowed us to reconstruct the model solutions at the same precision as a reasonably fine FEM solution while reducing computational time by 85%.

What are the perspectives of this work?

We believe this work shows promise for the future of reduced basis and variational data assimilation methods in the context of air quality modeling. However we end this current project with many open questions to which we have considered constructive responses for the next steps. Here we will discuss future work on the theory and practice of the PBDW method, and practical considerations for these studies in air quality applications.

- *Operational use of PBDW state estimation*

As described in chapter 4 we used a basic PDE for advection-diffusion-reaction in our case studies, to allow full understanding of the phenomena we modeled and for lack of a more precise small-scale operational model. This means of course that we neglected some less significant physical phenomena. When comparing to real-world data we may find that the model error is too great for any meaningful correction by the update of the PBDW formulation. Employing the method with an operational PDE-based air quality model would be necessary for improved implementation in real-world studies.

Another promising method of improvement of the model \mathcal{P}^{bk} would be coupling with larger-scale operational models, as discussed briefly in section 7.3. While larger-scale models do not provide the small-scale precision we aimed for in our studies, they could be useful in informing the model \mathcal{P}^{bk} for initial conditions (in the case of more realistic time-dependent modeling), boundary conditions, and background conditions. As discussed in chapter 1, error propagation from initial, boundary, and background conditions is quite significant, and this could be a (relatively) cost-efficient solution to reduce this source of modeling error. While we do not expect the PBDW method to compensate for error that is too significant, a model \mathcal{P}^{bk} with the most precise (while remaining practical) description of the physical states and best informed conditions and parameters will render the PBDW effective.

- *Future work to build upon our progress*

In this work we assumed noise in the observations was negligible. Unfortunately, this is not always a reasonable assumption. Future work should consider a probabilistic element (or at least offer a provision for uncertainty such as the discrepancy

principal or Tikhonov regularization) to the incorporation of the measurement data, as proposed in [117, 182]. This probabilistic element should ideally be dependent on the physical quantity being measured; pollutant concentration sensors and air pressure sensors don't necessarily follow the same error distribution, for example.

We discussed the importance of the norm used in the variational problem and the construction of the update space, and this could be a topic of further study.

We must also note that complex states such as air quality are generally not likely to be associated to low-dimensional solution spaces. While the concept of "low-dimensional" can evolve depending on computational capacity and available measurement data (for example $\mathcal{O}(10)$ to $\mathcal{O}(100)$ or even $\mathcal{O}(1000)$ could be considered low-dimension), we must provide solutions for cases when parametric variation may influence strong variations of solutions. In [120] locally adaptive RBMs are proposed to partition the parameter space, and consider N -dimensional RBMs over a solution manifold \mathcal{M}^{bk} approximated by $K \gg N$ solutions, method which could prove particularly useful in applications where meteorological conditions are parameters of the model \mathcal{P}^{bk} . As we saw in chapters 5-7, computational costs for the offline construction of RB spaces in large-scale problems are high, and a high-dimensional solution manifold \mathcal{M}^{bk} will only increase these costs. A solution for more efficient offline Greedy algorithms is proposed in [82] using an algorithm to adaptively enrich the training set from which the RB basis functions are selected, and could be extremely useful in applications when an appropriate error estimator is lacking and computing a large sample of solutions is necessary.

A logical next step for implementation in air quality applications would be the extension to treating time-varying wind. We considered here steady velocity representing wind fields under relatively steady conditions. This is a gross simplification of reality. If the variations of meteorological conditions are relatively small and within the span of the parameter set \mathcal{D}^{bk} and the solution manifold \mathcal{M}^{bk} used to construct the RB space, we assume *a priori* that the steady-state method may be able to handle the state estimation. If meteorological conditions are strongly variable during a period of study, techniques for RBMs with unsteady models should be necessary, but remains a somewhat open question.

We learned during our study that the computation of CFD wind fields and CTM pollution fields on large-scale domains (from urban neighborhood size to full city size) at small-scale resolution (read, under $1m$ grid sizes) is extremely computationally heavy on office computational machines (e.g. machines with less than 80GB of RAM), and may not be feasible for larger domains than the one studied in chapter 7. We aim to keep these methods feasible for use by those who may have limited or no access to high-powered computational machines, and thus would like in future work to consider decomposition methods of the large computational domains into N_d smaller more manageable blocks, $\Omega = \Omega_1 \cup \dots \cup \Omega_{N_d}$. A possible method to implement this would be to incorporate geometrical parameters \mathbf{p}_g into the reduced basis, and treat each subdomain Ω_i as corresponding to some value of the geometrical parameter $\mathbf{p}_g \in \mathcal{D}_g^{bk}$. Difficulties expected would be the treatment of the interfaces between subdomains, and the definition and treatment of the appropriate

geometrical parameters \mathbf{p}_g .

Concluding Remarks

Operational methods of air quality modeling and data assimilation, of great importance in research, development and regulation investigations, are generally known to be computationally heavy endeavors, particularly in cases of urban-scale application of physically-based mathematical models. We have shown in this work that reduced basis data assimilation methods can be feasible even in these complex applications, greatly reducing calculation times and necessity for powerful and expensive machines, while maintaining the advantages offered by sophisticated models and assimilation of measurement data to provide precise, real-time air quality approximations.

The contributions presented here provide a foundation for continued extension of these methods to application in operational air quality studies, with the potential to provide detailed, spatially-resolved air pollution data at adaptive scales and time periods, actionable in real-time for varying inputs and parameters, for an array of uses in the field of air quality modeling.

Part V

Appendices and References

Appendix A

Introduction - English

Motivation and Context

In 2012, a ninth of all deaths worldwide were related to air pollution; three million, of these deaths were attributed solely to ambient outdoor air pollution [144]. A study over 22 cohorts from 13 countries across Europe [18] found that long-term exposure to fine particles $PM_{2.5}$ was associated with natural-cause mortalities, and that these associations remained statistically significant over concentrations below the European annual mean limit value of $25 \frac{\mu g}{m^3}$. In [101] at least 40,000 deaths per year were found attributable to outdoor and traffic-related pollution in Austria, Switzerland and France.

Health outcomes such as acute lower respiratory disease, chronic obstructive pulmonary disease, stroke, ischemic heart disease and lung cancer, have been analyzed by the WHO [144] for estimates of the global disease burden of air pollution, however many other diseases associated with air pollution were not included in the assessment because the evidence was not considered sufficiently robust. While these studies focused on fine particle pollution, other pollutant species have been shown to play an important role in many more adverse health effects, e.g. in [147]. Reliable exposure estimates and understanding of the impacts from air pollutants are indispensable to better inform studies on disease burden and public health, policy-making, and urban developers.

While air pollution sensor technology has greatly improved in recent years and rendered sensors much more affordable, smaller, and more mobile, the complexity and range of the effects of air pollution requires more tools for improved understanding and control.

In order to understand the health effects of exposure to air pollution, exposure-response relationships must be studied for individual pollutant species, requiring individual exposure data [42]. These studies generally include large sample sizes, such as in [147] where nearly 43,000 births were studied for exposure to polycyclic aromatic hydrocarbons (PAH) in relation to risk of preterm birth. In this study not only does the sample size preclude any reasonable pretention to individual measurements for each participant, but the focus is on the effects of pollutant species which are not among the criteria pollutants routinely monitored by air quality sensors.

Spatial variation of pollutants over Fresno, CA				
Pollutant	Observations	Median	Inter-quartile range	90 th : 10 th percentile ratio
Particle-bound PAH	171	0.45	0.25 – 0.67	9.1
Elemental Carbon	114	0.77	0.42 – 1.10	6.4
Endotoxin	182	1.20	0.89 – 1.67	3.7
<i>PM</i> ₁₀	278	0.42	0.35 – 0.51	2.2
<i>PM</i> _{2.5}	283	0.96	0.83 – 1.14	1.9

Table A.1 – Ratio of daily residential outdoor concentration to central site concentration measurements, within the high season for each pollutant [137].

Additionally, studies on health effects often need retrospective data on individual exposures. Some pathologies require the study of exposure on much shorter time frames, such as birth defects related to exposures over one- to two-week time windows, which implies the necessity for more spatial and temporal detail in exposure evaluations. Continuous, ongoing measurements of air pollution are typically taken at only one or two fixed sites for an entire city, and health studies often assign identical exposures to all people in an epidemiologic study. Air quality models (AQM) can provide the spatially-resolved pollution approximations necessary for exposure assessment from available measurements over the desired time frame, retrospectively, and for varied pollutant species without sensors at each point of interest.

The detection and identification of pollutant emission sources is also a common theme in air quality studies, for regulation and development, as well as crisis management studies. Doing this without the use of AQMs is entirely unfeasible, unless the sensors were to be placed in close proximity to the (often unknown a priori) source.

In addition to the study of pollution sources and health effects, understanding the fate of air pollution is necessary in prediction, regulation (e.g. changes in fuel or traffic restrictions) and urban planning. Models allow for the study of hypothetical air quality, meaning the effects of future accidents or pollution peaks can be estimated, the impacts of proposed regulations can be properly informed, schools and hospitals can be built in locations with lower pollution, and urban developers can take into account possible adverse effects of new constructions on air quality. None of this would have the flexibility it does, or perhaps even be possible, without AQMs enabling the study of future changes before decision-making.

The spatially dense predictions at adaptive scales offered by numerical simulation of AQMs, combined with the relatively sparse data measurements, can provide greatly improved detail to inform these indispensable studies on exposure at the individual scale and the consequent health effects, the understanding of pollutant emissions and dispersion, the development of smarter urban planning and operations, and crisis management.

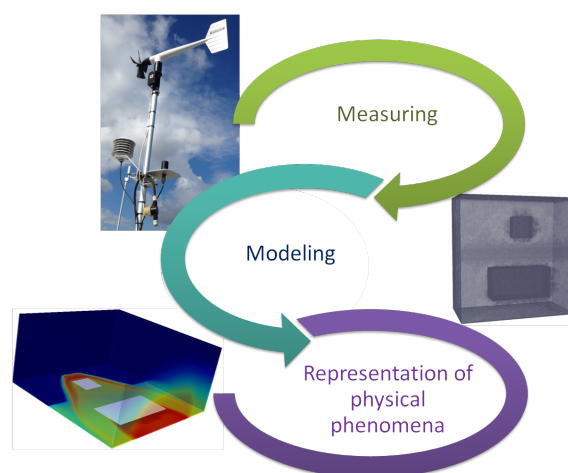


Figure A.1 – Illustration of the process of modeling physical phenomena with available measurement data.

From societal problem to scientific study

Many air quality modeling methods exist, of varying sophistication (an excellent survey can be found in [202], in which methods from empirical and statistical approaches to various deterministic approaches are described). Within the category of deterministic models approaches vary in sophistication from simple box models (described briefly in [180]), to Gaussian plume models, to physically-based Lagrangian methods (e.g., a study using a highly sophisticated operational Lagrangian model can be found in [89]) and Eulerian Computational Fluid Dynamics (CFD) models (such as the simple model applied in this thesis). The more sophisticated models, when applied with precise information on the environment and pollutant emissions, and if correctly calibrated, can provide very detailed information on spatial and time-varying pollutant concentrations, as well as the physical phenomena affecting air quality. On urban scales, air pollution is known to be highly variable, and real-world applications often involve complex geometries. Detailed, small-scale approximations and improved understanding of the underlying physics offered by physically-based deterministic models are of great interest to current air quality modeling efforts, but development and use of such models is challenging due to several significant limitations.

State of the art air quality modeling is limited by the complex nature of the problem to be solved: the challenges of highly non-linear physical effects and complex urban geometries are compounded by significant uncertainties in input data such as meteorological conditions, boundary conditions, and emissions data. Given the complexity of real-world applications, one cannot assume that even a highly informed and sophisticated deterministic (or non-deterministic for that matter) model can exactly represent all the physical phenomena at play.

Improvements in the quality of available data (meteorological, emissions and background concentrations, etc.), and in the mathematical treatment of physical

phenomena (e.g. turbulence schemes for wind field modeling) and chemical mechanisms (e.g. chemical reaction) greatly increase modeling accuracy. Operational AQMs can also be improved upon by techniques from available data and models such as statistical methods including bias correction and probabilistic forecasting, ensemble modeling (where multiple models or inputs are used and solutions are combined in the expectation of reducing overall modeling error), and data assimilation.

Data assimilation refers to the integration of this physical understanding described by a mathematical model and experimental observations. Methods include various approaches which focus on the correction of the model parameter. Sequential methods rely on the assimilation of observations as they arrive to find the best estimate of the state (e.g. Kalman filtering [127]). Inverse methods aim to identify the optimal parameter, \mathbf{p}^{opt} , to minimize the mismatch between model approximation and available data generally by the minimization of a cost functional, and the optimal solution is $u(\mathbf{p}^{opt})$. Variational methods generally involve the minimization of a cost function to quantify the gap between model approximation and observations, seeking the optimal state and thus allowing the observations to correct model error.

Many studies have been conducted at multiple levels of the processes influencing air quality, from traffic modeling, to emissions, to pollutant transport and finally human exposure modeling. Ideal implementation of all this knowledge requires a modeling chain, using output from the previous "level" of the chain as input to the next level to improve results, but requires hefty computations at multiple stages and calibration of the outputs of one model to inputs of another. Companies in France and worldwide specialize in the implementation of such modeling chains for operational use, using in which they utilize state of the art techniques for client needs and develop modeling software; these tools contribute significantly to available tools which could be candidates for use in further research developments.

While data assimilation and modeling chain techniques provide significant improvement in the modeling of complex and not-fully-known physics, and operational models exist, they generally do not treat the problem of explosive computational times for sophisticated models over large, complex domains and the many forward solutions necessary for data assimilation methods. The need for model reduction is particularly pertinent in these applications, which require ever smaller scales and more precision for studies on causes, fate, and effects of air pollution.

Model order reduction refers to methods of reducing the computational cost of solution by simplifying the problem or reducing the dimension by representing prior knowledge of the system in a low-dimensional representation. Methods include surrogate modeling, in which a simpler model is substituted for the initial problem \mathcal{P} , and projection-based methods, for example using reduced spaces onto which the model operators are mapped. The latter methods, including reduced-basis methods, seek to exploit the parametric character of the problem, and focus on the dimension of the solution manifold \mathcal{M} for parameter set \mathcal{D} . Methods range from interpolation methods, such as the Empirical Interpolation Method (EIM) [16] which relies on knowledge of the solution at so-called interpolation points in the domain, to de-

composition methods such as Proper Orthogonal Decomposition [22] and Proper Galerkin Decomposition [41], and Certified Reduced Basis Methods, which can all be combined together.

The objective of this thesis is to combine model reduction and data assimilation procedures for air quality modeling applications. The remainder of this introduction is organized around a series of questions to pose about a research project, known as Heilmeier’s catechism.

(1) What is the challenge? We aim to advance the feasibility of sophisticated deterministic air quality models based on partial differential equations (PDEs) by adapting reduced basis methods and data assimilation techniques to these applications. Rendering such precise models and sophisticated data assimilation methods affordable (with respect to computational time) on low-cost machines could allow the best available techniques to be used in practical application relying on AQMs for the study, regulation, and improvement of air quality. The combination of model reduction and methods to efficiently treat the parametric variation with data assimilation is promising for the improvement of practicality.

(2) What is the solution today? Multiple methods exist today to the problem of fast modeling and data assimilation. For example, kriging [203] is a stochastic method often used as sequential data assimilation (see section 2.2.2), which relies on linear interpolation of model outputs and measurements, and accounts for spatial variability of the physical state. However, while this method is low-cost, it requires appropriate data at sufficiently numerous points to describe the physical phenomena at play. Inverse modeling for parameter identification (see section 2.2.3) can be done in a cost-effective way by employing reduced basis methods to reduce computational costs of the problem \mathcal{P} and its adjoint problem. However, this method treats error from parametric variation, not from model error, and can be complex to implement in non-linear problems or cases with many data points.

(3) How do we propose to improve the solution for tomorrow? We want to build upon available improvements to AQMs and adapt model order reduction and data assimilation techniques to these complex models. In this thesis we will apply non-intrusive reduced order methods of data assimilation for parameterized PDEs modeling pollutant concentration.

More particularly, we will focus on two methods: the generalized empirical interpolation method (GEIM), based on empirical interpolation, which was first introduced in [114, 115], and the more recent PBDW method developed in the reduced basis framework, which was first introduced in [117, 118] with application in acoustics. These methods provide particular advantages, which we aim to show may be extendible to the air quality context, where common model order reduction (MOR) methods are difficult to use due to the complexity of the phenomena and modeling. These two methods are non-intrusive and non-iterative, and so provide real-time

state estimation. The methods aim to optimally employ model order reduction and data assimilation to approximate best a physical state, taking into consideration not only parametric variation, but also model error in an imperfect mathematical model.

(4) What’s new about our approach? New contributions to the field tackled in this thesis include:

- Application of non-intrusive reduced order data assimilation methods to applications in exterior air quality modeling at the district scale.
- Method compatible with large data sets.
- Data assimilation without the reconstruction of the wind field.
- Real-time approximations.
- Formulation does not require numerous sensors on meteorological conditions.

(5) Why do we think these methods will work? Our motivation for our work in the context of air quality studies is multiple. The non-intrusive characteristic of the PBDW and GEIM methods allows for them to be applied to any suitable parameterized calculation code, whereas more intrusive methods (such as adjoint inverse methods) require access to the code in order to modify it. Non-intrusivity can also allow fast prototyping of computational methods for a given problem, to test before developing more robust applications in an operational context.

The data-assimilation techniques used to correct unmodeled physics (for example as we see in the simplification from equation (4.37) to (4.39) in section 4.2.2) in the PBDW method are of particular interest in fields such as air quality modeling, where many parameters and some physical effects are not well known. Another feature of these methods is the development of a technique that requires neither assessment of the velocity parameter (the wind field transporting pollutants) nor data assimilation on a non-linear turbulent Navier-Stokes problem. Neither the PBDW nor the GEIM are inverse methods and so do not aim to identify the model parameter \mathbf{p} . In our applications the goal is to estimate the state without the necessity to also identify the parameter; this would be advantageous, since the reconstruction of the velocity field is known to challenge computational capacities. Additionally, RBMs applied to turbulent velocity fields often yield inadequate approximation properties; however, time-averaging the spurious turbulence effects to smooth the solutions may improve approximations. In our case, considering the velocity field as a parameter and building the RB on the concentration can have a similar smoothing effect and seems to help us construct a solution manifold of small dimension.

Moreover, the PBDW is well-suited to the emerging paradigm of connected devices delivering sensor outputs with no need to scale up the computational model to handle larger numbers of data points. For example in the adjoint inverse method the optimal parameter which minimizes error at the sensor locations is found, and a large number of sensors could lead to non-convergence of the iterative method.

(6) How will we measure progress? We first study the results of these methods with only parametric variation (no model error), then with measurements from a shifted model, denoted \mathcal{P}^{trial} , and study relative errors. Over our first two-dimensional test domain, we also consider more extensive study of the PBDW method results. We first compare the performance of the PBDW and the GEIM.

We then consider a comparison of the PBDW and GEIM methods to the adjoint inverse method. An inverse method via adjoint problem [134, 193] is a typical method to treat the reconstruction of a physical state from a mathematical model and measurement data. This method is presented in detail in chapter 2. This last comparison is important given the widespread use of the adjoint method in problems similar to (2.45) with a relatively precise model \mathcal{P} . Finally, we discuss and compare the advantages of each approach.

Appendix B

Glossary

GIS: a system designed to capture, store, manipulate, analyze, manage, and present spatial or geographic data.

Neutrally Stratified Atmospheric Conditions: the ABL dilution state is considered neutral, as opposed to stable or unstable.

Settling Velocity: the rate at which suspended solids subside and are deposited.

Stably Stratified Atmospheric Conditions: weak dilution state during which pollutants accumulate at ground level, typically at night. Little turbulent mixing.

Unstably Stratified Atmospheric Conditions: high dilution state, due to strong turbulent mixing.

Urban Canopy: Assemblage of buildings, trees, other objects composing a town or city and the spaces in between.

Urban Boundary Layer: The internal boundary layer formed when air flows over a city. A mesoscale phenomenon, it is characterized by the nature of the urban surface.

Acronyms

ABL	A tmospheric B oundary L ayer
AQM	A ir Q uality M odel
BC	B oundary C ondition
CFD	C omputational F luid D ynamics
CTM	C hemical T ransport M odel
DNS	D irect N umerical S imulation
EPA	E nvironmental P rotection A gency
GIS	G eographic I nformation S ystem
HVAC	H eating V entilation and A ir C onditioning
IC	I nitial C ondition
LES	L arge E ddy S imulation
LUC	L and U se C ategory
MC	M onte C arlo
MOR	M odel O der R eduction
MUST	M ock U rban S etting T est
PBDW	P arameterized- B ackground D ata- W eak
PDE	P artial D ifferential E quation
PM	P articulate M atter
RANS	R eynolds- A veraged N avier- S tokes
RB	R educed B asis
SUPG	S treamline U pwind P etrov- G alerkin
VKT	V ehicle K ilometers T raveled

Physical Constants and Symbols

Air Density	ρ	$1.225 \frac{kg}{m^3}$
Molecular Diffusion in Air	ϵ_m	$1.72e^{-5} \frac{m^2}{s}$
Kinematic Viscosity	ν	$\frac{m^2}{s}$
Schmidt Number	sc	
Prandtl Number	σ_t	

List of Figures

0.1	Illustration de la procédure de modélisation de phénomènes physiques avec des données de mesure.	4
0.2	2D test domain with traffic pollution source.	12
0.3	Concentration solution (logarithmic scale) over velocity field with $\mathbf{p}_v = 0.1 \frac{m}{s}$ and $\mathbf{p}_s = 1 \times 10^{-3} \frac{mg}{m^3}$, and inflow velocity direction $\vec{d} = (1, 1)^T$. . .	12
0.4	Sensor locations chosen randomly (left) ; Sensor locations chosen by a Greedy algorithm (right).	13
0.5	Relative mean PBDW approximation error maps for $N = 2$ (left), $N = 6$ (right), and for $M = 8$ (top) and $M = 15$ (bottom). $\mathbf{p} \in \mathcal{D}^{trial}$, model error with $R = 0.001$. Sensors chosen by a Greedy procedure.	14
0.6	Relative mean PBDW approximation error as a function of N for various M values, $\mathbf{p} \in \mathcal{D}^{trial}$. No model error (left), and model error with $R = 0.001$ (right). Sensors chosen by a Greedy procedure.	14
0.7	Left: Neighborhood in Fresno over which a wind field was computed using <i>Code_Saturne</i> . Right: Fluid domain used to study pollutant concentrations.	15
0.8	Wind field corresponding to conditions over Fresno on April 1, 2001 (left). Dimensionless concentration solution to \mathcal{P}^{bk} with two pollution sources (right).	15
0.9	Relative mean PBDW approximation error over a set of 8 trial solutions to \mathcal{P}^{trial} with no model error (left) and with $R = 0.0001$ (right). Here $M = 8$ and $N = 3$	16
1.1	Diagram representing various types of models used for air pollution studies.	28
1.2	Diagram representing the structure of a modeling chain from traffic to air and water quality models.	48
4.1	$\beta_{M,N}$ stability coefficients (3.17) for the 2D case study presented in chapter 5. Comparing stability coefficients for the PBDW system with update basis functions defined by (3.8) where the functional φ is represented with a characteristic function as in (4.19), or without the characteristic function as in (3.4).	105
4.2	q_m basis functions constructed with the H^1 norm (left) and constructed with the \tilde{H}^1 norm with $L_g = 75m$ (right), over the 2D case study introduced in chapter 5	106

4.3	Relative mean (4.26) (left) and maximal (4.27) (right) projection errors for the 2D case study presented in chapter 5. Comparing RB background spaces constructed using a POD method and a Greedy algorithm over an identical set of training solutions for parameters $\mathbf{p} \in \mathcal{D}^{bk}$	107
4.4	Chart summarizing differences between the PBDW and classical inverse method by adjoint problem, as well as the weak constraint 4D-Var.	111
4.5	Representation of wind field inflow profile: graph of $ v_{in} (z)$ (left), 2D-view physical representation of the inflow boundary condition over a 3D domain (right).	114
4.6	Left: Section at $z = 1m$ of velocity field. Right: vertical section of velocity field showing vertical logarithmic flow profile.	114
4.7	Illustration of domain transformation for the dimensionless formulation on a two-dimensional example which has already been meshed.	121
5.1	2D test domain with boundaries corresponding to the velocity field (left) and traffic pollution source (right).	128
5.2	Concentration solution (logarithmic scale) over velocity field with $(\mathbf{p}_v, \mathbf{p}_s) = (0.1 \frac{m}{s}, 1 \times 10^{-3} \frac{mg}{m^3})$ (left), and $(\mathbf{p}_v, \mathbf{p}_s) = (1.3 \frac{m}{s}, 1 \times 10^{-2} \frac{mg}{m^3})$ (right).	129
5.3	Eigenvalues of the POD mass matrix \mathbf{M} (2.9) (left) ; Relative L^2 -norm POD projection (2.11) errors for pollutant concentration simulations (right)	130
5.4	Relative mean and maximal projection errors in H^1 norm, equations (4.26) and (4.27) respectively, during the greedy construction of the RB space \mathcal{Z}_N , as a function of N	131
5.5	Mean projection error over domain Ω , equation (5.4), during the greedy construction of the RB space \mathcal{Z}_N , for $N = 1$ (top left), $N = 5$ (top right), $N = 10$ (bottom left), $N = 15$ (bottom right).	132
5.6	Sensor locations chosen randomly.	133
5.7	Sensor locations chosen by a GEIM-based greedy algorithm (section section 4.1.2.1).	133
5.8	Stability constant $\beta_{N,M}$ (3.17) with $\ \cdot\ _{\mathcal{X}} = \ \cdot\ _{H^1}$, as a function of M for $N = 5, 6, 8, 12$. PBDW system corresponding to sensor locations in figure 5.6(left) ; PBDW system corresponding to sensor locations chosen by a GEIM-based greedy algorithm (section 4.1.2.1).	134
5.9	Condition number of PBDW matrices, with $\ \cdot\ _{\mathcal{X}} = \ \cdot\ _{H^1}$, as a function of M for $N = 5, 6, 8, 12$. PBDW system corresponding to random sensor locations from figure 5.6 (left) ; PBDW system corresponding to sensor locations chosen by a GEIM-based greedy algorithm (section 4.1.2.1) (right).	134
5.10	Relative mean projection error (5.5) in H^1 -norm, projection $\Pi_{\mathcal{Z}_N}$ defined by (4.24), of each of the sets of trial solutions for parameter set Ξ^{trial} . Left: no model error (model \mathcal{P}^{bk}). Right: added reaction term $R = 0.001$ (model \mathcal{P}^{trial}).	140

5.11	Approximation of the concentration for $\mathbf{p} = \mathbf{p}_{max}$, logarithmic scale. Trial solution to \mathcal{P}^{trial} with model error simulated by areaction term of $R = 0.0001$. True FEM solution (left), PBDW approximation using simulated measurement data, with random sensors (middle), PBDW approximation with greedy selected sensors (right).	140
5.12	Approximation of the concentration for $\mathbf{p} = \mathbf{p}_{max}$, logarithmic scale. Trial solution to \mathcal{P}^{trial} with model error simulated by a reaction term of $R = 0.001$. True FEM solution (left), PBDW approximation using synthetic data, with random sensors (middle), PBDW approximation with greedy selected sensors (right).	140
5.13	Best-fit error, equation (4.17), of the set of trial solutions over $\mathbf{p} \in \mathcal{D}^{trial}$ and model error with an added reaction term of $0.001c$, projected onto the approximation space $\mathcal{Z}_N \oplus (\mathcal{U}_M \cap \mathcal{Z}_N^\perp)$ as a function of M . H^1 -norm (left) and L^∞ -norm (right). Compared to mean error (5.7) over trial solutions of relative PBDW approximation error in the L^∞ norm (right). Sensors chosen by GEIM.	141
5.14	Relative mean (5.10) (left) and maximal (5.11) (right) PBDW approximation error as a function of N for fixed M values. Using synthetic trial data for parameter set Ξ^{trial} with no model error (model \mathcal{P}^{bk}). Sensor locations chosen randomly.	141
5.15	Relative mean PBDW approximation error maps for $N = 2$ (left), $N = 6$ (right), and for $M = 8$ (top) and $M = 15$ (bottom). Using synthetic trial data for parameter set Ξ^{trial} with no model error (model \mathcal{P}^{bk}). Sensor locations chosen randomly.	142
5.16	Relative mean (5.10) (left) and maximal (5.11) (right) PBDW approximation error as a function of N for fixed M values. Using synthetic trial data for parameter set Ξ^{trial} with added reaction term $R = 0.0001$ (model \mathcal{P}^{trial}). Sensor locations chosen randomly.	142
5.17	Relative mean (5.10) (left) and maximal (5.11) (right) PBDW approximation error as a function of N for fixed M values. Using synthetic trial data for parameter set Ξ^{trial} with added reaction term $R = 0.001$ (model \mathcal{P}^{trial}). Sensor locations chosen randomly.	143
5.18	Relative mean PBDW approximation error maps for $N = 2$ (left), $N = 6$ (right), and for $M = 8$ (top) and $M = 15$ (bottom). Using synthetic trial data for parameter set Ξ^{trial} with added reaction term $R = 0.001$ (model \mathcal{P}^{trial}). Sensor locations chosen randomly.	143
5.19	Relative mean (5.10) (left) and maximal (5.11) (right) PBDW approximation error as a function of N for fixed M values. Using synthetic trial data for parameter set Ξ^{trial} with no model error (model \mathcal{P}^{bk}). Sensor locations chosen by a greedy procedure.	144
5.20	Relative mean PBDW approximation error maps for $N = 2$ (left), $N = 6$ (right), and for $M = 8$ (top) and $M = 15$ (bottom). Using synthetic trial data for parameter set Ξ^{trial} with no model error (model \mathcal{P}^{bk}). Sensor locations chosen by a greedy procedure.	144

5.21	Relative mean (5.10) (left) and maximal (5.11) (right) PBDW approximation error as a function of N for fixed M values. Using synthetic trial data for parameter set Ξ^{trial} with added reaction term $R = 0.0001$ (model \mathcal{P}^{trial}). Sensor locations chosen by a greedy procedure.	145
5.22	Relative mean (5.10) (left) and maximal (5.11) (right) PBDW approximation error as a function of N for fixed M values. Using synthetic trial data for parameter set Ξ^{trial} with added reaction term $R = 0.0001$ (model \mathcal{P}^{trial}). Sensor locations chosen by a greedy procedure.	145
5.23	Relative mean PBDW approximation error maps for $N = 2$ (left), $N = 6$ (right), and for $M = 8$ (top) and $M = 15$ (bottom). Using synthetic trial data for parameter set Ξ^{trial} with added reaction term $R = 0.001$ (model \mathcal{P}^{trial}). Sensor locations chosen by a greedy procedure.	146
5.24	Representation of a domain of interest Ω_{out} in the full computational domain Ω	146
5.25	Relative mean error of the PBDW approximation (5.14) over a domain of interest as a function of N for various M values. Using synthetic trial data for parameter set Ξ^{trial} with no model error (model \mathcal{P}^{bk} , left), and with added reaction term $R = 0.001$ (model \mathcal{P}^{trial} , right). Sensor locations chosen by a greedy procedure.	147
5.26	Relative mean PBDW results as a function of number of data points M for background basis dimension $N = 6$ values. Using synthetic trial data for parameter set Ξ^{trial} with no model error (model \mathcal{P}^{bk}). Sensor locations chosen by a greedy procedure (left), and randomly (right).	147
5.27	Relative mean PBDW results as a function of number of data points M for background basis dimension $N = 6$ values. Using synthetic trial data for parameter set Ξ^{trial} with added reaction term $R = 0.001$ (model \mathcal{P}^{trial}). Sensor locations chosen by a greedy procedure (left), and randomly (right).	148
5.28	Stability constant $\beta_{N,M}$ (3.17) in \tilde{H}^1 norm, for $L_g = 1$ (left), and $L_g = 75$ (right) as a function of M , for sensor locations chosen randomly.	149
5.29	Stability constant $\beta_{N,M}$ (3.17) in \tilde{H}^1 norm for $L_g = 1$ (left), and $L_g = 75$ (right) as a function of M , for sensor locations chosen by a greedy procedure.	149
5.30	PBDW matrix conditioning number in \tilde{H}^1 norm for $L_g = 1$ (left), and $L_g = 75$ (right) as a function of M , for sensor locations chosen randomly.	150
5.31	PBDW matrix conditioning number in \tilde{H}^1 norm for $L_g = 1$ (left), and $L_g = 75$ (right) as a function of M , for sensor locations chosen by a greedy procedure.	150
5.32	Relative mean PBDW approximation errors, calculated in the H^1 norm, for the PBDW system using the H^1 norm (left) vs. the \tilde{H}^1 norm (right), with random sensor locations. Using synthetic trial data for parameter set Ξ^{trial} with no model error (model \mathcal{P}^{bk}).	150

5.33	Relative mean PBDW approximation errors, calculated in the H^1 norm, for the PBDW system using the H^1 norm (left) vs. the \tilde{H}^1 norm (right), with sensor locations chosen by a greedy procedure. Using synthetic trial data for parameter set Ξ^{trial} with no model error (model \mathcal{P}^{bk}).	151
5.34	Relative mean PBDW approximation errors, mapped over the domain, for the PBDW system using the H^1 norm (left column) vs. the \tilde{H}^1 norm (right column), with $M = 8$ and $N = 5$ (top row) and with $M = 13$ and $N = 8$ (bottom row). Using synthetic trial data for parameter set Ξ^{trial} with no model error (model \mathcal{P}^{bk}), and sensor locations chosen by a greedy procedure.	151
5.35	Relative mean PBDW approximation errors, calculated in the H^1 norm, for the PBDW system using the H^1 norm (left) vs. the \tilde{H}^1 norm (right), with random sensor locations. Using synthetic trial data for parameter set Ξ^{trial} with added reaction term $R = 0.001$ (model \mathcal{P}^{trial}).	152
5.36	Relative mean PBDW approximation errors, calculated in the H^1 norm, for the PBDW system using the H^1 norm (left) vs. the \tilde{H}^1 norm (right), with sensor locations chosen by a greedy procedure. Using synthetic trial data for parameter set Ξ^{trial} with added reaction term $R = 0.001$ (model \mathcal{P}^{trial}).	152
5.37	Relative mean PBDW approximation errors, mapped over the domain, for the PBDW system using the H^1 norm (left column) vs. the \tilde{H}^1 norm (right column), with $M = 8$ and $N = 5$ (top row) and with $M = 13$ and $N = 8$ (bottom row). Using synthetic trial data for parameter set Ξ^{trial} with added reaction term $R = 0.001$ (model \mathcal{P}^{trial}), and sensor locations chosen by a greedy procedure.	153
5.38	Sensors locations chosen by a GEIM-based Greedy algorithm over \tilde{H}^1 Update basis functions q_m defined by equation (3.8).	155
5.39	Approximation of the concentration for $\mathbf{p} = \mathbf{p}_{max}$. Trial solution with model error simulated by a reaction term of $R = 0.001$. FEM solution c^{true} (left), \tilde{H}^1 PBDW approximation using synthetic data, with random sensors (middle), \tilde{H}^1 PBDW approximation with greedy selected sensors of figure 5.38 (right). We set $M = 13$ and $N = 6$ here.	155
5.40	Relative mean best-fit error onto the \tilde{H}^1 PBDW approximation spaces, equation (4.17). Set of trial solutions over $\mathbf{p} \in \mathcal{D}^{trial}$, as a function of M in H^1 -norm. No model error (left), and model error with an added reaction term of $0.001c$ (right). Greedy selected sensors of figure 5.38.	155
5.41	Relative mean (equation (5.10), left) and maximal (equation (5.11), right) \tilde{H}^1 PBDW approximation error in H^1 -norm as a function of Background RB dimension N for various numbers of data points M , over $\mathbf{p} \in \mathcal{D}^{trial}$ with no model error. Greedy selected sensors of figure 5.38.	156

5.42	Relative mean (equation (5.10), left) and maximal (equation (5.11), right) \tilde{H}^1 PBDW approximation error in H^1 -norm as a function of Background RB dimension N for various numbers of data points M , over $\mathbf{p} \in \mathcal{D}^{trial}$, model error with an added reaction term of $R = 0.001$. Greedy selected sensors of figure 5.38.	156
5.43	Relative mean pointwise \tilde{H}^1 PBDW approximation error maps, equation (5.9), for $N = 2$ (left), $N = 6$ (right), and for $M = 8$ (top) and $M = 13$ (bottom), over $\mathbf{p} \in \mathcal{D}^{trial}$ with no model error. The lowest contour line shows 1% error. Greedy selected sensors of figure 5.38.	157
5.44	Relative mean pointwise \tilde{H}^1 PBDW approximation error maps, equation (5.9), for $N = 2$ (left), $N = 6$ (right), and for $M = 8$ (top) and $M = 13$ (bottom), over $\mathbf{p} \in \mathcal{D}^{trial}$ with model error by an added reaction term of $0.001c$. The lowest contour line shows 1% error. Greedy selected sensors of figure 5.38.	158
5.45	Relative mean (5.10) and maximal (5.11) PBDW approximation error as a function of number of data points M for background basis dimension $N = 6$, and GEIM interpolation errors as a function of $M = N$. Using synthetic trial data for parameter set Ξ^{trial} from model \mathcal{P}^{trial} with a small added reaction term of $R = 0.0001$ (left), and significant model error from $R = 0.001$ (right). Sensor locations chosen by a greedy procedure.	159
5.46	Relative mean errors of the GEIM (left) with $M = 10$ and the PBDW (right) with $M = 10$, $N = 6$, approximations, mapped over the calculation domain. Using greedy selected sensors and synthetic trial data over parameters Ξ^{trial} on model \mathcal{P}^{trial} , with model error added by a reaction term of $R = 0.0001$. Mapping of the errors is truncated at 1×10^{-6} , and the lowest contour line shows 1% error.	159
5.47	Relative mean errors of the GEIM (left) with $M = 10$ and the PBDW (right) with $M = 10$, $N = 6$, approximations, mapped over the calculation domain. Using greedy selected sensors and synthetic trial data over parameters Ξ^{trial} on model \mathcal{P}^{trial} , with model error added by a reaction term of $R = 0.001$. Mapping of the errors is truncated at 1×10^{-6} , and the lowest contour line shows 1% error.	160
5.48	Relative mean and maximal \tilde{H}^1 PBDW errors as a function of number of data points M for PBDW Background basis dimension $N = 6$, and GEIM interpolation errors as a function of $M = N$, over $\mathbf{p} \in \mathcal{D}^{trial}$. Model error by an added reaction term $0.001c$. Greedy selected sensors of figure 5.38 for the PBDW estimation, and of figure 5.7 for the GEIM approximation.	160
5.49	Relative mean pointwise GEIM (left) and \tilde{H}^1 PBDW (right) approximation error maps for $M = 10$ and $N = 6-M = 10$, respectively, over $\mathbf{p} \in \mathcal{D}^{trial}$. Model error of $0.0001c$ (top) and $0.001c$ (bottom). Mapping of the errors is truncated at 1×10^{-6} , and the lowest contour line shows 1% error. Greedy selected sensors of figure 5.38 for the PBDW estimation, and of figure 5.7 for the GEIM approximation.	161

5.50	Relative error of the POD projection measured in H^1 norm for several sets of concentration	165
5.51	Sensor locations considered for the Adjoint vs. PBDW comparison, sparse grid on which we performed a Greedy selection.	166
5.52	Sensor locations considered for the Adjoint vs. PBDW comparison. Selected sensors for $M = 1, 2, 3, 4$	166
5.53	Wind field computed by Navier-Stokes with $k-\epsilon$ turbulence closure (left), compared to a wind field computed by Stokes (right).	167
5.54	Concentration field from \mathcal{P}^{bk} over a Navier-Stokes wind/turbulence field (left), compared to a concentration field over a Stokes wind field with a single aggregated Navier-Stokes turbulence field (right).	168
5.55	Sensor locations considered for the PBDW method, a grid of 100 possible sensors on which we perform a Greedy selection.	170
5.56	Grid of sensor locations considered for the PBDW method. Selected sensors for $M = 1$ through $M = 6$	170
6.1	3D test domain with boundaries corresponding to the velocity field (left), and with various combustion pollution sources (right).	177
6.2	Concentration solution over velocity field with parameters $(3.33 \times 10^{-4} \frac{kg}{m^3}, 3.33 \times 10^{-4} \frac{kg}{m^3})$ (left), and $(1.11 \times 10^{-4} \frac{kg}{m^3}, 1.11 \times 10^{-4})$ (right), for two sets of source locations. Horizontal slice taken at $z = 1m$	178
6.3	Greedy H^1 projection errors of a training set of solutions.	179
6.4	Sensor locations Σ_1 (left-middle), and Σ_2 (right).	179
6.5	Sensor locations Σ_3 chosen by a greedy algorithm. Left: sensors at height $z = 0.5m$. Right: sensors at height $z = 1.5m$	180
6.6	Stability constant $\beta_{N,M}$ in H^1 norm as a function of M for various N values, for sensor locations Σ_1 (top left), and Σ_2 (top right), and for sensor locations Σ_3 chosen by a greedy procedure (bottom).	181
6.7	Condition Number of PBDW matrices in H^1 norm as a function of M for various N values, for sensor locations Σ_1 (top left), Σ_2 (top right), and for Σ_3 chosen by a greedy procedure (bottom).	182
6.8	PBDW approximated concentration using non-noisy synthetic data as compared with the FEM concentration solution with source intensity $\mathcal{I} = 1.11 \times 10^{-4}$. FEM solution (top), POD-PBDW approximation (bottom left), Greedy-PBDW approximation (bottom right).	185
6.9	Relative PBDW approximation error using non-noisy synthetic data in log scale. Solution with intensity $\mathcal{I} = 1.11 \times 10^{-4}$	186
6.10	FEM concentration simulation (left) ; relative PBDW approximated concentration using non-noisy synthetic data (right).	187
6.11	Relative mean (5.10) (left) and maximal (5.11) (right) PBDW approximation errors in the H^1 -norm as a function of N for various M -values, using synthetic trial data for parameter set Ξ^{trial} with no model error (model \mathcal{P}^{bk}), and sensor locations Σ_2	187

6.12	Relative mean (5.10) (left) and maximal (5.11) (right) PBDW approximation errors in the H^1 -norm as a function of N for various M -values, using synthetic trial data for parameter set Ξ^{trial} with reaction coefficient $R = 0.0001$ (model \mathcal{P}^{trial}), and sensor locations Σ_2	188
6.13	Relative mean (5.10) (left) and maximal (5.11) (right) PBDW approximation errors in the H^1 -norm as a function of N for various M -values, using synthetic trial data for parameter set Ξ^{trial} with no model error (model \mathcal{P}^{bk}), and sensor locations Σ_3	188
6.14	Relative mean (5.10) (left) and maximal (5.11) (right) PBDW approximation errors in the H^1 -norm as a function of N for various M -values, using synthetic trial data for parameter set Ξ^{trial} with reaction coefficient $R = 0.0001$ (model \mathcal{P}^{trial}), and sensor locations Σ_3	189
6.15	Relative mean (5.10) (left) and maximal (5.11) (right) PBDW approximation errors in the H^1 -norm as a function of N for various M -values, using synthetic trial data for parameter set Ξ^{trial} with reaction coefficient $R = 0.001$ (model \mathcal{P}^{trial}), and sensor locations Σ_3	189
6.16	Relative mean PBDW errors (5.9) for $M = 20$, using synthetic trial data for parameter set Ξ^{trial} and sensor locations Σ_2 . Left: no model error. Right: reaction coefficient $R = 0.0001$ (model \mathcal{P}^{trial}).	190
6.17	Relative mean PBDW errors (5.9) for $M = 20$, using synthetic trial data for parameter set Ξ^{trial} and sensor locations Σ_3 . Left: no model error. Right: reaction coefficient $R = 0.0001$ (model \mathcal{P}^{trial}).	191
6.18	Relative mean PBDW error (5.9) for $M = 20$ and $N = 8$, using synthetic trial data for parameter set Ξ^{trial} , sensor locations Σ_3 , and reaction coefficient $R = 0.0001$ (model \mathcal{P}^{trial}).	192
6.19	Computational times for the PBDW method online for this case study.	193
6.20	Update basis functions constructed by Riesz representation (3.7) in the H^1 -norm (left), as compared to those constructed in the \tilde{H}^1 -norm (4.21) (right), presented on a common scale.	194
6.21	Relative mean PBDW errors (5.9) for $M = 20$ and $N = 12$, using synthetic trial data for parameter set Ξ^{trial} with reaction coefficient $R = 0.001$ (model \mathcal{P}^{trial}), and sensor locations Σ_2 . PBDW approximation in H^1 norm (left), and \tilde{H}^1 norm (right). Relative errors computed in the H^1 -norm.	194
6.22	Relative mean PBDW errors in the H^1 -norm as a function of N for $M = 20$, using synthetic trial data for parameter set Ξ^{train} (model error only) with reaction coefficients $R = 0.001$ and $R = 0.0001$ (model \mathcal{P}^{trial}), and sensor locations Σ_2 . In H^1 norm (left), and \tilde{H}^1 norm (right).	195
6.23	3D test domain with combustion and traffic pollution sources.	196
6.24	Concentration solution (logarithmic scale) over velocity field with $\mathbf{p} = (1 \times 10^{-8}, 0, 1 \times 10^{-6}, 5 \times 10^{-10}) \frac{kg}{m^3}$ (left), and $\mathbf{p} = (1 \times 10^{-12}, 1 \times 10^{-6}, 1 \times 10^{-7}, 1 \times 10^{-7}) \frac{kg}{m^3}$ (right).	197
6.25	Set of $N = 4$ solutions to \mathcal{P}^{bk} for $\mathbf{p} \in \mathcal{D}^{bk}$, spanning the solution manifold \mathcal{M}^{bk}	198

6.26	Projection errors of a training ensemble of solutions to \mathcal{P}^{bk} onto the set of up to 4 solutions shown in figure 6.25 . Relative mean and maximal errors in H^1 norm as a function of N	199
6.27	Sensor locations chosen by GEIM algorithm over the training set in section 6.2. Left: sensors at height $z = 0.5m$. Middle: sensors at height $z = 1m$. Right: sensors at height $z = 1.5m$	199
6.28	Stability constant $\beta_{N,M}$ in H^1 norm as a function of M for various N values, for sensor locations chosen by a greedy procedure.	200
6.29	Trial solution corresponding to maximal error, $p_{max} \in \mathcal{D}_{trial}^{bk}$ (5.6), logarithmic scale. Using synthetic trial data for parameter set Ξ^{trial} with model error with no model error. FEM solution (left), PBDW approximation (right). We set $M = 8$ and $N = 3$ here.	201
6.30	Trial solution corresponding to maximal error, $p_{max} \in \mathcal{D}_{trial}^{bk}$ (5.6), logarithmic scale. Using synthetic trial data for parameter set Ξ^{trial} with model error with an added reaction term of $R = 0.001$. FEM solution (left), PBDW approximation (right). We set $M = 8$ and $N = 3$ here.	202
6.31	Relative mean (5.10) (left) and maximal (5.11) (right) PBDW approximation error as a function of N for fixed M values. Using synthetic trial data for parameter set Ξ^{trial} with no model error (model \mathcal{P}^{bk}). Sensor locations chosen by a greedy procedure.	202
6.32	Relative mean PBDW approximation error maps for $M = 4$ and $N = 3$ (left), and $M = 10$ and $N = 4$ (right). Using synthetic trial data for parameter set Ξ^{trial} with no model error (model \mathcal{P}^{bk}). Sensor locations chosen by a greedy procedure.	203
6.33	Relative mean (5.10) (left) and maximal (5.11) (right) PBDW approximation error as a function of N for fixed M values. Using synthetic trial data for parameter set Ξ^{trial} with $R = 0.001$ (model \mathcal{P}^{trial}). Sensor locations chosen by a greedy procedure.	203
7.1	Geographical location of interest: San Joaquin Valley.	206
7.2	Maps of sensor locations and subjects' homes in Fresno. Left: FACES spatially-rich monitoring. Homes with sampling sites are marked by orange squares, other subjects' homes by blue dots. 8 schools were also monitored. Right: CHAPS spatially-rich monitoring sites, in yellow and magenta. [197]	207
7.3	Pollution and meteorological sensors in Fresno [139]	208
7.4	Maps of calculation domains in Fresno. Left: Full view. Right: Zoom on reduced domain (Map data: Google 2015)	208
7.5	Representations of the domain in QGIS [183]. Left: available GIS data over Domain 1. Right: supplemented and formatted GIS data.	210
7.6	ArcGIS [68] representation of the neighborhood from geographical data, with constructed residential homes at locations of addresses.	210
7.7	Salomé [32] representation of a 3D geometrical domain made by extrusion of the 2D data, centered at a chosen data point (left). Zoom on the 3D calculation mesh (right).	211

7.8	Wind field over a neighborhood of Fresno for $\vec{v}_{in} = 1.3 * z^{0.4}$ in SE direction (308 deg), corresponding to conditions over Fresno on 1/4/2001. Left: a horizontal cut at $z = 1m$. Right: illustration of the vertical flow profile with an added vertical cut.	212
7.9	Representation (ArcGIS) of a neighborhood in Fresno over which a wind field was computed using <i>Code_Saturne</i> (left). Representation of a subdomain of the fluid domain used to study pollutant concentrations (right).	213
7.10	A concentration solution to \mathcal{P}^{bk} with two street pollution sources.	214
7.11	Left: Eigenvalues of H^1 -norm correlation matrix associated to the ensemble of solutions to \mathcal{P}^{bk} for $\mathbf{p} \in \mathcal{D}^{bk}$. Right: Mean and max relative POD projection errors of these solutions.	215
7.12	Potential sensor locations, from a set of 2250 at varying heights (left), and 25 Greedy-selected sensors (right).	215
7.13	Left: stability constant $\beta_{N,M}$ (3.17) with $\ \cdot\ _{\mathcal{X}} = \ \cdot\ _{H^1}$. Right: condition number of PBDW matrices, with $\ \cdot\ _{\mathcal{X}} = \ \cdot\ _{H^1}$. As a function of M for $N = 3, 5, 8, 13$. Sensor locations chosen by a greedy algorithm	216
7.14	FEM solution (left), PBDW approximation for $M = 8$ and $N = 3$ (right) with $p_{max} \in \mathcal{D}_{trial}^{bk}$ (5.6) and synthetic data with reaction term of $R = 0.0001$ (model \mathcal{P}^{trial}).	217
7.15	Relative mean (5.10) (left) and maximal (5.11) (right) PBDW approximation error as a function of N for fixed M values. Using synthetic trial data from \mathcal{P}^{bk} , $\mathbf{p} \in \Xi^{trial}$, no model error. Sensor locations chosen by a greedy procedure.	217
7.16	Relative mean (5.10) (left) and maximal (5.11) (right) PBDW approximation error as a function of N for fixed M values. Using synthetic trial data from \mathcal{P}^{trial} , $\mathbf{p} \in \Xi^{trial}$, reaction term $R = 0.0001$. Sensor locations chosen by a greedy procedure.	218
7.17	Relative mean (5.10) and maximal (5.11) PBDW approximation error as a function of N for $M = 8$. Using synthetic trial data with added reaction terms of $R = 0.0001$ and $R = 0.0005$ in model \mathcal{P}^{trial} . Sensor locations chosen by a greedy procedure.	218
7.18	Relative mean PBDW approximation error over a set of 8 trial solutions to \mathcal{P}^{bk} for $\mathbf{p} \in \Xi^{trial}$ with no model error. Left: $M = 8, N = 3$. Right: $M = 10$ and $N = 5$	219
7.19	Relative mean PBDW approximation error over a set of 8 trial solutions to \mathcal{P}^{trial} for $\mathbf{p} \in \Xi^{trial}$ with $R = 0.0001$. Left: $M = 8, N = 3$. Right: $M = 10$ and $N = 5$	220
8.1	Geometry of the physical domains : single tunnel (left) and twin tunnels (right)	228
8.2	Boundaries of domain Ω_a	231
8.3	Boundaries of domain Ω_b	231

8.4	Top: Embedded meshes used in case study 8.2.1.4 – coarse (left), fine (middle) and reference (right) – Bottom : embedded meshes in case study 8.2.1.5 – coarse (left), fine (middle) and reference (right).	235
8.5	Relative errors of the POD projection. Top: study case 8.2.1.4 using \mathbb{P}_1 (left) and \mathbb{P}_2 (right) FE snapshots ; Bottom: study case 8.2.1.5 using \mathbb{P}_2 -FE snapshots	236
8.6	Average error of the POD projection vs FEM error. Top: study case 8.2.1.4 using \mathbb{P}_1 (left) and \mathbb{P}_2 (right) FEsnapshots ; Bottom: study case 8.2.1.5 using \mathbb{P}_2 -FE snapshots	237
8.7	Maximal error of the POD projection vs FEM error. Top: study case 8.2.1.4 using \mathbb{P}_1 (left) and \mathbb{P}_2 (right) FEsnapshots ; Bottom: study case 8.2.1.5 using \mathbb{P}_2 -FE snapshots	237
8.8	Condition number of the different rectification matrices: A_N , D_N , and K_N during the offline stage (\mathbb{P}_2 FEM solutions) in case study 8.2.1.4 . . .	241
8.9	Average rectification errors the offline stage (\mathbb{P}_2 FEM solutions) depending on the rectification matrix in case study 8.2.1.4	241
8.10	Average (left) and maximal (right) errors during offline stage with $R_N = K_N$ and $N_{max} = 16$	242
8.11	Average (left) and maximal (right) rectified RB projection errors on trial space during the online stage with $R_N = K_N$ and $N_{max} = 16$	242
8.12	Displacement value for $\mu_{max} = (125, 0.35, 23, 0.03)$	242
8.13	Relative error maps of the two-grid FE/RB approximation without (left) and with (right) rectification as function of N for $\mu = \mu_{max} = (125, 0.35, 23, 0.03)$	243
8.14	Error maps for N=15 and $\mu_{max} = (125, 0.35, 23, 0.03)$	244
8.15	Value of the vertical displacement on the surface for $\mu = \mu_{max} = (125, 0.35, 23, 0.03)$	244
8.16	Comparaison of calculation times of \mathbb{P}_2 -FE and two-grid FE/RB Methods	245
8.17	Average errors during offline (left) and online (right) stage with $R_N = K_N$ and $N_{max} = 21$	245
8.18	Displacement value for $\mu_{max} = (125, 0.35, 23, 0.03)$	246
8.19	Error maps for N=15 and $\mu_{max} = (125, 0.35, 23, 0.03)$ Top left : $u_{ref} - P_N u_H$; Top right $u_{ref} - R_N P_N u_H$; Bottom $u_{ref} - P_N u_h$;	246
A.1	Illustration of the process of modeling physical phenomena with available measurement data.	259

List of Tables

0.1	Variation spatiale de la concentration de polluants extérieurs sur un site d’observations dans le centre de Fresno (CA), durant la haute saison de chaque polluant [137].	2
1.1	Pollutants to monitor, health concerns, and sources.	22
4.1	Table summarizing units in equation (4.37).	115
5.1	Table summarizing data used from [188]: general information from various tables in the document.	127
5.2	Global Error measured in H^1 -norm (relative error) using greedy sensor position (1 iteration = 1 FEM direct approximation + 1 FEM adjoint approximation)	167
5.3	Global Error measured in H^1 -norm (relative error) using greedy sensor position (1 iteration = 1 FEM direct approximation + 1 FEM adjoint approximation)	168
5.4	Global Error (relative error) using greedy sensors position with no Model Error	169
5.5	Global Error (relative error) using greedy sensor position with Model Error: true solution with linear reaction $r = 10^{-3}$	169
5.6	Global Error (relative error) using greedy sensors position with Model Error: true solution with Navier-Stokes with $k - \epsilon$ turbulence closure wind field	169
5.7	Global relative error (measured in H^1 norm) of the PBDW method . . .	171
5.8	Computational times of two MOR-data assimilation methods over the full calculation domain and estimation of average concentration over a sub-domain Ω_{out} (see figure 5.24), compared to FEM approximation. Average over the set of trial solutions considered here.	172
5.9	Computational times of the adjoint method compared to the PBDW and GEIM for the state estimate of the Stokes-based 2D case study.	173
6.1	Offline computational times of the PBDW method over the 3D calculation domain.	192
7.1	Computational times of the FEM approximation of \mathcal{P}^{bk} . Average over the set of training solutions considered here.	220

7.2	Computational times of the PBDW state estimation for various M and N values. Average over the set of trial solutions considered here.	220
8.1	Comparison of calculation times of \mathbb{P}_2 -FE and two-grid FE/RB Methods (for $N = 15$, providing approximation error equivalent to the fine FEM solution).	245
A.1	Ratio of daily residential outdoor concentration to central site concentration measurements, within the high season for each pollutant [137].	258

Appendix C

Technical Implementation Notes

C.1 Code_Saturne for Fluid Dynamics

The hydraulic diameter for an inlet is needed for turbulent models in *Code_Saturne* and is defined as follows:

$$D_h = \frac{4S}{\mathcal{P}}, \quad (\text{C.1})$$

where \mathcal{P} is the perimeter of the surface. The hydraulic diameter of a 2D slice is equal to the usual diameter.

Code_Saturne's module *rough walls* can represent flow entering non-air-tight buildings, and coefficient $\sim \frac{H}{10}$ was chosen, where H is the building height.

To set an exponential inlet profile for fluid simulations, we set the inlet BC to, for example, $\|\vec{u}\| = 2z^\alpha$ and direction $(x^*, y^*)^T$ in practice: `norm_u = 2z0.4`.

C.2 MOR Algorithms

Algorithm 3 : Weak Greedy algorithm to construct a Reduced Basis approximation space

- 1: **Initialization:** GIVEN
 $\Xi_{test} = (\mathbf{p}_1, \dots, \mathbf{p}_{n_{test}}) \in \mathcal{D}^{n_{test}}, n_{test} \gg 1$
 - 2: CHOOSE RANDOMLY $\mathbf{p}_1 \in \mathcal{D}$
 - 3: SET $S_1 = \{\mathbf{p}_1\}$ and $X_h^1 = \text{span}(u_h(\mathbf{p}_1))$.
 - 4: **for** $N = 2$ to N_{max} **do**
 - 5: $\mathbf{p}_N = \underset{\mathbf{p} \in \Xi_{test}}{\text{argmax}} \frac{\|u_h(\mathbf{p}) - P_{N-1}u_h(\mathbf{p})\|_{L^2}}{\|u_h(\mathbf{p})\|_{L^2}}$
(where P_{N-1} is the L^2 -orthogonal projection operator from \mathcal{X}_h into X_h^{N-1})
 - 6: $S_N = S_{N-1} \cup \mathbf{p}_N$
 - 7: $X_h^N = X_h^{N-1} + \text{span}(u_h(\mathbf{p}_N))$
 - 8: **end for**
-

Algorithm 4 : Update Space algorithm

1: **Initialization:**

- Load mesh and build associated FE space, scalar products.
- Load sensor size and locations

2: **for** $m = 1$ to M **do**3: Define: sensor functionals over ball $B(\vec{x}_m, r)$

$$\varphi_m = \left(e^{\left(\frac{-1}{r^2}\right) * ((x-x_m)^2 + (y-y_m)^2 + (z-z_m)^2)} \right);$$

4: Define and solve variational form for test function v :

$$\text{solve } a(q, v) = \int_{\Omega} (\nabla q \cdot \nabla v + q * v) - \int_{\Omega} (\varphi_h^m * v) = 0$$

5: Save basis functions $q_m = q$:6: **end for**

Algorithm 5 : GEIM algorithm

- 1: **Initialization:** the first interpolating function and associated linear form are, for example:

$$\begin{aligned} u(\mathbf{p}_1) &= \operatorname{argsup}_{u \in \mathcal{M}^{bk}} \|u\|_{\mathcal{X}} \\ \sigma_1 &= \operatorname{argsup}_{\sigma \in \Sigma} |\sigma(u(\mathbf{p}_1))| \end{aligned}$$

- 2: The first basis function is: $\tilde{q}_1 = \frac{u(\mathbf{p}_1)}{\sigma_1(u(\mathbf{p}_1))}$
 3: The second interpolating function and associated linear form are:

$$\begin{aligned} u(\mathbf{p}_2) &= \operatorname{argsup}_{u \in \mathcal{M}^{bk}} \|u - \sigma_1(u) \cdot \tilde{q}_1\|_{\mathcal{X}} \\ \sigma_2 &= \operatorname{argsup}_{\sigma \in \Sigma} |\sigma(u(\mathbf{p}_2) - \sigma_1(u(\mathbf{p}_2)) \cdot \tilde{q}_1)| \end{aligned}$$

- 4: The second basis function is: $\tilde{q}_2 = \frac{u(\mathbf{p}_2) - \sigma_1(u(\mathbf{p}_2)) \cdot \tilde{q}_1}{\sigma_2(u(\mathbf{p}_2) - \sigma_1(u(\mathbf{p}_2)) \cdot \tilde{q}_1)}$
 5: **for** $m = 3$ to M **do**
 6: Solve the m^{th} interpolation problem: find $\{\tilde{\alpha}_j^{m-1}(\varphi)\}_j$ such that

$$\forall 1 \leq i \leq m-1 \quad \sigma_i(u) = \sum_{j=1}^{m-1} \tilde{\alpha}_j^{m-1}(u) \sigma_i(\tilde{q}_j)$$

- 7: Compute $\mathcal{I}_{m-1}[u] = \sum_{j=1}^{m-1} \tilde{\alpha}_j^{m-1}(u) \cdot \tilde{q}_j$
 8: Evaluate $\epsilon_{m-1}(u) = \|u - \mathcal{I}_{m-1}[u]\|_{L^2(\Omega)}$
 9: Define:

$$\begin{aligned} u(\mathbf{p}_m) &= \operatorname{argsup}_{u \in \mathcal{M}^{bk}} \epsilon_{m-1}(u) \\ \sigma_m &= \operatorname{argsup}_{\sigma \in \Sigma} |\sigma(u(\mathbf{p}_m) - \mathcal{I}_{m-1}[u(\mathbf{p}_m)])| \\ \tilde{q}_m &= \frac{u(\mathbf{p}_m) - \mathcal{I}_{m-1}[u(\mathbf{p}_m)]}{\sigma_m(u(\mathbf{p}_m) - \mathcal{I}_{m-1}[u(\mathbf{p}_m)])} \end{aligned}$$

- 10: **end for**
 11: Solve the final interpolation problem: find $\{\tilde{\alpha}_j^M(u)\}_j$ such that

$$\forall 1 \leq i \leq M \quad \sigma_i(u) = \sum_{j=1}^M \tilde{\alpha}_j^{m-1}(u) \sigma_i(\tilde{q}_j)$$

- 12: Compute $\mathcal{I}_M[u] = \sum_{j=1}^M \tilde{\alpha}_j^M(u) \cdot \tilde{q}_j$
-

Bibliography

- [1] CEDVAL dataset. Technical report, Hamburg University, 2002.
- [2] SolidWorks, 2002.
- [3] DAPPLE Air Pollution Project dataset. Technical report, U.K. Engineering and Physical Sciences Research Council, 2008.
- [4] K. Afanasiev and M. Hinze. Adaptive control of a wake flow using proper orthogonal decomposition. *Lecture Notes in Pure and Applied Mathematics*, pages 317–332, 2001.
- [5] K. Ahmad, M. Khare, and K. K. Chaudhry. Wind tunnel simulation studies on dispersion at urban street canyons and intersections—a review. *Journal of Wind Engineering and Industrial Aerodynamics*, 93(9):697–717, 2005.
- [6] P.E. Allier, L. Chamoin, and P. Ladevèze. Proper Generalized Decomposition computational methods on a benchm. problem: introducing a new strategy based on Constitutive Relation Error minimization. *Adv. Model. and Simul. in Eng. Sci.*, 2(1):17, 2015.
- [7] G. Antonioni, S. Burkhart, J. Burman, A. Dejoan, A. Fusco, R. Gaasbeek, T. Gjesdal, A. Jappinen, K. Riikonen, P. Morra, O. Parmhed, and J.L. Santiago. Comparison of CFD and operational dispersion models in an urban-like environment. *Atmospheric Environment*, 47:365–372, 2012.
- [8] F. Archambeau, N. Mehitoua, and M. Sakiz. Code Saturne: a Finite Volume Code for the Computation of Turbulent Incompressible flows Int. *J. Finite Volumes, Electronical edition: <http://averoes.math.univ-paris13.fr/html>*, 2004.
- [9] E. Bader, M. Karcher, M.A. Grepl, and K. Veroy. Certified Reduced Basis Methods for Parametrized Distributed Elliptic Optimal Control Problems with Control Constraints. *SIAM Journal on Scientific Computing*, 38(6):A3921–A3946, 2016.
- [10] Z. Bai. Krylov subspace techniques for reduced-order modeling of large-scale dynamical systems. *Applied numerical mathematics*, 43(1-2):9–44, 2002.
- [11] J.J. Baik, S.B. Park, and J.J. Kim. Urban flow and dispersion simulation using a cfd model coupled to a mesoscale model. *Journal of Applied Meteorology and Climatology*, 48(8):1667–1681, 2009.

- [12] C. J. Baker and D. M. Hargreaves. Wind tunnel evaluation of a vehicle pollution dispersion model. *Journal of Wind Engineering and Industrial Aerodynamics*, 89(2):187–200, 2001.
- [13] A. Bakker. Applied Computational Fluid Dynamics - Lecture 10 Turbulence Models, 2008.
- [14] A. Baklanov. Application of CFD Methods for Modelling in Air Pollution Problems: Possibilities and Gaps. *Environmental Monitoring and Assessment*, 65(1-2):181–189, 2000.
- [15] A. L. Barbu, A. J. Segers, M. Schaap, A. W. Heemink, and P. J. H. Builtjes. A multi-component data assimilation experiment directed to sulphur dioxide and sulphate over Europe. *Atmospheric Environment*, 43(9):1622–1631, 2009.
- [16] M. Barrault, Y. Maday, N.C. Nguyen, and A. T. Patera. An 'empirical interpolation' method: application to efficient reduced-basis discretization of partial differential equations. *Comptes Rendus Mathematique*, 339(9):667–672, 2004.
- [17] R. R. Barton. Metamodeling: a state of the art review. In *Proceedings of Winter Simulation Conference*, pages 237–244, 1994.
- [18] R. Beelen, O. Raaschou-Nielsen, M. Stafoggia, Z. J. Andersen, G. Weinmayr, B. Hoffmann, K. Wolf, E. Samoli, P. Fischer, M. Nieuwenhuijsen, P. Vineis, W.W. Xun, K. Katsouyanni, K. Dimakopoulou, A. Oudin, B. Forsberg, L. Modig, A.S. Havulinna, T. Lanki, A. Turunen, B. Oftedal, W. Nystad, P. Nafstad, U. De Faire, N.L. Pedersen, C.G. Ostenson, L. Fratiglioni, J. Penell, M. Korek, G. Pershagen, K.T. Eriksen, K. Overvad, T. Ellermann, M. Eeftens, P.H. Peeters, K. Meliefste, M. Wang, B. Bueno-de Mesquita, D. Sugiri, U. Kramer, J. Heinrich, K. de Hoogh, T. Key, A. Peters, R. Hampel, H. Concin, G. Nagel, A. Ineichen, E. Schaffner, N. Probst-Hensch, N. Kunzli, C. Schindler, T. Schikowski, M. Adam, H. Phuleria, A. Vilier, F. Clavel-Chapelon, C. Declercq, S. Grioni, V. Krogh, M.Y. Tsai, F. Ricceri, C. Sacerdote, C. Galassi, E. Migliore, A. Ranzi, G. Cesaroni, C. Badaloni, F. Forastiere, I. Tamayo, P. Amiano, M. Dorronsoro, M. Katsoulis, A. Trichopoulou, B. Brunekreef, and G. Hoek. Effects of long-term exposure to air pollution on natural-cause mortality: an analysis of 22 European cohorts within the multicentre ESCAPE project. *The Lancet*, 383(9919):785–795, 2014.
- [19] L. Benes and Viktor S. Numerical ptiiization of near-road vegetation barriers. Crete, Greece, 2016.
- [20] P. Benner, S. Gugercin, and K. Willcox. A survey of projection-based model reduction methods for parametric dynamical systems. *SIAM review*, 57(4):483–531, 2015.
- [21] A. F. Bennett. Array design by inverse methods. *Progress in Oceanography*, 15(2):129–156, 1985.

- [22] G. Berkooz, P. Holmes, and J.L. Lumley. The proper orthogonal decomposition in the analysis of turbulent flows. *Annual review of fluid mechanics*, 25(1):539–575, 1993.
- [23] B. Blocken, T. Stathopoulos, J. Carmeliet, and J.L.M. Hensen. Application of computational fluid dynamics in building performance simulation for the outdoor environment: an overview. *Journal of Building Performance Simulation*, 4(2):157–184, 2011.
- [24] N. Blond and R. Vautard. Three-dimensional ozone analyses and their use for short-term ozone forecasts. *J. Geophys. Res.*, 109(D17):D17303, 2004.
- [25] G. Bolzon and V. Buljak. An effective computational tool for parametric studies and identification problems in materials mechanics. *Comput Mech*, 48(6):675–687, 2011.
- [26] R.P. Bonet Chaple. Numerical stabilization of convection-diffusion-reaction problems. *Reports of the Department of Applied Mathematical Analysis*, 2006.
- [27] S. Branford, O. Coceal, T. G. Thomas, and S. E. Belcher. Dispersion of a Point-Source Release of a Passive Scalar Through an Urban-Like Array for Different Wind Directions. *Boundary-Layer Meteorology*, 139(3):367–394, 2011.
- [28] A.N. Brooks and T.J.R. Hughes. Streamline upwind/Petrov-Galerkin formulations for convection dominated flows with particular emphasis on the incompressible Navier-Stokes equations. *Computer Methods in Applied Mechanics and Engineering*, 32(1):199–259, 1982.
- [29] R. Buccolieri, M. Sandberg, and S. Di Sabatino. City breathability and its link to pollutant concentration distribution within urban-like geometries. *Atmospheric Environment*, 44(15):1894–1903, 2010.
- [30] M. Canaud and N-E El Faouzi. ECOSTAND: Towards a Standard Methodology for Environmental Evaluation of ITS. *Transportation Research Procedia*, 6:377–390, 2015.
- [31] M. Casey, T. Wintergerste, and Turbulence and Combustion European Research Community on Flow. *Best practice guidelines: ERCOFTAC Special Interest Group on quality and trust in industrial CFD*. ERCOFTAC, [Switzerland], 2000.
- [32] CEA, EDF, and Open Cascade. Salome-Platform.
- [33] W. César. *Outils numériques et technologiques pour l’analyse de la qualité de l’air intérieur*. PhD thesis, Paris Est, 2014.
- [34] R. Chakir and Y. Maday. A two-grid finite-element/reduced basis scheme for the approximation of the solution of parameter dependent PDE. In *Actes de congrès du 9ème colloque national en calcul des structures, Giens*, 2009.

- [35] R. Chakir and Y. Maday. Une méthode combinée d'éléments finis à deux grilles/bases réduites pour l'approximation des solutions d'une EDP paramétrique. *Comptes Rendus Mathématique*, 347(7):435–440, 2009.
- [36] L. Chamoin, P. Ladèveze, and J. Waeytens. Goal-oriented updating of mechanical models using the adjoint framework. *Computational mechanics*, 54(6):1415–1430, 2014.
- [37] J. C. Chang and S. R. Hanna. Air quality model performance evaluation. *Meteorology and Atmospheric Physics*, 87(1-3):167–196, 2004.
- [38] M. Chavez, B. Hajra, T. Stathopoulos, and A. Bahloul. Near-field pollutant dispersion in the built environment by CFD and wind tunnel simulations. *Journal of Wind Engineering and Industrial Aerodynamics*, 99(4):330–339, 2011.
- [39] W. C. Cheng and C.H. Liu. Large-eddy simulation of turbulent transports in urban street canyons in different thermal stabilities. *Journal of Wind Engineering and Industrial Aerodynamics*, 99(4):434–442, 2011.
- [40] F. Chinesta, A. Ammar, A. Leygue, and R. Keunings. An overview of the proper generalized decomposition with applications in computational rheology. *Journal of Non-Newtonian Fluid Mechanics*, 166(11):578–592, 2011.
- [41] F. Chinesta, P. Ladeveze, and E. Cueto. A Short Review on Model Order Reduction Based on Proper Generalized Decomposition. *Archives of Computational Methods in Engineering*, 18(4):395–404, 2011.
- [42] H. Choi, F. Perera, A. Pac, L. Wang, E. Flak, E. Mroz, R. Jacek, T. Chai-Onn, W. Jedrychowski, E. Masters, and others. Estimating individual-level exposure to airborne polycyclic aromatic hydrocarbons throughout the gestational period based on personal, indoor, and outdoor monitoring. *Environmental health perspectives*, 116(11):1509, 2008.
- [43] S.L. Choudrie, L. Brown, R. Miln, T.P. Murrells, G. Thidtlethwaite, J.D. Watterson, and J. Jackson. UK Greencoulementsenshouse Gas Inventory, 1990 to 2006. Technical report, AEA Technology, Harwell, Oxfordshire, 2008.
- [44] F.K. Chow, B. Kosović, and S. Chan. Source Inversion for Contaminant Plume Dispersion in Urban Environments Using Building-Resolving Simulations. *Journal of Applied Meteorology and Climatology*, 47(6):1553–1572, 2008.
- [45] City of Calgary. Vehicle Kilometres Travelled in Calgary: Proposed Methodology. Technical report, 2010.
- [46] A. Cohen and R. Devore. Kolmogorov widths under holomorphic mappings. *IMA Journal of Numerical Analysis*, 36(1):1–12, 2016.
- [47] S. Coquillay. *Prise en compte de la non linéarité du comportement des sols soumis à de petites déformations pour le calcul des ouvrages géotechniques*. PhD thesis, Ecole des Ponts ParisTech, 2005.

- [48] A. Corigliano, M. Dossi, and S. Mariani. Model order reduction and domain decomposition strategies for the solution of the dynamic elastic-plastic structural problem. *Computer Methods in Applied Mechanics and Engineering*, 290:127–155, 2015.
- [49] C. Daversin and C. Prud’homme. Simultaneous empirical interpolation and reduced basis method for non-linear problems. *Comptes Rendus Mathematique*, 353(12):1105–1109, 2015.
- [50] C. Daversin, S. Veys, C. Trophime, and C. Prud’homme. A Reduced Basis Framework: Application to large scale non-linear multi-physics problems. *ESAIM: Proceedings*, 43:225–254, 2013.
- [51] N. Davis, J. Lents, M. Osses, N. Nikkila, and M. Barth. Part 3: Developing countries: development and application of an international vehicle emissions model. *Transportation Research Record: Journal of the Transportation Research Board*, (1939):155–165, 2005.
- [52] L. Dede. *Adaptive and reduced basis methods for optimal control problems in environmental applications*. PhD Dissertation, Politecnico di Milano, Milan, 2008.
- [53] L. Dede. Reduced basis method for parametrized advection-reaction problems. *J. Comput. Math*, 28(1):122–148, 2010.
- [54] L. Dede. Reduced basis method and error estimation for parametrized optimal control problems with control constraints. *Journal of Scientific Computing*, 50(2):287–305, 2012.
- [55] A. Dejoan, J. L. Santiago, A. Martilli, F. Martin, and A. Pinelli. Comparison between large-eddy simulation and reynolds-averaged navier-stokes computations for the MUST field experiment. Part II: effects of incident wind angle deviation on the mean flow and plume dispersion. *Boundary-layer meteorology*, 135(1):133–150, 2010.
- [56] B. Denby, M. Schaap, A. Segers, P. Builtjes, and J. Horàlek. Comparison of two data assimilation methods for assessing PM10 exceedances on the European scale. *Atmospheric Environment*, 42(30):7122–7134, 2008.
- [57] S. Di Sabatino, R. Buccolieri, B. Pulvirenti, and R. Britter. Simulations of pollutant dispersion within idealised urban-type geometries with CFD and integral models. *Atmospheric Environment*, 41(37):8316–8329, 2007.
- [58] F.X. Le DIMET and O. Talagrand. Variational algorithms for analysis and assimilation of meteorological observations: theoretical aspects. *Tellus A*, 38(2):97–110, 1986.
- [59] B.K. Eder, D. Kang, R. Mathur, S. Yu, and K. Schere. An operational evaluation of the Eta-CMAQ air quality forecast model. *Atmospheric Environment*, 40(26):4894–4905, 2006.

- [60] EDF Single Phase Thermal-Hydraulics Group. CodeSaturne 4.0.0 Theory Guide. Technical report, EDF R&D Fluid Dynamics, Power Generation and Environment Department, Chatou Cedex, 2015.
- [61] H. Eibern and H. Schmidt. A four-dimensional variational chemistry data assimilation scheme for Eulerian chemistry transport modeling. *Journal of Geophysical Research: Atmospheres*, 104(D15):18583–18598, 1999.
- [62] J. Eichhorn and A. Kniffka. The numerical flow model MISKAM: State of development and evaluation of the basic version. *Meteorologische Zeitschrift*, 19(1):81–90, 2010.
- [63] H. Elbern, A. Strunk, H. Schmidt, and O. Talagrand. Emission rate and chemical state estimation by 4-dimensional variational inversion. *Atmospheric Chemistry and Physics*, 7(14):3749–3769, 2007.
- [64] E. Emili, S. Gürol, and D. Cariolle. Accounting for model error in air quality forecasts: an application of 4denvar to the assimilation of atmospheric composition using QG-Chem 1.0. *Geoscientific Model Development*, 9(11):3933, 2016.
- [65] US EPA. User’s Guide to MOBILE5 (Mobile Source Emission Factor Model). Technical Report EPA-AA-AQAB-94-01, Office of Air and Radiation & Office of Mobile Sources, Ann Arbor, Michigan, 1994.
- [66] US EPA. Air quality criteria for particulate matter. Technical report, Office of Research and Development, Office of Health and Environmental Assessment, Triangle Park, NC, 1996.
- [67] A. Ern and J.L. Guermond. *Theory and practice of finite elements. Number 159 in Applied Mathematical Sciences*. Springer, New York, 2004.
- [68] ESRI. ArcGIS Desktop, 2011.
- [69] R. Everson and L. Sirovich. Karhunen-Loeve procedure for gappy data. *JOSA A*, 12(8):1657–1664, 1995.
- [70] M. Fallah Shorshani, M. André, C. Bonhomme, and C. Seigneur. Modelling chain for the effect of road traffic on air and water quality: Techniques, current status and future prospects. *Environmental Modelling & Software*, 64:102–123, 2015.
- [71] L. Formaggia, F. Saleri, and A. Veneziani. *Solving Numerical PDEs: Problems, Applications, Exercises*. UNITEXT. Springer Milan, Milano, 2012.
- [72] D. Garaud and V. Mallet. Automatic calibration of an ensemble for uncertainty estimation and probabilistic forecast: Application to air quality. *Journal of Geophysical Research: Atmospheres*, 116(D19), 2011.

- [73] S. Giere, T. Iliescu, V. John, and D. Wells. SUPG reduced order models for convection-dominated convection-diffusion-reaction equations. *Computer Methods in Applied Mechanics and Engineering*, 289:454–474, 2015.
- [74] P. Gousseau, B. Blocken, T. Stathopoulos, and G.J.F. van Heijst. CFD simulation of near-field pollutant dispersion on a high-resolution grid: A case study by LES and RANS for a building group in downtown Montreal. *Atmospheric Environment*, 45(2):428–438, 2011.
- [75] P. Gousseau, B. Blocken, and G. J. F. Van Heijst. CFD simulation of pollutant dispersion around isolated buildings: On the role of convective and turbulent mass fluxes in the prediction accuracy. *Journal of Hazardous Materials*, 194:422–434, 2011.
- [76] S. R. Hanna, M. J. Brown, Fernando E. Camelli, Stevens T. Chan, W. J. Coirier, Sura Kim, Olav R. Hansen, Alan H. Huber, and R. M. Reynolds. Detailed Simulations of Atmospheric Flow and Dispersion in Downtown Manhattan: An Application of Five Computational Fluid Dynamics Models. *Bulletin of the American Meteorological Society*, 87(12):1713–1726, 2006.
- [77] S. R. Hanna, Z. Lu, H. C. Frey, N. Wheeler, J. Vukovich, S. Arunachalam, M. Fernau, and D. A. Hansen. Uncertainties in predicted ozone concentrations due to input uncertainties for the UAM-V photochemical grid model applied to the July 1995 OTAG domain. *Atmospheric Environment*, 35(5):891–903, 2001.
- [78] HBEFA. *Handbook Emission Factors for Road Transport*. INFRAS, hbefa 3.1 edition, 2010.
- [79] F. Hecht. New development in freefem++. *J. Numer. Math.*, 20(3-4):251–265, 2012.
- [80] H. Herrero, Y. Maday, and F. Pla. RB (Reduced basis) for RB (Rayleigh-Bénard). *Computer Methods in Applied Mechanics and Engineering*, 261:132–141, 2013.
- [81] M.W. Hess, S. Grundel, and P. Benner. estimating the inf-sup constant in reduced basis methods for time-harmonic Maxwell’s equations. *IEEE Transactions on Microwave Theory and Techniques*, 63(11):3549–3557, 2015.
- [82] J.S. Hesthaven, B. Stamm, and S. Zhang. Efficient greedy algorithms for high-dimensional parameter spaces with applications to empirical interpolation and reduced basis methods. *ESAIM: Mathematical Modelling and Numerical Analysis*, 48(01):259–283, 2014.
- [83] K.C. Hoang, P. Kerfriden, and S.P.A. Bordas. A fast, certified and “tuning free” two-field reduced basis method for the metamodelling of affinely-parametrised elasticity problems. *Computer Methods in Applied Mechanics and Engineering*, 298:121–158, 2016.

- [84] K. J. Holmes, J.A. Graham, T. McKone, and C. Whipple. Regulatory models and the environment: practice, pitfalls, and prospects. *Risk analysis*, 29(2):159–170, 2009.
- [85] J.E. Houck, J. Crouch, and R.H. Huntley. Review of Wood Heater and Fireplace Emission Factors. In *10th Annual Emission Inventory Meeting, 30th April-3rd May*, 2001.
- [86] J.T. Houghton, L.G. Meira Filho, B. Lim, K. Treanton, I. Mamaty, I. Bonduki, D.J. Griggs, and B.A. Callender. *Revised IPCC guidelines for national greenhouse gas inventories: reference manual*, volume 3 of *Reference Manual*. Cambridge: University Press, 1996.
- [87] K. E. Howes. *Accounting for model error in four-dimensional variational data assimilation*. PhD thesis, PhD thesis. University of Reading: Reading, UK, 2016.
- [88] J. Hu, H. Zhang, S. Chen, Q. Ying, C. Wiedinmyer, F. Vandenberghe, and M.J. Kleeman. Identifying PM_{2.5} and PM_{0.1} Sources for Epidemiological Studies in California. *Environmental Science & Technology*, 48(9):4980–4990, 2014.
- [89] J. Hu, H. Zhang, S.H. Chen, C. Wiedinmyer, F. Vandenberghe, Q. Ying, and M.J. Kleeman. Predicting Primary PM_{2.5} and PM_{0.1} Trace Composition for Epidemiological Studies in California. *Environmental Science & Technology*, 48(9):4971–4979, 2014.
- [90] T.J.R. Hughes and A. Brooks. A multidimensional upwind scheme with no crosswind diffusion. *Finite element methods for convection dominated flows*, 34:19–35, 1979.
- [91] P. Humbert, A. Dubouchet, G. Fezans, and D. Remaud. CESAR-LCPC: A computation software package dedicated to civil engineering uses. *Bulletin des laboratoires des ponts et chaussées*, 256(257):7–37, 2005.
- [92] D.B.P. Huynh and A. T. Patera. Reduced basis approximation and a posteriori error estimation for stress intensity factors. *International Journal for Numerical Methods in Engineering*, 72(10):1219–1259, 2007.
- [93] A. C. Ionita and A. C. Antoulas. Case Study: Parametrized Reduction Using Reduced-Basis and the Loewner Framework. In A. Quarteroni and G. Rozza, editors, *Reduced Order Methods for Modeling and Computational Reduction*, number 9 in MS&A - Modeling, Simulation and Applications, pages 51–66. Springer International Publishing, 2014.
- [94] M. Z. Jacobson. Control of fossil-fuel particulate black carbon and organic matter, possibly the most effective method of slowing global warming. *Journal of Geophysical Research: Atmospheres*, 107(D19), 2002.

- [95] M. Jicha, J. Pospisil, and J. Katolicky. Dispersion of pollutants in street canyon under traffic induced flow and turbulence. *Environmental monitoring and assessment*, 65(1-2):343–351, 2000.
- [96] R.E. et al Kalman. A new approach to linear filtering and prediction problems. *Journal of basic Engineering*, 82(1):35–45, 1960.
- [97] M. Karcher, S. Boyaval, M. Grepl, and K. Veroy. Reduced basis approximation and a posteriori error bounds for 4d-Var data assimilation. 2017.
- [98] K. Khaledi and S. Miro. Robust and reliable metamodells for mechanized tunnel simulations. *Computers and Geotechnics*, 61:1–12, 2014.
- [99] J. Kim. A numerical study of the effects of ambient wind direction on flow and dispersion in urban street canyons using the RNG k-epsilon turbulence model. *Atmospheric Environment*, 38(19):3039–3048, 2004.
- [100] A. Kolmogoroff. Uber die beste Annäherung von Funktionen einer gegebenen Funktionenklasse. *Annals of Mathematics*, pages 107–110, 1936.
- [101] N. Kunzli, R. Kaiser, S. Medina, M. Studnicka, O. Chanel, P. Filliger, M. Herry, F. Horak, V. Puybonnieux-Textier, P. Quénel, J. Schneider, R. Seethaler, J-C Vergnaud, and H. Sommer. Public-health impact of outdoor and traffic-related air pollution: a European assessment. *The Lancet*, 356(9232):795–801, 2000.
- [102] T. Kuwayama, C.R. Ruehl, and M.J. Kleeman. Daily Trends and Source Apportionment of Ultrafine Particulate Mass ($PM_{0.1}$) over an Annual Cycle in a Typical California City. *Environmental Science & Technology*, 47(24):13957–13966, 2013.
- [103] P. Ladevèze and L. Chamoin. On the verification of model reduction methods based on the proper generalized decomposition. *Computer Methods in Applied Mechanics and Engineering*, 200(23):2032–2047, 2011.
- [104] T. Lassila, A. Manzoni, A. Quarteroni, and G. Rozza. A reduced computational and geometrical framework for inverse problems in hemodynamics. *International journal for numerical methods in biomedical engineering*, 29(7):741–776, 2013.
- [105] L. Leclercq, C. Parzani, V.L. Knoop, J. Amourette, and Serge P. Hoogenboom. Macroscopic Traffic Dynamics with Heterogeneous Route Patterns. *Transportation Research Procedia*, 7:631–650, 2015.
- [106] D. Lejri. Analyse comparée des différentes méthodes pour l’évaluation environnementale d’aménagements et de stratégies de régulation routière. Technical report, IFSTTAR - COSYS - LICIT, 2015.
- [107] D. Lejri, L. Leclercq, F. Golay, M. D’Auria, and M. André. Coherence des échelles de représentation des trafics et de polluants. CoERT-P 2.2, 2012.

- [108] X.X. Li, C.H. Liu, D. YC Leung, and K. M. Lam. Recent progress in CFD modelling of wind field and pollutant transport in street canyons. *Atmospheric Environment*, 40(29):5640–5658, 2006.
- [109] Y. F. Li, Szu Hui Ng, Min Xie, and T. N. Goh. A systematic comparison of metamodeling techniques for simulation optimization in decision support systems. *Applied Soft Computing*, 10(4):1257–1273, 2010.
- [110] G.R. Liu, K. Zaw, Y.Y. Wang, and B. Deng. A novel reduced-basis method with upper and lower bounds for real-time computation of linear elasticity problems. *Computer Methods in Applied Mechanics and Engineering*, 198(2):269–279, 2008.
- [111] A.C. Lorenc. A global three-dimensional multivariate statistical interpolation scheme. *Monthly Weather Review*, 109(4):701–721, 1981.
- [112] R. Lowe and A. Tomlin. Low-dimensional manifolds and reduced chemical models for tropospheric chemistry simulations. *Atmospheric Environment*, 34(15):2425–2436, 2000.
- [113] J. L. Lumley. The structure of inhomogeneous turbulent flows. *Atmospheric turbulence and radio wave propagation*, pages 166–178, 1967.
- [114] Y. Maday and O. Mula. A generalized empirical interpolation method: application of reduced basis techniques to data assimilation. In *Analysis and numerics of partial differential equations*, pages 221–235. Springer, 2013.
- [115] Y. Maday, O. Mula, A.T. Patera, and M. Yano. The Generalized Empirical Interpolation Method: Stability theory on Hilbert spaces with an application to the Stokes equation. *Computer Methods in Applied Mechanics and Engineering*, 287:310–334, 2015.
- [116] Y. Maday, O. Mula, and G. Turinici. Convergence analysis of the generalized empirical interpolation method. *SIAM Journal on Numerical Analysis*, 54(3):1713–1731, 2016.
- [117] Y. Maday, A.T. Patera, J.D. Penn, and M. Yano. PBDW state estimation: Noisy observations; configuration-adaptive background spaces; physical interpretations. *Proceedings SMAI CANUM 2014, Carry-le-Rouet, France, in ESAIM: Proceedings and Surveys*, 2014.
- [118] Y. Maday, A.T. Patera, J.D. Penn, and M. Yano. A parameterized-background data-weak approach to variational data assimilation: formulation, analysis, and application to acoustics. *International Journal for Numerical Methods in Engineering*, 102(5):933–965, 2015.
- [119] Y. Maday, A.T. Patera, J.D. Penn, and M. Yano. A parameterized-background data-weak approach to variational data assimilation: formulation, analysis, and application to acoustics. *Int. J. Numer. Meth. Engng*, 102(5):933–965, 2015.

- [120] Y. Maday and B. Stamm. Locally Adaptive Greedy Approximations for Anisotropic Parameter Reduced Basis Spaces. *SIAM J. Sci. Comput.*, 35(6):A2417–A2441, 2013.
- [121] D.S. Malkus. Eigenproblems associated with the discrete LBB condition for incompressible finite elements. *International Journal of Engineering Science*, 19(10):1299–1310, 1981.
- [122] V. Mallet and B. Sportisse. Uncertainty in a chemistry-transport model due to physical parameterizations and numerical approximations: An ensemble approach applied to ozone modeling. *Journal of Geophysical Research: Atmospheres*, 111(D1), 2006.
- [123] A. Manzoni. An efficient computational framework for reduced basis approximation and *a posteriori* error estimation of parametrized Navier-Stokes flows. *ESAIM: Mathematical Modelling and Numerical Analysis*, 48(4):1199–1226, 2014.
- [124] B. Marchand, L. Chamoin, and C. Rey. Real-time updating of structural mechanics models using Kalman filtering, modified constitutive relation error, and proper generalized decomposition. *International Journal for Numerical Methods in Engineering*, 107(9):786–810, 2016.
- [125] A. Matzoros. Results from a model of road traffic air pollution, featuring junction effects and vehicle operating modes. *Traffic Engineering and Control*, 31:24–35, 1990.
- [126] I. Mavroidis, S. Andronopoulos, and J. G. Bartzis. Computational simulation of the residence of air pollutants in the wake of a 3-dimensional cubical building. The effect of atmospheric stability. *Atmospheric Environment*, 63:189–202, 2012.
- [127] S. McKeen, G. Grell, S. Peckham, J. Wilczak, I. Djalalova, E.-Y. Hsie, G. Frost, J. Peischl, J. Schwarz, R. Spackman, J. Holloway, J. de Gouw, C. Warneke, W. Gong, V. Bouchet, S. Gaudreault, J. Racine, J. McHenry, J. McQueen, P. Lee, Y. Tang, G. R. Carmichael, and R. Mathur. An evaluation of real-time air quality forecasts and their urban emissions over eastern texas during the summer of 2006 - second texas air quality study field study. *Journal of Geophysical Research: Atmospheres*, 114(D7):D00F11, 2009.
- [128] P. Mestat. Lois de comportement des géomatériaux et modélisation par la méthode des éléments finis. *Etudes et recherches des Laboratoires des Ponts et Chaussées - Serie Geotechnique*, (GT 52), 1993.
- [129] R. Milani, A. Quarteroni, and G. Rozza. Reduced basis method for linear elasticity problems with many parameters. *Computer Methods in Applied Mechanics and Engineering*, 197(51):4812–4829, 2008.

- [130] M. Milliez and B. Carissimo. Computational Fluid Dynamical Modelling of Concentration Fluctuations in an Idealized Urban Area. *Boundary-Layer Meteorology*, 127(2):241–259, 2008.
- [131] A. Mochida and I.Y.F. Lun. Prediction of wind environment and thermal comfort at pedestrian level in urban area. *Journal of Wind Engineering and Industrial Aerodynamics*, 96(10):1498–1527, 2008.
- [132] B. Mohammadi and O. Pironneau. *Analysis of the k-epsilon turbulence model*. Research in Applied Mathematics. Masson, Paris, 1993.
- [133] O. Mula Hernandez. *Quelques contributions vers la simulation parallèle de la cinétique neutronique et la prise en compte de données observées en temps réel*. PhD thesis, Université Pierre et Marie Curie, 2014.
- [134] A. Nassiopoulos and F. Bourquin. Fast three-dimensional temperature reconstruction. *Computer Methods in Applied Mechanics and Engineering*, 199(49):3169–3178, 2010.
- [135] L. Neary, J. W. Kaminski, A. Lupu, and J. C. McConnell. Developments and Results from a Global Multiscale Air Quality Model (GEM-AQ). In *Air Pollution Modeling and Its Application XVII*, pages 403–410. Springer, 2007.
- [136] F. Negri, G. Rozza, A. Manzoni, and A. Quarteroni. Reduced basis method for parametrized elliptic optimal control problems. *SIAM Journal on Scientific Computing*, 35(5):A2316–A2340, 2013.
- [137] E.M. Noth. Spatial Uncertainty. Private Communication, 2016.
- [138] E.M. Noth, C. Dixon-Ernst, S. Liu, L. Cantley, B. Tessier-Sherman, E.A. Eisen, M.R. Cullen, and S.K. Hammond. Development of a job-exposure matrix for exposure to total and fine particulate matter in the aluminum industry. *Journal of Exposure Science and Environmental Epidemiology*, 24(1):89–99, 2014.
- [139] E.M. Noth, S. K. Hammond, G.S. Biging, and I.B. Tager. A spatial-temporal regression model to predict daily outdoor residential PAH concentrations in an epidemiologic study in Fresno, CA. *Atmospheric Environment*, 45(14):2394–2403, 2011.
- [140] A. Nouy. A priori model reduction through Proper Generalized Decomposition for solving time-dependent partial differential equations. *Computer Methods in Applied Mechanics and Engineering*, 199(23):1603–1626, 2010.
- [141] L. Ntziachristos, D. Gkatzoflias, C. Kouridis, and Z. Samaras. COPERT: A European Road Transport Emission Inventory Model. pages 491–504, 2009.
- [142] J.T. Oden, I. Babuška, and C.E. Baumann. A Discontinuous h_p Finite Element Method for Diffusion Problems. *Journal of Computational Physics*, 146(2):491–519, 1998.

- [143] M.A. Olshanskii, A. Reusken, and X. Xu. A stabilized finite element method for advection-diffusion equations on surfaces. *IMA Journal of Numerical Analysis*, 34(2):732–758, 2014.
- [144] World Health Organization. Ambient air pollution: A global assessment of exposure and burden of disease. Technical report, 2016.
- [145] T.L. Otte, G. Pouliot, J.E. Pleim, J.O Young, K.L. Schere, D.C. Wong, P.C.S. Lee, M. Tsidulko, J.T. McQueen, P. Davidson, R. Mathur, H.Y. Chuang, G. DiMego, and N.L. Seaman. Linking the Eta Model with the Community Multiscale Air Quality (CMAQ) Modeling System to Build a National Air Quality Forecasting System. *Weather and Forecasting*, 20(3), 2005.
- [146] P. Pacciarini and G. Rozza. Stabilized reduced basis method for parametrized advection-diffusion PDEs. *Computer Methods in Applied Mechanics and Engineering*, 274:1–18, 2014.
- [147] A. M. Padula, E. M. Noth, S. K. Hammond, F. W. Lurmann, W. Yang, I. B. Tager, and G. M. Shaw. Exposure to airborne polycyclic aromatic hydrocarbons during pregnancy and risk of preterm birth. *Environmental research*, 135:221–226, 2014.
- [148] M. Pagowski, G. A. Grell, D. Devenyi, S. E. Peckham, S. A. McKeen, W. Gong, L. Delle Monache, J. N. McHenry, J. McQueen, and P. Lee. Application of dynamic linear regression to improve the skill of ensemble-based deterministic ozone forecasts. *Atmospheric Environment*, 40(18):3240–3250, 2006.
- [149] B. Peherstorfer and K. Willcox. Data-driven operator inference for nonintrusive projection-based model reduction. *Computer Methods in Applied Mechanics and Engineering*, 306:196–215, 2016.
- [150] R. W. Pinder, R. C. Gilliam, K. W. Appel, S. L. Napelenok, K. M. Foley, and A. B. Gilliland. Efficient probabilistic estimates of surface ozone concentration using an ensemble of model configurations and direct sensitivity calculations. *Environmental science & technology*, 43(7):2388–2393, 2009.
- [151] M. Pontiggia, M. Derudi, M. Alba, M. Scaioni, and R. Rota. Hazardous gas releases in urban areas: Assessment of consequences through CFD modelling. *Journal of Hazardous Materials*, 176(1-3):589–596, 2010.
- [152] M. Pontiggia, G. Landucci, V. Busini, M. Derudi, M. Alba, M. Scaioni, S. Bonvicini, V. Cozzani, and R. Rota. CFD model simulation of LPG dispersion in urban areas. *Atmospheric Environment*, 45(24):3913–3923, 2011.
- [153] C. Prud’homme, D. V. Rovas, K. Veroy, L. Machiels, Y. Maday, A. T. Patera, and G. Turinici. Reliable real-time solution of parametrized partial differential equations: Reduced-basis output bound methods. *Journal of Fluids Engineering*, 124(1):70–80, 2002.

- [154] C. Prud’Homme, D.V. Rovas, K. Veroy, L. Machiels, Y. Maday, A. T. Patera, and G. Turinici. Reliable Real-Time Solution of Parametrized Partial Differential Equations: Reduced-Basis Output Bound Methods. *Journal of Fluids Engineering*, 124(1):70–80, 2001.
- [155] E. Pruliere, F. Chinesta, and A. Ammar. On the deterministic solution of multidimensional parametric models using the proper generalized decomposition. *Mathematics and Computers in Simulation*, 81(4):791–810, 2010.
- [156] A. Quarteroni, G. Rozza, and A. Quaini. Reduced basis methods for optimal control of advection-diffusion problems. In *Advances in Numerical Mathematics*, pages 193–216. RAS and University of Houston, 2007.
- [157] D. Quélo, V. Mallet, and B. Sportisse. Inverse modeling of NOx emissions at regional scale over northern France: Preliminary investigation of the second-order sensitivity. *Journal of Geophysical Research: Atmospheres*, 110(D24), 2005.
- [158] A. Radermacher and S. Reese. Model reduction in elastoplasticity: proper orthogonal decomposition combined with adaptive sub-structuring. *Computational Mechanics*, 54(3):677–687, 2014.
- [159] C. Robert, S. Durbiano, E. Blayo, J. Verron, J. Blum, and F.X. Le Dimet. A reduced-order strategy for 4d-Var data assimilation. *Journal of Marine Systems*, 57(1):70–82, 2005.
- [160] C. Robinson. *Image data assimilation with fluid dynamics models: Application to 3D flow reconstruction*. PhD thesis, Université de Rennes 1, 2015.
- [161] L.M. Romero and F.G. Benitez. A boundary element numerical scheme for the two-dimensional convection-diffusion equation. *International journal for numerical methods in engineering*, 76(13):2063–2090, 2008.
- [162] Y. Roustan and M. Bocquet. Inverse modelling for mercury over Europe. *Atmospheric Chemistry and Physics*, 6(10):3085–3098, 2006.
- [163] A. Russell and R. Dennis. NARSTO critical review of photochemical models and modeling. *Atmospheric Environment*, 34(12):2283–2324, 2000.
- [164] D. Ryckelynck. Hyper Reduction of finite strain elasto-plastic models. *International Journal of Material Forming*, 2(1):567–571, 2009.
- [165] D. Ryckelynck and D. Missoum Benziane. Multi-level a priori hyper-reduction of mechanical models involving internal variables. *Computer Methods in Applied Mechanics and Engineering*, 199(17-20):1134–1142, 2010.
- [166] D. Ryckelynck, F. Vincent, and S. Cantournet. Multidimensional a priori hyper-reduction of mechanical models involving internal variables. *Computer Methods in Applied Mechanics and Engineering*, 225-228:28–43, 2012.

- [167] S. Peckham, G.A. Grell, S.A. McKeen, M. Barth, G. Pfister, C. Wiedinmyer, J.D. Fast, W.I. Gustafson, R. Zaveri, R. Easter, J. Barnard, E. Chapman, M. Hewson, R. Schmitz, M. Salzmann, and S. Freitas. WRF-Chem Version 3.7 User’s Guide. NOAA Technical Memo, NCAR, 2015.
- [168] S.M. Salim, R. Buccolieri, A. Chan, and S. Di Sabatino. Numerical simulation of atmospheric pollutant dispersion in an urban street canyon: comparison between RANS and LES. *Journal of Wind Engineering and Industrial Aerodynamics*, 99(2):103–113, 2011.
- [169] Adrian Sandu, Dacian N. Daescu, Gregory R. Carmichael, and Tianfeng Chai. Adjoint sensitivity analysis of regional air quality models. *Journal of Computational Physics*, 204(1):222–252, 2005.
- [170] J. L. Santiago, A. Dejoan, A. Martilli, F. Martin, and A. Pinelli. Comparison between large-eddy simulation and reynolds-averaged navier-stokes computations for the must field experiment. part i: Study of the flow for an incident wind directed perpendicularly to the front array of containers. *Boundary-Layer Meteorology*, 135(1):109–132, 2010.
- [171] J. Luis Santiago, A. Martilli, and F. Martín. CFD simulation of airflow over a regular array of cubes. Part I: Three-dimensional simulation of the flow and validation with wind-tunnel measurements. *Boundary-Layer Meteorology*, 122(3):609–634, 2007.
- [172] J.M. Santos, N. C. Reis, E.V. Goulart, and I. Mavroidis. Numerical simulation of flow and dispersion around an isolated cubical building: The effect of the atmospheric stratification. *Atmospheric Environment*, 43(34):5484–5492, 2009.
- [173] M. Schatzmann and R. Britter. Quality assurance and improvement of micro-scale meteorological models. *International Journal of Environment and Pollution*, 44(1-4):139–146, 2011.
- [174] C. Seigneur, X.A. Wu, E. Constantinou, P. Gillespie, R. W. Bergstrom, I. Sykes, A. Venkatram, and P. Karamchandani. Formulation of a second-generation reactive plume and visibility model. *Journal of the Air & Waste Management Association*, 47(2):176–184, 1997.
- [175] S. Sen, K. Veroy, D.B.P. Huynh, S. Deparis, N.C. Nguyen, and A.T. Patera. ”Natural norm” a posteriori error estimators for reduced basis approximations. *Journal of Computational Physics*, 217(1):37–62, 2006.
- [176] M. Signorini, S. Zlotnik, and P. Dìez. Proper generalized decomposition solution of the parameterized Helmholtz problem: application to inverse geophysical problems. *Int. J. Numer. Meth. Engng*, 109(8):1085–1102, 2017.
- [177] L. Soulhac, P. Salizzoni, F.X. Cierco, and R. Perkins. The model SIRANE for atmospheric urban pollutant dispersion; part I, presentation of the model. *Atmospheric Environment*, 45(39):7379–7395, 2011.

- [178] L. Soulhac, P. Salizzoni, P. Mejean, D. Didier, and I. Rios. The model SIRANE for atmospheric urban pollutant dispersion; part ii: validation of the model on a real case study. *Atmospheric Environment*, 49:320–337, 2012.
- [179] B. Sportisse. Atmospheric Boundary Layer. In *Fundamentals in Air Pollution*, pages 93–132. Springer Netherlands, Dordrecht, 2010.
- [180] B. Sportisse. *Fundamentals in Air Pollution*. Springer Netherlands, Dordrecht, 2010.
- [181] T. Stathopoulos, L. Lazure, P. Saathoff, and A. Gupta, editors. *The effect of stack height, stack location and rooftop structures on air intake contamination: a laboratory and full-scale study*. Number R-392 in Studies and research projects. Report. Institut de recherche Robert-Sauvé en santé et en sécurité du travail du Québec, Montréal, 2004.
- [182] Taddei, T. *Model order reduction methods for data assimilation; state estimation and structural health monitoring*. PhD thesis, Massachusetts Institute of Technology, 2016.
- [183] QGIS Development Team. QGIS, 2014.
- [184] Y. Tominaga and T. Stathopoulos. Turbulent Schmidt numbers for CFD analysis with various types of flowfield. *Atmospheric Environment*, 41(37):8091–8099, 2007.
- [185] Y. Tominaga and T. Stathopoulos. Numerical simulation of dispersion around an isolated cubic building: model evaluation of RANS and LES. *Building and Environment*, 45(10):2231–2239, 2010.
- [186] Y. Tominaga and T. Stathopoulos. CFD simulation of near-field pollutant dispersion in the urban environment: A review of current modeling techniques. *Atmospheric Environment*, 79:716–730, 2013.
- [187] Y. Trémolet. Accounting for an imperfect model in 4d-Var. *Quarterly Journal of the Royal Meteorological Society*, 132(621):2483–2504, 2006.
- [188] USEPA. Emission Factor Documentation for AP-42, Section 13.2.1 Paved Roads. Technical report, Measurement Policy Group, Office of Air Quality Planning and Standards,, 2011.
- [189] A. G. Venetsanos, D. Vlachogiannis, A. Papadopoulos, J. G. Bartzis, and S. Andronopoulos. Studies on pollutant dispersion from moving vehicles. *Water, Air and Soil Pollution: Focus*, 2(5-6):325–337, 2002.
- [190] P. T. M. Vermeulen and A. W. Heemink. Model-reduced variational data assimilation. *Monthly weather review*, 134(10):2888–2899, 2006.
- [191] K. Veroy. *Reduced-basis methods applied to problems in elasticity: Analysis and applications*. PhD thesis, Massachusetts Institute of Technology, 2003.

- [192] K. Veroy and A.T. Patera. Certified real-time solution of the parametrized steady incompressible Navier-Stokes equations: rigorous reduced-basis a posteriori error bounds. *International Journal for Numerical Methods in Fluids*, 47(8):773–788, 2005.
- [193] J. Waeytens, P. Chatellier, and F. Bourquin. Inverse computational fluid dynamics: Influence of discretization and model errors on flows in water network including junctions. *Journal of Fluids Engineering*, 139(5), 2017.
- [194] J. Waeytens, I. Mahfoudhi, M.A. Chabchoub, and P. Chatellier. Adjoint-based numerical method using standard engineering software for the optimal placement of chlorine sensors in drinking water networks. *Environmental Modelling & Software*, 92:229–238, 2017.
- [195] B.C. Wang, E. Yee, and F.S. Lien. Numerical study of dispersing pollutant clouds in a built-up environment. *International Journal of Heat and Fluid Flow*, 30(1):3–19, 2009.
- [196] WHO Europe. WHO guidelines for indoor air quality: selected pollutants, 2014.
- [197] J.G. Wilson, S. Kingham, J. Pearce, and A.P. Sturman. A review of intra-urban variations in particulate air pollution: Implications for epidemiological research. *Atmospheric Environment*, 39(34):6444–6462, 2005.
- [198] Z.T. Xie. Large-eddy simulation of stratification effects on dispersion in urban environments. *Journal of Hydrodynamics, Ser. B*, 22(5):1003–1008, 2010.
- [199] Z.T. Xie and I.P. Castro. Large-eddy simulation for flow and dispersion in urban streets. *Atmospheric Environment*, 43(13):2174–2185, 2009.
- [200] R.J. Yamartino. Gaussian puff modeling. In *Chapter 8A: Air Quality Modeling*, volume 1. EnviroComp Institute and Air & Waste management Association, 2008.
- [201] E. Yee and C.A. Biltoft. Concentration Fluctuation Measurements in a Plume Dispersing Through a Regular Array of Obstacles. *Boundary-Layer Meteorology*, 111(3):363–415, 2004.
- [202] Y. Zhang, M. Bocquet, V. Mallet, C. Seigneur, and A. Baklanov. Real-time air quality forecasting, part I: History, techniques, and current status. *Atmospheric Environment*, 60:632–655, 2012.
- [203] Y. Zhang, M. Bocquet, V. Mallet, C. Seigneur, and A. Baklanov. Real-time air quality forecasting, part II: State of the science, current research needs, and future prospects. *Atmospheric Environment*, 60:656–676, 2012.
- [204] Y. Zhang, A. Combescure, and A. Gravouil. Efficient hyper reduced-order model (HROM) for parametric studies of the 3d thermo-elasto-plastic calculation. *Finite Elements in Analysis and Design*, 102:37–51, 2015.

- [205] Y. Q. Zhang, S. P. Arya, and W. H. Snyder. A comparison of numerical and physical modeling of stable atmospheric flow and dispersion around a cubical building. *Atmospheric Environment*, 30(8):1327–1345, 1996.
- [206] Z. Zhang and Q. Chen. Comparison of the Eulerian and Lagrangian methods for predicting particle transport in enclosed spaces. *Atmospheric Environment*, 41(25):5236–5248, 2007.
- [207] Z. Zhang, G. Cui, R.F. Shi, Z. S. Wang, and C. Xu. Large Eddy Simulation of traffic pollutant dispersion in a residence area. pages YN–014. Begellhouse, 2009.